SEISMIC INTERFACE STABILITY OF COMPOSITE DAMS

by

Fatih Öncül

B.S., Middle East Technical University, 1992

M.S., University of Colorado at Denver, 1995

A thesis submitted to the

University of Colorado at Denver

in partial fulfillment

of the requirements for the degree of

Doctor of Philosophy

Civil Engineering

2001

AL

This thesis for the Doctor of Philosophy

degree by

Fatih Öncül

has been approved

by

Nien-Yin Chang

Hon-Yim Ko

Benson Shing

John R. Mays

Brian T. Brady

4/26/01

Date

Öncül, Fatih (Ph.D., Civil Engineering)

SEISMIC INTERFACE STABILITY OF COMPOSITE DAMS

Thesis directed by Professor Nien-Yin Chang

ABSTRACT

Many earth dams failed or suffer great distress in the past earthquakes. The potential grave consequence of dam failures has led research scientists to pay great attention to the investigation of the potential causes of dam failures and the formulation of the mechanism for their prevention. Because of the site condition and the need for the power generation, many dam are of composite type. This means the body of the dam is composed of a concrete dam, embankment wing dams and the transitional (or wrapped-around) section. There are over one hundred composite dams in the world that are higher than 100 feet and some of them are located in seismically active areas. Thus, it is important to study the seismic safety of composite dams.

Though much research effort has been devoted to the seismic dam safety in the last three decades, the seismic soil-concrete interface stability in a composite dam has received insignificant attention. The late Professor H. B. Seed pointed out the need for the investigating the seismic interface stability in one of its research memorandum. Then, in early 1980's, the Earthquake Engineering and Geoscience Division, Geotechnical and Structural Laboratory, the Waterways Experiment Station, the U.S. Army Corps of Engineers began the study of the seismic stability of the soil-concrete interface stability. The research was hindered by the lack of appropriate computer code.

The University of Colorado at Denver (UCD) was involved in this initial effort. Initially, FLUSH developed at the UC Berkeley was used in the study and the potential for the interface separation was confirmed. However, the evaluation of the size and depth of separation was not possible, until the availability of NIKE3D computer code developed at the Lawrence Livermore National Laboratory (LLNL) through the collaborative agreement between LLNL and UCD.

NIKE3D computer code has the interface formulation needed for the assessment of the interface behavior under seismic load and it has been used extensively in this study. Its effectiveness in evaluating the interface behavior was calibrated using the dynamic centrifuge test on a retaining wall model with a dry sand backfill. The centrifuge test was performed at the University of Colorado at Boulder (Stadler, 1996). The excellent agreement between the centrifuge model test and the numerical analysis using NIKE3D confirms the validity of the NIKE3D as a study tool for the soil-structure interface behavior under seismic shaking.

Extensive numerical analyses were performed to study the seismic interface stability of composite dams. Numerous plane-strain analyses were performed to assess the effect of the slope of embankment and concrete dam on the size and depth of interface separation of composite dams with height ranging from 100 to 400 feet during strong seismic shaking. The results show the interface behavior is strongly affected by the slope of the respective side of the dam and the height of the dam. Six 3-dimensional analyses were also performed. The significant difference in 2-D and 3-D results indicate the need for 3-D analysis for accurate assessment of the performance of the interface in a composite dam.

Both elastic model and Ramberg-Osgood model were used in the investigation of the soil model effect. It was determined that an appropriate soil model is critical to the effective assessment of the interface behavior.

The effect of the imposition of all three components of earthquake ground motion on the interface performance was also studied. It was found that while the effect on the transverse interface was pronounced, its effect on the upstream and downstream interfaces was not.

While the study is extensive, it only touches the surface of the problem. Much research work is needed to critically examine the seismic stability of interface and the overall stability of composite dams.

This abstract accurately represents the content of the candidate's thesis. I recommend its publication.

Signed 

Nien-Yin Chang

DEDICATION

Dedicated to my wife EBRU ÖNCÜL and my son ÖMER

ACKNOWLEDGMENTS

I would like to take this opportunity to express my gratitude to those who have contributed to the development of this thesis.

Firstly, I am greatly indebted to Prof. Nien-Yin Chang for his guidance, support, friendship, and valuable comments on each part of the thesis. Having the opportunity to work with Prof. N. Y. Chang was an experience that helped me gain broader perspective on many areas.

I also wish to thank the members of the committee, Prof. H.Y. Ko, Prof. Benson Shing, Prof. John Mays, and Prof. Brian Brady for their helpful comments and suggestions.

The guidance and support from Dr. Mike Puso is greatly acknowledged. Phone conversations during the numerical analysis part of the thesis was very helpful.

The financial support of the Dumlupinar University in Kutahya, Turkey is gratefully acknowledged. Special thanks to Colorado Department of Transportation (CDOT) for providing financial support during the final years of my doctoral study.

I also would like to thank Dr. Liu Jiang who helped me on using NIKE3D, and numerous occasions. Special thanks to Jan Chang for his encouragement, and valuable friendship during my study. My thanks are extended to Mr. Cengiz Alkan, and Mr. Kevin Lee for their support.

I profoundly thank my parents, sister, brother, and their families for providing me moral support and for their patience. Finally, but not the least, I am grateful to my dear wife Ebru and my son Ömer for their continuous love and patience during my Ph.D. study.

CONTENTS

FIGURES

Figure

TABLES

Table

1. Introduction

1.1 Problem Statement

Many earth dams either failed or suffered severe distress in past earthquakes. Thus, it is critical to analyze their performance during strong motion earthquakes to provide sufficient information for dam- safety assessment. Though many dynamic analysis methods have been developed in the past two and a half decades, the complicated Interface Behavior of Composite Dams (IBCD) has never received significant attention because of the lack of more realistic soil models and soil-concrete interface models.

In the evaluation of the seismic stability of a composite dam, besides others, the main problem is the dynamic interaction between concrete gravity dam and soil embankment. The wrap-around sections are the transitional sections of a dam where it changes from concrete dam to embankment wing dams. As an example; Folsom Dam is shown in Figure 1.1. Soil-concrete interface areas between concrete dam and both upstream and downstream embankment wing dams are also illustrated in Figure 1.1. Figure 1.2 shows a typical two dimensional composite section in the wrap around region. The disastrous consequences of a dam failure provides incentives for a precise analysis of the problem. During strong earthquake shaking, the soil may slip and/or separate (debond) from concrete and, upon the reversal of the direction of motion, the soil may reattach

(rebond) itself to the concrete surface. Debonding along the upstream surface allows water to enter the gap created during the process and water is expelled upon rebonding from the gap. The repeated debonding-rebonding can result in a permanent gap due to plastic embankment deformation, internal erosion due to the water pumping action and further the dam failure. Due to the lack of necessary analysis tools it has been difficult to perform the rational analysis of the interface performance. This thesis aims to provide more insight into IBCD.

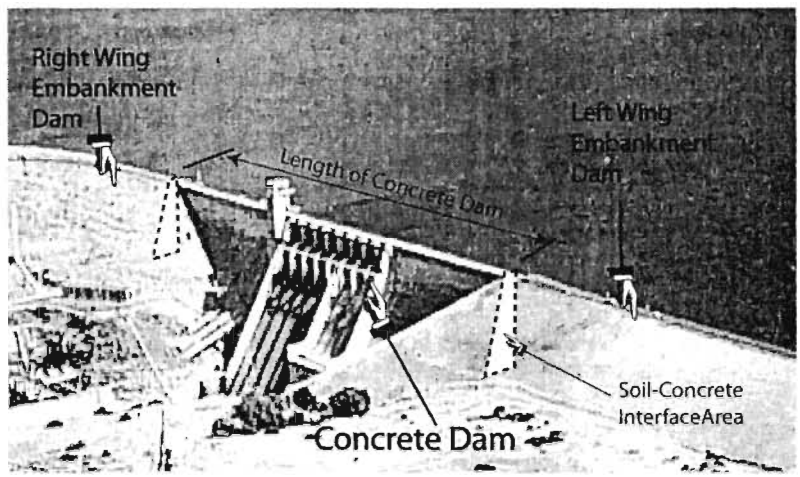

Figure 1.1 Folsom Dam, California.

The study covers both 2-D and 3-D modelling of interface area, elastic-plastic material model, effect of different geometric configurations of the interface on the separation, separation depth, horizontal acceleration, and earthquake induced stresses along the both upstream and downstream interfaces.

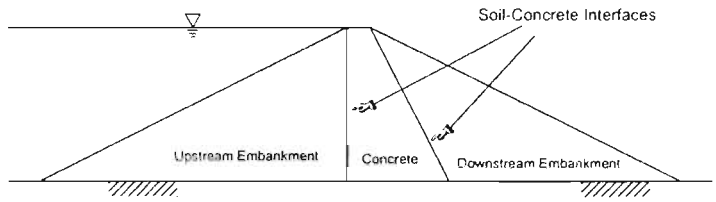

Figure 1.2 A typical soil-concrete interface of a composite dam.

1.2 Significance of Research

Because of the growing public concern for the safety of dams and reservoir and the oversimplifications of the analysis methods used in designing dams it is urgently needed to reevaluate the original designs and current procedures using new and more realistic computation tools.

So far the soil-concrete interface has not been reported as the major reason for the earthquake induced dam failure or distress. However, this does not mean that the seismic safety of IBCD is not of concern. In fact, the analysis results indicate the possibility of interface separation, acceleration amplification, and high pressure which could lead to the dam distress or failure and the problem requires immediate research attention. In the list of The World's Major Dams and Hyroplants [53], it is reported that there are 36 concrete dams having wing dams in the countries other than US. In the US alone, there are more than 40 dams, higher than 100 ft, having composite sections. Figure 1.3 shows the U.S. earthquake hazard map and the circled numbers represent the number of composite dams by state.

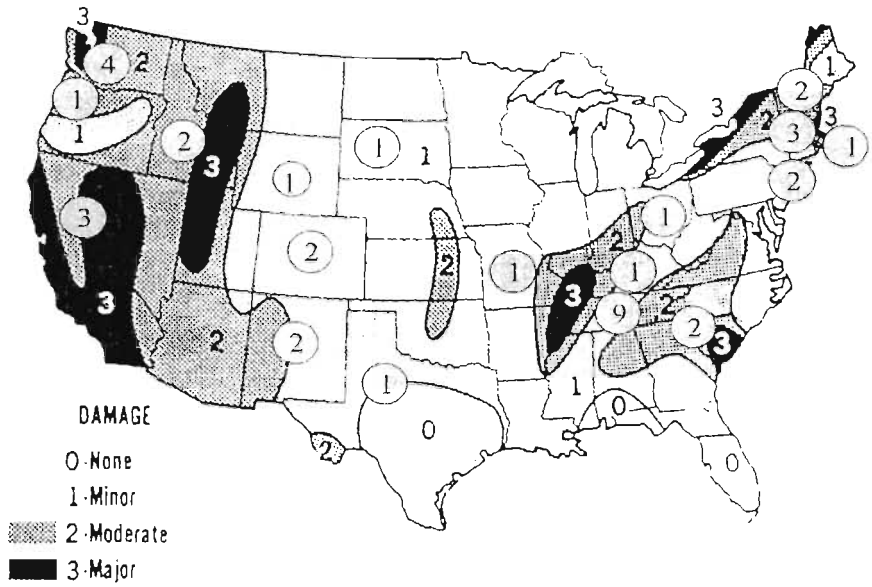

Figure 1.3 The U.S earthquake hazard map and the number of composite dams by state (circled numbers).

The ability to evaluate the earthquake effect on the behavior of the composite dam is critical to the assessment of the overall seismic safety of dams, to the design of remedial measures, and to the new design strategy combating this potential problem.

1.3 Research Objectives

This study uses the finite element analysis to study the composite dam interface behavior in lieu of the many other research tools available, mainly because of its cost effectiveness over physical model tests. An extensive survey was carried out to find computer codes appropriate for the study, particularly the code with a suitable interface formulation for simulating the soil-concrete interface effect in a composite dams. NIKE3D developed at the Lawrence Livermore National Laboratory (LLNL) was selected for use in this study and beyond for the availability of its source code and technical consultation as long as the LLNL and the University has an appropriate collaborative agreement. The effectiveness of the code in simulating the interface behavior was calibrated using the centrifuge model test results. An excellent agreement was achieved. This provides a great confidence in the ability of NIKE3D in simulating the interface problems in composite dams under seismic shaking. The objectives of this study are multiple:

- To develop a better understanding of the behavior of the soil-concrete interface in a composite dam under strong seismic shaking in terms of the potential

repetitive debonding and rebonding, the depth of such action, and the extend of such problem.

- To clearly delineate the critical problems for future research on the interface behavior in composite dams.
- To investigate the effect of the slope of the concrete dam and embankment in the wrapped-around section on the magnitude of separation and separation depth.
- To assess the distribution of the dynamic earth pressure along the interface, and the motion amplification.
- To assess the three-dimensional effect by performing three-dimensional modelling of the wrapped-around section.
- To assess the effect of soil models on the interface behavior.
- To assess the effect of imposing all three components (N/S, E/W and Vertical) of ground motion on the interface behavior.

1.4 Research Approach

To achieve the research objectives a systematic approach was adopted. It should also be noted that no other work has been found on IBCD in the literature, except some numerical analyses. Therefore this study is the first detailed research effort on IBCD.

The steps of the research approach followed in this study can be itemized as follows:

- Selection of numerical analysis computer code, and verification of its reliability.
- Building hypothetical 2-D, and 3-D finite element model,

- Determining controlling parameters, and interface performance parameters,
- Performing 2-D, and 3-D parametric finite element analyses,
- Comparing 2-D, and 3-D finite element analysis results,
- Statistical assessment of finite element results,
- Offering recommendations on remedial measures for existing dams, and new design strategies.

A proper analysis of the dynamic interface behavior of a composite dam requires a numerical analysis computer code(s) with a nonlinear soil model and soil-structure interface characteristics. The interface characteristics must include the capability of modelling the interface slippage, debonding and rebonding. NIKE3D was selected for this study with Ramberg-Osgood non-linear material model and interface algorithm that allows separation and frictional sliding.

Hypothetical FE models were created using the mesh generator code TrueGrid. The effect of overburden pressure on the material properties was considered by dividing upstream and downstream embankments into different layers.

Geometric cross-sectional parameters were selected as the controlling parameters; they are the upstream soil slope, upstream interface angle, downstream soil slope, downstream interface angle, and height. As the interface performance parameters the separation, separation depth, maximum acceleration, maximum RMS acceleration, and minimum, static, and maximum pressures along the interface were selected.

Numerous 2-D FE analyses have been performed. Due to the time consuming nature of 3-D FE analysis, limited number of 3-D FE analyses were performed. Results are compared and interpreted.

To investigate the degree of dependency of interface performance parameters on the controlling parameters, statistical assessment has been performed.

2. Literature Survey

2.1 Introduction

In this chapter, a survey has been carried out on existing concrete dams with embankment abutment or wing dams in the US and in the world. Besides the existing dams, an extensive literature survey has been conducted about interface behavior study of composite dams. Moreover, literature review on dynamic interface effects, available computer codes to analyze IBCD and constitutive soil models are included.

2.2 Existing Composite Dams

In order to locate the existing concrete dam with soil in its cross-section, numerous databases have been searched. Bureau of Reclamation online database is one of them. USACE's (US Army Corpse of Engineers) database called NID (National Inventory of Dams) has also been used. NID has around 75,000 records and 59 information fields.

NID database does not have any specific field entry to search composite dams, but dams classified as "concrete gravity & earth or rock fill" can be searched. This is the closest definition for composite dams. Findings of all database research are tabulated in Table 2.1. Additionally, The World's Major Dams and Hydroplant [53] lists 36 "concrete &

earthfill" dams outside the US. Table 2.2 shows the distribution of these dams by country.

2.3 Literature Review on Analysis of Composite Dams

An extensive literature survey has been conducted about interface behavior study of composite dams. Because of the lack of necessary analysis tools only a few calculations have been made that account for the nonlinear effects with rebonding and debonding behavior of the soil-concrete interface of composite dams. In the literature it is possible to find extensive research reports about concrete gravity and embankment dams studying the effect of dam-water and dam-water-foundation interactions, water compressibility, base sliding of concrete monoliths, reservoir bottom absorption, cavitation , flexibility of concrete dams etc., but none of these addresses the soil-concrete interface separation problem. In the literature, the interface separation phenomenon was first mentioned in Seismic Analysis of Wing Dams of Folsom Dam reports [80, 74]. Because of the lack of necessary tools, no numerical analysis results, related to separation, were presented in these reports.

The interface behavior of composite dams was first studied by Chang [10] and Oncul [57]. Chang [10] conducted analyses using the code FLUSH with nonlinear shear modulus and damping ratio versus shear strain. Oncul performed analyses on IBCD using computer code NIKE2D [21] with Ramberg-Osgood (R-O) non-linear material model. The NIKE2D code also contains the interface algorithm that allows debonding,

Table 2.1 List of Dams with Embankment Wing Dams

Some Geometric and Dynamic Properties of Composite Dams							
Name of Dam	State	Height (ft)	Crest Width (ft)	Base Width (ft)	Dynamic Properties		
					MCE(M)	Peak Acce. (g)	$f(hz)$
Concrete Gravity Dams							
American Falls	ID	104	43	59	7.5	0.67	10.3
Angostura	SD	193	10	230	6.7	0.19	-
Jackson Lake	WY	66	24	72	-	-	-
Keswick	CA	157	20	111	-	-	-
Marshall Ford	TX	278	20	286	5.3	0.09	2.70
Olympus	CO	70	10	50	5.0	0.17	-
Shosta	CA	602	30	543	6.25	0.46	2.90
Brantley	NM	-	-	-	-	-	-
Folsom	CA	170	32	139	6.5	0.35	-
Lower Monumental	WA	155	-	-	-	-	-
Little Goose	WA	-	-	-	-	-	-
Ice Harbor	WA	123	-	-	-	-	-
Lower Granite	WA	-	-	-	-	-	-
Butress Dams							
Lake Tahoe	CA	18	11	19	6.0	0.58	-
Minidoka	ID	86	-	-	-	-	-
Pueblo	CO	250	30	147	5.0	0.13	-
Thin Arch Dams							
Nambe Falls	NM	150	5	15	6.5	0.69	6.67
Dams Classified as "Concrete Gravity & Earth " in NID Database							
Thomaston	CT	137	-	-	-	-	-
Colebrook	CT	215	-	-	-	-	-
Black Rock	CT	130	-	-	-	-	-
Carters Main	GA	464	-	-	-	-	-
Carters Reregulation	GA	105	-	-	-	-	-
Borden Broook	MA	110	-	-	-	-	-
Knightville	MA	150	-	-	-	-	-
Stockton	MO	161	-	-	-	-	-
Everett	NH	110	-	-	-	-	-
Franklin Falls	NH	116	-	-	-	-	-
Kinzua	PA	177	-	-	-	-	-
Ball Mountain	VT	247	-	-	-	-	-
North Hartland	VT	182	-	-	-	-	-
Townshend	VT	126	-	-	-	-	-
Dams Classified as "Concrete Gravity & Rockfill " in NID Database							
Kentucky	KY	206	-	-	-	-	-
Hoover	OH	124	-	-	-	-	-
Menary	OR	220	-	-	-	-	-
Gainer Memorial	RI	109	-	-	-	-	-
Norris	TN	265	-	-	-	-	-
Normandy	TN	110	-	-	-	-	-
Chickamauga	TN	129	-	-	-	-	-
Pickwick Landing	TN	113	-	-	-	-	-
Fort Loudoun	TN	125	-	-	-	-	-
Tellico	TN	129	-	-	-	-	-
Columbia	TN	105	-	-	-	-	-
Watts Bar	TN	112	-	-	-	-	-
Boone	TN	168	-	-	-	-	-

Table 2.2 Number of dams, higher than 150 meters, classified as "concrete & earth" outside the US [53].

Country	# of Dams	Country	# of Dams
Argentina	7	India	5
Brazil	13	Netherlands	1
Canada	3	Nigeria	1
Czechoslovakia	1	Paraguay	3
Hungary	1	Turkey	1

rebonding and frictional sliding. Analysis results are compared to assess the effectiveness of these two computer codes in evaluating the phenomenon of interface separation [57]. The Left Wing Dam of the Folsom Dam, 180 ft high, is chosen in the analyses. Koyna Dam Earthquake Record with $a_{max} = 0.87$g was used in both NIKE2D and FLUSH analyses.

In summary, the NIKE2D analysis confirmed the suspicion of the interface separation using FLUSH with the following observations: i) the soil-concrete interface can separate under a strong motion earthquake, ii) the separation is significant and repetitive, and iii) the separation can reach a significant depth.

To get a better understanding of IBCD parametric studies should be performed to see the effects of different ground motions, interface geometry and material models. Chang et al. [11] performed preliminary parametric analysis on a 100 ft high hypothetical composite dam using NIKE3D. Results indicate that angle of upstream interface has significant effect on separation and separation depth.

Due to the fact that hydraulic fracture is very possible in the interface area because of its debonding and rebonding nature, it is necessary to mention the literature on

hydraulic fracture. As the soil and concrete separate the minor principal reduces to zero at the soil face and that causes hydraulic fracture to occur. Hydraulic fracture is promoted by the presence of the discontinuity, such as borehole, an existing crack, or loose soil adjacent to rock joint. Hydraulic separation may occur at an interface between soil and adjacent dissimilar material such as concrete or rock as soon as the water pressure reaches the same magnitude as the normal stress across the interface [38]. Hydraulic separation is more likely to occur than hydraulic fracturing because there is no tensile strength to resist separation. Jaworski et al. [38] showed in experimental studies that initial hydraulic fracturing requires, in general, hydraulic pressure in the range of 1.5 to 1.8 times larger than the minor total principal stress. However they also show that existing crack would require hydraulic pressure equal to minor total principal stress. Sherard [70] states that very steep rock abutments and near vertical concrete structures produce zones susceptible to cracking and leakage, because heavy compaction equipment can not operate close to concrete structures due to limited space, and compaction is done with hand operated small machines.

In terms of centrifuge testing, there is no particular composite dam centrifuge test attempt. Arulanandan et. al. [1, 54] has performed dynamic centrifuge tests on an earth dam that has sand-clay interfaces. The results show that failure mode on the dam is greatly influenced by the reduction in strength caused by the void-ratio increase at the sand-clay interface and the corresponding decrease in effective stress.

Aforementioned hydraulic fracture and clay-sand interface performance indicate the complexity of interface behavior between dissimilar materials. There has been no complete and reliable analytical methodology to resolve the soil-concrete interface problems. On the other hand computer programs developed recently with powerful algorithms may serve as important tools to understand the dynamic soil-concrete interface.

2.4 Soil-Concrete Interface Models

Besides the non-linear stress-strain relation of soils, contact-impact problems are among the most difficult nonlinear problems because the response in contact-impact problems is not smooth. The velocities normal to the contact surface are discontinuous in time when impact occurs. For Coulomb friction models, the tangential velocities along the interface are discontinuous when stick-slip behavior encountered, and they introduce significant difficulties in the time integration of the discrete equations [4].

Desai et al. [18] performed numerous lab tests on the interface behavior and developed an interface model using Ramberg-Osgood model without debonding and rebonding features. In the lab environment it is very difficult to obtain accurate volume change and stress measurements required to determine parameters for advanced interface models such as those based on the theory of plasticity [18].

A realistic interface algorithm should be able to simulate frictional slippage, separation and re-bonding behavior of the soil-concrete interface at any loading step. The ideal interface algorithm should possess the following characteristics;

- closely simulate the soil-concrete interface behavior during seismic shaking,
- easily adaptable to existing FEM codes,
- should maintain numerical stability.
- should be verifiable with physical test results.

The literature survey reveals various interface algorithms. They can be classified as [39]; 1) stiffness approach (e.g. directionally stiff elements), 2) constrained approach (e.g. Lagrange multipliers, penalty method), 3) mixed approach.

2.4.1 Stiffness Approach

One of the commonly used interface element is based on the joint element proposed by Goodman, Taylor and Brekke [28]. The element formulation is derived on the basis of relative nodal displacements of the solid elements surrounding the interface element as shown in Figure 2.1. This formulation can simulate slip conditions well, but has penetration problems. Using high normal stiffness causes numerical problems. In two dimensional analysis, the constitutive or stress-relative displacement relation is given in Equation 2.1:

$$\left\{ \begin{array}{c} \sigma_n \\ \tau \end{array} \right\} = \left[\begin{array}{cc} k_n & 0 \\ 0 & k_s \end{array} \right] \left\{ \begin{array}{c} v_r \\ u_r \end{array} \right\} = [C]_i \left\{ \begin{array}{c} v_r \\ u_r \end{array} \right\} \tag{2.1}$$

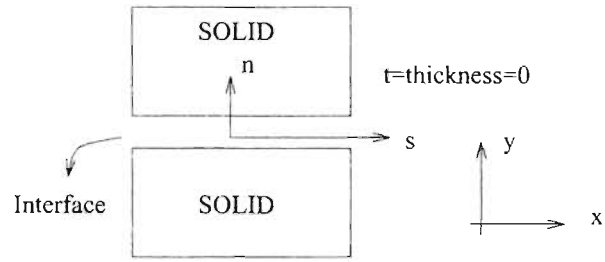

Figure 2.1 Relative displacement element [17]

where σ_n =normal stress, τ =shear stress, k_s =shear stiffness, k_n =normal stiffness and v_r and u_r =relative normal and shear displacements, respectively, and $[C]_i$ =constitutive matrix for the interface element. In the last two decades many researchers have attempted to develop models to simulate the behavior in normal and tangential directions.

Ghabussi, Wilson, Isenberg [27] proposed a formulation which is derived by considering relative motions between surrounding solid elements as independent degrees-of-freedom. This proposed model has less numerical errors and has the ability to simulate positive and negative dilatancy resulting from shear deformations.

For nondilatant joints there is no volume change due to shearing strains and therefore shear and normal components of deformation are uncoupled and Stress-strain relations is given in Equation 2.2:

$$\begin{Bmatrix} \sigma_n \\ \sigma_s \end{Bmatrix} = \begin{bmatrix} C_{nn} & 0 \\ 0 & C_{ss} \end{bmatrix} \begin{Bmatrix} \epsilon_n \\ \epsilon_s \end{Bmatrix} \tag{2.2}$$

where C_{nn} and C_{ss} are nonlinear functions. In relating stress to deformation in the direction normal to the joint, three distinct regions are defined: (1) Separation $C_{nn} = C_{ss} = 0$ when $\epsilon_n \geq 0$; (2) crushing of surface irregularities $C_{nn} = E_c(\epsilon_n^c < \epsilon_n < 0)$, for smooth surfaces $\epsilon_n^c = 0$; and (3) contact, $C_{nn} = E_f(\epsilon_n < \epsilon_n^c)$.

The tangential stress-strain relationship is assumed to be elastic-perfectly plastic using Mohr-Coulomb yield criterion: $C_{ss} = G$ for $\sigma_s < c + tan\phi$(elastic); $C_{ss} = 0$ for $\sigma_s = c + tan\phi$ (plastic, σ_s has reached limiting shear strength).

Herrmann [34] introduced an interface algorithm considering various modes of interface behavior such as re-bonding, de-bonding and slippage. Herrmann's interface algorithm assumes there are tangential and normal springs along the interface to model frictional slip and de-bonding. Although using relative movements as global unknowns eliminates the numerical problems [81], when the spring coefficient is very large, very severe bond stress gradients may result which in return may cause convergence problems.

Katona [39] developed a procedure for friction-contact interface which simulates frictional slippage, separation and re-bonding by using principle of virtual work. Figure 2.2 represents the proposed element in a separated state. At the end of any load step k, the interface responses are characterized by interface forces λ_n^k and λ_s^k, and/or relative movements Δ_n^k and Δ_s^k where subscripts n and s refer to normal and tangent directions. In order to define relative movements, the nodes 1 and 2 in Figure 2.2 are assumed to be in the same location prior to any loading.

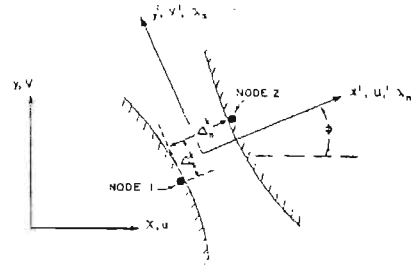

Figure 2.2 Interface element representation in separated state [39].

The use of thin layer elements has shown significant promise in terms of dynamic behavior of interfaces. The idea of thin layer is based on the assumption that the behavior near the interface involves a thin zone, rather than a zero thickness in several investigations [84]. The choice of thickness is very important for dynamic analysis where the mass and damping properties need to be considered.

The idea of "thin-layer" sounds reasonable and studied by many researchers.

Pande and Sharma [59] used 8-node iso-parametric parabolic element using relative displacements as independent degrees of freedom. In this study, the numerical ill-conditioning associated with the choice of thickness for thin joint elements was also presented. If the thickness is too large then it is going to behave like a solid element. If it is too small then numerical problems are very likely to occur.

Desai et. al. [17] proposed a thin-layer element for interfaces and joints. The element is essentially treated like any other solid (soil, rock or structural) element. Since penetration is not allowed at the interface, a high value, of the order of $10^8 - 10^{12}$ units,

is assigned for the normal stiffness k_n which, in fact, has no physical explanation. Therefore, normal stiffness of the element is determined by considering the surrounding geological and structural materials as well as the interface itself. Interpenetration of nodes is treated with special algorithm explained in [17].

Zaman [84] has shown the implementation of the same thin-layer element into dynamic soil-structure interaction problems with debonding and rebonding capabilities.

Furthermore in most problems, the formulations mentioned above can provide satisfactory solutions for the stick and slip modes for which the normal stress remains compressive. For other modes such as de-bonding, the solutions are often unreliable [17].

As a brief summary the advantages and disadvantages of stiffness approach can be itemized as follows;

Advantages;

- easy to implement into existing FEM codes,
- complicated constitutive models can be used for interface elements,
- works well for no separation case,
- a wide literature is available on theory and application in soil mechanics.

Disadvantages;

- not reliable in case of separation,

- implementations are based on "small strains" assumptions,
- selection of thickness of interface elements may cause numerical problems,
- materials must be initially in contact at the discontinuities,
- in most of the current implementations, mesh discontinuity at the interface is not allowed.

2.4.2 Constrained Approach

In contact problems involving friction there are three methods called as Lagrange Multipliers, Penalty Method and Augmented Lagrangian Method. Basically these methods treat the interface as surfaces on each side without introducing any elements into the interface area. Lagrange multipliers are studied by many researchers [3, 35] and implemented in computer codes such as ADINA. Penalty formulation is studied by [31, 32] and implemented in NIKE [21, 47] codes. Augmented lagrangian method is a hybrid of the other two and is accepted as an improved formulation [71, 82]. It is also implemented in NIKE codes.

In the next section each of these methods will be explained briefly together with their shortcomings and advantages. Consider the variational formulation of a discrete structural modal for a steady-state analysis:

$$\Pi^* = \frac{1}{2}\mathbf{U}^T\mathbf{K}\mathbf{U} - \mathbf{U}^T\mathbf{R} \tag{2.3}$$

where Π^* is the total potential energy of the system, $\mathbf{U}$ is the displacement vector, $\mathbf{R}$ is the load vector and $\mathbf{K}$ is the stiffness matrix of the system and with the conditions

$\partial\Pi^* = 0$ for all i. Assume that the displacement at the degree of freedom U_i with $U_i = U_i^*$ needs to be imposed. Next subsections discuss how this constraint is handled in each method.

Lagrange Multipliers

In the Lagrange Multiplier method we amend the right hand side of Equation2.3 to obtain:

$$\mathbf{\Pi}^* = \frac{1}{2}\mathbf{U}^T\mathbf{K}\mathbf{U} - \mathbf{U}^T\mathbf{R} + \lambda(U_i - U_i^*) \tag{2.4}$$

where λ is an additional variable, and invoke $\partial\mathbf{\Pi}^* = \mathbf{0}$, which gives:

$$\begin{bmatrix} \mathbf{K} & e_i \\ e_i^T & 0 \end{bmatrix} \begin{bmatrix} \mathbf{U} \\ \lambda \end{bmatrix} = \begin{bmatrix} \mathbf{R} \\ U_i^* \end{bmatrix} \tag{2.5}$$

where e_i is a vector with all entries equal to zero except ith entry, which is equal to one.

Disadvantages of this method can be listed as;

- may lead to singular stiffness matrices unless partitioning method is used,
- new variables introduced which require more computational effort

Advantages are;

- effective procedure,
- easy to implement,
- no numerical ill-conditioning,

Penalty Formulation

In the penalty method we also amend the right-hand side of Equation2.3 but without introducing an additional variable. Consider the Equation 2.6:

$$\Pi^{**} = \frac{1}{2}\mathbf{U}^T\mathbf{K}\mathbf{U} - \mathbf{U}^T\mathbf{R} + \frac{\alpha}{2}(U_i - U_i^*)^2 \tag{2.6}$$

in which α is a constant of relatively large magnitude, $\alpha \gg \max(k_{ii})$. The condition $\partial\Pi^{**} = 0$ now yields:

$$\partial\mathbf{U}^T\mathbf{K}\mathbf{U} - \partial\mathbf{U}^T\mathbf{R} + \alpha(U_i - U_i^*)\partial U_i = 0 \tag{2.7}$$

and

$$(K + \alpha e_i e_i^T)U = R + \alpha U_i^* e_i \tag{2.8}$$

Hence using this technique, a large value is added to the ith diagonal element of $\mathbf{K}$ and a corresponding force is added so that the requirement displacement U_i is approximately equal to U_i^*.

Advantages:

- no additional variables,
- has simple technique,
- can be interpreted from a physical standpoint.

Disadvantages;

- solution is sensitive to the choice of penalty number α.
- numerical ill-conditioning due to a very large penalty number α,
- exact satisfaction of constraint can only be achieved at a value of infinite for penalty number.

Therefore maximum attention should be given to the choice of penalty number. The optimum choice for penalty number is studied in [2].

In penalty formulation, any node that penetrates through its respective contact surface causes a linear interface spring to be inserted into the stiffness matrix.

Augmented Lagrangian Method

It has been proposed to reduce or eliminate the shortcomings of the previous two methods. Augmented Lagrangian technique has been applied to incompressible finite deformation elasticity, frictionless contact problems and viscoplasticity [71]. Simo et. al.[71] extended the method to apply to frictional problems.

Advantages;

- convergence is achieved with finite penalty numbers,
- inherits advantages of Lagrange multipliers method,
- no additional variables.

Disadvantages;

- by experience it is observed that this method needs more computation time.

2.5 A Brief Review of Computer Codes

There are various numerical analysis codes that has interface model and nonlinear soil models. In this section a list of computer codes for dynamic analysis of dams and their main features are given.

Table 2.3 is the summary of the survey about computer codes suitable for dynamic analyses of dams. Besides the interface property, other features such as pore pressure generation ability, solution method and type of elements are also included.

Since the analysis of IBCD is very complicated, it is required to have a powerful computer code with interface model and pore pressure generation (e.g. Biot Theory) algorithms. Unfortunately none of the computer codes has Biot theory and interface algorithm at the same time. Among all computer codes, NIKE2D & 3D and FLAC with dynamic option are chosen to study IBCD. When appropriate other programs may be added in the future.

NIKE2D and NIKE3D

Computer programs NIKE2D and NIKE3D developed at Lawrence Livermore National Laboratory (LLNL) for defense program applications provide a powerful tool that can

Table 2.3 Codes for Dynamic Analysis

Codes for Dynamic Analysis of Dams								
Software	Type	Element Type		2D	3D	Pore Pressure	Soil Model	Interface
		CO	ST					
CESAR-LCPC	FE	•	•	•	•	•	M-C,D-P,CC,VE,H-B	–
DIANA	FE	•	•	•	•	–	T,M-C,D-P	•
TARA-3	FE	•	–	•	–	•	F	–
ADINA	FE	•	•	•	•	–	D-P	•
ABAQUS	FE	•	•	•	•	•	CC,D-P,M-C	•
NIKE2D	FE,IMP	•	–	•	–	–	R-O	•
NIKE3D(*)	FE,IMP	•	•	•	•	–	R-O	•
DYNA2D	FE,EXP	•	–	•	–	–	R-O	•
DYNA3D	FE,EXP	•	•	•	•	–	R-O	•
DYNAFLOW	FE,IMP	•	•	•	•	•(Biot)	D-P,M-C	•
FLAC	FD,EXP	•	•	•	–	•	M-C,DY,D-P	•
FLAC3D	FD,EXP	•	•	•	•	•	D-P,M-C	•
Sigma-2D	FE	•	•	•	–	–	-	•
Sigma-3D	FE	•	•	•	•	–	-	•
FLUSH	FE,FR	•	•	•	•	–	EQL	–
QUAD4M	FE	•	–	•	–	–	EQL	–
TELDYN	FE	•	–	•	–	•	-	•
RHEO-STAUB	FE	•	–	•	–	–	VE,VP,AEP	–
DIANA-SWANDYNE II	FE	•	–	•	–	•(Biot)	M-C,TSH	Slip Elem
SASSI	FE,FR	•	•	•	•	–	-	–
DYSAC2	FE	•	–	•	–	•(Biot)	–	–

CO=Continuum **ST**=Structural, **FE**=Finite Element, **IMP**=Implicit, **FR**=Frequency Domain, **FD**=Finite Diffrence, **EXP**=Explicit **M-C**=Mohr-Coulomb, **D-P**=Drucker-Prager **CC**=Cam Clay, **VN**=von Mises, **CC**=Cam Clay **VE**=Visco-elastic **VP**=Visco-plastic **W-W**=William-Wronkle, **DY**=Double yield **H-B**=Hoek-Brown, **T**=Tresca, **F**=Finn's Model, **EQL**=Equivalent Linear, **R-O**=Ramberg-Osgood, **TSH**=Two-surface hardening, **LA**=Lade's Model, **AEP**=Anisotropic elastic-plastic (•)=Modified Cam Clay and Lade's model have been implemented by the research group at the University of Colorado at Denver through its colloborative agreement with LLNL

be used to analyze the response of important structures to large earthquakes. Computer simulation of nonlinear behavior is quite complex and the nonlinear finite element computer programs developed at the LLNL are some of the world's most powerful programs for performing nonlinear structural analysis.

NIKE2D is an implicit finite element code for analyzing the finite deformation, quasistatic and dynamic response of two dimensional, axisymmetric, plane stress and plane strain solids. The finite element formulation accounts for both material and geometric non-linearities. A number of material models are incorporated to simulate a wide range of material behavior including, elasto-plasticity, anisotropy, creep, and rate dependence. Arbitrary contact between independent bodies is handled by a variety of slideline algorithms. These algorithms model gaps and sliding along material interfaces, including frictional interface.

NIKE3D is fully implicit three dimensional finite element code for analyzing the finite strain static and dynamic response of inelastic solids, shells and beams. There are more than twenty material models implemented in the code. Like in NIKE2D contact-impact algorithms permit gaps, frictional sliding and mesh discontinuities along material interfaces.

Chapter 3 discusses theoretical background of NIKE codes in detail.

FLAC

FLAC [37] is an explicit 2D finite difference program. Constitutive equations are solved incrementally, thus allow large strains, material anisotropies, sliding interfaces and other nonlinearities. It has library of material models such as elastic, Mohr-Coulomb plasticity, ubiquitous joint, double yield, viscous and strain softening. Some of its main features are: several automatic grid generators, statistical distribution of any property, groundwater flow with full coupling to mechanical calculation including negative pore pressure for saturated soil, structural elements (including non-linear cables) with general coupling to continuum. FLAC has built-in language called FISH to add user defined features (new constitutive models, variables or commands).

2.5.1 Interface formulation in FLAC

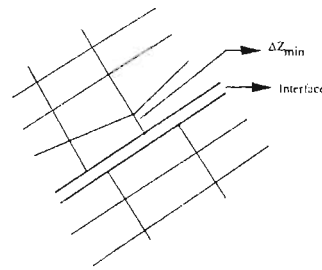

Figure 2.3 A typical interface and zone dimensions of FLAC interface.

FLAC has three options to define an interface;

(1) Glued interface: No slip or opening is allowed.

(2) Coulomb Shear-Strength: The Coulomb shear-strength criterion limits the shear force by the following relation:

$$F_{s\max} = cL + \tan\phi F_n \tag{2.9}$$

where c =cohesion L =effective contact length and ϕ =friction angle of interface, F_s =tangential force, F_n =normal force along the interface.

If the criterion is satisfied (i.e., if $|F_s| \geq F_{s\max}$), then $F_s = F_{s\max}$.

(3) Tension Bond: If the tension at the interface exceeds the tension bond interface breaks and all forces are set to zero.

Stability and time step adjustments are strongly affected by interface stiffness parameters k_n and k_s. The effect of pore pressure is included in the interface calculation by using effective stress as the basis for the slip condition. No pressure drop normal to the joint and no influence of normal displacement on pore pressure are calculated. Also condition of fluid along the interface is not modelled.

In FLAC manual [37] it is recommended to choose k_n and k_s as ten times equivalent stiffness of the stiffest neighboring zone. The stiffness of a zone in the normal direction is;

$$\max\left[\frac{(K + \frac{4}{3}G)}{\Delta Z_{\min}}\right] \tag{2.10}$$

where K and G are the bulk and shear moduli, and $\Delta Z_{\min}$ is the smallest width of an adjoining zone in the normal direction and it is shown in Figure 2.3.

Selection of interface stiffness parameters requires utmost attention. High values may cause very small calculation timestep and low values may not reflect the real behavior of the interface.

2.6 Constitutive Models

A material model idealization should possess the following necassary properties (Prevost, 1996);

(1) The model should be complete, i.e. able to make statements about the material behavior for all strain and stress paths, and not merely restricted to a single class of paths;

(2) It should be possible to identify the model parameters by means of a small number of standart or simple material tests;

(3) The model should be founded on some physical interpretation of the ways in which the material is responding to changes in applied stress or strain (e.g., the material should not be modeled as elastic if permanent deformations are observed upon loading).

2.6.1 Equivalent Linear Elastic Model

Under strong shaking the soil may undergo large deformations and that might introduce nonlinear effects. In order to take this into account equivalent elastic linear procedure was developed by Seed and Idriss (1969). In this representation the shear modulus

(G/G_{max}) and damping ratio of the soil are expressed as a function of shear strain. Nonlinear stress-strain behavior of the soil is accounted for by iteratively adjusting the modulus and damping values until a reasonable consistency is obtained between the selected parameters and the computed strain levels throughout the analysis. Seed and Idriss (1970) have published effective shear strain versus shear modulus reduction factor and damping ratio data for sand and clay. Currently the computer codes such as FLUSH and QUAD4M use this approach to reflect the nonlinear soil behavior in FEM analyses. The drawback of equivalent linear analysis is it is not possible to obtain permanent deformations.

2.6.2 Hyperbolic Model

Duncan and Chang [20] proposed a stress-strain relation to approximate the non-linear soil behavior. Stress-strain curve is given by the equation:

$$E_t = \left[1 - \frac{R_f\,(1 - sin\phi)\,(\sigma_1 - \sigma_3)}{2ccos\phi + 2\sigma_3 sin\phi}\right]^2 E_i \tag{2.11}$$

where n =modulus exponent, K =modulus number, $E_i = KP_a\left(\frac{\sigma_3}{P_a}\right)^n$,
P_a =atmospheric pressure, $R_f = \frac{(\sigma_1-\sigma_3)_f}{(\sigma_1-\sigma_3)_{ult}}$, c =cohesion, and ϕ =angle of internal friction.

The usefullness of Equation 2.11 lies in its simplicity with regard to two factors [20];

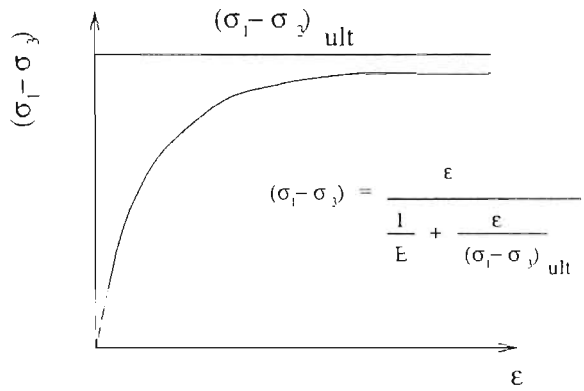

Figure 2.4 Deviatoric stress vs strain relation for hyperbolic model.

(1) Because the tangent modulus is expressed in terms of stresses only it may be employed in analyses for problems involving any arbitrary initial stress conditions without any additional complications,

(2) The parameters K, n, and R_f may be determined readily from series of triaxial test tests for different confining pressure. The amount of effort required to determine parameters K, n, and R_f is not much greater than that required to determine the values of c and ϕ.

The model mentioned above has been implemented into many FEM codes. It is being used for static and cyclic loading with small hysteresis. For cyclic loading, modulus-confining pressure relation is;

$$E_{ur} = K_{ur} P_a \left(\frac{\sigma_3}{P_a}\right)^n \tag{2.12}$$

in which E_{ur} =is the unloading-reloading modulus, and K_{ur} =is the corresponding modulus number and lets users to obtain permanent deformation upon unloading. Deviatoric stress and stress relation of hyperbolic model is shown in Figure 2.4.

2.6.3 Mohr-Coulomb Model

Mohr-Coulomb is the most commmonly used failure criterion in engineering practice. The relation between shear strength and the normal stress can be expressed as;

$$\tau = c + \sigma_n \tan\phi \tag{2.13}$$

$$(\sigma_1 - \sigma_3) = \sin\phi\,(\sigma_1 + \sigma_3) + 2c\cos\phi \tag{2.14}$$

where ϕ is the friction angle and c is the cohesion. Since Mohr-Coulomb failure criterion relates two parameters τ and σ_n or σ_1 and σ_3 it can be represented by Figure 2.5. In addition Figure 2.5 shows the failure criteria in a three-dimensional stress space where axes are principal stresses σ_1, σ_2 and σ_3. Hydrostatic axis is the line which forms equal angles with the three axes.

Since intermadiate principle stress σ_2 is not included in the failure criterion it assumed not to have any influence on the strength. Mohr-Culomb theory is widely used in engineering practice because it is well understood and strength parameters ϕ and c can easily be obtained from confined compression and direct shear tests.

2.6.4 Ramberg-Osgood Model

The R-O model is an analytical model and it is often used to represent the hysteretic behavior of soil materials subjected to cyclic loading. Although unloading and reloading are included in the model, inelastic deformations are not included in the sense of theory of plasticity.

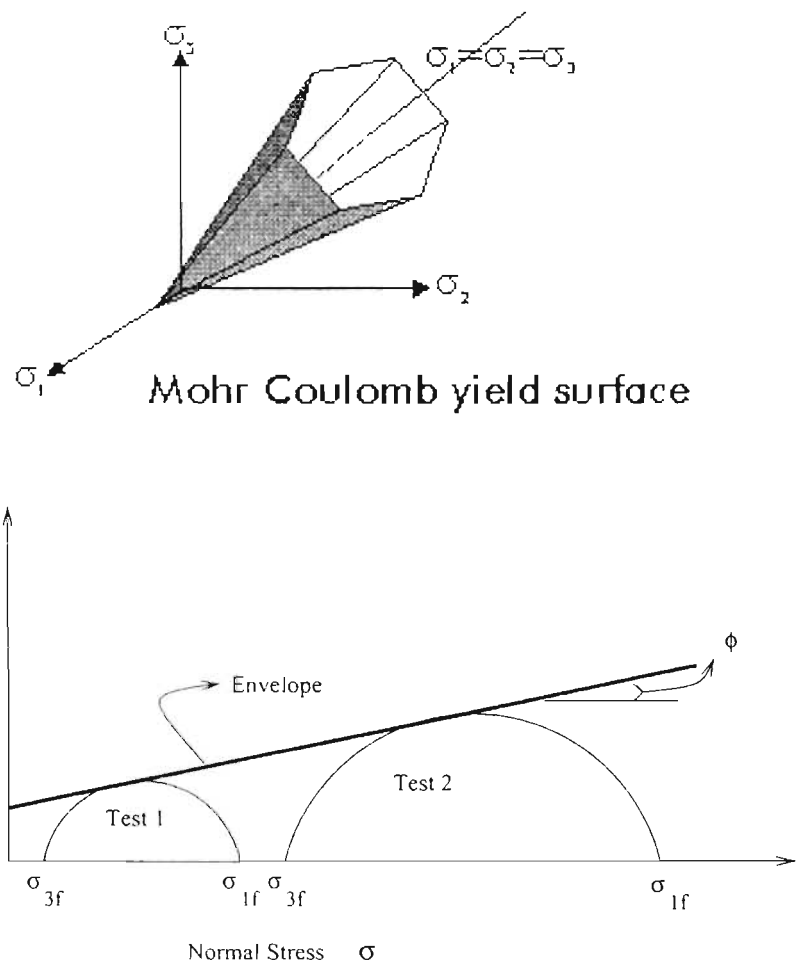

Figure 2.5 Mohr Coulomb yield surface.

The backbone (monotonic loading) strain-stress relation of the Ramberg-Osgood elasto-plastic model can be expressed by:

$$\frac{\gamma}{\gamma_y} = \frac{\tau}{\tau_y}\left(1 + \alpha\left|\frac{\tau}{\tau_y}\right|^{r-1}\right) \tag{2.15}$$

where γ=shear strain, τ=shear stress, γ_y=reference shear strain, τ_y=reference shear stress, α=constant ≥ 0, and r=constant ≥ 1. The factor α can be varied to adjust the position of the curve along the strain axis and the value r controls the curvature of the graph. When r=1 a linear relationship between shear stress and shear strain is described. Formulation of R-O permits the use of integer value r which provides more flexibility in fitting laboratory test data.

The Ramberg-Osgood equation is inherently one dimensional and is strictly applicable to shear components. To generalized this equation to the multidimensional case, it is assumed that each component of the deviatoric stress, and deviatoric strain is independently related by the above Equation 2.15. The volumetric behavior is assumed to elastic, and therefore the pressure, p, is determined using the elastic relation:

$$p = -K\epsilon_v \tag{2.16}$$

where ϵ_v is the volumetric strain, and K is the bulk modulus.

Figure 2.6 shows a typical loading and unloading curve for Ramberg-Osgood model. For unloading and reloading, according to Masing's rule the relation becomes:

$$\frac{\gamma - \gamma_o}{2\gamma_y} = \frac{\tau - \tau_o}{2\tau_y}\left(1 + \alpha\left|\frac{\tau - \tau_y}{2\tau_y}\right|^{r-1}\right) \tag{2.17}$$

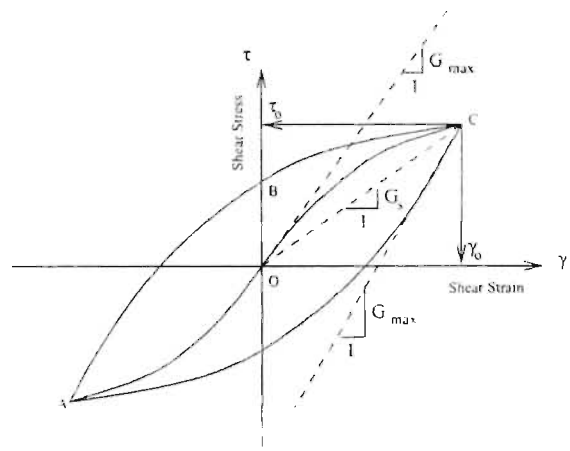

Figure 2.6 Typical loading and unloading curve for Ramberg-Osgood Model.

where γ_o=shear strain at point of stress reversal, and τ_o =shear stress at point of stress reversal. The values of γ_y, τ_y, α, and r are to be determined from the laboratory experiment results.

Ueng and Chen [77] developed an iterative procedure to obtain R-O parameters for soils using G/G_{max} and damping ratio versus shear strain curves. Richart [61] performed curve fitting studies by changing R-O parameters α and r for clay and sand.

By rearranging Equation 2.15 , the secant modulus for the backbone curve can be expressed as:

$$G_o = \frac{\tau}{\gamma} = \frac{\tau_y}{\gamma_y}\left(\frac{1}{1+\alpha\left|\frac{\tau}{\tau_y}\right|^{r-1}}\right) \tag{2.18}$$

For very small strain, i.e., $\gamma \longrightarrow 0$ and $\tau \longrightarrow 0$. since r >1,

$$(G_o)_{\gamma=0} = G_{\max} = \frac{\tau_y}{\gamma_y} \tag{2.19}$$

Then the backbone relation can be rewritten as:

$$\frac{\gamma}{\gamma_y} = \frac{\tau}{G_{\max}\gamma_y}\left(1+\alpha\left|\frac{\tau}{G_{\max}\gamma_y}\right|^{r-1}\right) \tag{2.20}$$

Therefore, besides G_{max} , other parameters γ_y, α, r should be determined for the Ramberg-Osgood model. Substituting $\tau = G_o\gamma$ and rearranging Egn. 2.20 we get:

$$\frac{G_{\max}}{G_o} - 1 = \alpha\left|\frac{G_o\gamma}{G_{\max}\gamma_y}\right|^{r-1} \tag{2.21}$$

$$\log\left(\frac{G_{\max}}{G_o} - 1\right) = \log\alpha + (r-1)\log\left(\frac{G_o\gamma}{G_{\max}\gamma_y}\right) \tag{2.22}$$

Equation 2.22 can be plotted using only G/G_{max} data and then the values of r and α can be determined from slope and intercept respectively. Next step is plotting a similar

curve using only damping ratio curve and obtaining the same parameters one more time. Final values of r and $\alpha$are determined by taking the average. α and r are determined using only damping ratio curve as follows: The equivalent critical damping ratio, β, for a hysteresis loop with the tip at (γ_o, τ_o) can be expressed as:

$$\beta = \frac{\Delta E}{2\pi\tau_o\gamma_o} = \frac{2\alpha(r-1)}{\pi(r+1)}(\frac{G_o}{G_{\max}})^r(\frac{\gamma_o}{\gamma_y})^{r-1} \tag{2.23}$$

where ΔE= energy dissipation in one loading cycle. Substituting Equation 2.21 in Equation 2.23 we get;

$$\beta = \frac{2(r-1)}{\pi(r+1)}(1 - \frac{G_o}{G_{\max}}) \tag{2.24}$$

or

$$\frac{G_o}{G_{\max}} = 1 - \frac{\beta\pi(r+1)}{2(r-1)} \tag{2.25}$$

Substitute Equation 2.25 in Equation 2.22 , we obtain:

$$\log\left[\frac{\beta\pi(r+1)}{2(r-1)-\beta\pi(r+1)}\right] = \log(\alpha) + (r-1)\log\left(\left[1 - \frac{\beta\pi(r+1)}{2(r-1)}\right]\frac{\gamma}{\gamma_y}\right) \tag{2.26}$$

Finally Equation 2.26 can be plotted like Equation 2.22. Thus, a best fit straight line, and values of α and r can be found for data including both modulus and damping data. If we examine Equation's 2.22 and 2.26 we see that both have γ_y . Therefore to determine γ_y and the other parameters an iterative procedure is followed as below;

(1) Assume a value for γ_y and obtain the values of α and r by plotting the data according to Equation's 2.22 and 2.26.

(2) Compute γ_y according to Equation 2.23 from the given modulus and obtain an average value of γ_y.

(3) Compare the new value of γ_y with the previous value. Repeat steps 1 and 2 if the difference is too great.

Finally α, γ_y, and r are all obtained. Then τ_y can be calculated by using Equation 2.19 and this finishes the procedure for obtaining the Ramberg-Osgood material properties.

2.6.5 Other Models

The other widely used soil models, Modified Cam Clay and Lade's Model, have been implemented in NIKE3D by the research group at the University of Colorado at Denver through its colloborative agreement with Lawrance Livermore National Laboratory (LLNL). This newly enhanced NIKE3D may be used in the study of composite dams. Theoretical discussion of these models are not included in this study.

2.7 Pore Pressure Generation Models

There are several pore pressure generation procedures developed for the last three decades. These procedures can be gathered under three headings; 1)uncoupled method, 2)partially coupled method, 3)fully coupled method.

Uncoupled method is based on an emprical relationship for pore pressure development in uniform cyclic tests as a function of the number of cycles of loading normalized by the number of cycles to initiate liquefaction. This method was developed by Seed [67] and will be expalined shortly in the next section.

In partially coupled method [25] the change in pore pressure is related to change in volumetric strain. Therefore pore pressure generation mechanism is linked to the nonlinear analysis results. Finn's model falls in this category and it will be discussed later in this chapter.

In fully coupled method, pore pressure generation and dissipation are directly connected to the soil skeleton deformation according to Biot's formulation. This is the most rational method of analysis.

2.7.1 Uncoupled Seed's Method

In this model, actual measurements of pore water pressure build-up in cyclic loading are used. The only criteria is to determine the number of uniform stress cycles N_l which will produce a condition of initial liquefaction under undrained conditions. This can be obtained from cyclic simple shear or triaxial tests on representative samples. This method of analysis is implemented in the computer code APOLLO [51] and based on the emprical findings that the development of pore water pressure in granular soils under cyclic loading is of the form:

$$u_g = \sigma_o' F\left(\frac{N}{N_l}\right) \tag{2.27}$$

where σ_o' is the effective overburden pressure, N is the number of uniform cycles undergone by the soil sample and N_l is the accumulative number cycles at the same stress level required to reach initial liquefaction. As it has been stated in [51], for many

soils. the function F may be expressed as;

$$F\left(\frac{N}{N_l}\right) = \frac{2}{\pi}\arcsin\left(\frac{N}{N_l}\right)^{\frac{1}{2\alpha}} \tag{2.28}$$

where α is an emprical constant and has a value of 0.7 which represent the average curve for many soils.

Chameau [12] modified Seed's equation and obtained two parameter equation which is found to better follow pore pressure generation characteristics observed in laboratory tests;

$$\frac{N}{N_l} = 1 - \left[\sin\frac{\pi}{2}\left(1 - R^{\frac{1}{\beta}}\right)\right]^{2\alpha} \tag{2.29}$$

where α and β are shape parameters and R is the excess pore pressure Δu, divided by initial effective confining pressure σ_o'. Chamaeu suggested that these parameters are cyclic stress ratio dependent.

2.7.2 Partially Coupled Model of Finn

An effective stress model based on strain controlled simple shear tests was developed by Finn, Lee and Martin [25] to account for the nonlinear accumulation of pore pressure during cyclic loading. The first assumption of this model is that the pore pressure development occurs due to the potential for the volumetric deformation of the soil when tested under drained condition. Pore water is assumed to be incompressible, in comparison with the soil skeleton. These assumptions yield the change in pore pressure as;

$$\Delta u = E_r \Delta \epsilon_v \tag{2.30}$$

Where Δu is the change in pore prssure, E_r is the elastic rebound modulus of the soil skeleton and $\Delta \epsilon_v$ is the change in volumetric strain during a drained simple shear test. The incremental volumetric strain is a function of the total accumulated total volumetric strain, ϵ_v, and the applied shear strain γ. The change in volumetric strain, $\Delta \epsilon_v$, is calculated as:

$$\Delta \epsilon_v = C_1 \left(\gamma - C_2 \epsilon_v\right) \frac{C_3 {\epsilon_v}^2}{\gamma + C_4 \epsilon_v} \tag{2.31}$$

where C_1, C_2, C_3, and C_4 are emprically determined constants and γ is determined from a hyperbolic stress-strain relationship;

$$\tau = \frac{\sqrt{{\sigma_v}'}\gamma}{a + b\gamma} \tag{2.32}$$

where a and b are emprical parameters. By knowing the stress history the development of pore pressures can be calculated by a sequential procedure. All the emprical parameters mentioned above are determined from strain controlled simple shear tests.

2.7.3 Fully Coupled Method: Biot Theory

A freely moving fluid in a porous material causes changes in the behavior of bulk material. An increase in pore pressure causes the dilation of or contraction of solid results in the change in pore pressure. The theory of linear 3D consolidation of soil was formulated by Biot [5, 6]. Later this theory was extended to include various non-linear effects, both material and geometrical. A finite element formulation of Biot's theory was first presented by Sandhu [62]. Currently, Biot's principle is implemented in numerical analysis codes such as DIANA-SWANDYNE, DYSAC2 and DYNAFLOW, etc.

Biot's model of poroelastic materials addresses a coherent solid skeleton and a freely moving pore fluid in which solid and liquid phases are fully connected. Biot made the following assumptions:

- soils are homogeneous and isotropic,
- the strains are very small,
- stress-strain relations are linear and perfectly elastic,
- pore water is compressible and has no shear resistance,
- the flow of water is viscous and follow Darcy's law,
- no capillary effects.

Then he obtained the following equations for streses;

$$\sigma_{ij} = 2Ne_{ij} + Me_{kk}\delta_{ij} + Q\epsilon\delta_{ij} \tag{2.33}$$

$$u_{ij} = Qe_{kk}\delta_{ij} + R\epsilon\delta_{ij} \tag{2.34}$$

where ϵ is the dilatancy of the fluid and expressed by $\epsilon = \Delta \cdot w_p$ and w_p is the fluid displacement vector, δ_{ij} is the Kronecker's delta and , e_{ij} is the strain tensor of soil skeleton.

A close examination of constants N, M shows that these constants corresponds to Lamé's constants in the theory of elesticity, The coefficient N represents shear modulus G of the bulk material, and the coefficient R is a measure of the pore pressure required on the fluid phase to force a certain volume of the fluid into the pores of the soil aggregate while the total volume remains constant. The coefficient Q is of the nature of a coupling between the volume change of the solid and that of fluid phase. Biot claimed that one can perform experiments to measure the four elastic constants [69]. The shear modulus can be measured directly.

In Biot's theory the assumption that the pore fluid is compressible introduces significant improvement over previos theories and provides a more realistic explanation for the pore pressure generation. The treatment of soil as two-phase medium, accounting for the coupling between phases, and, therefore, determining the stress distribution in both the fluid and the soil phases, gives a more accurate and realistic representation of actual soil behavior.

2.8 Summary and Conclusion

This chapter discusses the literature survey on composite dams, soil-concrete interface models, numerical analysis codes to analyze IBCD, constitutive soil models, and pore pressure generation models.

The literature survey revealed that there is no concrete and reliable method to investigate IBCD.

Two different interface treatment approach was explained: stiffness approach and constraint approach. Stiffness approach techniques are are simple to implement but not reliable in case of separation. Therefore to study IBCD constrained approach is more appropriate.

Several computer codes are listed including their main features. It has been shown that among others NIKE3D is one of most suitable FE software to analyze IBCD.

Several soil constitutive models including Ramberg-Osgood, Mohr-Coulomb, etc. are presented. In terms of availability in NIKE3D, Ramberg-Osgood is most suitable soil model that can be used in dynamic analysis.

Different pore pressure schemes are also presented. Biot's coupled method is the most realistic pore pressure generation algorithm. Since it is not available in NIKE3D, analyzing IBCD using pore pressure generation models is left as a future study.

3. Finite Element Analysis Codes

3.1 Introduction

This chapter describes the softwares used in 2-D, and 3-D parametric FE analyses. Pre and post processors, and NIKE3D are presented. TrueGrid [83] and GRIZ have been used as the pre-processor and post-processor, respectively. Theoretical background of NIKE3D, its interface algorithm, and solution strategy are discussed.

First, an input batch file is used by TrueGrid to produce an input file for NIKE3D. Then NIKE3D produces series of binary plot files to be read by GRIZ storing all nodal and element information throughout the analysis. Finally, one can obtain time history data using GRIZ. The analysis sequence is illustrated in Figure 3.1.

3.2 TRUEGRID

TrueGrid [83] is a powerful, easy-to-use interactive and batch mesh generator. TrueGrid generates meshes for finite difference and finite element simulation codes that model the behavior of fluids and structures. However, TrueGrid can generate complete input files for many simulation codes, such as ADINA, ANSYS, MARC, LS-DYNA, LS-NIKE, etc. Along with defining the mesh, you can specify physical properties on the mesh.

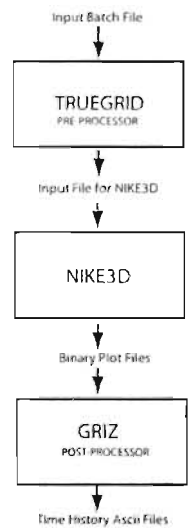

Figure 3.1 Analysis sequence.

TrueGrid generates multi-block, structured meshes. Each block is composed of solid hexahedral (six-sided) elements and/or structural quadrilateral shell and beam elements arranged in rows, columns, and layers. TrueGrid uses a special projection method for mapping a block mesh onto one or more surfaces. Therefore a complex looking mesh can be built from a simple block very easily. An example is shown in Figure 3.2 with a simple block and cylindrical projection surfaces.

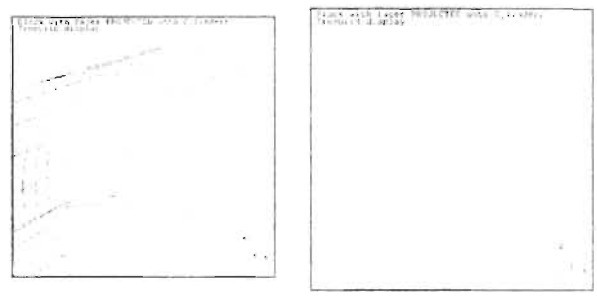

Figure 3.2 A simple block part and cylindrical projection surfaces [83].

TrueGrid have been used in all 2-D, and 3-D modelling efforts. Particularly, the complicated 3-D FE model was created easily saving considerable time.

3.3 NIKE3D

NIKE3D developed at Lawrence Livermore National Laboratory (LLNL) for defense program applications provide a powerful tool that can be used to analyze the response of important structures to large earthquakes. Computer simulation of nonlinear behavior is quite complex and the nonlinear finite element computer programs developed at the LLNL are some of the world's most powerful programs for performing nonlinear structural analysis [47].

NIKE3D is fully implicit three dimensional finite element code for analyzing the finite strain static and dynamic response of inelastic solids, shells and beams. A number of material models are incorporated to simulate a wide range of material behavior including, elasto-plasticity, anisotropy, creep , and rate dependence. Arbitrary contact between independent bodies is handled by a variety of slideline algorithms. These algorithms model gaps and sliding along material interfaces, including frictional interface.

3.3.1 Element Library

NIKE3D utilizes a relatively small set of elements. All elements use low order interpolation, requiring no midside node definitions. This approach chooses highly efficient elements over more costly higher order elements. The available elements are solid, beam, and/or shell elements, and they are shown in Figure 3.3. Eight node solid elements are integrated with a 2x2x2 point Gauss quadrature rule. Four node shell elements use 2x2 Gauss integration in the plane, and one of many available schemes for integration through the thickness. Two node beam elements use one integration point along the length, with many options for integration of the cross section.

3.3.2 Solution Strategy

In NIKE3D, several nonlinear solution strategies are available, including Full-, Modified-, and Quasi-Newton method. By default, NIKE3D uses the BFGS method. An

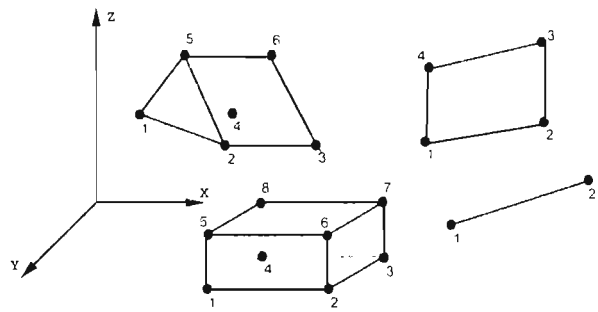

Figure 3.3 Elements available in NIKE3D [47].

extensive set of diagnostic messages have been incorporated into the quasi-Newton solvers to allow their convergence progress to be monitored.

NIKE3D is based on updated Lagrangian formulation. During each load step, nodal displacement increments which produce a geometry that satisfies equilibrium at the end of the step are computed. After obtaining updated displacement increments, the displacement, energy, and residual norms are computed, and equilibrium convergence is tested using user defined tolerances. Once convergence is obtained, displacements and stresses are updated and proceeded to the next load step. If convergence is not achieved within the user-specified iteration limits, the optional automatic time step controller will adjust the time step size and try again.

3.3.3 Element Formulation

The governing equation which is called equation of motion is:

$$\tau_{ij} + b_i = \rho \ddot{u}_i \tag{3.1}$$

where τ is the Cauchy total stress tensor, b_i is the body force per unit volume, ρ is the density, u_i are the relative displacements, Ω represents the continuum domain. The boundary of continuum can be divided into two parts as the boundary $\Gamma_{\mathbf{u}}$ where displacements are described and the boundary Γ_τ where stresses are described and the conditions on the boundary can be defined as:

$$u_i = \bar{u}_i \tag{3.2}$$

and

$$\tau_{ij} n_j = \bar{\tau}_i \tag{3.3}$$

respectively.

The initial conditions are:

$$u_i(0) = u_{io} \tag{3.4}$$

$$\dot{u}_i(0) = \dot{u}_{io} \tag{3.5}$$

The rate deformation tensor $\dot{d}_{ij}$ is defined in terms of velocity $\dot{u}$ as:

$$\dot{d}_{ij} = \frac{1}{2}(\dot{u}_{i,j} + \dot{u}_{j,i}) \tag{3.6}$$

The Cauchy stress is, in general, a function of rate of deformation $\dot{d}_{ij}$ a set of history variables $\mathbf{H}$, and the temperature $\mathbf{T}$:

$$\tau_{ij} = \tau_{ij}(\dot{d}_{ij}, \mathbf{H}, \mathbf{T}) \tag{3.7}$$

In NIKE codes, quadrilateral elements are used for the spatial discretization, yielding a system of ordinary differential equations:

$$\mathbf{M}\ddot{\mathbf{u}} + \mathbf{F}^{\text{int}}(\mathbf{u}, \dot{\mathbf{u}}, \mathbf{T}) = \mathbf{P}(\mathbf{u}, \mathbf{b}, t, \mathbf{T}) \tag{3.8}$$

Where $\mathbf{M}$ is the mass matrix, $\mathbf{F}$ is the internal nodal force vector, and $\mathbf{P}$ is the external nodal force vector. $\mathbf{P}$ can be a function of nodal displacement $\mathbf{u}$, body force per unit volume $\mathbf{b}$, time t, and nodal temperature $\mathbf{T}$. In dynamic analysis the Equation 3.8 is solved by Newmark β method. For quasistatic analysis the Equation 3.8 becomes:

$$\mathbf{F}^{\text{int}}(\mathbf{u}, \dot{\mathbf{u}}, \mathbf{T}) = \mathbf{P}(\mathbf{u}, \mathbf{b}, t, \mathbf{T}) \tag{3.9}$$

In quasistatic analysis the equation 3.9 is solved incrementally by an iterative strategy. Without thermal and viscous effects the Equation 3.9 becomes:

$$\mathbf{F}^{\text{int}}(\mathbf{u_{n+1}}) = \mathbf{P_{n+1}} \tag{3.10}$$

where $\mathbf{u_{n+1}}$ and $\mathbf{P_{n+1}}$ are the nodal displacements and external load evaluation at time t_{n+1}. At each time step, quantities are known at t_n, and the solution involves finding the displacement $\mathbf{u_{n+1}}$ that satisfies the equation below:

$$\mathbf{K}^{\mathbf{i}}\Delta\mathbf{u}^{\mathbf{i}} = \mathbf{P_{n+1}} - \mathbf{F}^{\text{int}}(\mathbf{u}^{\mathbf{i}}_{\mathbf{n+1}}) \tag{3.11}$$

This new equilibrium solution is found by iteration. To obtain the solution at t_{n+1}, the finite element Equations 3.9 are first linearized about the configuration at t_n and the displacements at t_{n+1} are determined. Later the Equation 3.11 solved iteratively.

Convergence is determined by examining the both the displacement and energy norms. For displacement norm

$$\frac{\|\Delta u^i\|}{u_{\max}} \leq e_d \tag{3.12}$$

where u_{max} is the maximum displacement norm obtained overall of the n steps is used, and for energy norm:

$$\frac{(\Delta u^i)^T Q^i_{n+1}}{(\Delta u^o) Q^o_{n+1}} \leq e_d \tag{3.13}$$

is used. Where e_d and e_r are tolerances that are typically 10^{-2} to 10^{-3} or smaller.

For dynamic analysis the Newmark-β method is used to integrate the semidiscretized finite element equations 3.1 in time. The Newmark-β family methods is given by:

$$\mathbf{u}_{n+1} = \mathbf{u}_n + \Delta t \dot{\mathbf{u}}_n + (1/2 - \beta)\Delta t^2 \ddot{\mathbf{u}}_n + \beta \Delta t^2 \ddot{\mathbf{u}}_{n+1} \tag{3.14}$$

$$\dot{\mathbf{u}}_{n+1} = \dot{\mathbf{u}}_n + (1 - \gamma)\Delta t \ddot{\mathbf{u}}_n + \gamma \Delta t \ddot{\mathbf{u}}_{n+1} \tag{3.15}$$

In NIKE2D the default values for β and γ are $1/4$ and $1/2$ respectively. This choice of parameters represents the trapezoidal rule which is second order accurate in time, is energy conserving for linear problems and does not introduce numerical dissipation.

To obtain the dynamic solution at t_{n+1}, the finite element equations 3.1 are first linearized about the configuration at t_n and using the Expressions 3.14 and 3.15 the nodal acceleration, velocity, and displacements at t_{n+1} are obtained. Finally the

equilibrium iterations performed with:

$$\mathbf{K}^* \Delta \mathbf{u}^i = \mathbf{P}_{n+1} - \mathbf{F}^*(\mathbf{u}^i_{n+1}) \tag{3.16}$$

where

$$\mathbf{F}^* = \mathbf{F}(\mathbf{u}^i_{n+1}) + \mathbf{M}\ddot{\mathbf{u}}^i_{n+1} + \mathbf{D}\dot{\mathbf{u}}^i_{n+1} \tag{3.17}$$

$$\mathbf{K}^* = \mathbf{K} + \frac{1}{\beta \Delta t^2}\mathbf{M} + \frac{\gamma}{\beta \Delta t}\mathbf{D} \tag{3.18}$$

where M is the damping matrix. For dynamic analysis, damping can be incorporated into the model at the element level in two ways: through the specification of dissipative material behavior or by a nonlinear adaptation of Rayleigh damping. Dissipative mechanisms in material behavior are pointwise in nature and include viscoelasticity and include hysteretic damping caused by cyclic plasticity. Generalized Rayleigh damping is more global in nature. However, it is implemented at the element level to maximize computational efficiency.

3.3.4 Material Models

NIKE3D has a wide range of material library. Among others Ramberg-Osgood with its hysteresis behavior is most suitable material model for soils. Ramberg-Osgood material model is discussed in Section 2.6.4 in detail. UCD Geotechnical Engineering Center is collaborating with Lawrence Livermore National Laboratory to make new soil models

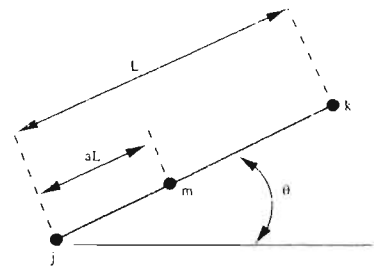

Figure 3.4 Contact of node m with segment of jk [21].

such as Cam Clay and Lade's model efficient and available in NIKE codes. Analysis with new material models are left as a future study.

3.3.5 Interface models

In NIKE3D, interfaces are modelled with penalty formulation which is a constraint approach as discussed in Section 2.4.2.

3.3.6 Penalty Formulation in NIKE3D

If there is no penetration during the analysis of a contact problem nothing is done. If there is penetration then an interface force is applied between the surfaces of dissimilar materials. The magnitude of the force is proportional to the amount of penetration. This maybe considered as the addition of an interface spring. Now consider a slideline with separation and closure. The following illustrates the NIKE3D's argumentation of stiffness matrix $\mathbf{K}^s$ and the internal nodal force $\mathbf{F}^s$ when penetration is detected, in a plane strain condition.

Figure 3.4 shows an isolated portion of the interface where node m is penetrating through segment jk [21]. A local equilibrium relationship can be written as:

$$\mathbf{K}^s \Delta \mathbf{u}^s = \mathbf{P}^s - \mathbf{F}^s \tag{3.19}$$

where $\Delta \mathbf{u}$ is the incremental displacement vector containing the penalty spring degrees-of-freedom, $\mathbf{K}^s$ is the spring stiffness, $\mathbf{F}^s$ is the spring internal force , and $\mathbf{P}^s$ is the external force arising from internal stress in the interface elements. The spring degrees of freedom are ordered:

$$\Delta \mathbf{u}^s = [\Delta v_m, \Delta w_m, \Delta v_j, \Delta w_j, \Delta v_k, \Delta w_k] \tag{3.20}$$

The spring stiffness matrix $\mathbf{K^s}$ is defined as:

$$\mathbf{K^s} = \kappa \begin{bmatrix} s^2 & -sc & -(1-a)s^2 & (1-a)sc & -as^2 & asc \\ -sc & c^2 & (1-a)sc & -(1-a)c^2 & asc & -ac^2 \\ -(1-a)s^2 & (1-a)sc & (1-a)^2 s^2 & -(1-a)^2 sc & (1-a)as^2 & -(1-a)asc \\ (1-a)sc & -(1-a)c^2 & -(1-a)^2 sc & (1-a)^2 c^2 & -(1-a)asc & (1-a)ac^2 \\ as^2 & asc & (1-a)as^2 & -(1-a)asc & a^2 s^2 & -a^2 sc \\ asc & -ac^2 & -(1-a)asc & (1-a)ac^2 & -a^2 sc & a^2 c^2 \end{bmatrix} \tag{3.21}$$

where $c = cos(\theta), s = sin(\theta)$, and κ is the penalty stiffness. The spring internal force $\mathbf{F^s}$ is defined by:

$$\mathbf{F}^s = -\kappa\delta \begin{bmatrix} -s \\ c \\ (1-a)s \\ -(1-a)c \\ as \\ -ac \end{bmatrix} \tag{3.22}$$

where $-\delta$ is the amount of penetration of node m through segment jk. The spring stiffness $\mathbf{K}^s$ and force $\mathbf{F}^s$ are computed for all active slideline nodes and segments, and are assembled into the global finite element equations. Thus the stiffness profile changes as analysis with slidelines evolve.

The penalty stiffness κ is unique for each segment, and is based on the contact area and bulk modulus of the penetrated material, and it is calculated with Equation 3.23:

$$\kappa = \frac{f_{si} K_i A_i}{V_i} \tag{3.23}$$

where f_{si} is the penalty stiffness scale factor, and K_i, A_i, and V_i are the bulk modulus, area, and volume of the penetrated material segment.

If noticeable penetration is observed, the penalty scale factor can be increased. However high penalty numbers can be detrimental to the convergence of global iterations unless the time step size is scaled back. In NIKE3D the default value of f_{si} has been chosen as 0.1 to balance global convergence rate with slideline constraint enforcement on a wide variety of problems.

3.3.7 Damping Methods

In NIKE3D codes damping is handled in three different ways :

(1) algorithmic (or numerical or artificial) damping,

(2) damping with concentrated nodal dampers,

(3) generalized Rayleigh Damping.

Algorithmic damping is introduced in integration of finite element equations with the Newmark-β method. Nodal dampers are considered purely viscous and represented by dashpot analogy. In Rayleigh Damping, damping matrix $[C]$ is constructed by a linear combination of mass and stiffness matrices.

In following sections only algorithmic and Rayleigh Damping will be discussed.

3.3.8 Algorithmic Damping

In integrating the semidiscretized finite element equations:

$$M\ddot{u} + F^{int}(u, \dot{u}) = P(u, b, t) \tag{3.24}$$

in time the Newmark-β method is used. The Newmark family of methods is given by [56]:

$$u_{n+1} = u_n + \Delta t\dot{u}_n + (1/2 - \beta)\Delta t^2\ddot{u}_n + \beta\Delta t^2\ddot{u}_{n+1} \tag{3.25}$$

$$\dot{u}_{n+1} = \dot{u}_{n+1} + (1 - \gamma)\Delta t\ddot{u}_n + \gamma\Delta t\ddot{u}_{n+1} \tag{3.26}$$

where β and γ are free parameters governing the accuracy and stability of the time integration [21]. Stability of this algorithm is:

unconditional stability when:

$$2\beta \geq \gamma \geq \frac{1}{2} \tag{3.27}$$

conditional stability when

$$\gamma \geq \frac{1}{2}, \quad \beta < \frac{1}{2} \quad \text{and} \quad \Delta t \leq \frac{\xi(\gamma - 1/2) + \sqrt{\gamma/2 - \beta + \xi^2(\gamma - 1/2)^2}}{\omega_{\max}(\gamma/2 - \beta)} \tag{3.28}$$

where ω_{max} is maximum undamped natural frequency and ξ is critical damping ratio.

The default setting of the parameters in NIKE3D is $\beta = 1/4$ and $\gamma = 1/2$. This choice of parameters represents the trapezoidal rule which is second order accurate in time and *does not introduce numerical dissipation* [21]. Taking $\gamma > 1/2$ introduces numerical damping, but also reduces the accuracy of Newmark methods to the first order. Taking

$$\beta = \frac{1}{4}(\gamma + 1/2)^2 \tag{3.29}$$

maximizes the high-frequency dissipation for a given value of $\gamma > 1/2$ [14]. Because the higher modes of semidiscrete structural equations are the artifacts of the discretization process and not representative of the behavior of the governing partial differential equations, it is generally viewed as desirable and often is considered is absolutely necessary to have some form of algorithmic damping present to remove the participation of the high-frequency modal components. In terms of Newmark method, $\gamma > 1/2$ is necessary to introduce high-frequency dissipation. For a fixed $\gamma > 1/2$, one can select β (see Equation 3.29) such that high frequency dissipation is maximized [35].

A disadvantage of Newmark method is that algorithmic damping can only be obtained at the expense of reduced accuracy. In introducing high frequency dissipation by selecting $\gamma > 1/2$, it is, of course, desirable to maintain good accuracy in the low modes. Unfortunately $\gamma \neq 1/2$ results in a drop to first-order accuracy [35]. A variety of useful techniques obtained from the Newmark family is listed in [14].

3.3.9 Rayleigh Damping

The common Rayleigh damping proposed by Caughey [8] given by:

$$[C] = [M] \sum_{k=0}^{p-1} \sigma_k ([M]^{-1}[K])^k \tag{3.30}$$

is a reasonable approximation for small levels of damping [50]. Conceptually, in NIKE3D, Rayleigh damping is incorporated by replacing the internal nodal force vector $\mathbf{F}$ by:

$$\mathbf{F}^{int} \longleftarrow \mathbf{F}^{int}(u) + \alpha \mathbf{M}\dot{u} + \beta \mathbf{K}\dot{u} \tag{3.31}$$

In other words, the special case of Equation 3.30 when $p = 2$ is taken as the damping matrix $[C]$ like a linear combination of the stiffness and mass matrices, also called two-term model, that is:

$$[C] = \alpha[M] + \beta[K] \tag{3.32}$$

where α and β are called the stiffness and mass proportional damping constants respectively. The relation between α, β and and the fraction of critical damping ξ at frequency ω is given by:

$$\xi = \frac{1}{2}\left(\beta\omega + \frac{\alpha}{\omega}\right) \tag{3.33}$$

The advantage of Rayleigh damping is that no alteration is introduced to the mode shapes and the eigensolution or calculated response is thus greatly simplified. The two-parameter model as shown in Equation 3.32 has been used in some other large FEM codes such as NASTRAN and SAP5 [50].

In practice, reasonable Rayleigh coefficients in the analysis of a specific structure may often be selected using available information on the damping characteristics of a typical similar structure; i.e., approximately the same α and β values are used in the analysis of similar structures [3].

For a linear elastic model, the model fraction of critical damping can be specified at two natural frequencies ω_1 and ω_2, and using Equation 3.33 α and β are found by solving simultenous equations as:

$$\beta = 2(\xi_2\omega_2 - \xi_1\omega_1)/(\omega_2^2 - \omega_1^2)$$
$$\alpha = 2\omega_1\omega_2(\xi_1\omega_2 - \xi_2\omega_1)/(\omega_2^2 - \omega_1^2) \tag{3.34}$$

Damping associated with $\beta[K]$ increases with increasing frequency, whereas damping associated with $\alpha[M]$ increases with decreasing frequency. Usually ω_1 is taken as the lowest natural frequency of the structure and and ω_2 is the maximum natural frequency of interest in the loading or response. For example in seismic analysis, **30 Hz** is often used as the upper frequency because the spectral content of seismic design spectra are insignificant above that frequency [14].

Using the coefficients α and β and the initial tangent stiffness matrix **K** in Equation 3.32, together with the mass matrix for the structure, provides a damping matrix that is suitable for representing *viscous* energy losses thorough the entire response range of the structure (linear and nonlinear). Additional hysteretic energy losses will be accounted

for directly by the changing values of the stiffness matrix coefficients during the step by step computation [14].

In the analyses of structures with widely varying material properties, nonproportional may need to be used. For example in the analyses of foundation-structure interaction problems, significantly more damping may be observed in the foundation than in the surface structure. In this case it may be reasonable to assign in the construction of the damping matrix different Rayleigh coefficients α and β to different parts of the structure [5]. NIKE3D allows to use different coefficients for different material parts.

3.4 GRIZ

GRIZ [72] is an interactive application for visualizing finite element analysis results on three-dimensional unstructured grids. It was developed by the Methods Development Group at Lawrence Livermore National Laboratory (LLNL). GRIZ has the ability to animate all representations over time with its user friendly graphical user interface (GUI). Time histories of desired results can easily be stored in a text file for further processing.

3.5 Summary and Conclusions

NIKE3D, main numerical analysis code used in this study, TrueGrid, mesh generating software, and GRIZ as the post-processor are explained in this chapter. Theory background, element library, interface models of NIKE3D are discussed. It is shown that

based on the capability and availability, NIKE3D is the most appropriate software to study dynamic IBCD.

4. Centrifuge Testing and A Retaining Wall Simulation with NIKE3D

4.1 Introduction

Because of the dependence of the mechanical properties of soil on ambient stress conditions (i.e., gravity), centrifuge modelling has evolved as an important tool for the simulation of the behavior of a prototype dam and verification of numerical modelling results.

To calibrate the reliability of NIKE3D as a seismic design tool the dynamic analysis was performed and results were compared with the dynamic centrifuge test of a retaining wall by Stadler [73] using the centrifuge facility at the University of Colorado at Boulder.

Stadler investigated the dynamic behavior of 30 ft and 45 ft high retaining walls with the Nevada #100 Test Sand as the dry backfill. In the study the lateral deflection, and acceleration of the stem, acceleration and settlement of the backfill, and the wall-soil interface pressure (earth pressure) were measured.

In the following sections the principles of dynamic centrifuge testing with emphasis on composite dams, and NIKE3D simulation of Stadler's centrifuge test are presented. Wall deflection, earth pressure, and horizontal accelerations of both soil and wall are compared with experimental measurements. Moreover, horizontal acceleration of soil

along the wall-soil interface is presented. Good agreements validate the NIKE3D as a good analysis computer code. Stadler's test results are extensively referenced in the NIKE3D calibration effort.

4.2 Dynamic Centrifuge Testing

Literature survey on dynamic centrifuge testing of IBCD has not yielded any significant results because nobody has worked on this topic before. It is possible to find numerous centrifuge studies on earth dams and concrete dams, but none of them addresses the interface behavior of composite dams.

"Since centrifuge modelling and numerical analysis are often used in conjunction, and the soil properties, boundary conditions, and input earthquake accelerations of the centrifuge model are easily controlled in the laboratory, it is an excellent tool to collect data for numerical analysis verification. Once validated, numerical analysis is used to predict prototype response [44]." Thus, the author recommends to perform limited number of dynamic centrifuge test to gain a better understanding of IBCD and to verify NIKE3D results as a future study.

The principle in centrifuge modelling is to simulate the stress and strain fields in a model, identical to that prototype dam. This can be achieved by subjecting a scaled soil model, where all linear dimensions are reduced by a factor N, to a centrifugal acceleration of N gravities, Ng. In order to obtain a true model of prototype all the appropriate laws of similitude must be satisfied. Thus scaling relations, to extrapolate

Table 4.1 Scaling relations [41, 15]. It is assumed that same soil and fluids are used in model and prototype.

Quantity	Prototype	Model	Quantity	Prototype	Model
length	N	1	time (dynamic)	N	1
area	N^2	1	time (diffusion)	N^2	1
volume	N^3	1	time (creep)	1	1
velocity	1	1	frequency	1	N
acceleration	1	N	fluid pressure	1	1
mass	N^3	1	hydraulic conductivity	1	N
force	N^2	1	soil intrinsic permeability	1	1
energy	N^3	1	soil porosity	1	1
stress	1	1	fluid density	1	1
strain	1	1	fluid viscosity	1	1
mass density	1	1	pore fluid velocity	1	N
energy density	1	1			

the prototype response from the model response, must be well established. Scaling relations may differ depending on the materials used in the model and the problem type. A list of scaling relations is given in Table 4.1.

Using the centrifuge machine, the static stress and strain fields are first simulated by raising the g-level of the centrifuge model and then shaking is initiated to simulate the seismic behavior.

In the next sections some essential features, that must be considered in obtaining fidelity between model and prototype, will be discussed in terms of studying dynamic behavior of composite dams. Figure 4.1 shows a representative composite dam cross-section in a centrifuge test container. Main components of the dam are concrete, soil and water. Modelling considerations of a composite dam can be grouped under three headings: geometric, material and boundary effect considerations.

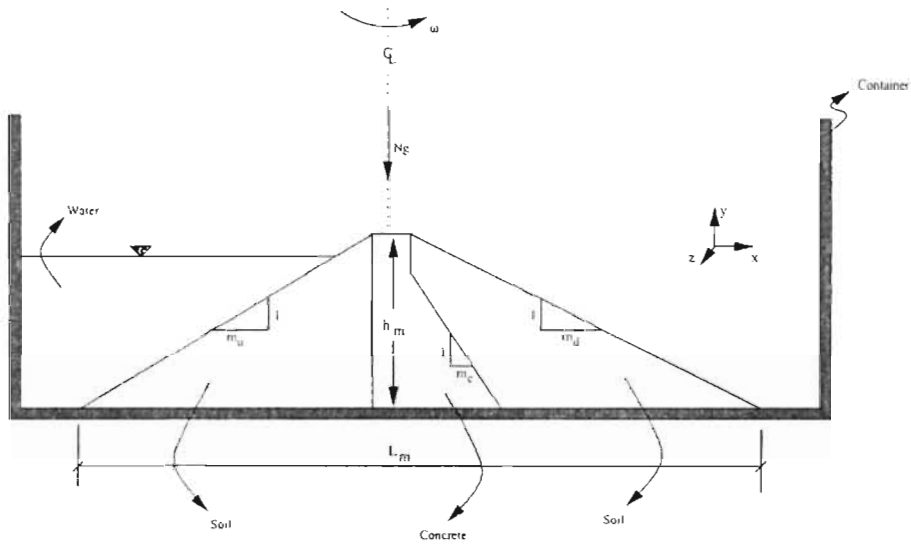

Figure 4.1 A representative composite dam cross-section in a centrifuge test container. (Not drawn to scale.)

4.2.1 Geometry Considerations

Like the other geotechnical structures, the behavior of composite dam is dominated by gravity effects. Consequently, gravity field should be simulated in a 1/N scale model by swinging it with N times stronger g-level. Therefore the primary geometric consideration is scaling all physical dimensions by the desired factor. On the other hand the capacity of centrifuge testing equipment is a limiting factor in determining the desired prototype dimensions.

4.2.2 Material Considerations

In general if different material is used in the model material properties must be scaled, too. The use of identical materials enables the issue of material property scaling to be bypassed, as homologous points in the geometrically similar model and prototype will be subjected to the same stresses and hence will develop the same strains [41]. In the proposed study same soil will be used in model. There is a chance that concrete can be modelled with aluminum. Even though the same materials are used there are still some factors that need to be considered such as model size for concrete and particle size effects for soil.

4.2.3 Concrete

Interface behavior of a composite dam is mainly characterized by separation and separation depth along the soil-concrete interface. Separation phenomena is greatly

Table 4.2 Scaling relations for retaining wall interpretations [19].

Quantity	Prototype	Model
flexural stiffness (EI)	N^4	1
flexural stiffness per unit width (EI)	N^3	1
thickness	$\left(\frac{E_m}{E_p}\right)^{\frac{1}{3}} N$	1
width	N	1
height	N	1

affected by the flexibility of concrete. Therefore maximum care should be given to modelling concrete monoliths. Models of concrete monoliths can be made using concrete or another material such as aluminum.

It is very well known that concrete at small scales is potentially even more variable in its stress-strain properties than it is at larger scales [7]. Therefore small concrete models may not reflect the real behavior. Waggoner et. al [78] have used normal strength concrete for 1.8 ft concrete dam model to study fracture and concrete dam-rock foundation interaction. Bolton and Steedman [7] used 0.6 ft high microconcrete model under 80 g to study seismic behavior of a retaining wall.

Another alternative is using different material such as aluminium which has uniform stress-strain properties. Many researchers has successfully used aluminium to model concrete walls in centrifuge testing of retaining walls [19, 58]. The flexural stiffness of the aluminium model must be scaled to represent hypothetical reinforced concrete monoliths that they were intended to simulate. Table 4.2 shows some scaling relations derived for retaining wall modelling but also applicable to concrete monolith modelling of a composite dam. E_m and E_p corresponds to Young's Modulus of model and prototype respectively.

4.2.4 Soil and water

As it is seen in Table 4.1, there is a conflict in terms of time scaling. Dynamic time is scaled by a factor of 1/N whereas diffusion or consolidation time is scaled by $1/N^2$. In this case it becomes difficult to extrapolate model response to the prototype scale. This problem can be resolved by two ways [19]:

- either by using small soil particles to reduce the permeability of the model soil.
- or by using a substitute fluid which is N times more viscous than water therefore making the soil permeability N smaller. The soil skeleton remains unchanged.

Scaling particle size of soil is not attractive. If different fluid is to be used then there are some factors that must be considered seriously. The substitute fluid should not alter the constitutive behavior of soil and must be able to generate pore pressure correctly in order to maintain effective stress relations.

Mandar [19] has shown that water-saturated soil models could not be considered as representative of the real behavior of the prototype. Furthermore as a substitute fluid "metolose" has been proposed as a better choice. Under the light of Mandar's study, metolose can also be used as a substitute fluid in centrifuge modelling of composite dams.

4.2.5 Boundary Effects

Because of the limited space in the container of the centrifuge, it is not possible to work with large models. This introduces serious boundary effects on the composite dam model. These effects can be investigated under four main groups; foundation-dam interaction, model-wall interaction, acceleration boundary conditions and instrumentation effects.

4.2.6 Foundation-composite dam interaction

If base sliding is not a concern then the foundation can be assumed as rigid fixed boundary. Therefore the concrete block must be bolted or fixed to the base so that no sliding takes place. For the foundation underneath the soil it is required to make it rigid and rough to reduce the potential sliding of the soil masses. Investigating the effect of base sliding and foundation stiffness on the dynamic behavior of composite dam can be another research area.

4.2.7 Box walls and the model

Since the models are very small it is strongly required to set some mechanism to dissipate energy inside the system. Otherwise, undamped travelling stress waves may introduce the unreal response of the structure. In order to improve energy absorbing boundary conditions, researchers have attempted to design special boxes that keeps the cross-sectional area constant. Layered box is one of the examples. It is also very

common to put some special material, such as duxseal, along the model-wall interface of the box. For the case of composite dam modelling, because of the sloping faces along the x-axis (see Figure 4.1), it is not required to put any energy absorbing material along the boundaries orthogonal to x-axis. On the other hand, in order to satisfy the plane strain conditions there must be a mechanism which eliminates the friction between model and walls orthogonal to z-axis. Oil soaked latex membranes have been used to minimize friction along the walls in retaining wall modelling studies [19] and this is also applicable to composite dam models.

4.2.8 Input ground motion

Input ground motion can be considered as acceleration boundary condition. To correctly scale inertial effects the model horizontal acceleration time history should have acceleration magnitudes equal to N times the prototype accelerations with a model frequency equal to N the prototype frequency.

4.2.9 Instrumentation

Instrumentations, such as accelerometer, total stress and pore pressure transducers are foreign materials embedded inside the small model. Instrumentation tools should not effect the behavior of soil, in other words, their size should be small enough not to disturb any constitutive behavior. Especially along the soil-concrete interface,

instrumentation should be done very carefully, otherwise real frictional behavior may be altered and erroneous results may come up during the test.

4.2.10 A Recommended Dynamic Composite Dam Centrifuge Test

A model of composite dam should be tested in centrifuge to:

(1) investigate separation amount and separation depth,

(2) obtain stress and pore pressure distribution along the interface.

A good instrumentation plan is required in order obtain the above information. Figure 4.2 shows a tentative instrumentation plan. The number of instrumentation can be determined by the success of funding opportunity.

Depending on the feasibility, an instrumentation priority has been set as follows:

(1) vertical and horizontal displacements must be monitored with LVDT_top_V and LVDT_top_H respectively.

(2) placing LC's at each instrumentation point.

(3) pore pressure monitoring by PPC at each point.

(4) placement of LVDT's at each point to monitor separation and separation depth.

On the other hand, because of the wide base, the model height maybe very small. This may cause difficulties in preparing and instrumenting the model. If the purpose of performing centrifuge is to verify numerical analysis, not to obtain the response of a

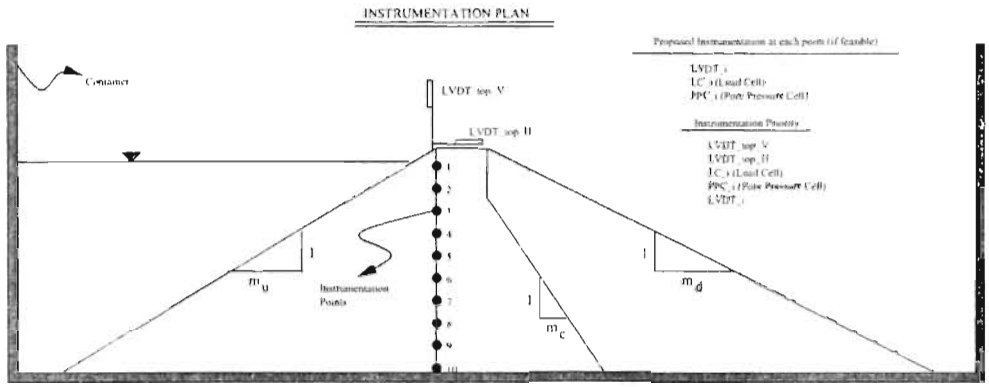

Figure 4.2 Instrumentation plan for centrifuge testing.

certain prototype, a simplified composite dam cross-section can be used in dynamic centrifuge testing. Simplified cross-section must allow to build bigger model and capture the essentials of IBCD. Therefore the cross-section without downstream soil embankment is shown in Figure 4.3 as a proposed composite dam geometry. This new geometry allows to have bigger model size and gives the basics of dynamic IBCD. Moreover, it will provide easiness in preparing computer model and shorter run time.

4.3 Stadler's Centrifuge Testing

4.3.1 Loading Sequence

The purpose of centrifuge modelling is to simulate the prototype stress and strain fields using a centrifuge model of its prototype structure. Figure 4.4 is an illustration of static and dynamic events employed in the centrifuge testing. First, the centrifuge is spun to the target g-level (from O to A), then it is held for several minutes to allow the

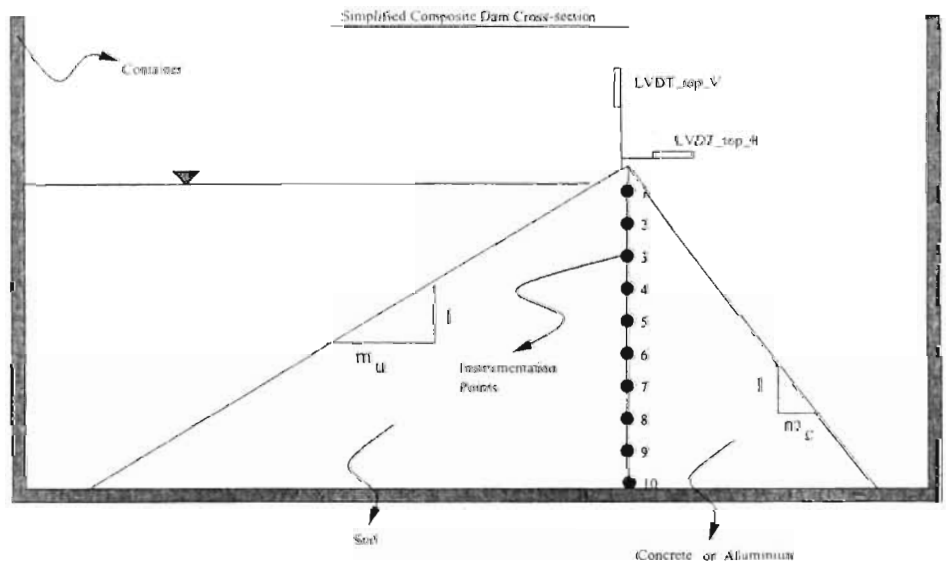

Figure 4.3 Simplified composite dam section.

instrumentation to stabilize (from A to B), and finally a dynamic event is initiated. The principles of centrifuge testing are discussed in detail in Section 4.

The CU-Boulder centrifuge is capable of spinning two tons of material at 200 times the force of gravity, and it is more powerful than any other civilian centrifuge outside the Soviet Union [44].

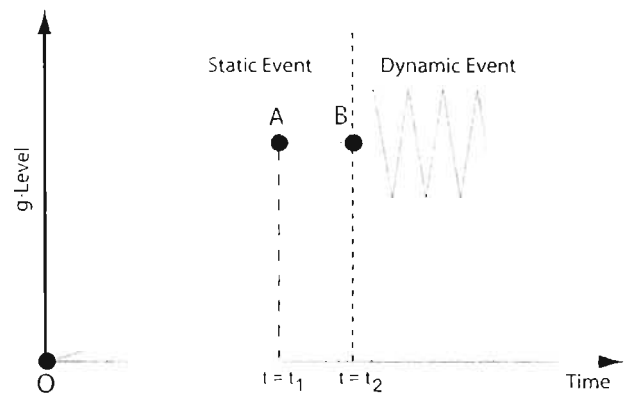

Figure 4.4 Sequence of static and dynamic events.

4.3.2 Wall Geometry and Material Properties

Stadler used T6061-T6 aluminum plate to model the wall. The Young's Modulus and Poisson's Ratio for this grade of aluminum are 10,000,000 psi and 0.32, respectively. Nevada #100 sand was used as the backfill. It has the specific gravity of 2.67 and maximum and minimum dry unit weight of 110.3 pcf and 88.3 pcf, respectively.

Among the three different wall configurations, the performance of the Model Wall Type B with 9.0 in stem height and 0.375 in stem thickness in model dimensions was used in the NIKE3D calibration effort. Under 40 g gravitational acceleration the selected model

wall height and stem thickness correspond to prototype dimensions of 30 ft and 12.6 in, respectively.

Figure 4.5 shows the centrifuge test box configuration and Figure 4.6 shows accelerometer and LVDT locations. Additionally, Figure 4.7 shows earth pressure transducer (EP), and strain gage (SG) locations on inboard face of the model wall.

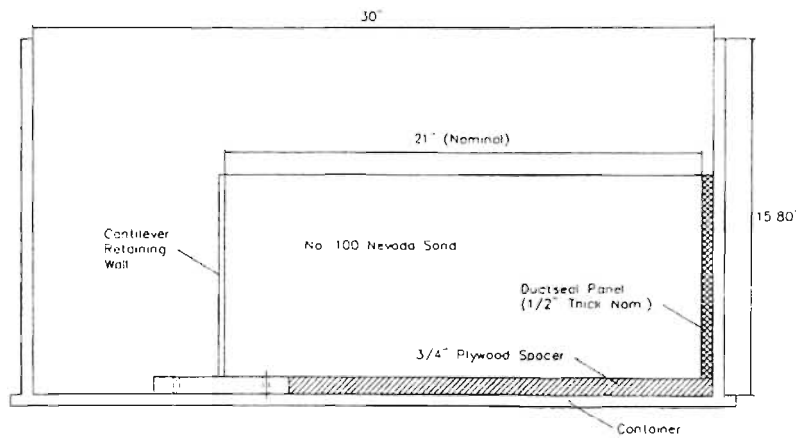

Figure 4.5 Centrifuge test box configuration. [73]

4.4 Finite Element Model of the Retaining Wall

Plain strain conditions were simulated using 8-node brick elements for wall, soil, plywood spacer, and ductseal. The mesh was created using TrueGrid [83], a mesh generating software for various numerical analysis softwares including NIKE3D. Wall-soil interface was simulated using NIKE3D's penalty formulation (a constraint approach) with Coulomb friction coefficient of 0.5. Figure 4.8 shows finite element mesh and the location of nodes along the wall-soil interface selected for data presentation.

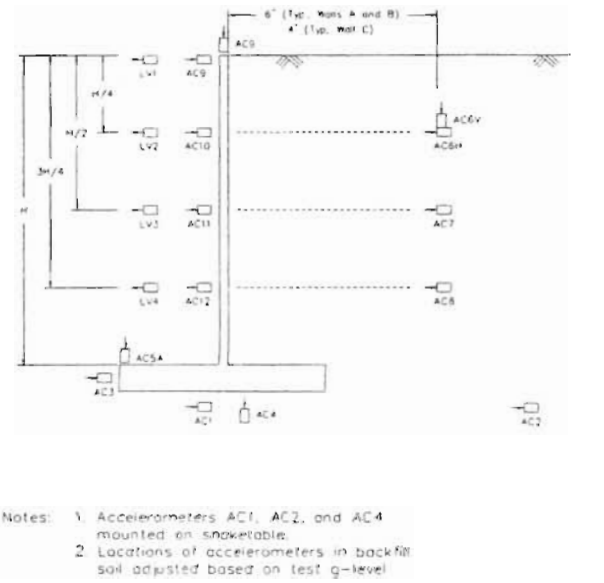

Figure 4.6 Accelerometer and LVDT locations [73].

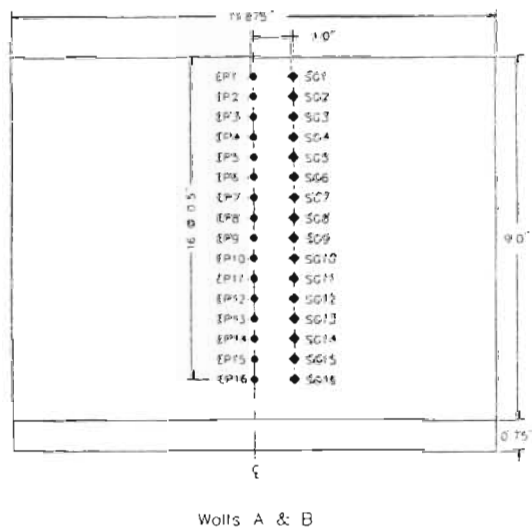

Figure 4.7 Earth pressure transducer (EP#), and strain gage (SG#) instrumentation on inboard face of the model wall. [73]

Table 4.3 Ramberg-Osgood and Elastic Model Parameters used in NIKE3D Analysis.

Model	Parameter	Backfill	Ductseal	Wall	Plywood
Elastic	Young's Modulus E (psi)	-	-	10,000,000	10,000,000
	Poisson's ratio ν	-	-	0.32	0.32
	Unit Weight (lb/in^3)	0.0578	0.0578	0.100	0.100
Ramberg-Osgood	Shear Wave Velocity V_s (ft/s)	700	700	-	-
	α	1.10	1.10	-	-
	r	2.35	2.35	-	-
	γ_y	0.000105	0.000105	-	-
	τ_y (psi)	1.11	1.11	-	-

The mesh has 912 brick elements and 868 nodes. Analyses were performed on a SGI R4400 Indigo2 Workstation.

Wall and soil material parameters used in NIKE3D analysis are summarized in Table 4.3. Soil and ductseal are modelled with Ramberg Osgood non-linear model whereas concrete and plywood are modelled as linear elastic materials.

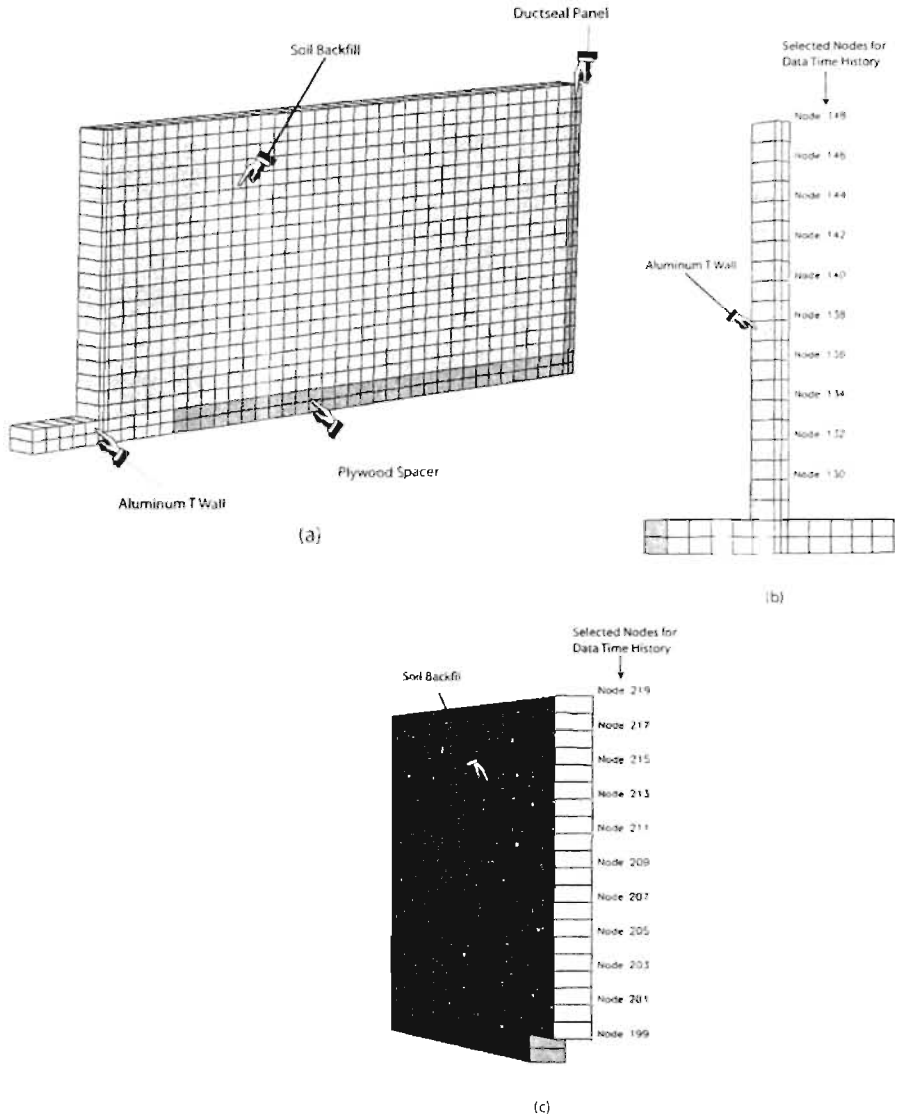

Figure 4.8 Wall mesh and selected nodes for data presentation.

Ramberg-Osgood material parameters of sand with unit weight of 100 pcf are listed in Table 4.4 for different shear wave velocities. The parameters were calculated using Seed's [68] average damping ratio and G/G_{max} versus shear strain curves for sand as shown in Figure 5.16. A special procedure was followed as explained in [77]. G_{max} is calculated using the equation proposed by Seed and Idriss [68];

$$G_{max} = 1000 K_{2max} (\sigma_m^{'})^{1/2} \tag{4.1}$$

where G_{max} is maximum shear modulus at low strains in psf, $\sigma_m^{'}$ is mean effective confining pressure in psf, K_{2max} is a factor which depends on relative density, maximum particle size, gradation, etc. of sand.

$\sigma_m^{'}$ is calculated at the mid-depth of the backfill, and K_{2max} is taken as 52 corresponding to 60% relative density. After calculating G_{max} the shear wave velocity is calculated using the relation;

$$V_s = \sqrt{\frac{G_{max}}{\rho}} \tag{4.2}$$

where V_s is the shear wave velocity, ρ is density.

Finally, V_s was calculated to be approximately 700 ft/s and corresponding Ramberg-Osgood material parameters (Table 4.4) were used in NIKE3D analysis.

Ramberg-Osgood Material Parameters for Average Sand (γ = 100 pcf)					
V_s (ft/s)	G_{max} $(10^3 psf)$	α	r	γ_y (10^{-3})	τ_y (psf)
100	31.10	1.10	2.35	0.105	3.27
150	69.97	1.10	2.35	0.105	7.36
200	124.40	1.10	2.35	0.105	13.09
250	194.38	1.10	2.35	0.105	20.46
300	279.90	1.10	2.35	0.105	29.46
350	380.98	1.10	2.35	0.105	40.10
400	497.60	1.10	2.35	0.105	52.37
450	629.78	1.10	2.35	0.105	66.28
500	777.50	1.10	2.35	0.105	81.83
550	940.77	1.10	2.35	0.105	99.02
600	1119.60	1.10	2.35	0.105	117.84
650	1313.97	1.10	2.35	0.105	138.29
700	1523.90	1.10	2.35	0.105	160.39
750	1749.38	1.10	2.35	0.105	184.12
800	1990.40	1.10	2.35	0.105	209.49
850	2246.98	1.10	2.35	0.105	236.49
900	2519.10	1.10	2.35	0.105	265.13
950	2806.77	1.10	2.35	0.105	295.41
1000	3110.00	1.10	2.35	0.105	327.32
1050	3428.77	1.10	2.35	0.105	360.87
1100	3763.10	1.10	2.35	0.105	396.06
1150	4112.97	1.10	2.35	0.105	432.88
1200	4478.40	1.10	2.35	0.105	471.34
1250	4859.38	1.10	2.35	0.105	511.44
1300	5255.90	1.10	2.35	0.105	553.18
1350	5667.98	1.10	2.35	0.105	596.55
1400	6095.60	1.10	2.35	0.105	641.55
1450	6538.77	1.10	2.35	0.105	688.20
1500	6997.50	1.10	2.35	0.105	736.48
1550	7471.77	1.10	2.35	0.105	786.39
1600	7961.60	1.10	2.35	0.105	837.95
1650	8466.97	1.10	2.35	0.105	891.14
1700	8987.90	1.10	2.35	0.105	945.96
1750	9524.38	1.10	2.35	0.105	1002.43
1800	10076.40	1.10	2.35	0.105	1060.53
1850	10643.97	1.10	2.35	0.105	1120.26
1900	11227.10	1.10	2.35	0.105	1181.63
1950	11825.78	1.10	2.35	0.105	1244.64
2000	12440.00	1.10	2.35	0.105	1309.29
2050	13069.78	1.10	2.35	0.105	1375.57
2100	13715.10	1.10	2.35	0.105	1443.49
2150	14375.97	1.10	2.35	0.105	1513.05
2200	15052.40	1.10	2.35	0.105	1584.24
2250	15744.37	1.10	2.35	0.105	1657.07
2300	16451.90	1.10	2.35	0.105	1731.54
2350	17174.97	1.10	2.35	0.105	1807.64
2400	17913.60	1.10	2.35	0.105	1885.38
2450	18667.77	1.10	2.35	0.105	1964.75
2500	19437.50	1.10	2.35	0.105	2045.77

Table 4.4 Ramberg-Osgood material properties for Seed's Average Sand with γ=100 pcf

4.5 Input Motion

In Stadler's centrifuge testing each static event was performed as follows: The centrifuge was spun to the target g-level in about 10 minutes. Once the centrifuge was at the target g-level, it was held there for several minutes. The same sequence was followed in NIKE3D analysis using a 40 g loading curve as shown in Figure 4.9. This curve was obtained from Stadler's study and digitized using scanning techniques.

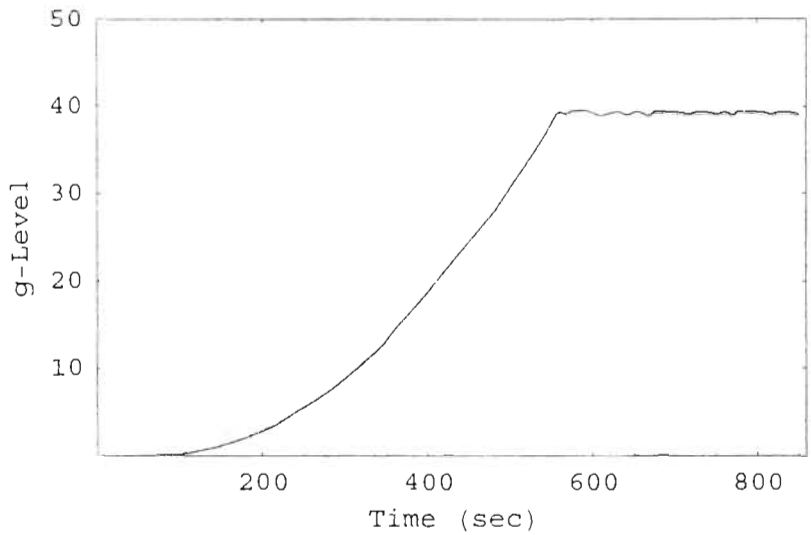

Figure 4.9 Input Motion for Static Loading.

Stadler used the prescribed input motion consisted of twelve cycles of approximately sinusoidal motion. The first and last two cycles were "ramp-up/ramp-down" and the middle eight were at the full amplitude. The frequency of input motion was adjusted to 1 Hz in prototype scale. Figure 4.10 shows the prescribed and measured horizontal input motion used in the centrifuge test. Due to the mechanical and electrical limitations of the shaking system the delivered motion was typically different from the

prescribed motion. Many attempts including email and personal conversations were made to obtain the digitized measured input motion without success. Finally the author scanned the measured input motion as shown in Figure 4.10 and digitized it using pixel readings on the image. Then the data was interpolated for every 0.0005 sec. The resulting acceleration time history is shown in Figure 4.11. RMS acceleration value of interpolated acceleration time history was calculated as 5.51 g which is very close to the actual value of 5.6 g.

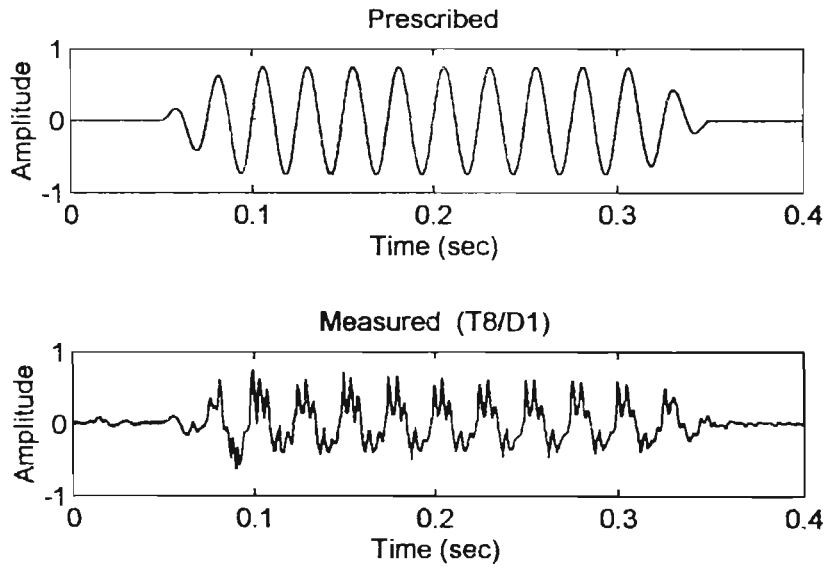

Figure 4.10 Typical Prescribed and Measured Horizontal Input Motions [73].

4.6 Centrifuge Test Results

Stadler presented dynamic profiles of wall-soil system at two time steps in addition to the initial state which represents the static condition before the dynamic excitation. The chosen time steps include the maximum positive horizontal input accelerations as

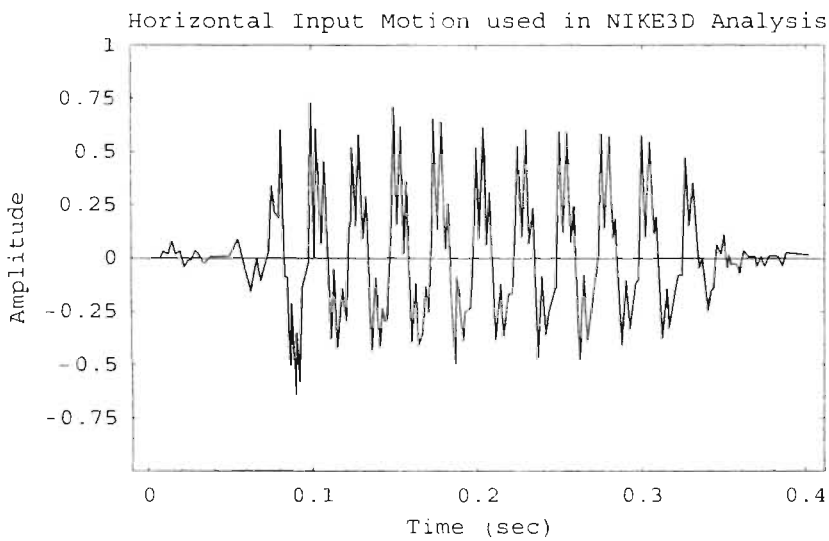

Figure 4.11 Input Motion for NIKE3D Analysis. Digitized from measured input motion in Figure 4.10

shown in Figure 4.12. The dynamic profiles at time steps 249 and 637 are provided in Figures 4.13 and 4.14, respectively. Each dynamic profile includes earth pressure (σ_y), moment (M), and wall deflection (y) versus wall height (z) plots. Earth pressure is normalized by vertical stress at the base (σ_{z-base}), moment is normalized by unit weight times the wall height cube (γH^3), finally wall deflection and height are normalized by the full wall height (H). in Figures 4.13 and 4.14, left column of plots shows the initial (static) and total (dynamic state including the static) states of the wall. The right column shows only the net change in response due to the dynamic loading and it is called as incremental (total-initial).

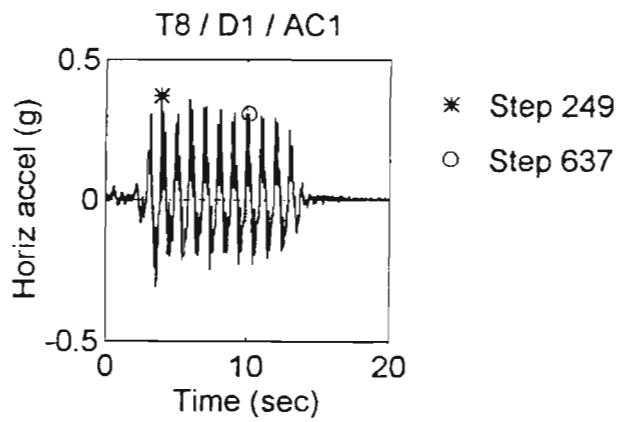

Figure 4.12 Measured Input Motion and step numbers for data gathering [73].

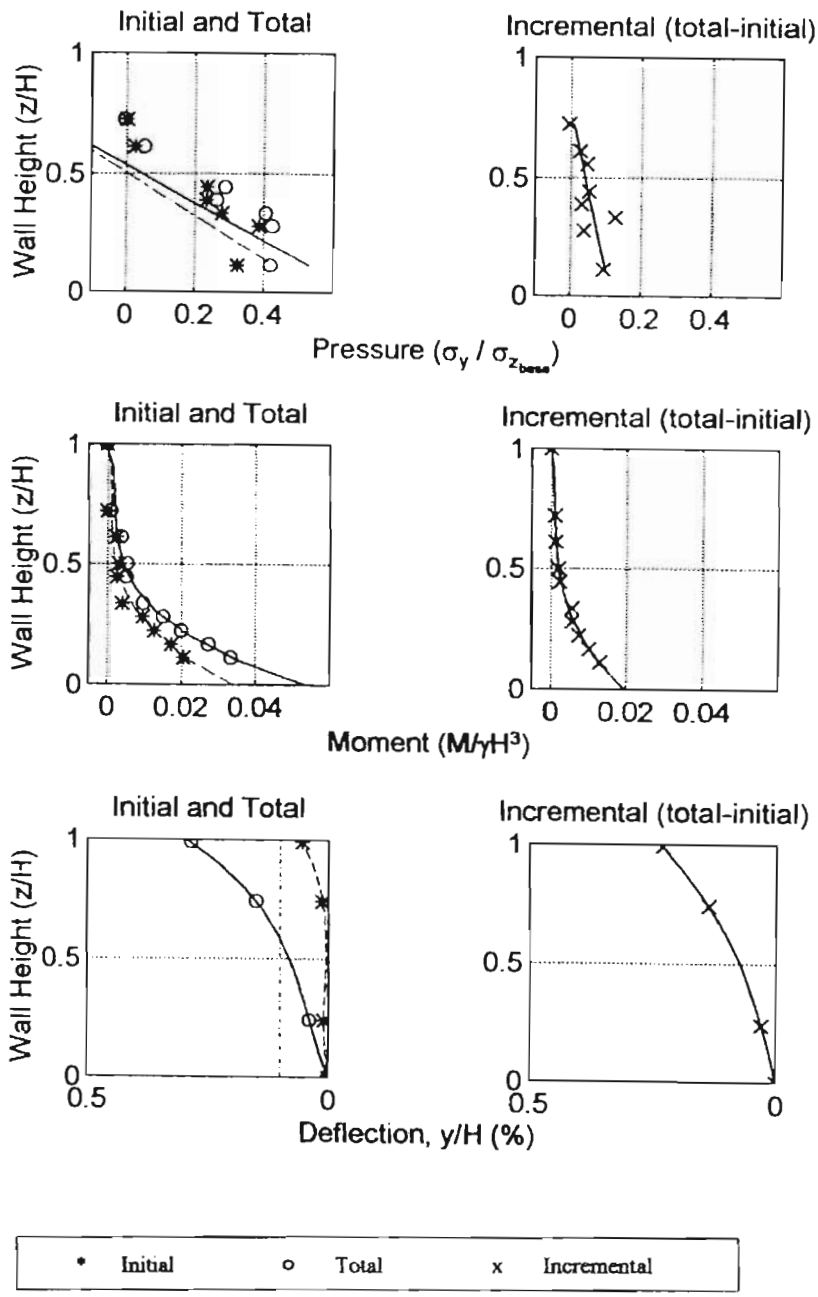

Figure 4.13 Dynamic Profiles at Step 249 [73].

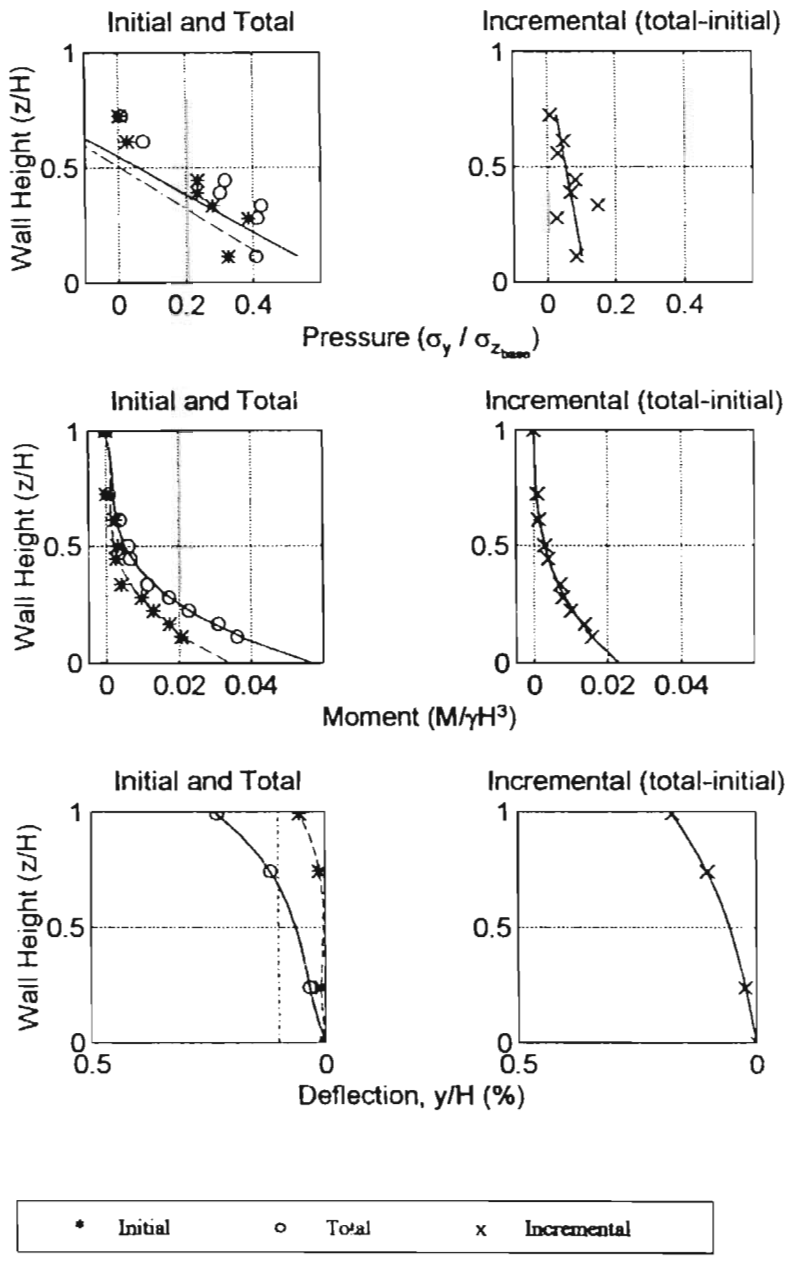

Figure 4.14 Dynamic Profiles at Step 637 [73].

Table 4.5 Numbers of figures illustrating the comparison of measured and calculated data.

Parameter	Damping Ratio (%)	Figure Numbers
Wall Deflection	0	4.16
	10	4.17
	20	4.18
Earth Pressure	0	4.19
	10	4.20
	20	4.21
RMS Acceleration Ratio	0	4.22
	10	4.23
	20	4.24

4.7 NIKE3D Simulation and Comparisons

Three NIKE3D analysis were performed with different Rayleigh damping ratios of 0, 10, and 20%. NIKE3D results were compared with measured data at two time steps chosen by Stadler. Wall deflection, earth pressure, and root mean square acceleration (RMS) ratios are compared. The root mean square acceleration ratio is defined as;

$$RMS = \left[\frac{1}{T}\int a^2 dt\right]^{1/2} \tag{4.3}$$

where RMS is the root mean square acceleration, t is time, and T is is time interval of the measurement. Measured and calculated data are presented in Figures listed in Table 4.5.

In order to make exact comparisons wall deflection (y), and earth pressure (σ_h) are normalized with full wall height (H), and vertical stress at the base (σ_{vbase}), respectively. Finally all parameters are plotted versus wall height, z, normalized by H. Figure 4.15 shows the representation of wall deflection and height.

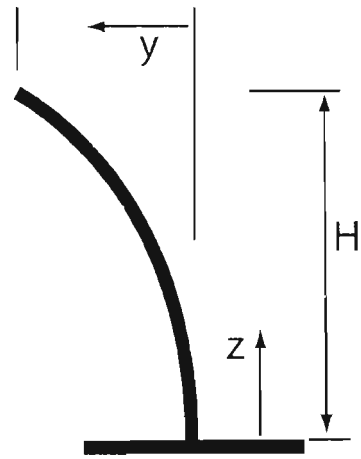

Figure 4.15 Representation of deflection, y, and depth, z.

NIKE3D predictions on wall deflection showed very good agreement with the measured data as shown in Figures 4.16, 4.17, and 4.18 for different Rayleigh damping parameters. Initial deflections calculated by NIKE3D are slightly bigger than measured data. On the other hand deflections at other two time steps show very good agreement, almost like best fit to the actual data. It should also be noted that the Raylegh damping does not seem to affect the wall deflection.

Earth pressure predictions are also in good agreement as shown in Figures 4.19, 4.20, and 4.21. Due to the suspicion in stress data measurements reported by Stadler it was not possible to make exact comparison of earth pressures. In general NIKE3D prediction follows the general trend of the measured stress data. Figures 4.19, 4.20, and 4.21 also show that the Raylegh damping does not seem to affect the earth pressure distribution. It should be noted that the separation potential in the top half or two thirds of the wall height is clearly demonstrated by both calculated and measured data. In the bottom half of the wall height the measured data were quite scatter and measurements were presented at only 7 locations out of 16 instrumentation points. This makes the comparison difficult.

RMS acceleration ratio comparisons are shown in Figures 4.22, 4.23, and 4.24. RMS ratio for both wall and soil are overpredicted by NIKE3D using Rayleigh damping ratio of 0%. Increasing the Rayleigh damping ratio to 10% resulted in more reasonable agreement as shown in Figure 4.23. Finally, increasing the Rayleigh damping ratio to 20% showed very good agreement for both wall and soil RMS accelerations as shown in

Figure 4.24. Increasing Rayleigh damping ratio from 0 to 20% decreased RMS acceleration ratio considerably while having very little effect on wall deflections and earth pressures. At the top of the wall measured data shows RMS acceleration ratio around 1.5 and it is predicted by NIKE3D to be slightly less than 1.8. This shows the amplification of ground motion as it propagates from base to the top.

Finally RMS acceleration ratio in soil along the wall-soil interface and at two different locations, 1.3 inches and 6 inches away from the wall-soil interface as shown in Figure 4.25, are presented. Figure 4.26 shows RMS acceleration ratio versus wall height for the above mentioned locations and for damping ratios of 0, 10, and 20%. RMS acceleration ratio, with a maximum around 2, is highest in soil at the wall-soil interface. It should also be noted that ground motion is amplified from bottom to 50% of the wall height. Then, amplification is decreased in top half of the wall with a slight increase at the very top. On the other hand at the other two locations amplification is almost linearly increased from bottom to the top. This shows the complicated dynamic behavior of wall-soil interface.

To see the damping ratio effect on the wall displacement at other time steps rather than the ones used for data comparisons, partial deflection time histories of wall top are presented in Figure 4.27. Parts (a) and (c) of Figure 4.27 show the deflection time histories in the vicinity of Time Step 249 and 637, respectively, and it is shown that at these specific time steps, wall deflection values are very close for different damping

ratios. Figure 4.27 also shows that the effect of damping is more clear when the wall moves towards the soil (passive condition).

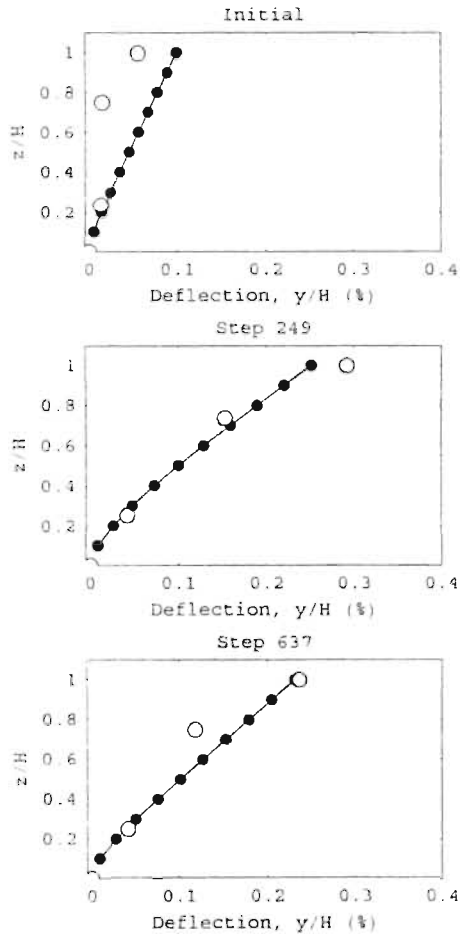

Figure 4.16 Wall deflection comparison for $\xi = 0\%$.

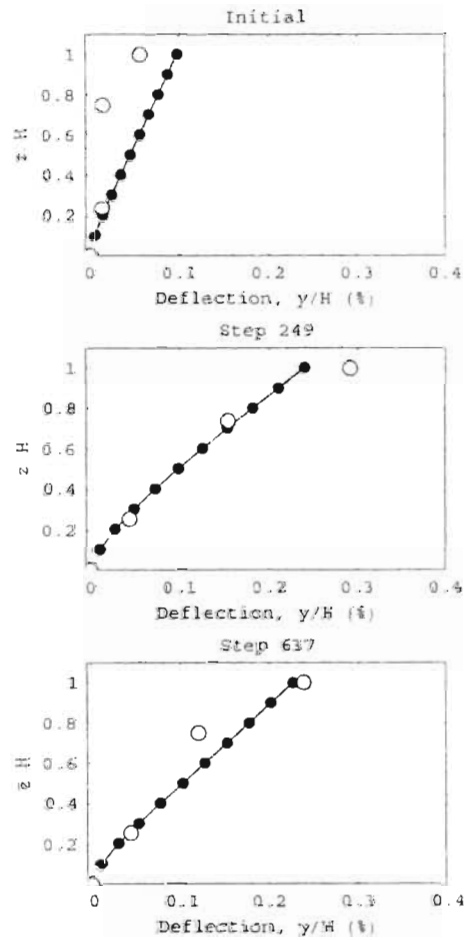

Figure 4.17 Wall deflection comparison for $\xi = 10\%$.

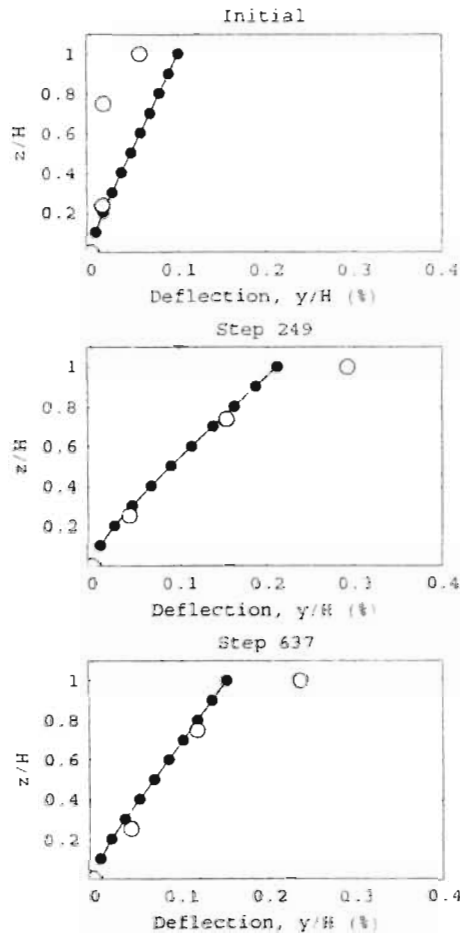

Figure 4.18 Wall deflection comparison for $\xi = 20\%$.

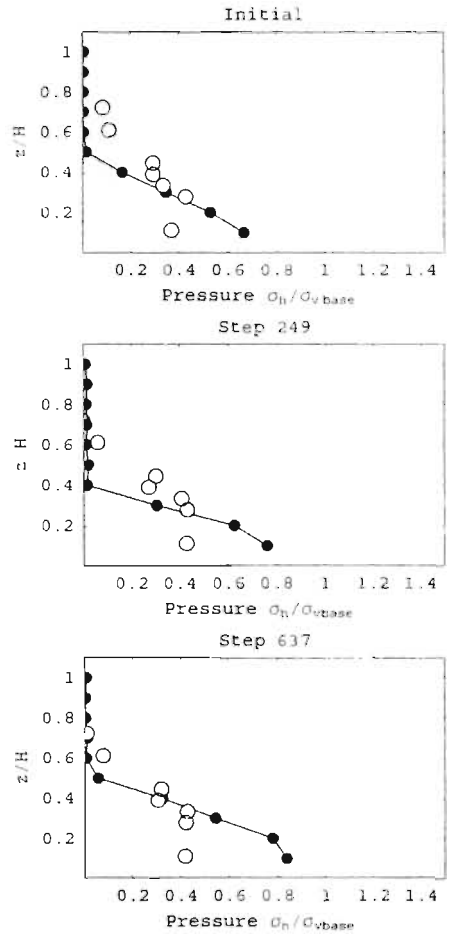

Figure 4.19 Earth pressure comparison for $\xi = 0\%$.

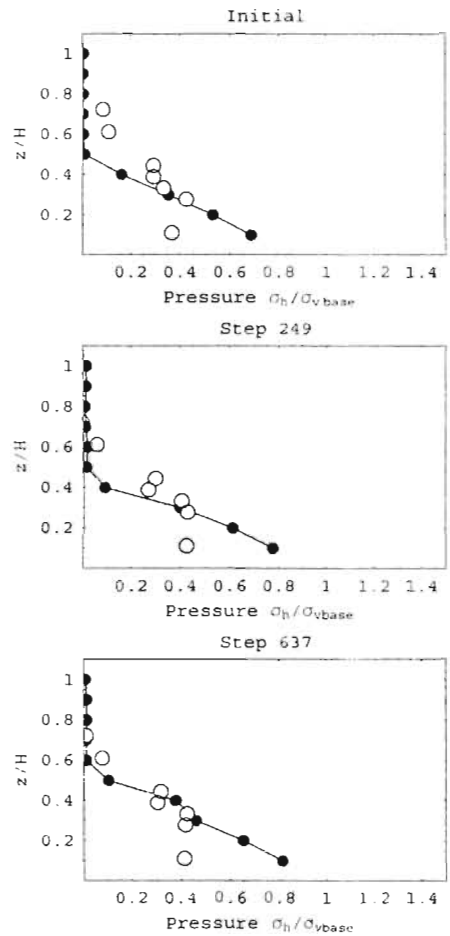

Figure 4.20 Earth pressure comparison for $\xi = 10\%$.

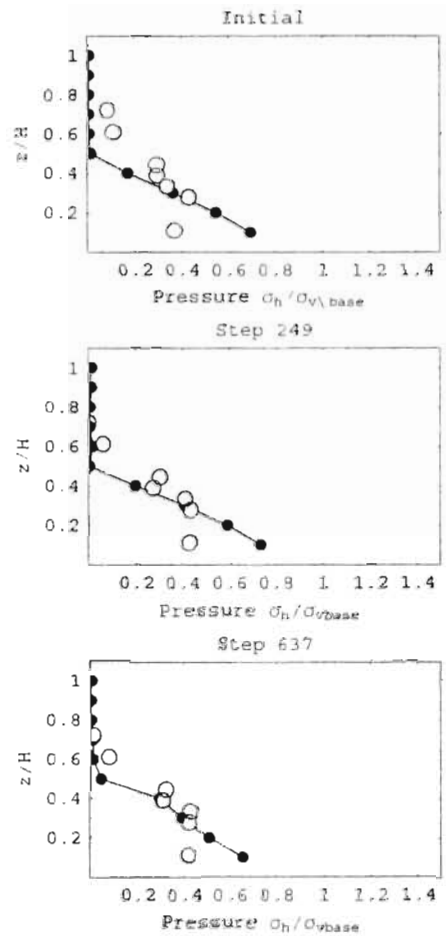

Figure 4.21 Earth pressure comparison for $\xi = 20\%$.

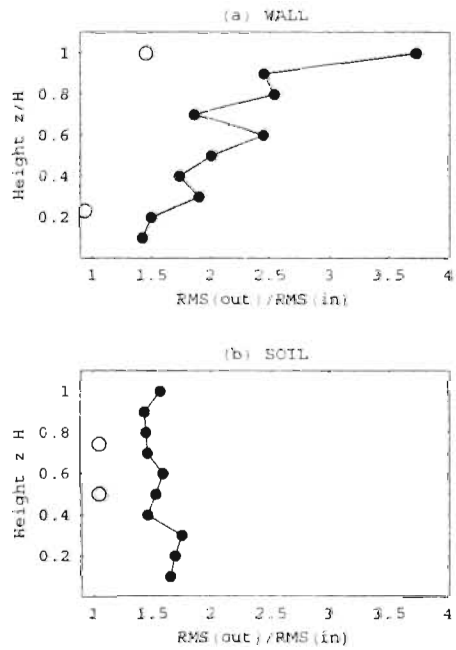

Figure 4.22 RMS acceleration ratio comparison for $\xi = 0\%$.

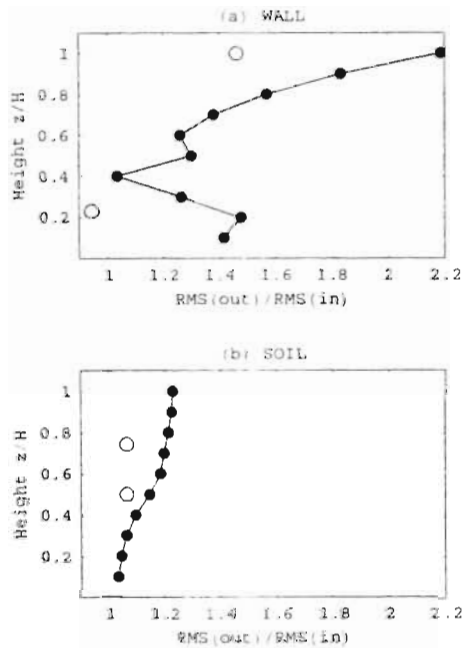

Figure 4.23 RMS acceleration ratio comparison for $\xi = 10\%$.

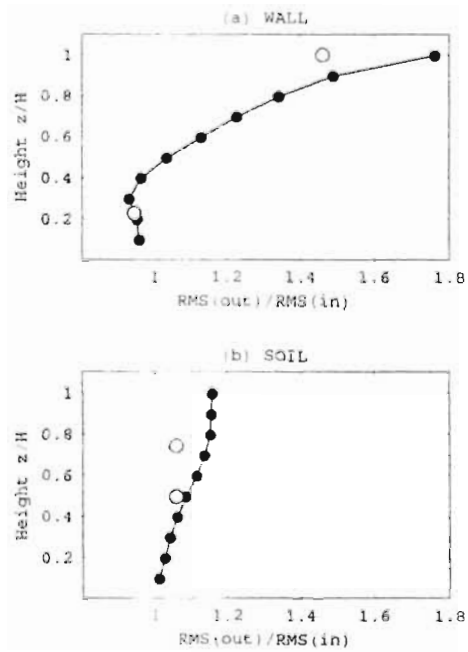

Figure 4.24 RMS acceleration ratio comparison for $\xi = 20\%$.

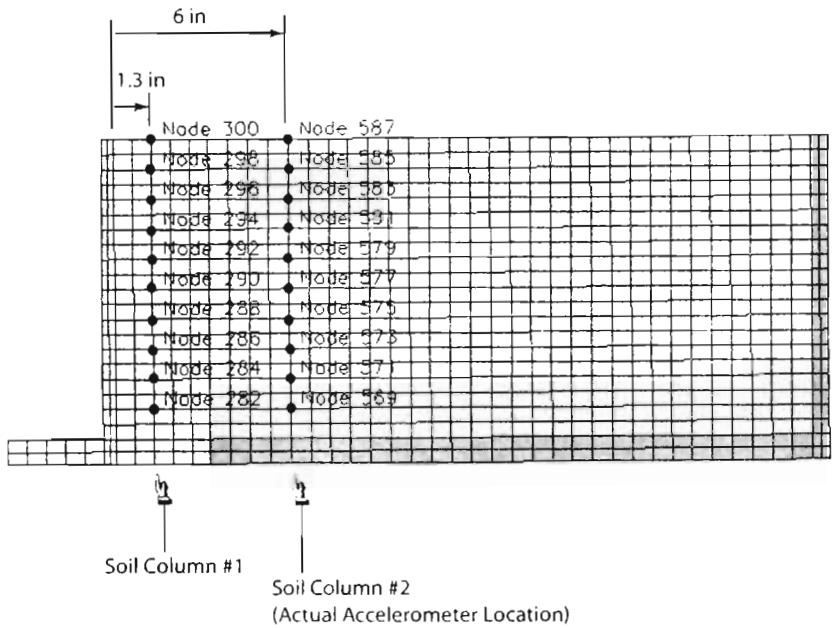

Figure 4.25 Location of soil columns for RMS comparisons.

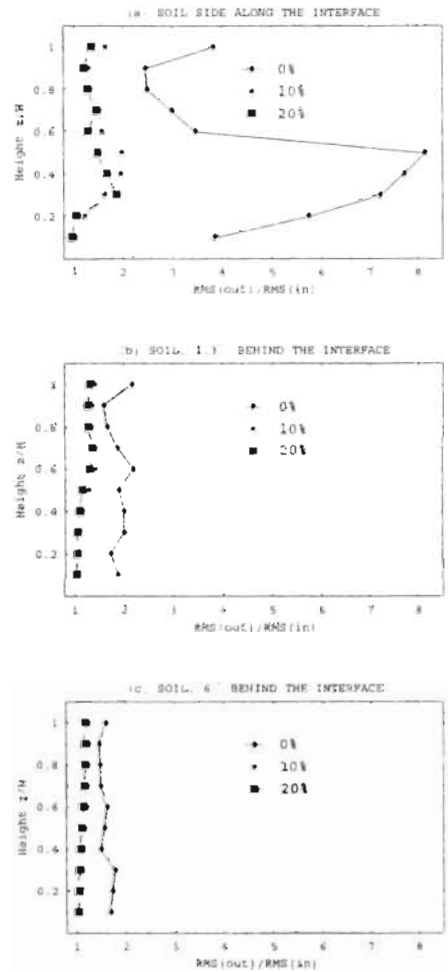

Figure 4.26 RMS acceleration ratio in soil along the interface, 1.3 and 6 inches away from the interface for $\xi = 0, 10$, and 20%.

4.8 Conclusions

Wall deflections calculated by NIKE3D are in excellent agreement with the measured data. Relatively good agreement was obtained in earth pressure comparison. RMS acceleration ratios were overpredicted by NIKE3D for low Rayleigh damping ratio. On the other hand the analysis with $\xi = 20\%$ showed very good RMS acceleration agreement as well as wall deflection and earth pressure. Increasing damping ratio resulted in decrease of RMS acceleration ratio while having very little effect on both wall deflection and earth pressure at the both time steps. Higher damping ratio can be used if one desires to have a better agreement of RMS acceleration ratio.

From the above mentioned comparisons it is concluded that the centrifuge test serve as an excellent calibrator for dynamic numerical analysis computer codes and the NIKE3D is proven to be the effective nonlinear dynamic analysis computer code.

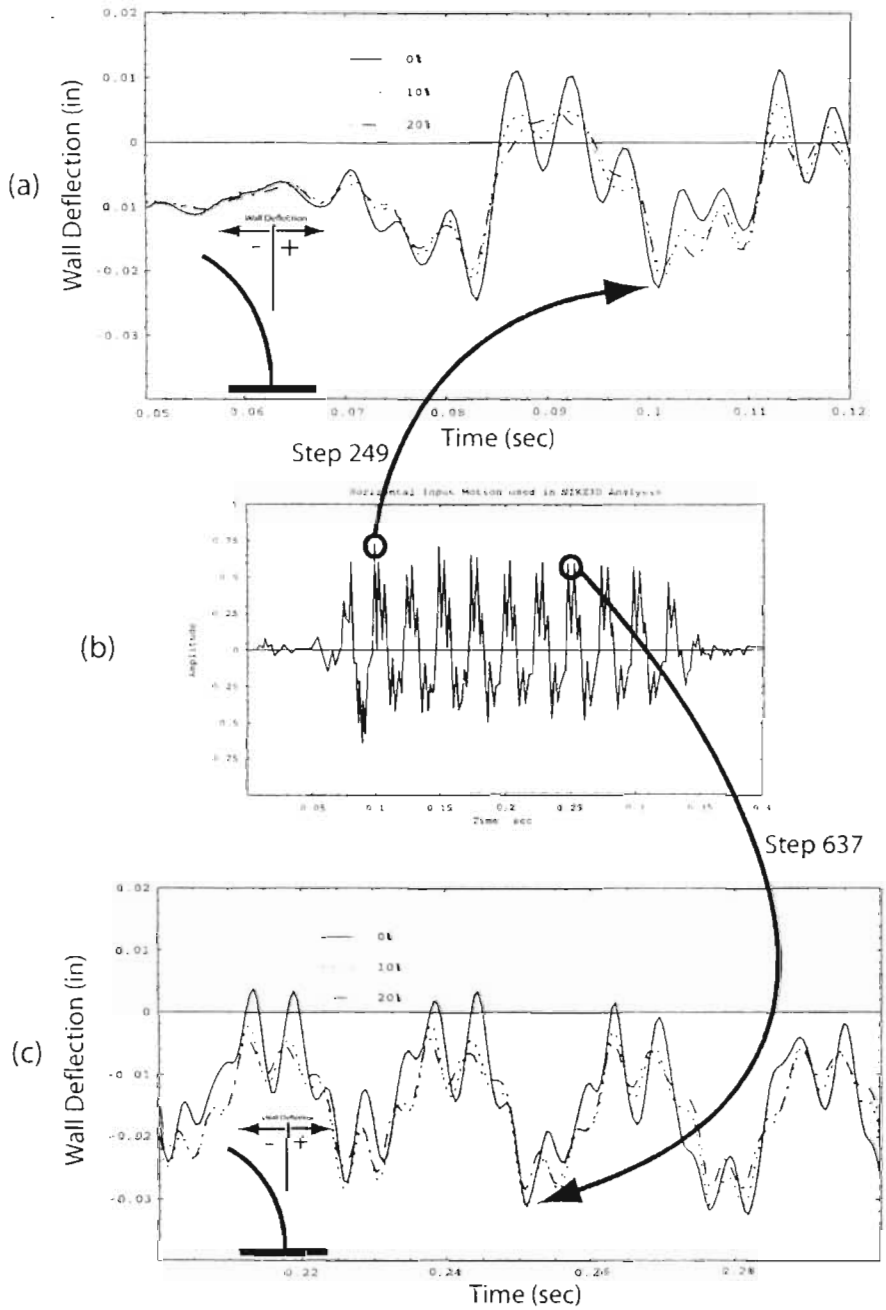

Figure 4.27 Deflection of wall top at different time steps for different damping ratios.

5. Selection of Numerical Analysis Parameters

5.1 Introduction

Reliability of a numerical analysis strongly depends on the quality of the input. Every analysis parameter used as an input must be justified. Incorrect parameters make problems more intricate and difficult to interpret. In particular dynamic soil-structure interaction problems have already complicated nature. Thus the input parameters must be carefully selected.

In this chapter all input parameters for both 2-D and 3-D FE analyses are explained in detail and referenced in the subsequent chapters. They include input motion, FE mesh, material model parameters, interface treatment, and global damping parameters.

5.2 Input Motion

In all parametric FE analyses, the ground motion record of Koyna Dam Earthquake of magnitude 6.5, with amax=0.87g in transverse direction, was used. Figure 5.1 shows time history of all three components of the ground motion. During the case study of Folsom Dam the transverse component was scaled to investigate the sensitivity of IBCD

to peak ground acceleration. Additionally, the transverse component of Koyna Record and its acceleration spectrum are presented in Figure 5.2.

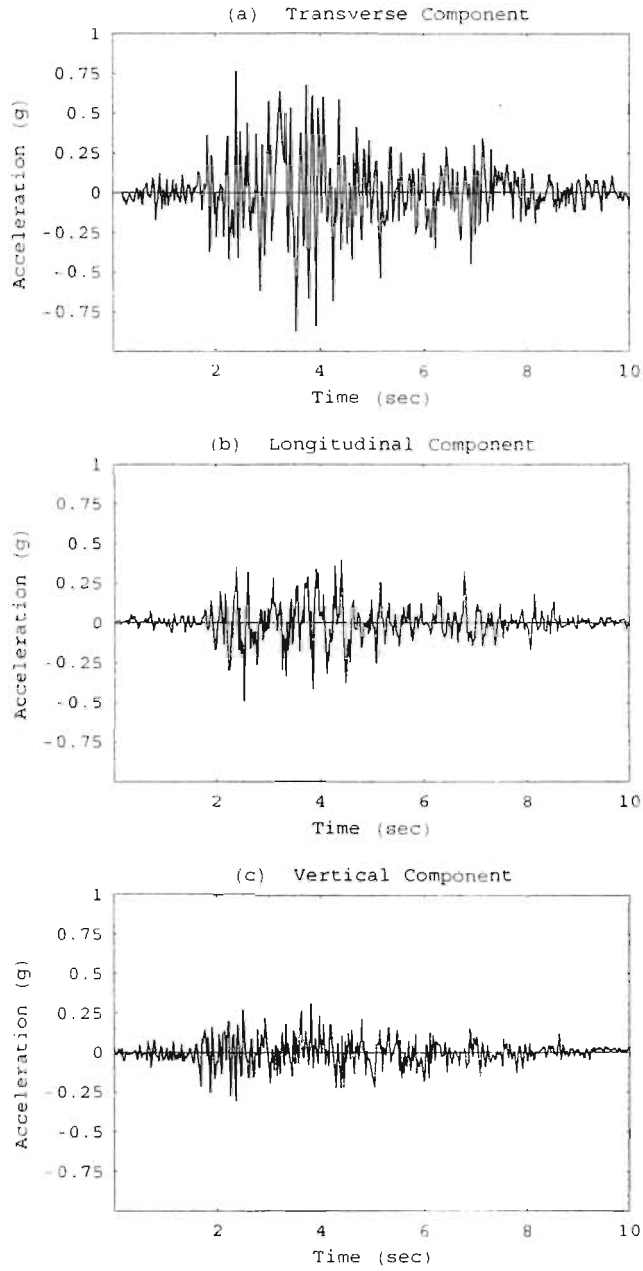

Figure 5.1 (a) Transverse, (b)Longitudinal, and (c)Vertical components of Koyna Dam Earthquake Record, 1967.

5.3 Finite Element Models

The mesh used in all FE analyses was built using powerful mesh generating software, TrueGrid [83]. Besides NIKE3D, TrueGrid has also the ability to produce mesh for other well known softwares such as ADINA, ANSYS, MARC, LS-DYNA, LS-NIKE, etc. Its user friendly tools and powerful algorithms have provided flexibility and easiness to build the mesh for complicated 3-D soil-concrete interface.

The following assumptions were made for all FE analyses:

(1) Foundation is assumed as fixed boundary condition.

(2) Hydrostatic pressure is applied along the upstream soil face.

(3) No reservoir bottom absorption.

(4) The Coulomb friction prevails along the soil-concrete interface with the coefficient of friction μ=0.5.

(5) Ramberg-Osgood non-linear model is used for soil, whereas concrete is assumed as elastic. In exploratory 3-D analysis, Chapter 7, soil was also assumed as elastic.

(6) No uplift pressure is assumed.

(7) Temperature effects are not considered.

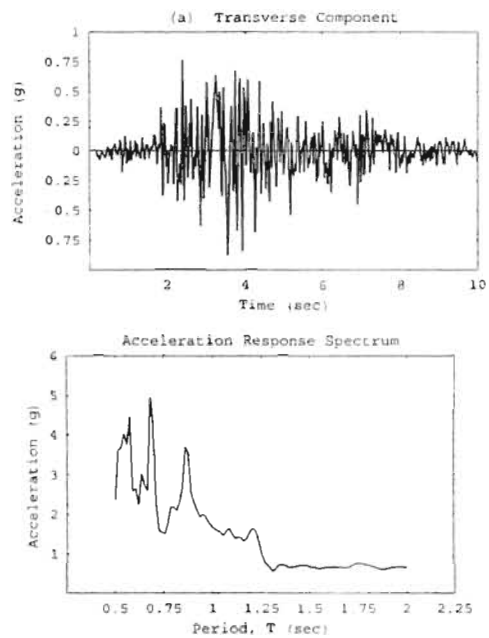

Figure 5.2 Horizontal component of Koyna Dam Earthquake Record and its acceleration response spectrum

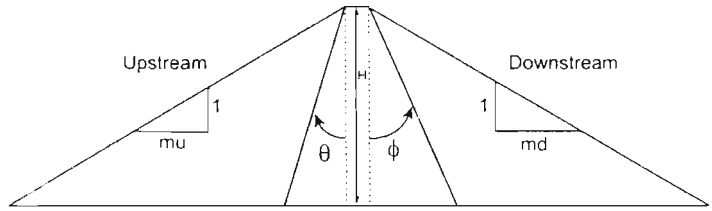

Figure 5.3 Hypothetical composite dam.

5.3.1 Two-Dimensional Model

For this parametric study a cross-section of a hypothetical dam is selected for analysis as illustrated in Figure 5.3. The followings are the controlling parameters of cross-sectional geometry: θ, the slope angle of the upstream interface; ϕ, the slope angle of the downstream interface; *mu*, upstream soil slope; *md*, downstream soil slope; and, H, height as shown in Figure 5.3. The initial geometry, in which θ=0 degrees, ϕ=26.6 degrees, *mu*=2.0, and *md*=2.0, is called as `reference configuration`. As presented in Chapter 6, the controlling parameters of the cross-section were varied in certain a range starting from the `reference configuration`.

Figure 5.4 shows the mesh created for plane strain analysis using 8-node brick elements. It has 536 nodal points and 218 brick elements. Plane strain conditions are simulated with three dimensional elements. The interface is modelled using penalty formulation of NIKE3D as explained earlier in Section 3.3.6. It allows frictional sliding and separation. Same mesh was created for all heights by scaling the height, H. Analyses were performed on a SGI R4400 Indigo2 Workstation. The material model parameters used in the analyses are presented later in Section 5.4.

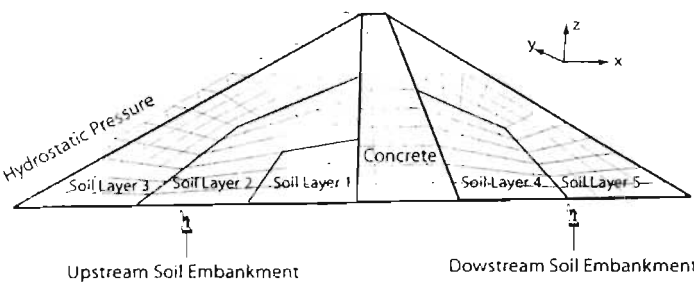

Figure 5.4 The mesh for plane strain analysis.

5.3.2 Three-Dimensional Model

Ideally a full 3-D model of a composite dam consists of three main parts; concrete monolith, left and right embankment wing dams as shown in Figure 5.5. Indeed, performing nonlinear FE analyses with the full 3-D model is quite time consuming. Thus it was decided to reduce the mesh to one half size. Figure 5.6 shows the actual mesh used in 3-D FE analysis. In order to eliminate the boundary effects it was decided to extend the concrete monolith by 3H in longitudinal direction, and soil embankment by 7H, where H is the height of the composite dam. As a result, the total length of the dam is 10H. Upstream soil slope, downstream soil slope, upstream interface angle, and downstream interface angle are taken as 2. 2. 0 degrees, and 26.6 degrees, respectively. Finally the transverse interface is assumed to be vertical. The free ends of soil embankment and concrete monolith are restricted to move in longitudinal direction and freed in other directions. The mesh has 4902 nodal points and 4056 brick elements.

Because of the complexity of the geometry, it is worthwhile to illustrate all the soil-concrete interface areas in detail. Figure 5.7 illustrates the plan view of composite dam and three cross-sections showing downstream, transverse, and upstream interfaces in parts (b), (c), and (d), respectively. For a better illustration, concrete monolith and downstream embankment are removed from the mesh to expose the transverse and upstream interfaces as shown in Figure 5.8. Next, the concrete monolith and upstream soil embankment are removed to expose downstream interface as shown in Figure 5.9. Finally, Figures 5.10, and 5.11 shows all three interfaces on the concrete monolith.

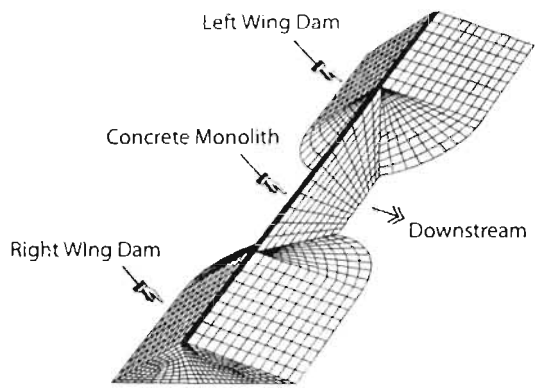

Figure 5.5 A complete 3-D model of a composite dam.

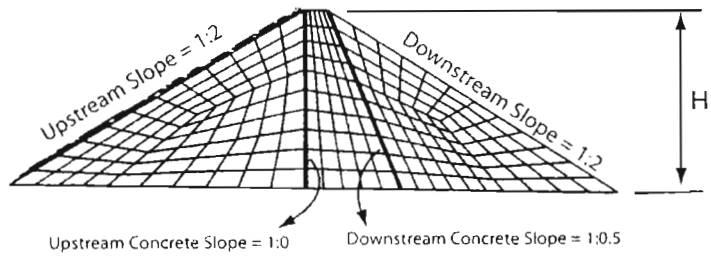

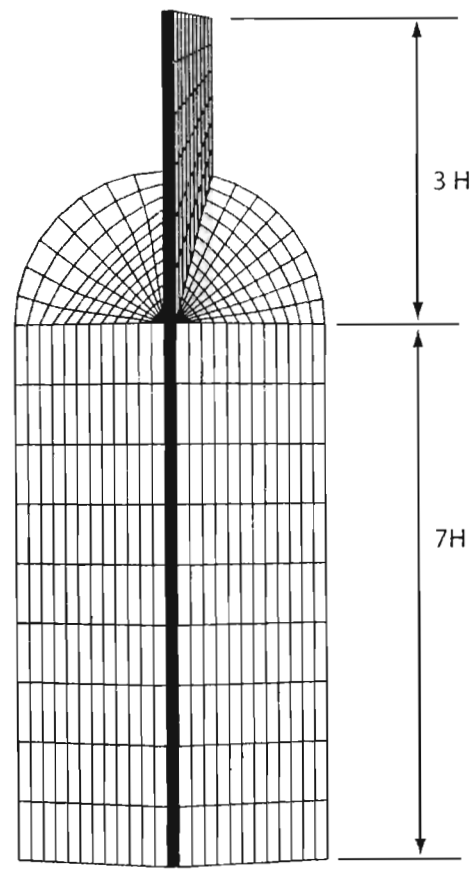

Figure 5.6 3-D Mesh of the composite dam and dimensions.

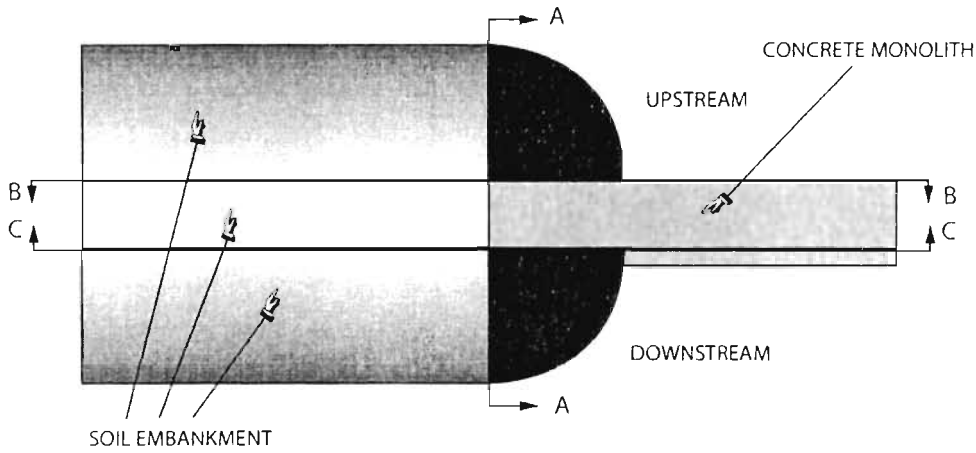

(a) Plan View of Soil-Concrete Interface Area

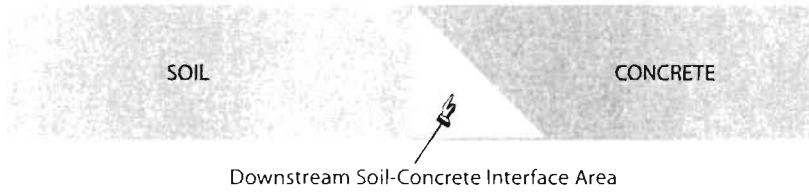

(b) Section C-C

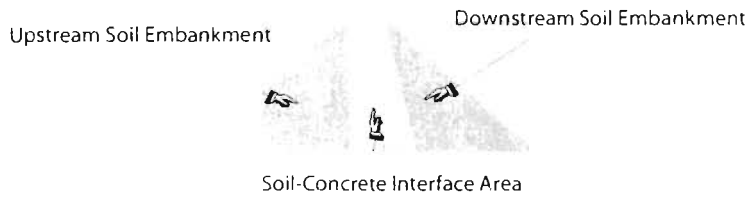

(c) Section A-A

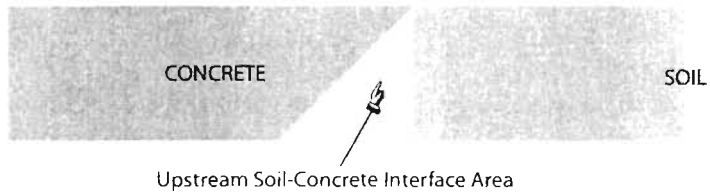

(d) Section B-B

Figure 5.7 Representations of upstream, transverse, and downstream soil-concrete interface areas.

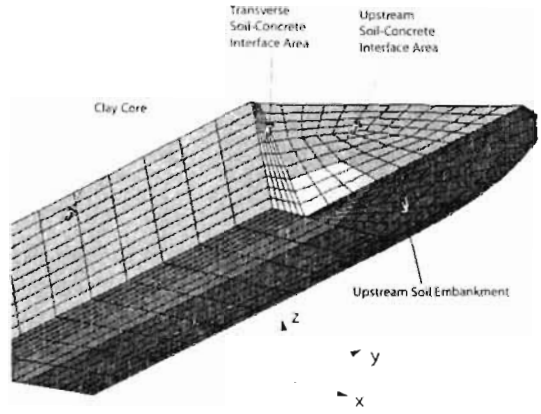

Figure 5.8 FE Mesh of upstream embankment and clay core.

5.4 Material Parameters

To reflect the effect of overburden pressure on the material properties, upstream and downstream embankments were divided into 3, and 2 layers, respectively. Figure 5.12 illustrates the idealized cross-section with soil layers.

Table 5.1 lists the unit weight, γ, and density, ρ, of different materials. Same densities were used for all geometric configurations.

The shear modulus at low strains, G_{max}, was calculated for each soil layer using the equation proposed by Seed and Idriss [68]:

$$G_{max} = 1000 K_{2max} (\sigma_m^{'})^{1/2} \tag{5.1}$$

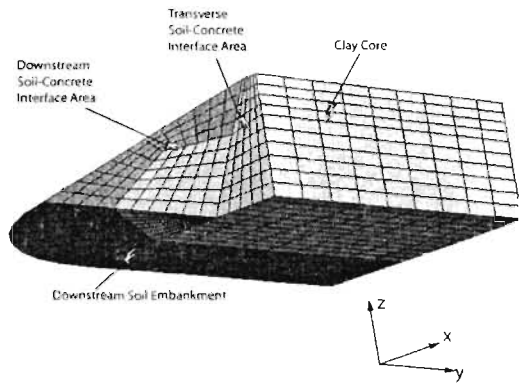

Figure 5.9 FE Mesh of downstream embankment and clay core.

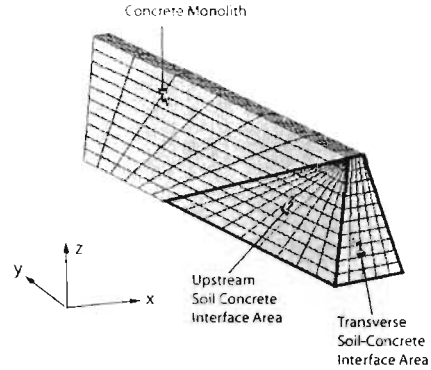

Figure 5.10 FE Mesh of concrete monolith and upstream interface.

Table 5.1 Unit Weight Distribution.

Material Number	Unit Weight, γ		Density, ρ	
	pcf	kN/m^3	$slugs/ft^3$	Mg/m^3
2	145	22.8	4.50	0.072
3	135	21.2	4.19	0.067
4	125	19.7	3.88	0.062
5	140	22.0	4.35	0.069
6	130	20.4	4.04	0.065
7(clay)	135	21.2	4.19	0.067

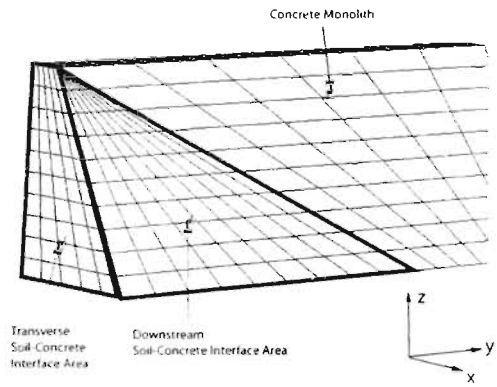

Figure 5.11 FE Mesh of concrete monolith and upstream interface.

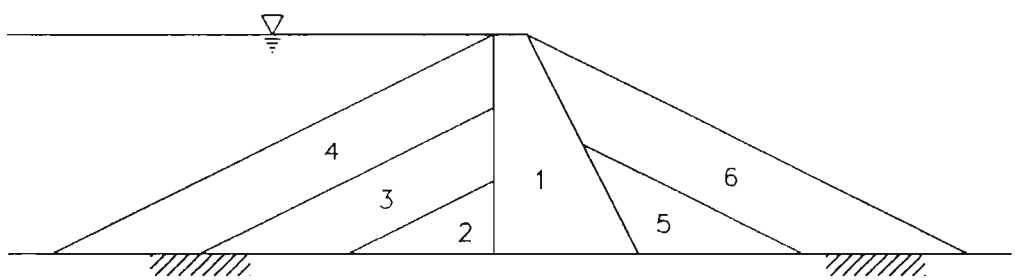

Figure 5.12 Idealized cross-section of a composite dam with soil layers.

where G_{max} is in psf, $\sigma_m^{'}$ is mean effective confining pressure in psf. K_{2max} is a factor which depends on relative density, maximum particle size, gradation, etc. of sand. $\sigma_m^{'}$ was calculated at the mid-depth of each layer.

K_{2max} was taken as 100. To decide which value to use for K_{2max}, three FE test runs were performed using the `reference configuration` of a 100 ft high composite dam. FE runs were performed for three K_{2max} values; 70, 100, and 130. Figures 5.13, and 5.14 show the maximum acceleration and maximum separation response of U/S interface, respectively, for the three K_{2max} values. As it is seen in Figures 5.13, and 5.14 the influence of change in K_{2max}, from 70 to 130, on the U/S interface performance is not significant. Therefore, the average value, which is 100 was selected for all G_{max} calculations. Once G_{max} was caculated the shear wave velocities were obtained using the relation:

$$V_s = \sqrt{\frac{G_{max}}{\rho}} \tag{5.2}$$

where V_s is the shear wave velocity, ρ is density. Finally, shear wave (V_s), and maximum shear modulus (G_{max}) distributions for all heights are listed in Table 5.2.

5.4.1 Ramberg-Osgood Model Parameters

In the present analysis, the Ramberg-Osgood non-linear model was used to represent soils and linear elastic model for concrete. In exploratory 3-D analysis, Chapter 7, except one case, elastic model was used for soil as well. One of the advantage of using R-O nonlinear model that it introduces hysteresis damping which increases with

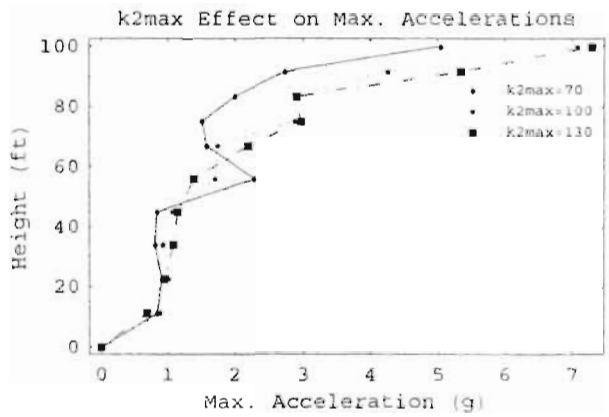

Figure 5.13 k_{2max} effect on maximum U/S interface acceleration.

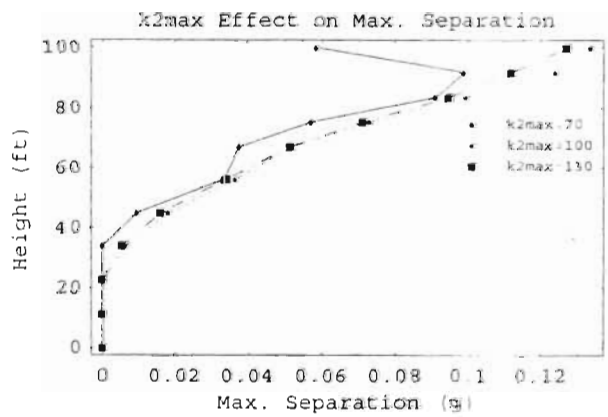

Figure 5.14 k_{2max} effect on maximum U/S interface separation.

Table 5.2 Shear wave (V_s), and maximum shear modulus (G_{max}) distributions.

Material Number	V_s		G_{max}	
	ft/s	m/s	ksf	$10^3 kPa$
H=100 ft				
2	1150	351	5790	227
3	1000	305	4290	205
4	750	227	2170	104
5	1250	381	6671	319
6	900	274	3396	163
H=200 ft				
2	1350	412	8020	384
3	1250	381	6395	306
4	900	274	3256	156
5	1450	442	9155	438
6	1100	335	5132	246
H=300 ft				
2	1450	442	9741	466
3	1350	412	7761	372
4	1050	320	4352	208
5	1650	503	12084	578
6	1250	381	6381	305
H=400 ft				
2	1550	473	10944	524
3	1400	427	8485	406
4	1100	335	4583	219
5	1700	518	12693	608
6	1400	427	7937	380

increasing strain amplitude and retains high frequency vibrations. One disadvantage is the symmetry in the hysteresis loop that allows soil to have the same resistance in tension as well as compression. The use of more appropriate soil models with failure mechanism are left as a future study.

The equation for Ramberg-Osgood stress-strain relation is given by Equation 2.15 in Section 2.6.4. The Ramberg-Osgood relations are inherently one-dimensional, and are assumed to apply to shear components. To generalize this theory to the multi-dimensional case, it is assumed that each component of the deviatoric stress and deviatoric tensorial strain is independently related by the one-dimensional stress- strain equations [47].

Ramberg-Osgood parameters were obtained using the computational procedure proposed by Ueng and Chen [77]. This procedure, as explained in Section 2.6.4, calculates the Ramberg-Osgood parameters using G_{max} value, and Seed's [68] average modulus and damping ratio versus shear strain curves as shown in Figures 5.15, and 5.16. Tables 5.3, and 5.4 list the Ramberg-Osgood model parameters for sand with unit weight of 125 pcf, and clay with unit weight of 135 pcf, respectively. Ramberg-Osgood model parameters for sands, used in FE analyses, with unit weights of 130, 135, 140, and 145 are presented in Tables B.1, B.2, B.3, and B.4, respectively in Appendix B. The tables were produced for a range of shear wave velocities from 100 ft/s to 2500 ft/s. Once the shear wave velocity of soil is calculated, one can obtain Ramberg-Osgood model parameters from those tables.

Since the volumetric behavior is elastic in Ramberg-Osgood model, elastic bulk modulus, K, is one of the material input parameters. The bulk modulus is calculated by:

$$K = \frac{2G(1+\mu)}{3(1-2\mu)} \tag{5.3}$$

where G is shear modulus, and μ is Poisson's ratio. To stay in the elastic range, shear modulus, G, was assumed to be 85% of G_{max} value, and μ was taken as 0.25. Then, the Equation 5.3 can be simplified to:

$$K = 1.4G_{max} \tag{5.4}$$

5.4.2 Linear Elastic Model Parameters

Linear elastic model has been used for soil in 3-D analyses only, whereas concrete has been modelled as linear elastic in all analyses. Young's modulus and Poisson's ratio of concrete was assumed to be 432,000 ksf, and 0.2 respectively. Young's modulus of soil was calculated using he equation:

$$E = 3K(1-2\mu) \tag{5.5}$$

where K is bulk modulus, and μ is Poisson's ratio. K was calculated using Equation 5.4, and μ was assumed to be 0.25, and 0.35 for sand and clay, respectively. Table 5.5 lists linear elastic model parameters used in FE analyses.

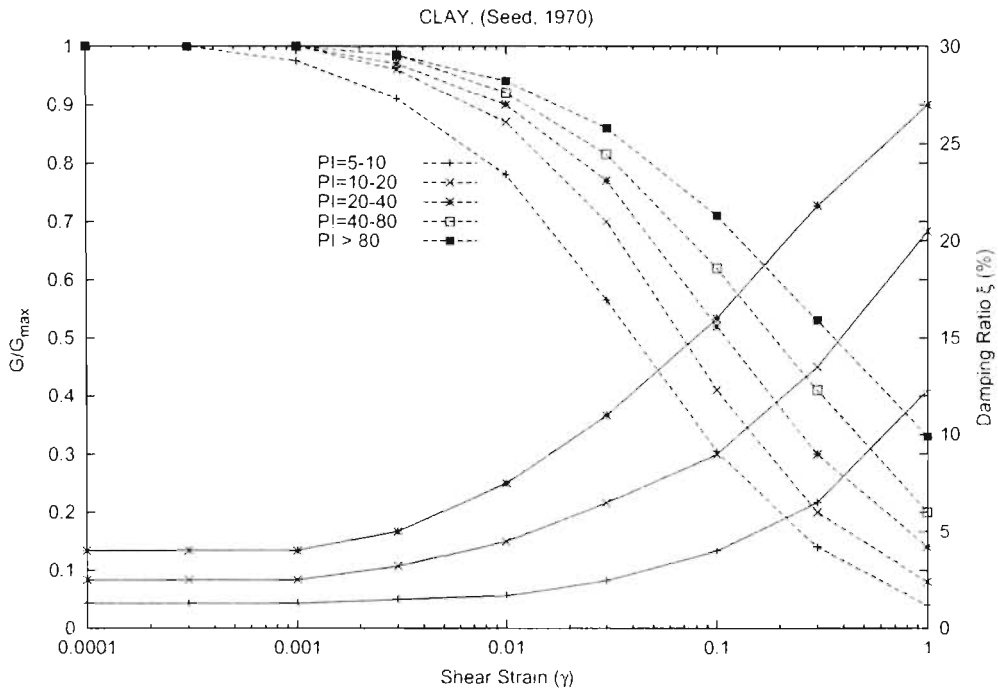

Figure 5.15 Damping ratio, ξ and G/G_{max} vs shear strain curves for clay.

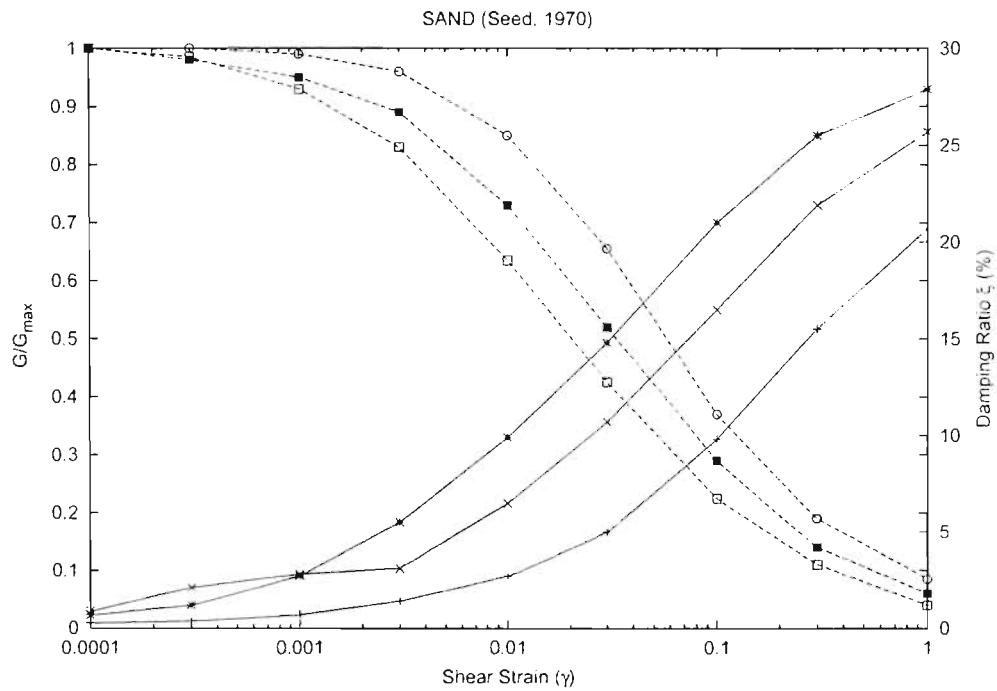

Figure 5.16 Damping ratio, ξ and G/G_{max} vs shear strain curves for sand.

Table 5.3 Ramberg-Osgood material properties for Seed's [68] average sand with γ = 125 pcf.

Ramberg-Osgood Material Parameters for Average Sand (γ = 125 pcf)					
V_s (ft/s)	G_{max} $(10^3 psf)$	α	r	γ_y (10^{-3})	τ_y (psf)
100	38.8	1.1	2.35	0.105	4.08
150	87.3	1.1	2.35	0.105	9.19
200	155.2	1.1	2.35	0.105	16.33
250	242.5	1.1	2.35	0.105	25.52
300	349.2	1.1	2.35	0.105	36.75
350	475.3	1.1	2.35	0.105	50.02
400	620.8	1.1	2.35	0.105	65.34
450	785.7	1.1	2.35	0.105	82.69
500	970	1.1	2.35	0.105	102.09
550	1173.7	1.1	2.35	0.105	123.53
600	1396.8	1.1	2.35	0.105	147.01
650	1639.3	1.1	2.35	0.105	172.53
700	1901.2	1.1	2.35	0.105	200.1
750	2182.5	1.1	2.35	0.105	229.7
800	2483.2	1.1	2.35	0.105	261.35
850	2803.3	1.1	2.35	0.105	295.04
900	3142.8	1.1	2.35	0.105	330.77
950	3501.7	1.1	2.35	0.105	368.55
1000	3880	1.1	2.35	0.105	408.36
1050	4277.7	1.1	2.35	0.105	450.22
1100	4694.8	1.1	2.35	0.105	494.12
1150	5131.3	1.1	2.35	0.105	540.06
1200	5587.2	1.1	2.35	0.105	588.04
1250	6062.5	1.1	2.35	0.105	638.07
1300	6557.2	1.1	2.35	0.105	690.13
1350	7071.3	1.1	2.35	0.105	744.24
1400	7604.8	1.1	2.35	0.105	800.39
1450	8157.7	1.1	2.35	0.105	858.58
1500	8730	1.1	2.35	0.105	918.82
1550	9321.7	1.1	2.35	0.105	981.09
1600	9932.8	1.1	2.35	0.105	1045.41
1650	10563.3	1.1	2.35	0.105	1111.77
1700	11213.2	1.1	2.35	0.105	1180.17
1750	11882.5	1.1	2.35	0.105	1250.61
1800	12571.2	1.1	2.35	0.105	1323.1
1850	13279.3	1.1	2.35	0.105	1397.63
1900	14006.8	1.1	2.35	0.105	1474.19
1950	14753.7	1.1	2.35	0.105	1552.8
2000	15520	1.1	2.35	0.105	1633.46
2050	16305.7	1.1	2.35	0.105	1716.15
2100	17110.8	1.1	2.35	0.105	1800.88
2150	17935.3	1.1	2.35	0.105	1887.66
2200	18779.2	1.1	2.35	0.105	1976.48
2250	19642.5	1.1	2.35	0.105	2067.34
2300	20525.2	1.1	2.35	0.105	2160.24
2350	21427.3	1.1	2.35	0.105	2255.19
2400	22348.8	1.1	2.35	0.105	2352.18
2450	23289.7	1.1	2.35	0.105	2451.2
2500	24250	1.1	2.35	0.105	2552.27

Table 5.4 Ramberg-Osgood material properties for Seed's [68] average clay with γ = 135 pcf.

Ramberg-Osgood Material Parameters for Average Clay (γ = 135 pcf)					
V_s (ft/s)	G_{max} $(10^3 psf)$	α	r	γ_y (10^{-3})	τ_y (psf)
100	41.90	1.26	2.44	0.36	15.03
150	94.28	1.26	2.44	0.36	33.82
200	167.60	1.26	2.44	0.36	60.13
250	261.88	1.26	2.44	0.36	93.95
300	377.10	1.26	2.44	0.36	135.29
350	513.28	1.26	2.44	0.36	184.15
400	670.40	1.26	2.44	0.36	240.52
450	848.47	1.26	2.44	0.36	304.41
500	1047.50	1.26	2.44	0.36	375.82
550	1267.47	1.26	2.44	0.36	454.74
600	1508.40	1.26	2.44	0.36	541.18
650	1770.28	1.26	2.44	0.36	635.13
700	2053.10	1.26	2.44	0.36	736.60
750	2356.88	1.26	2.44	0.36	845.59
800	2681.60	1.26	2.44	0.36	962.09
850	3027.27	1.26	2.44	0.36	1086.11
900	3393.90	1.26	2.44	0.36	1217.65
950	3781.48	1.26	2.44	0.36	1356.70
1000	4190.00	1.26	2.44	0.36	1503.27
1050	4619.48	1.26	2.44	0.36	1657.35
1100	5069.90	1.26	2.44	0.36	1818.95
1150	5541.27	1.26	2.44	0.36	1988.07
1200	6033.60	1.26	2.44	0.36	2164.71
1250	6546.88	1.26	2.44	0.36	2348.86
1300	7081.10	1.26	2.44	0.36	2540.52
1350	7636.27	1.26	2.44	0.36	2739.71
1400	8212.40	1.26	2.44	0.36	2946.41
1450	8809.47	1.26	2.44	0.36	3160.62
1500	9427.50	1.26	2.44	0.36	3382.35
1550	10066.47	1.26	2.44	0.36	3611.60
1600	10726.40	1.26	2.44	0.36	3848.37
1650	11407.28	1.26	2.44	0.36	4092.65
1700	12109.10	1.26	2.44	0.36	4344.45
1750	12831.88	1.26	2.44	0.36	4603.76
1800	13575.60	1.26	2.44	0.36	4870.59
1850	14340.28	1.26	2.44	0.36	5144.94
1900	15125.90	1.26	2.44	0.36	5426.80
1950	15932.47	1.26	2.44	0.36	5716.18
2000	16760.00	1.26	2.44	0.36	6013.07
2050	17608.48	1.26	2.44	0.36	6317.49
2100	18477.90	1.26	2.44	0.36	6629.41
2150	19368.28	1.26	2.44	0.36	6948.86
2200	20279.60	1.26	2.44	0.36	7275.82
2250	21211.88	1.26	2.44	0.36	7610.30
2300	22165.10	1.26	2.44	0.36	7952.29
2350	23139.28	1.26	2.44	0.36	8301.80
2400	24134.40	1.26	2.44	0.36	8658.83
2450	25150.48	1.26	2.44	0.36	9023.37
2500	26187.50	1.26	2.44	0.36	9395.43

Table 5.5 Young's modulus (E), and Poisson's ratio (μ) used in FE analyses.

Material Number	E (10^3 ksf)	E kPa	μ
H=100 ft			
2	12.29	588	0.25
3	9.10	436	0.25
4	4.60	220	0.25
5	1.40	67	0.25
6	7.20	344	0.25
7 (clay)	37.70	1805	0.35
H=200 ft			
2	17.00	814	0.25
3	13.50	646	0.25
4	6.90	330	0.25
5	19.40	929	0.25
6	10.9	522	0.25
7 (clay)	37.70	1805	0.35
H=300 ft			
2	20.70	991	0.25
3	16.50	790	0.25
4	9.25	443	0.25
5	25.60	1226	0.25
6	13.50	646	0.25
7 (clay)	37.70	1805	0.35
H=400 ft			
2	23.30	1116	0.25
3	18.00	861	0.25
4	9.73	466	0.25
5	26.90	1288	0.25
6	16.80	804	0.25
7 (clay)	37.70	1805	0.35

5.5 Interface Treatment

Soil-concrete interface was modelled using penalty formulation of NIKE3D. Penalty formulation is a constrained approach for contact problems, and it is discussed in detail in Section 2.4.2. No specific interface element is introduced between soil and concrete. Frictional behavior is governed by Coulomb type friction. In this study frictional coefficient, μ, was assumed to be 0.5 for all FE analyses.

Interface pressures have been calculated using horizontal, vertical, and shear stresses of the soil nodes along the soil-concrete interface. To verify the reliability of this approach two alternate methods were tested; inclusion of thin interface element between soil and concrete, and using nodal forces in stress calculations. Test FE runs were performed using `reference configuration` of 100 ft high composite dam and results were compared at the U/S interface.

First, a very thin layer of elements with 0.1 ft thickness were inserted along the U/S interface. Same material parameters were used with concrete. Analysis was performed using the Koyna Dam Earthquake Record as the ground motion. Minimum, static, and maximum normal stresses were gathered for all interface elements. Then, the results were compared with soil node stresses which were obtained in absence of the thin interface layer. Figure 5.17 shows that comparison. As shown in Figure 5.17 soil node stresses are very close to that of interface elements. It should also be noted that stress variation in interface elements exhibits a zigzag shape due to its peculiar behavior.

Moreover, towards the bottom of the dam there is a substantial decrease in static and maximum stresses which may be explained by boundary effects. Additionally, the inclusion of the thin layer of interface elements increased the number of interfaces which in turn increased the degree of nonlinearity of the problem. Therefore the CPU time was longer to complete the analysis. As a result, since the pressures are in close agreement it was decided not to use interface element approach.

Second, soil nodal forces were gathered along the soil-concrete interface. This was done with additional effort because NIKE3D requires extra input to save nodal force information. Then the gathered forces were divided by the area to calculate stresses. The comparison is presented in Figure 5.18. The stresses calculated from nodal forces are affected by fixed boundary condition in the 20 ft long section from the bottom as shown in Figure 5.18. Maximum and minimum stresses are in very good agreement, but static stresses are slightly overestimated by the nodal force approach. Consequently, it was decided that using soil nodal normal stresses as the interface pressures was quite reasonable.

5.6 Rayleigh Damping Parameters

Generalized Rayleigh damping is another important parameter that affects the dynamic response of structures. Some background issues on Rayleigh damping are discussed in Section 3.3.9.

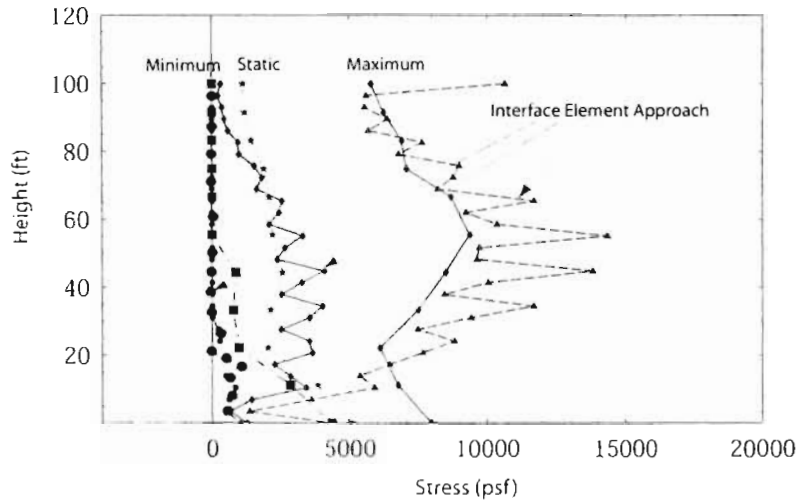

Figure 5.17 Comparison of interface pressures obtained from the interface element approach.

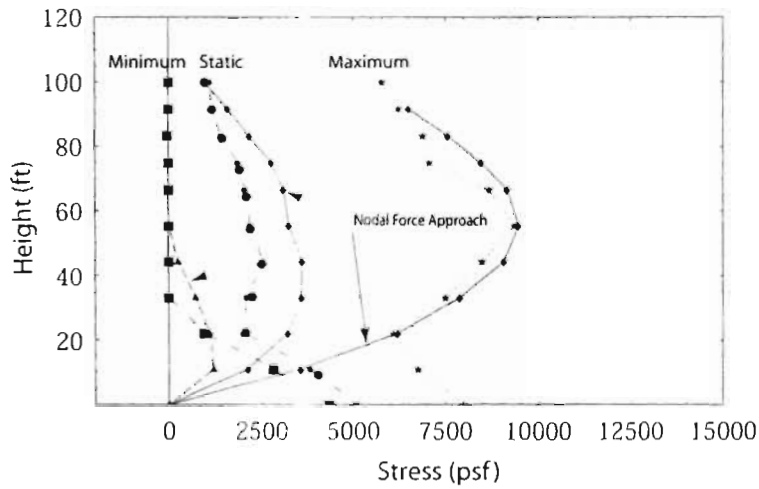

Figure 5.18 Comparison of interface pressures obtained from the nodal force approach.

In general, 15 to 20% is used for soil structures, and 5 to 10% for concrete structures. For a composite dam case it is too difficult to make a general statement on the amount of Rayleigh damping parameter. Therefore, in this study it was attempted to investigate the effect of change in Rayleigh damping parameter on the interface performance. As the performance criteria maximum separation and maximum acceleration were selected.

By definition it is required to determine two frequencies to calculate the Rayleigh damping parameters; α, and β. In this study first and fifth natural frequencies were selected. One can define different damping levels at different frequencies. Three FE analyses were performed with damping levels of 5-10%, 10-10%, and 20-20%. The first and second numbers in each pair correspond to desired damping levels at the first and fifth natural frequencies, respectively.

Figures 5.19 and 5.20 show the effects of all three damping levels on the maximum acceleration and maximum separation of U/S interface. As shown in Figure 5.19, increasing damping level from 10-10% to 20-20% did not cause significant change in maximum acceleration response. On the other hand increase in damping level caused almost 50% decrease in maximum separation at the crest of the dam as shown in Figure 5.20, and had no effect on separation depth. As a result it was decided to select 10% Rayleigh damping for the rest of the FE analyses.

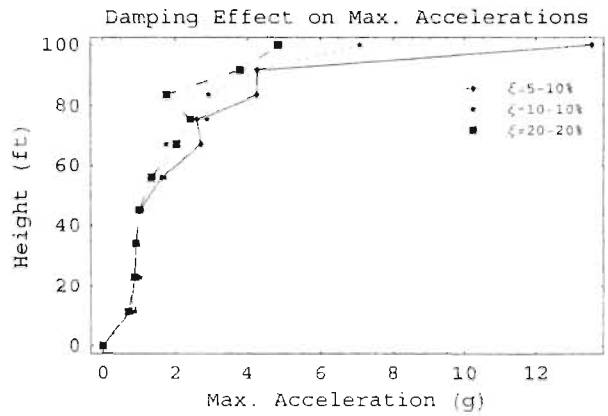

Figure 5.19 Damping ratio effect on maximum accelerations.

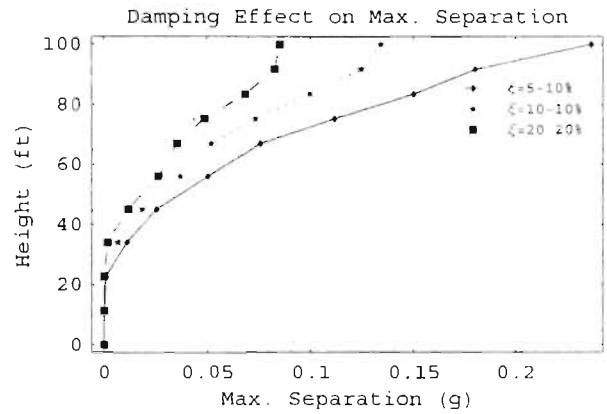

Figure 5.20 Damping ratio effect on maximum separation.

5.7 Summary and Conclusions

In this chapter the input parameters used in the FE analyses are discussed in detail. Input parameters include; input ground motion, FE mesh, material model parameters, and numerical damping parameters.

As the input ground motion, Koyna Dam Earthquake Record time history and its acceleration response spectrum are presented. FE mesh for both 2-D, and 3-D models are presented. Dimensions and boundary conditions of the mesh are discussed. Material model parameters used in FE analyses for both linear elastic and Ramberg-Osgood models are presented. K_{2max}, and Rayleigh damping ratio effects on dynamic interface performance are investigated through several FE runs and the results are presented. As an additional discussion, the effects of K_{2max}, and Rayleigh damping ratio on maximum of maximum interface acceleration and separation response are presented in Figure 5.21. Parts (a), and (b) of Figure 5.21 show K_{2max} effect on separation depth and maximum separation. It is clearly shown that K_{2max} values greater than 100 do not cause changes in separation depth and maximum separation. Parts (c), and (d) of Figure 5.21 illustrates damping effect on interface performance. Increase in damping ratio from 10 to 20% causes no change in separation depth but some decrease in maximum separation. In conclusion it is appropriate to use 10% Rayleigh damping ratio, and 100 for K_{2max}.

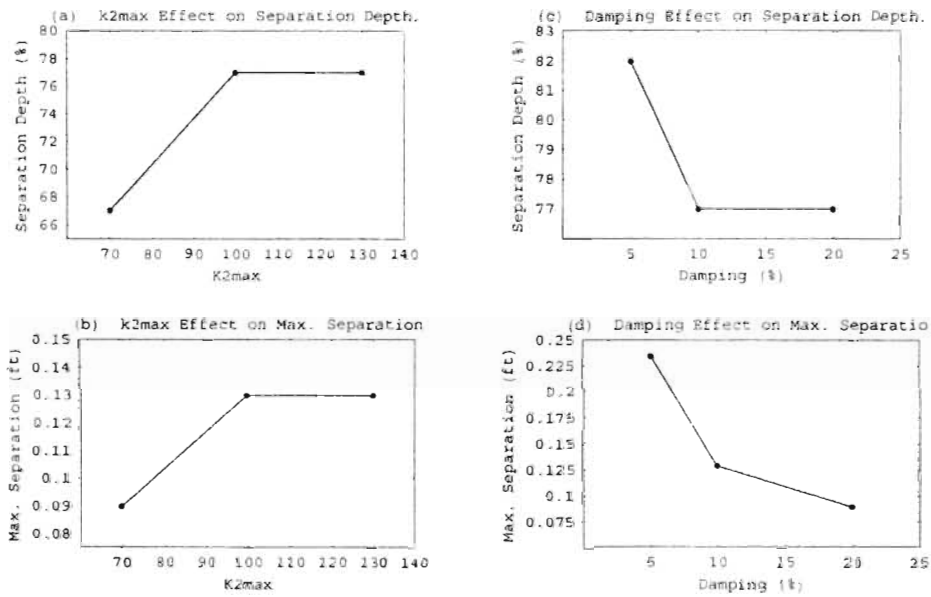

Figure 5.21 k_{2max} and damping ratio effects on maximum separation and separation depth.

6. Two-Dimensional Parametric Study

6.1 Introduction

To have a better understanding of IBCD numerous 2-D parametric FE analyses were performed. In fact the geometry of the interface area of composite dams is three dimensional and quite complicated. Since full blown 3-D FE analysis is extremely time consuming, it is appropriate to start with 2-D FE analysis of the maximum cross-section of soil-concrete interface area.

2-D FE analyses were performed on the hypothetical composite dam as shown earlier in Chapter 5. Four different heights were used; 100, 200, 300, and 400 ft. The followings are the controlling parameters of cross-sectional geometry: θ, the slope angle of the upstream interface; ϕ, the slope angle of the downstream interface; mu, upstream soil slope; and, md, downstream soil slope as shown in Figure 5.3. Including height, 5 controlling parameters were used to investigate IBCD.

There are 11, 9, 9, and 9 cases for θ, ϕ, mu, and md, respectively. This adds up to 38 cases for each dam height. Since there are four different heights, the total number of successful 2-D non-linear FE computer runs is 152. Four additional FE analyses were performed to demonstrate the effect of vertical component of ground motion on IBCD.

Moreover 12 FE analyses were performed to observe the natural vibration characteristics of composite dams. Therefore the total number of 2-D FE runs is 168.

In the following sections, natural vibration characteristics of composite dams are given, numerical analysis procedure is explained, and 2-D FE analysis results are demonstrated.

6.2 Natural Vibration Characteristics

First, NIKE3D eigenvalue analyses were performed to obtain first natural frequencies of all cases. Figures 6.1, 6.2, 6.3, and 6.4 shows natural frequencies of all cases for heights 100, 200, 300, and 400 ft, respectively. Finally Figure 6.5 shows the combined plots for all cases and all heights. Each of the above Figures is plotted Case # versus first natural frequency (Hz). Case numbers for each parameter are explained in Table 6.1. At the `reference configuration`, the natural frequencies are calculated by NIKE3D as 3.81, 2.3, 1.68, and 1.31 Hz for heights 100, 200, 300, and 400 ft, respectively. In general, the change in θ and ϕ do not have significant effect on the natural frequency of the composite dam. In fact there is a slight increase due to the change in θ for 200, 300, and 400 ft cases as shown in Figures 6.2, 6.3, 6.4, respectively. On the other hand increase in *mu* and *md* caused significant decrease of natural frequency for all heights. For 100 ft high dam, as shown in Figure 6.1, increase in *mu* caused more decrease in natural frequency than *md*. For other heights, the relative effects of *mu*, and *md* on natural frequency are very close.

Table 6.1 Case numbers for all parameters.

Case #	θ (Degrees)	Case #	ϕ (Degrees)	Case #	mu (Slope)	Case #	md (Slope)
1	0	1	26.6	1	2.00	1	2.00
2	1	2	27.8	2	2.25	2	2.25
3	2	3	28.8	3	2.50	3	2.50
4	3	4	29.9	4	2.75	4	2.75
5	4	5	30.9	5	3.00	5	3.00
6	5	6	32	6	3.25	6	3.25
7	6	7	33	7	3.50	7	3.50
8	7	8	34	8	3.75	8	3.75
9	8	9	35	9	4.00	9	4.00
10	9						
11	10						

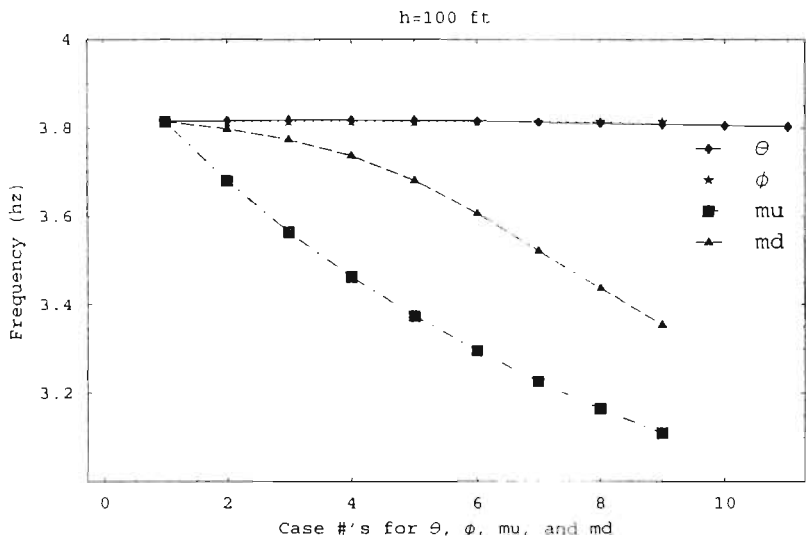

Figure 6.1 Natural frequencies for all cases of θ, ϕ, mu, and md (H=100).

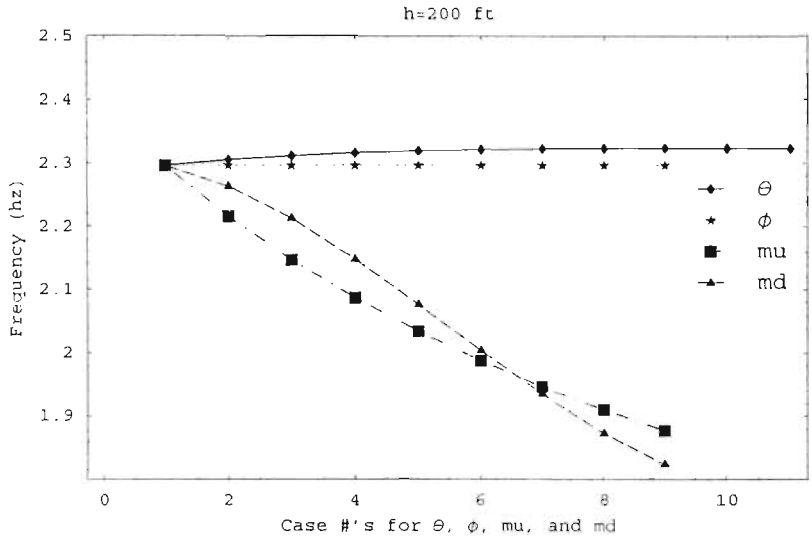

Figure 6.2 Natural frequencies for all cases of θ, ϕ, mu, and md (H=200).

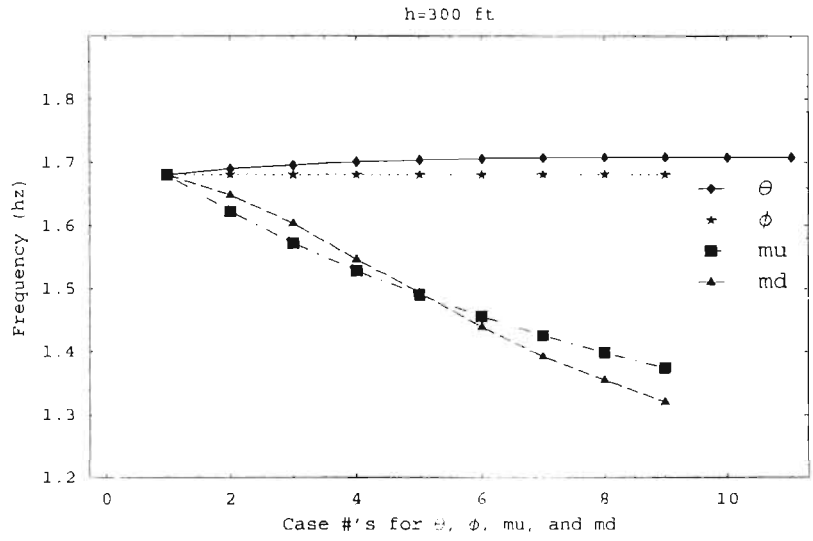

Figure 6.3 Natural frequencies for all cases of θ, ϕ, mu, and md (H=300).

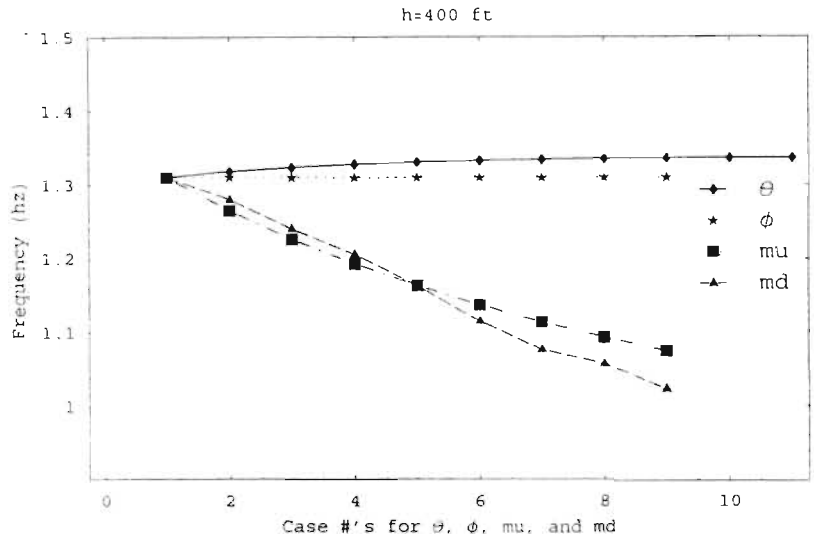

Figure 6.4 Natural frequencies for all cases of θ, ϕ, mu. and md (H=400).

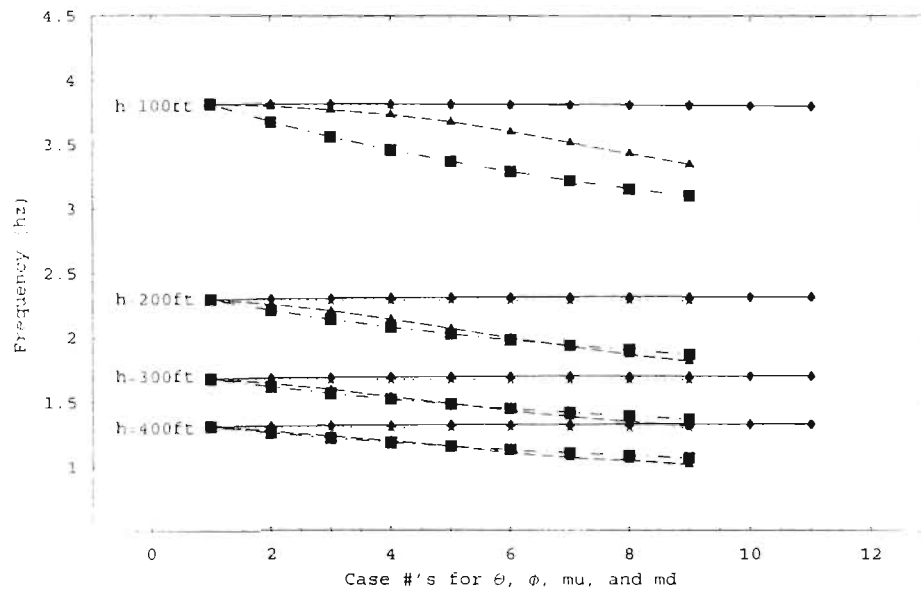

Figure 6.5 Natural frequencies for all cases of θ, ϕ, mu, md and all heights.

Figures 6.6. and 6.7 show the first five mode shapes of different cross-sectional geometries for 100 ft, and 400 ft high dams, respectively. The selected cross-sectional geometries are `reference configuration`, θ=10 degrees, and mu=4.0. As shown in Figure 6.6, reference configuration has separation in first, third, and fifth mode shapes along the U/S interface. Second geometric configuration, with θ=10, has no separation in the first four mode. Instead sliding behavior is more dominant in all modes. The third configuration, with mu=4.0, has separation in all modes except the third mode. Figure 6.7, which is for 400 ft high dam, has the same arrangement with Figure 6.6. In Figure 6.7, the mode shapes of `reference configuration` clearly show the contribution of the concrete flexibility. In the second configuration, with θ=10, the concrete is stiffer and sliding behavior is dominant in all modes . Finally, the third configuration, with mu=4.0, has separation in its first mode and sliding in others.

The response of dams during an earthquake depends upon the relationship between its natural frequency and the frequency of the input motion. If the frequency of the input motion is at or near one of the natural frequencies of the dam resonance may occur. The horizontal component of Koyna Dam Earthquake Record and its acceleration response spectrum are shown in Figure 5.2. The predominant frequency of the ground motion is around 1.4 Hz (T=0.7 sec). This predominant frequency is close to natural frequencies of a few configurations of 300 ft high composite dam as shown in Figure 6.3. and 6.5.

Secondly, to observe the natural vibrational behavior, a unit horizontal base acceleration impulse was introduced in 0.04 seconds as shown in Figure 6.8. The acceleration and

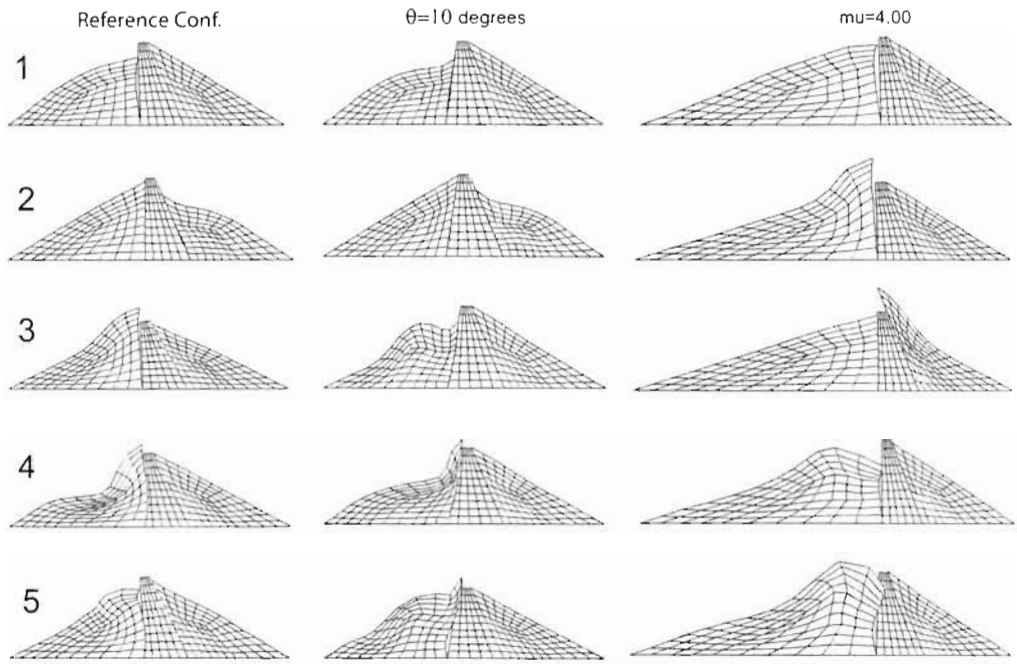

Figure 6.6 First five mode shapes of three different configurations, H=100 ft

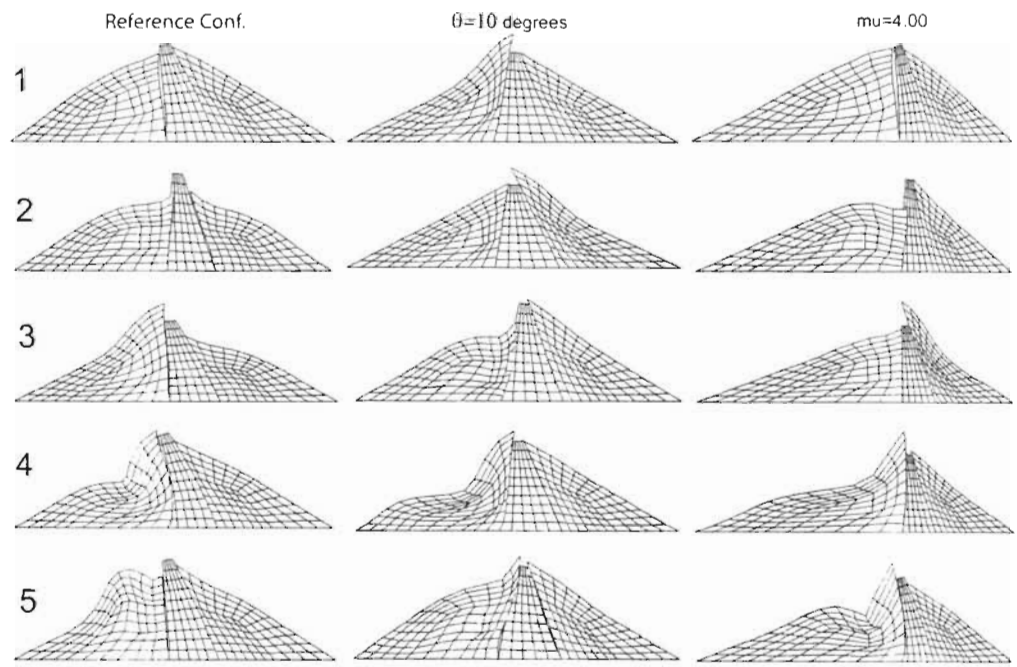

Figure 6.7 First five mode shapes of three different configurations, H=400 ft.

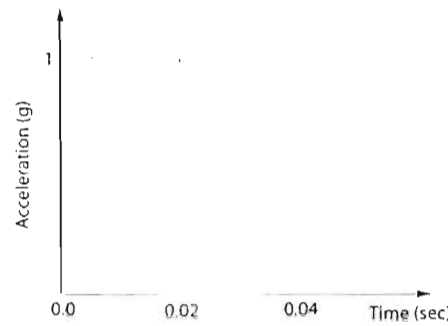

Figure 6.8 Unit base acceleration impulse.

displacement time histories of both soil and concrete nodes at the crest of the dam were gathered for 3 seconds. Using the `reference configuration`, three analyses were performed for each height with three different Rayleigh damping parameters of 0, 5, and 10%.

Acceleration and horizontal displacement time histories of both soil and concrete nodes at the dam crest are presented in Figures 6.10, 6.11, and 6.12 for 100 ft high dam, and Figures 6.13, 6.14, and 6.15 show the response of 200 ft high dam. The graphs for 300, and 400 ft high dams are presented in Figures A.1, A.2, A.3, and A.4, A.5, A.6, respectively in Appendix A.1.

Parts (a) and (b) of Figure 6.10 illustrates the horizontal displacement and acceleration of the soil node, respectively. Parts (c) and (d) show the horizontal displacement and acceleration of the concrete node, respectively. As shown in part (a) the soil node is separated from concrete, in other words debonding, for the first 0.5 sec due to the base acceleration input. Approximately at t=0.5 sec it comes back to original position and rebonding occurs. At this point, a special attention must be given to acceleration time

history of the same node at t=0.5 sec. Part (b) clearly shows the sudden acceleration magnification, up to 6 g, at t=0.5 sec and at subsequent rebonding instances. The same phenomenon was observed in other cases with different Rayleigh damping parameters as shown in Figures 6.11, 6.12. Increasing Rayleigh damping ratio resulted in decrease in acceleration magnitude and number of rebonding instances. The same behavior can be seen for all other heights.

The acceleration response of concrete node deserves attention as well. The acceleration time history of the concrete node exhibits different frequency content before and after the first rebonding action. This is best shown in part (d) of Figure 6.14 for 200 ft high dam with 5% Rayleigh damping. First rebonding takes place around t=0.75 sec. Before rebonding the acceleration response of concrete node has low frequency content, but after rebonding it has higher frequency content with lower magnitudes. With a careful observation, one can find the same behavior in all other cases with different heights and damping ratios.

The following conclusions can be made from the observations of natural vibrational behavior of composite dams;

(1) The soil node acceleration magnification and change in concrete acceleration response during the rebonding process indicate the complexity of the soil-concrete interface behavior under dynamic loading.

(2) Concrete displacements are very small compared to soil displacements.

(3) Acceleration magnification along the interface is generally higher in soil than concrete.

(4) Separation can be repetitive.

(5) Acceleration response of concrete has higher frequency content than soil.

(6) Upstream and downstream slopes have significant effect on the natural frequency of composite dams.

(7) Although the upstream interface angle, θ, has insignificant effect on natural frequency, it has significant effect on the mode shapes of the composite dam.

(8) As height increases the contribution of concrete flexibility to mode shapes increases.

In the next sections the results of dynamic FE analysis of composite dams with different geometric configurations using Koyna Dam Earthquake ground motion are presented.

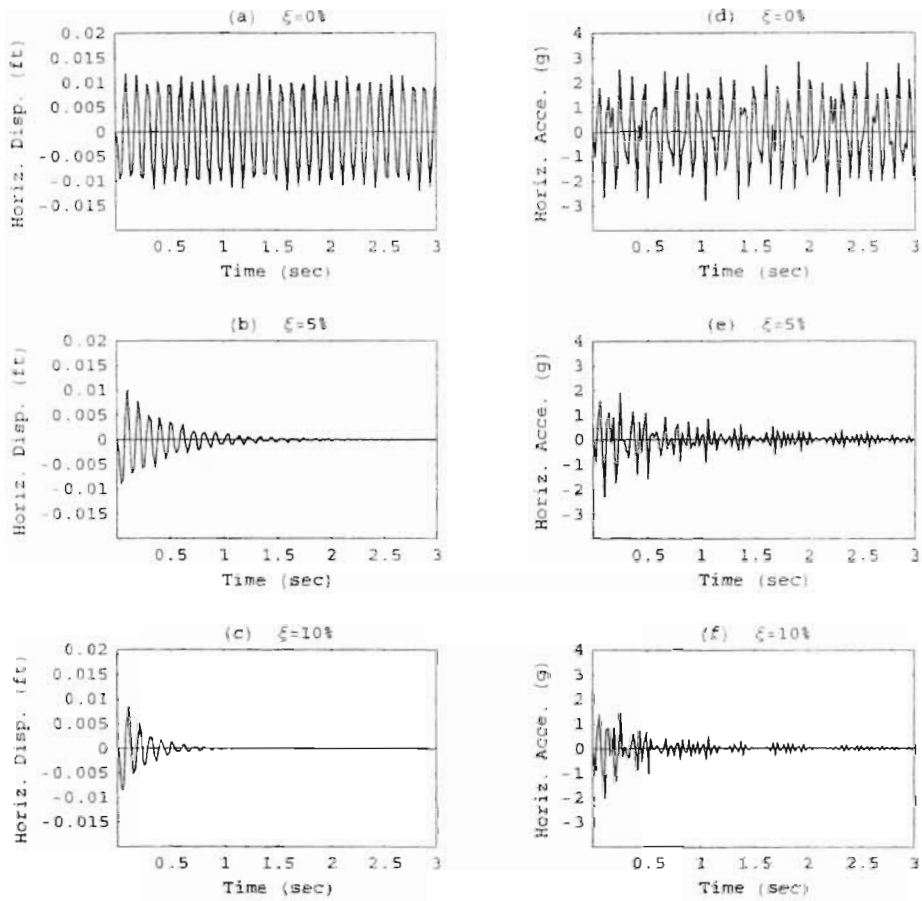

Figure 6.9 Crest horizontal displacement (a, b, and c) and acceleration (d, e, and f) time histories of concrete monolith without U/S and D/S soil embankments for 0%, 5%, and 10% damping ratios respectively.

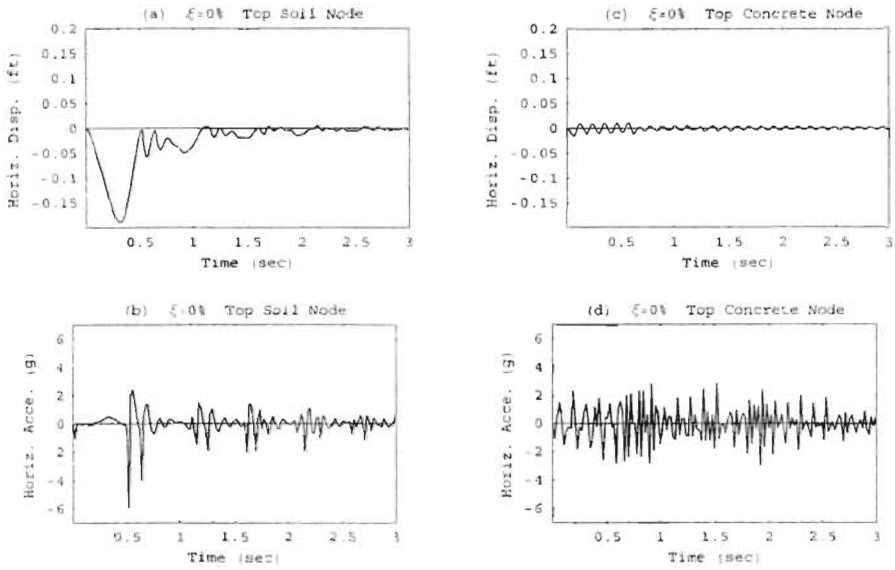

Figure 6.10 Horizontal displacement and acceleration time histories of soil and concrete nodes at the crest, $\xi = 0\%$ (H=100).

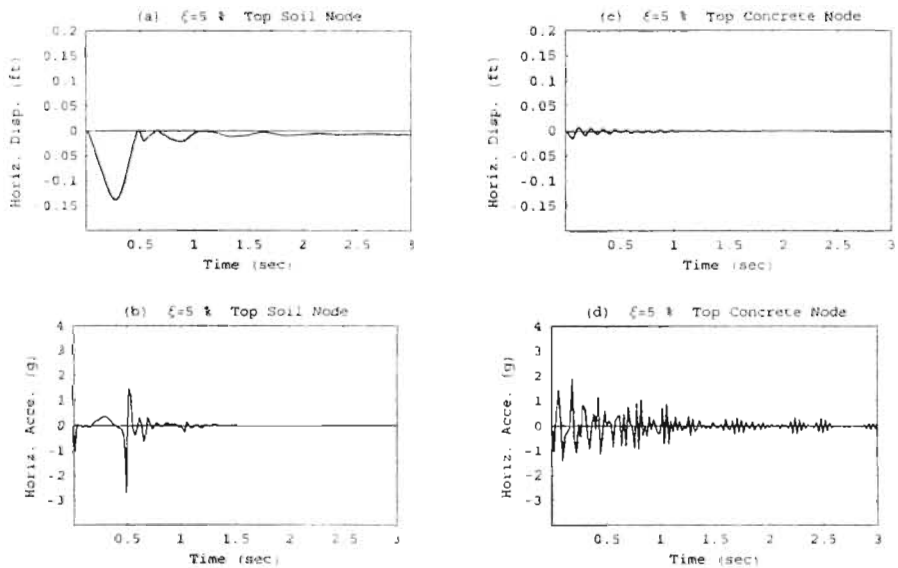

Figure 6.11 Horizontal displacement and acceleration time histories of soil and concrete nodes at the crest, $\xi = 5\%$ (H=100).

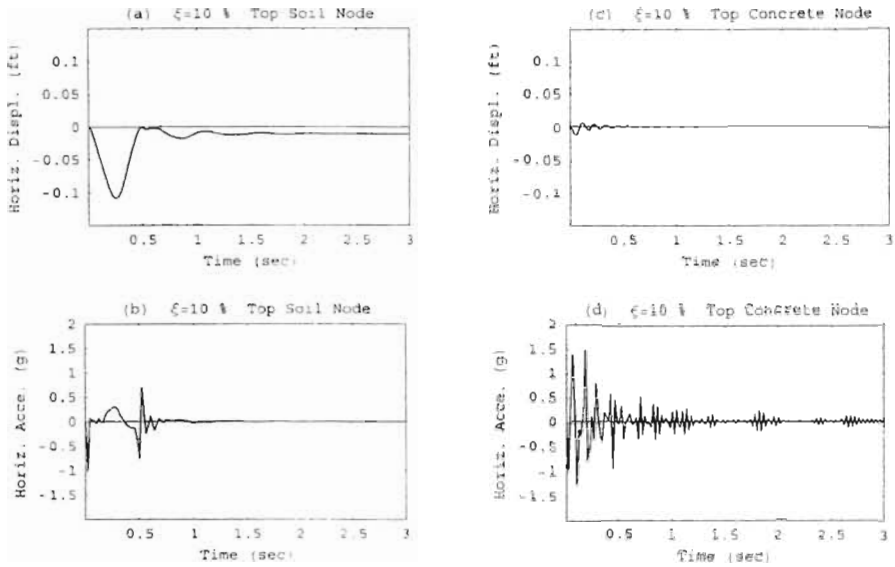

Figure 6.12 Horizontal displacement and acceleration time histories of soil and concrete nodes at the crest, $\xi = 10\%$ (H=100).

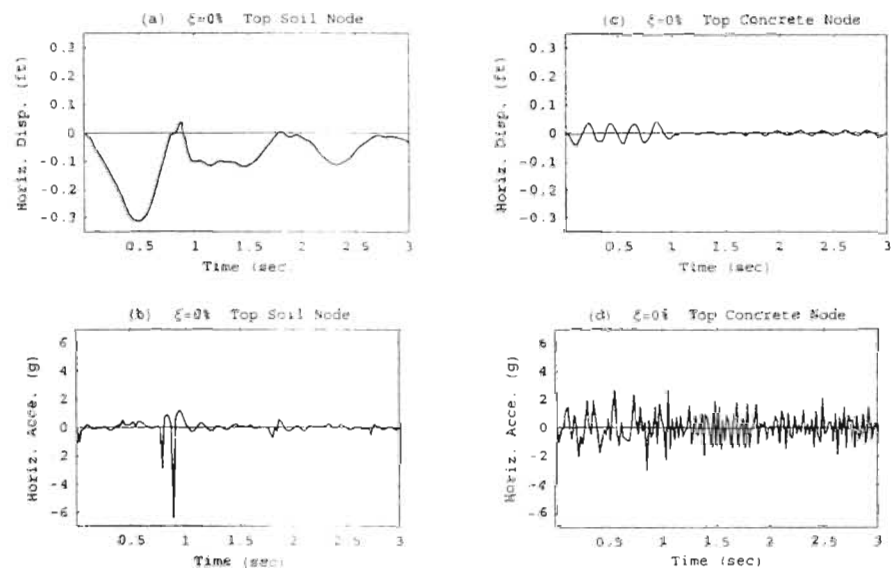

Figure 6.13 Horizontal displacement and acceleration time histories of soil and concrete nodes at the crest, $\xi = 0\%$ (H=200).

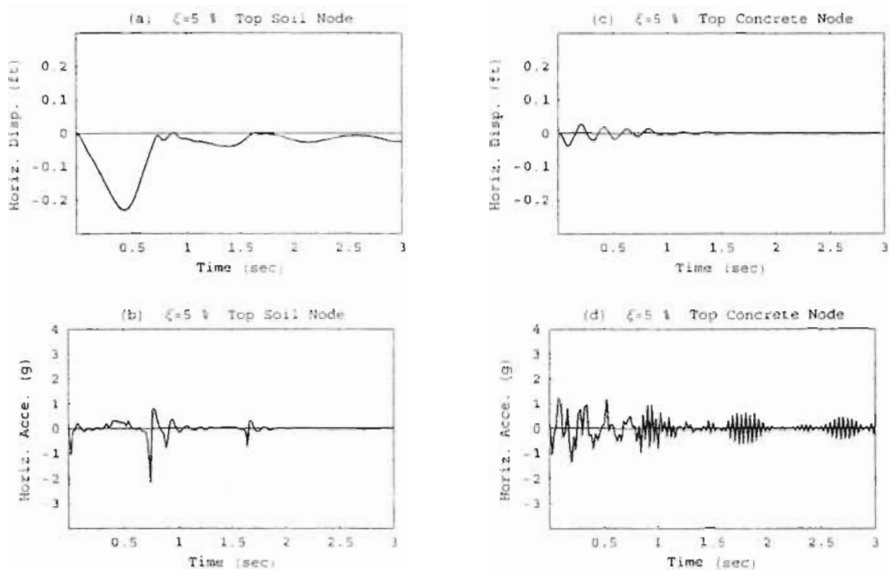

Figure 6.14 Horizontal displacement and acceleration time histories of soil and concrete nodes at the crest, $\xi = 5\%$ (H=200).

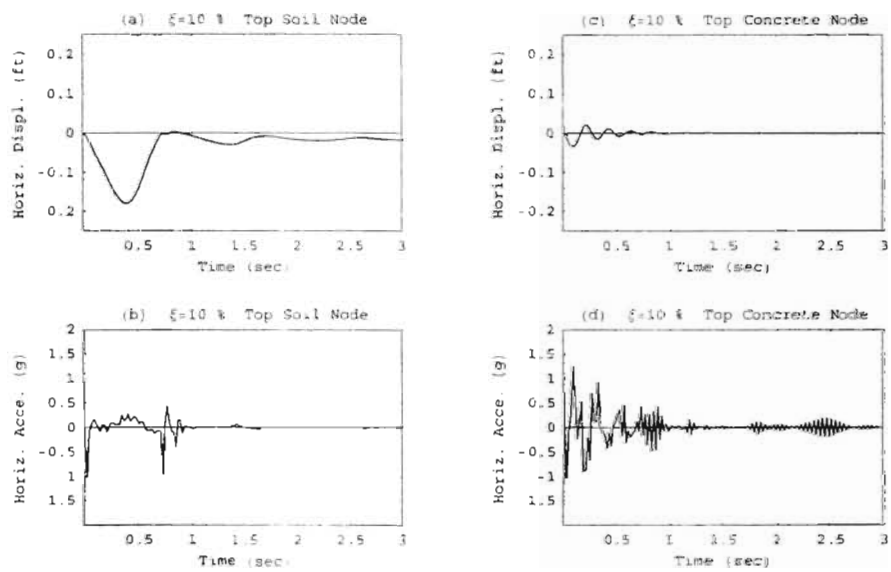

Figure 6.15 Horizontal displacement and acceleration time histories of soil and concrete nodes at the crest, $\xi = 10\%$ (H=200).

6.3 2-D Parametric Finite Element Analysis

A representative cross-section of the composite dam was explained earlier in Chapter 5. Among many factors affecting IBCD, upstream & downstream soil slopes and interface slope angles were selected for this parametric study. For each height, every parameter was varied independent of each other in a certain range. The mesh for 2-D model is shown in Figure 5.4.

In the next sections the FE analysis procedure, results of 2-D FE parametric study, effect of vertical ground motion on IBCD are presented, and all findings are interpreted.

6.3.1 FE Analysis Procedure

As mentioned earlier, totally, 156 non-linear FE analysis were performed for this 2-D parametric study. The FE analysis has two events; static and dynamic. Figure 6.16 illustrates the sequence of these events.

Static analysis has two stages; gravity turn on and application of hydrostatic pressure. Each stage was performed in 10 sec with 1 sec time intervals. After completion of static analysis dynamic event was initiated using a horizontal ground motion as an input with 0.02 sec time intervals. The change in analysis type (from static to dynamic) was done using `restart` feature of NIKE3D.

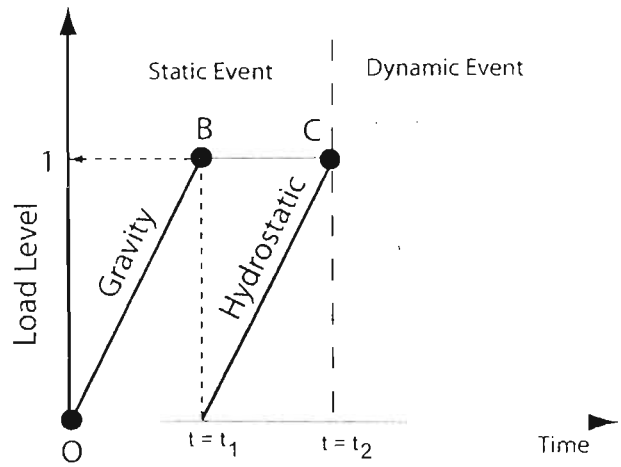

Figure 6.16 Sequence of static and dynamic events used in NIKE3D Analysis.

For each height, every geometric parameter was varied starting from `reference configuration` while other parameters remained constant. The term `reference configuration` is used to define the initial geometry of cross-section in which the upstream soil slope (mu) is 2.00, the upstream interface angle (θ) is 0.00 degrees, the downstream soil slope is 2.00, and finally the downstream interface angle (ϕ) is 26.6 degrees. First, the upstream concrete angle, θ, was varied from 0 to 10 degrees with 1 degree intervals. Second, downstream concrete angle, ϕ, was varied from 26.6 degrees to 35 degrees with approximately 1 degree intervals. Third, the upstream soil slope, mu, was varied from 2.00 to 4.00 with 0.25 intervals. Finally downstream soil slope, md, was varied in the same range with mu. After each analysis, the maximum separation, maximum acceleration, and interface pressure profiles were obtained for both upstream (U/S) and downstream (D/S) interfaces. In other words the effects of each parameter on both U/S and D/S interfaces were investigated. The selected nodes for data presentation of both interfaces are shown in Figure 6.17. The related plots are shown later in this chapter.

6.3.2 Separation Calculations

Since the concrete displacements are very small compared to the soil displacements, it is assumed that concrete U/S and D/S slopes remain unchanged. With this assumption, the separation of an interface, shown in Figure 6.18, was calculated using the following procedure;

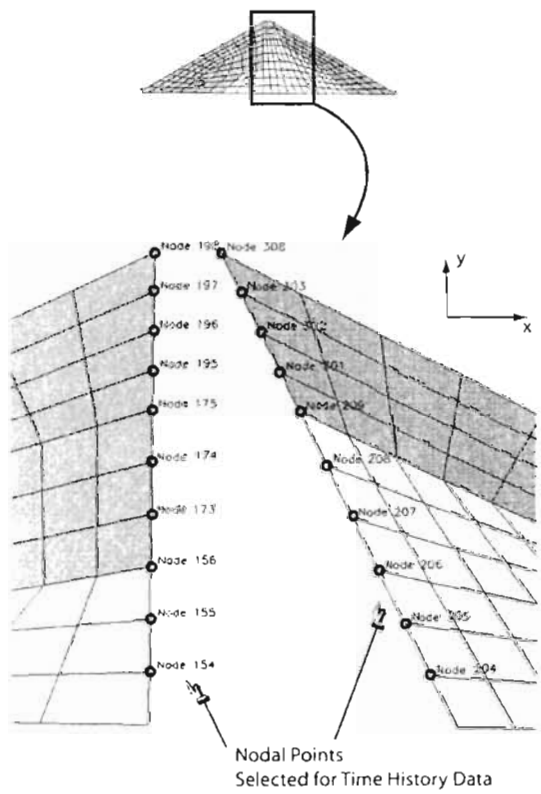

Figure 6.17 Location of selected nodes for data presentation.

(1) The soil and concrete nodes are initially matched along the interface.

(2) Vertical and horizontal displacements (dr_i, dz_i) are gathered for the corresponding soil and concrete nodes.

(3) The distance between two nodes is calculated in vector form, $\tilde{r}$.

(4) A unit vector, $\tilde{n}$, normal to the concrete surface is determined.

(5) The position vector, $\tilde{r}$, and unit normal vector, $\tilde{n}$, are multiplied to find the normal distance between the soil node and concrete surface. This normal distance is called as separation.

In fact the dot product of $\tilde{n}$ and $\tilde{r}$ is used to distinguish the sliding & separation and sliding only cases as shown in Figure 6.18. For sliding only case the dot product would produce a zero value, meaning no separation.

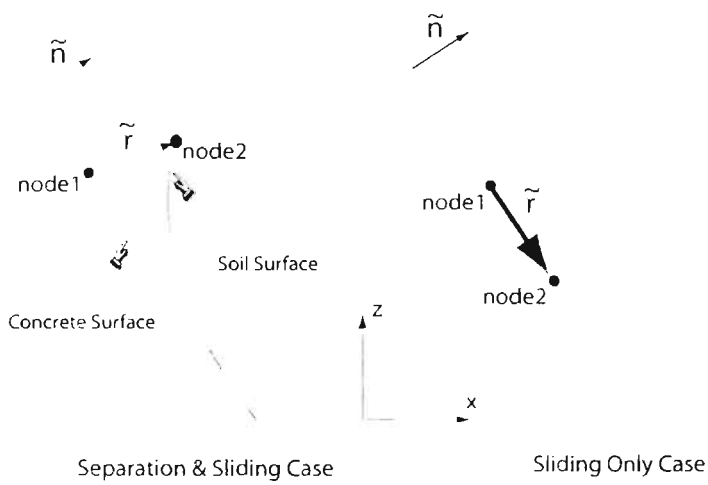

Figure 6.18 Illustration of SEPARATION for soil-concrete interface areas.

6.3.3 Acceleration Calculations

Horizontal acceleration time histories of all soil nodes along the interface were gathered, then maximum acceleration of each time history was calculated. Moreover, root mean square acceleration of each acceleration time history was also calculated. The root mean square acceleration ratio is defined as;

$$RMS = \left[\frac{1}{T}\int a^2 dt\right]^{1/2} \tag{6.1}$$

where RMS is the root mean square acceleration, t is time, and T is is time interval of the measurement. The RMS acceleration has an advantage over the maximum acceleration of a time history, because it considers the whole time history as opposed to the maximum acceleration. The a^2 in the equation removes the negative sign. The integration considers an accumulative effect and the $1/T$ takes an average over the time interval of the measurement. The RMS acceleration can also be considered an average rate of energy. Although the RMS acceleration has been used by structural engineers to quantify the intensity of earthquakes, it has been used to demonstrate the acceleration amplification along the soil-concrete interface in this study. RMS accelerations at the interface were also compared with maximum horizontal accelerations.

6.3.4 Interface Pressure Calculations

Interface pressures were calculated using horizontal (σ_x), vertical (σ_z), and shear stress (σ_{xz}) components of soil nodes along the interface. The stress normal to the interface which is called as interface pressure, was simply calculated by rotating the stresses

depending on the amount of inclination of the surface. The following equation;

$$\sigma_{n.U/S} = \sigma_x \sin\theta^2 + \sigma_z \cos\theta^2 - 2\sigma_{xz} \cos\theta \sin\theta \tag{6.2}$$

was used to calculate upstream interface pressure, where θ is the angle of U/S interface. Finally the following equation:

$$\sigma_{n.D/S} = \sigma_x \cos\phi^2 + \sigma_z \sin\phi^2 - 2\sigma_{xz} \cos\varphi \sin\phi \tag{6.3}$$

was used to determine downstream interface pressure, where ϕ is the angle of D/S interface.

All gathered and calculated data were plotted versus dam height and they are presented in the next section.

6.3.5 FE Analysis Results

After each FE run separation, interface pressure, and horizontal acceleration time histories were obtained for each soil node along the both U/S and D/S soil-concrete interfaces. As an example, the calculated time histories of the soil node located at the crest of the dam (node #198) are presented in Figures 6.19, and 6.20 for 100, and 400 ft high dams, respectively. In part (a) of Figure 6.19 the time instance (t=13.6 sec) of rebonding is marked with an arrow. The time instances of maximum interface stress, and maximum acceleration are also marked in parts (b), and (c) of Figure 6.19. It is clearly shown that maximum interface stress and horizontal acceleration take place at the same time step with rebonding action. The same phenomenon is shown in Figure

6.20 for 400 ft high dam, and the time instance of rebonding action causing maximum response is t=13.8 sec.

Then the interface performance parameters are presented for each dam height separately. They include maximum separation, maximum horizontal acceleration ratio, maximum root mean square acceleration (RMS) ratio, and minimum, static and maximum interface pressures. Table 6.2 lists the numbers of figures illustrating the response of each interface due to change in geometric controlling parameters.

In this section only the plots showing the effect of upstream interface angle, θ, on both U/S and D/S interface behavior are presented for dams with heights 100, 200, 300, and 400 ft as examples. The plots showing the effect of other parameters are presented in Appendix A.2.

Figures 6.24, 6.25, Figures 6.30, 6.31, Figures 6.36, 6.37, and Figures 6.42, 6.43, represent the U/S interface response due to increase in θ for heights 100, 200, 300, and 400 ft, respectively. Figures 6.27, 6.28, Figures 6.33, 6.34, Figures 6.39, 6.40, and Figures 6.45, 6.46, represent the D/S interface response due to increase in θ for heights 100, 200, 300, and 400 ft, respectively. Figures with the same arrangement were obtained for all other parameters.

To have a clear understanding of the arrangement of plots in the figures mentioned in the above paragraph, Figure 6.21 is provided to serve as a shared legend. In Figure 6.21 the first column represents the variation of maximum separation along the dam height.

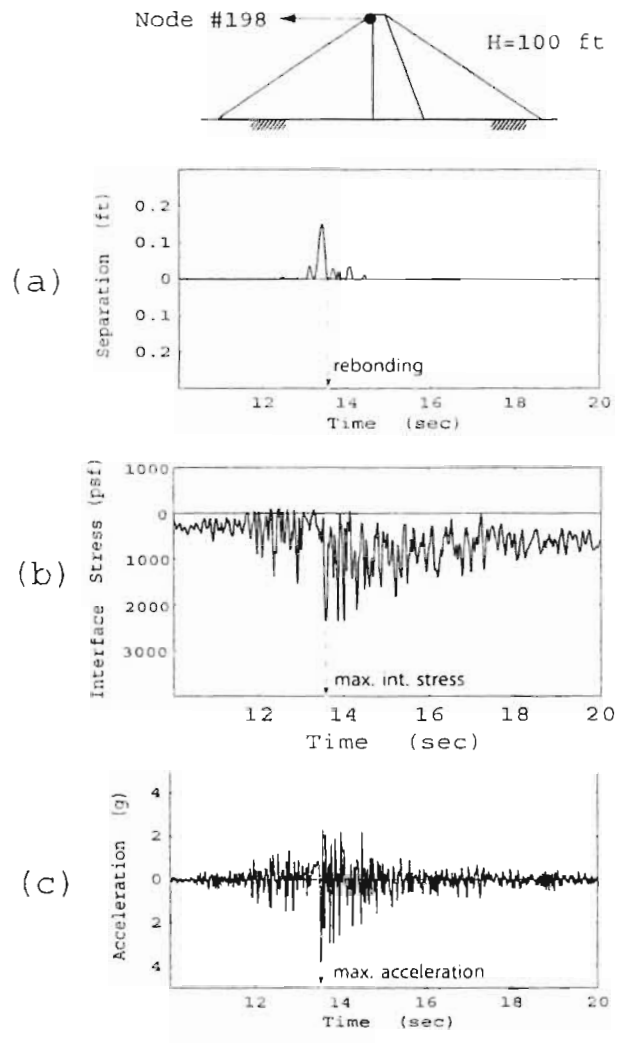

Figure 6.19 Sample time histories of soil node located at the crest of the dam (H=100 ft).

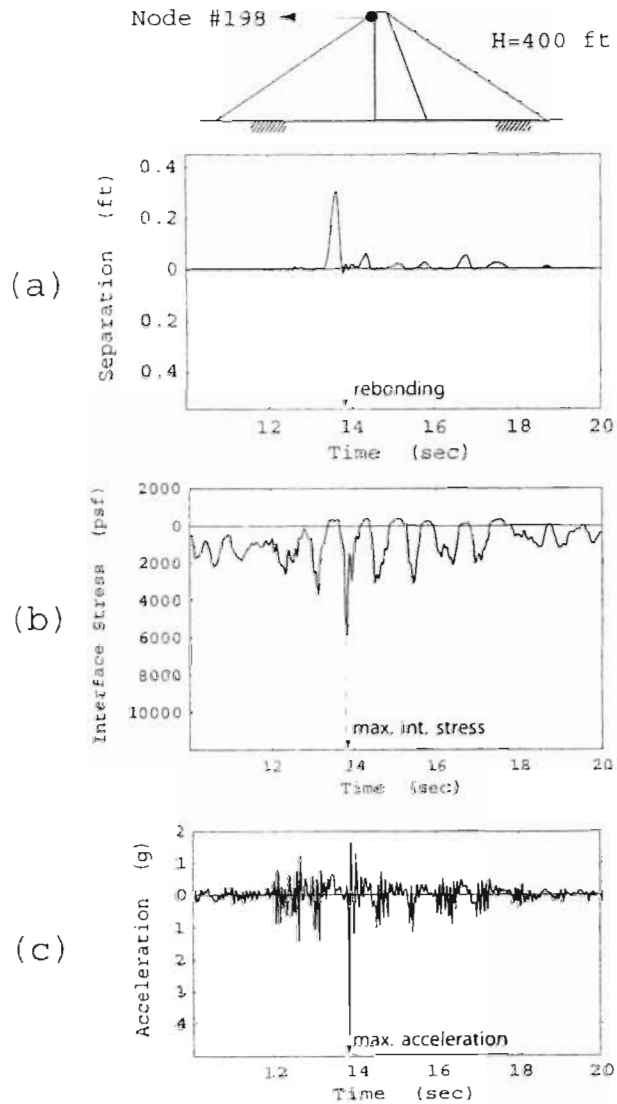

Figure 6.20 Sample time histories of soil node located at the crest of the dam (H=400 ft).

Table 6.2 Numbers of figures illustrating 2-D response

Height (ft)	Parameter	Response of	Figure Numbers
100	θ	u/s	6.24, 6.25, 6.26,9.1
		d/s	6.27, 6.28, 6.29,9.2
	ϕ	u/s	A.7, A.8, A.9,9.3
		d/s	A.10, A.11, A.12,9.4
	mu	u/s	A.13, A.14, A.15,9.5
		d/s	A.16, A.17, A.18,9.6
	md	u/s	A.19, A.20, A.21,9.7
		d/s	A.22, A.23, A.24,9.8
200	θ	u/s	6.30, 6.31, 6.32,A.79
		d/s	6.33, 6.34, 6.35,A.80
	ϕ	u/s	A.25, A.26, A.27,A.81
		d/s	A.28, A.29, A.30,A.82
	mu	u/s	A.31, A.32, A.33,A.83
		d/s	A.34, A.35, A.36,A.84
	md	u/s	A.37, A.32, A.39,A.85
		d/s	A.40, A.41, A.42,A.86
300	θ	u/s	6.36, 6.37, 6.38,A.87
		d/s	6.39, 6.40, 6.41,A.88
	ϕ	u/s	A.43, A.44, A.45,A.89
		d/s	A.46, A.47, A.48,A.90
	mu	u/s	A.49, A.50, A.51,A.91
		d/s	A.52, A.53, A.54,A.92
	md	u/s	A.55, A.56, A.57,A.93
		d/s	A.58, A.59, A.60,A.94
400	θ	u/s	6.42, 6.43, 6.44,A.95
		d/s	6.45, 6.46, 6.47,A.96
	ϕ	u/s	A.61, A.62, A.63,A.97
		d/s	A.64, A.65, A.66,A.98
	mu	u/s	A.67, A.68, A.69,A.99
		d/s	A.70, A.71, A.72,A.100
	md	u/s	A.73, A.74, A.75,A.101
		d/s	A.76, A.77, A.78,A.102

Maximum separation is presented as the percentage of the dam height, and vertical coordinate, z, of each node is normalized by the full dam height, H, as shown in Figure 6.22. Same height definition is used in other plots. Every plot in the second column has two curves: RMS acceleration ratio (RMS(out)/RMS(in)), and maximum horizontal acceleration ratio (Max. Acce.(out)/Max.Acce.(in)) versus height. Finally, each plot in the third column illustrates 3 curves: minimum, static, and maximum interface pressures. All three pressures are normalized by the bottom static interface pressure.

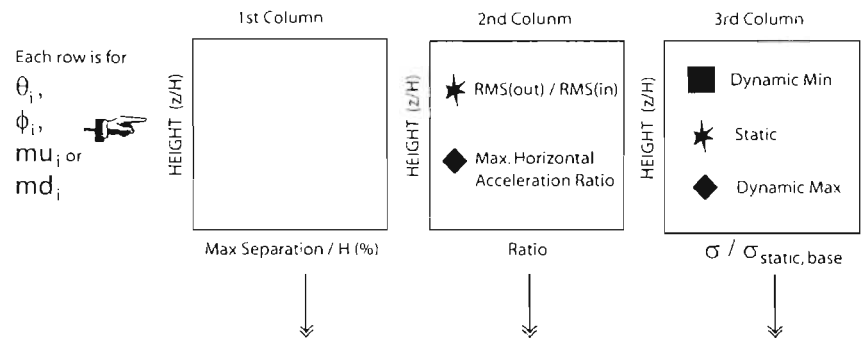

Figure 6.21 A shared legend for figures showing interface performance.

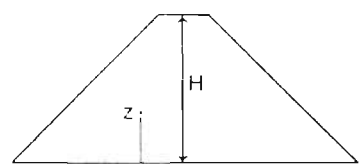

Figure 6.22 Representation of height, z/H.

Next, collective graphs of all response types are obtained. For example, Figure 6.26 represents the combined graphs for each response due to θ for 100 ft high dam along the U/S interface. In Figure 6.26 there are 6 plots. First column (parts (a), (b), and (c)) shows minimum, static, and maximum interface pressures, respectively. In the second column, parts (d), (e), and (f) represent maximum separation, maximum horizontal

acceleration ratio, and maximum RMS acceleration ratio, respectively. Same arrangement was made for the D/S response as shown in Figure 6.29. This representation of U/S and D/S performance are repeated for each parameters within each height, and they are presented in Appendix A.2.

Next, the maximum of maximum separation, maximum acceleration ratio, and maximum RMS acceleration ratio were determined. Additionally, using maximum separation profiles, maximum separation depths were calculated for all cases. Separation depth is defined as the ratio of separated distance, d, to the height, H, of the dam, and it is illustrated in Figure 6.23. To present the variation of the maximum value of these interface performance parameters versus both the control parameter and heights , bar charts are provided. Figures 6.48 and 6.49 illustrate the maximum separation, maximum separation depth, maximum acceleration ratio and maximum RMS acceleration ratio versus θ and height, H, for the U/S interface. Likewise, Figures 6.50 and 6.51 show the variation of all interface performance for D/S interface. Bar charts with the same arrangement are provided for other controlling parameters and presented in Appendix A.4.

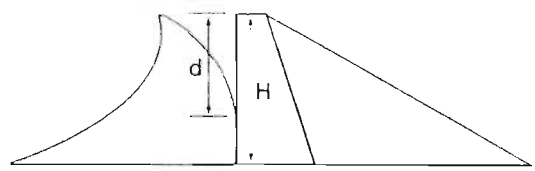

Figure 6.23 Representation of `separation depth`, d/H .

Finally, the variation of maximum and minimum dynamic interface pressures at the bottom of the dam are gathered and presented. For example, Figures 6.52, and 6.53

show the variation of maximum and minimum interface pressures versus θ for all heights at U/S and D/S interfaces, respectively. Next, all pressure profiles are collapsed in to one figure for each interface. Figure 6.54 show these collapsed figures for U/S and D/S interfaces. The pressure profiles for all other controlling parameters are presented in Appendix A.5.

Interpretations of FE analysis results are presented later in this chapter.

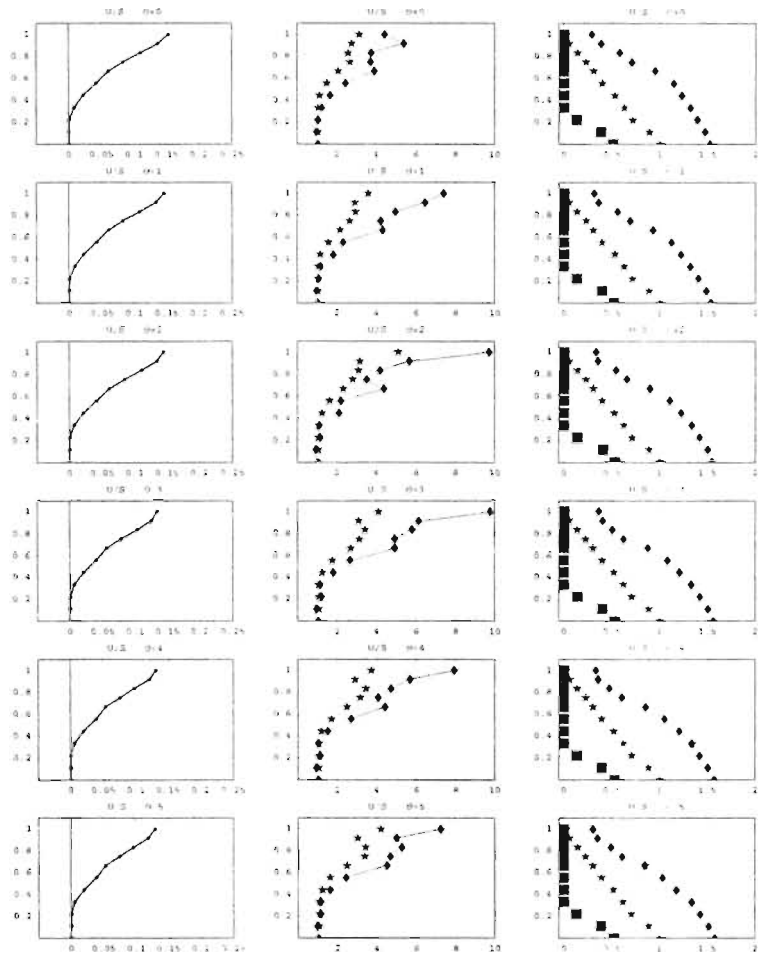

Figure 6.24 Max. Separation, Max. Acceleration, and Nodal Interface Stresses (Max., Static, Min.) along the *UPSTREAM* Interface due to change of θ (in degrees) (H=100)

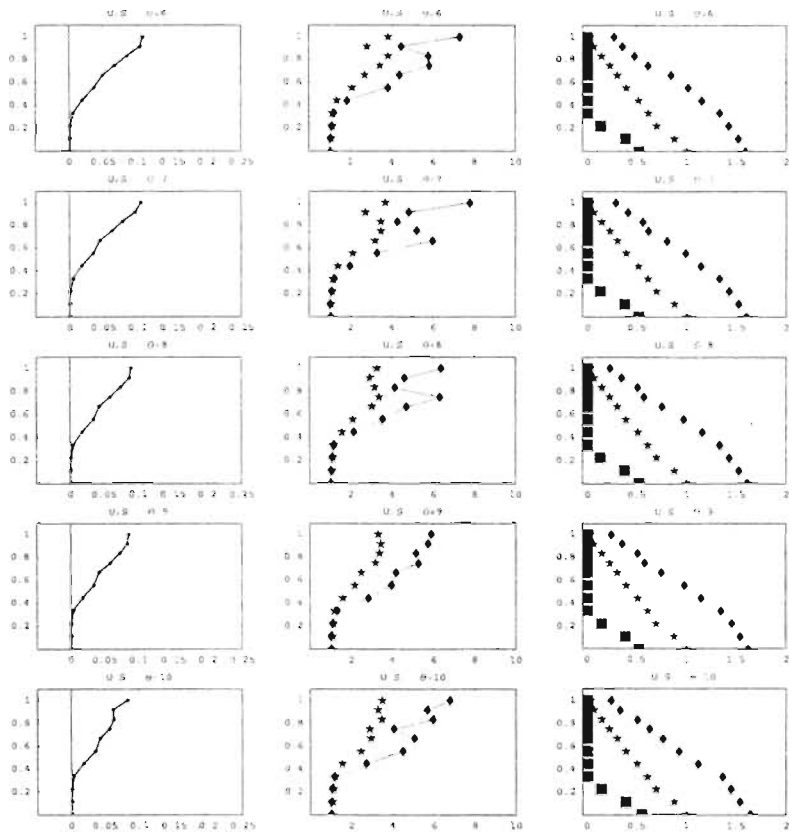

Figure 6.25 (Continued from previous figure) Max. Separation, Max. Acceleration, and Nodal Interface Stresses (Max., Static, Min.) along the *UPSTREAM* Interface due to change of θ (in degrees) (H=100)

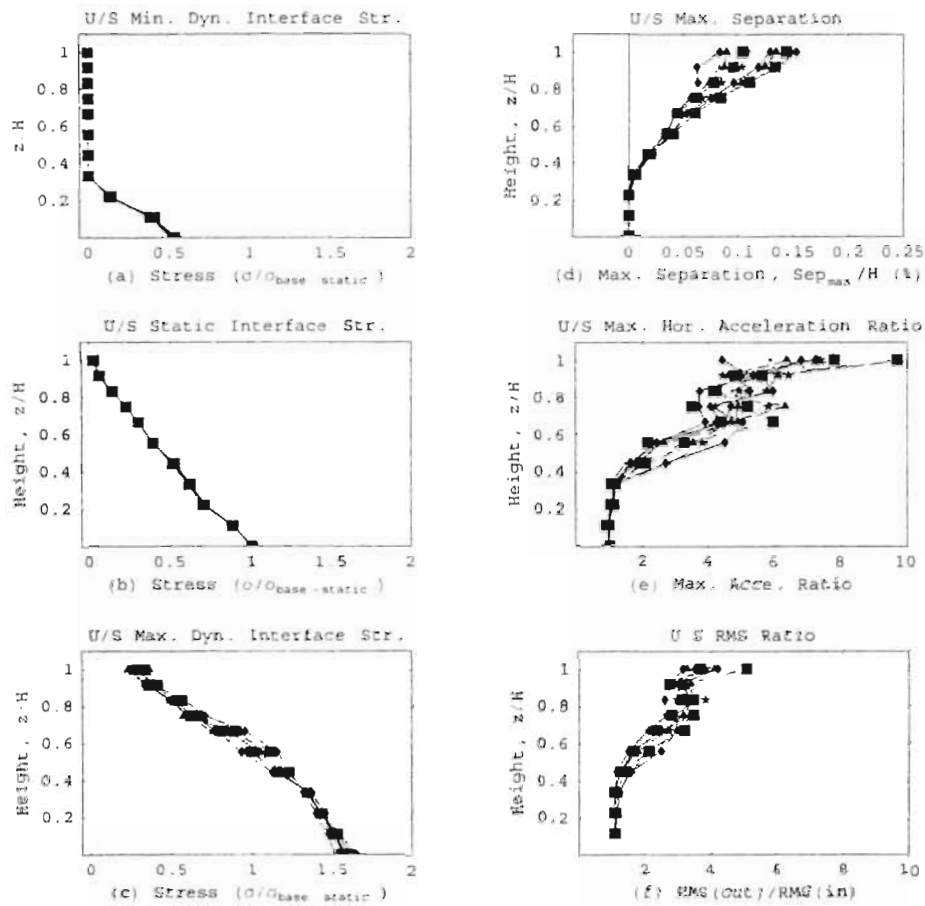

Figure 6.26 Collective graphs of Max. Separation, Acceleration, and interface pressures along the *UPSTREAM* Interface at all θ's (H=100)

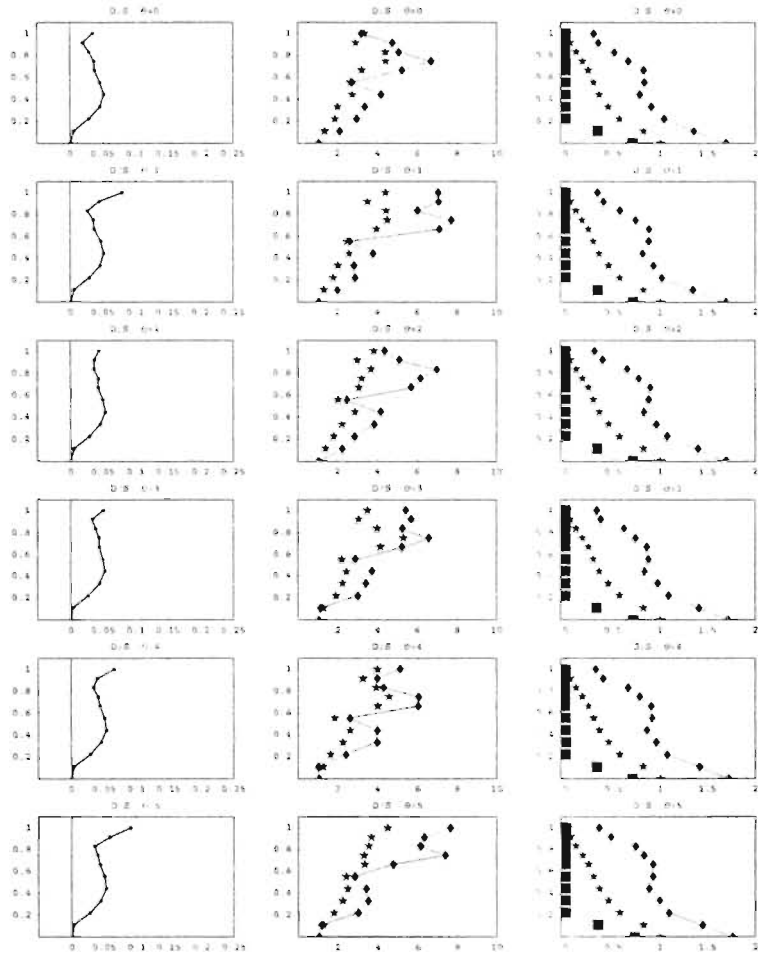

Figure 6.27 Max. Separation, Max. Acceleration, and Nodal Interface Stresses (Max., Static, Min.) along the *DOWNSTREAM* Interface due to change of θ (in degrees)(H=100)

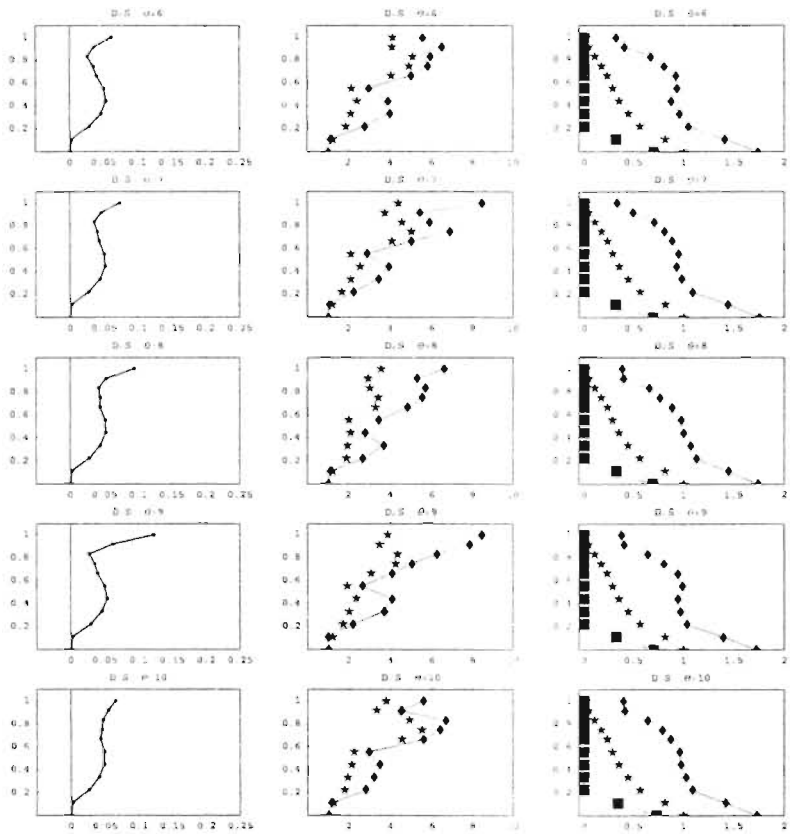

Figure 6.28 (Continued from previous figure) Max. Separation, Max. Acceleration, and Nodal Interface Stresses (Max., Static, Min.) along the *DOWNSTREAM* Interface due to change of θ (in degrees) (H=100)

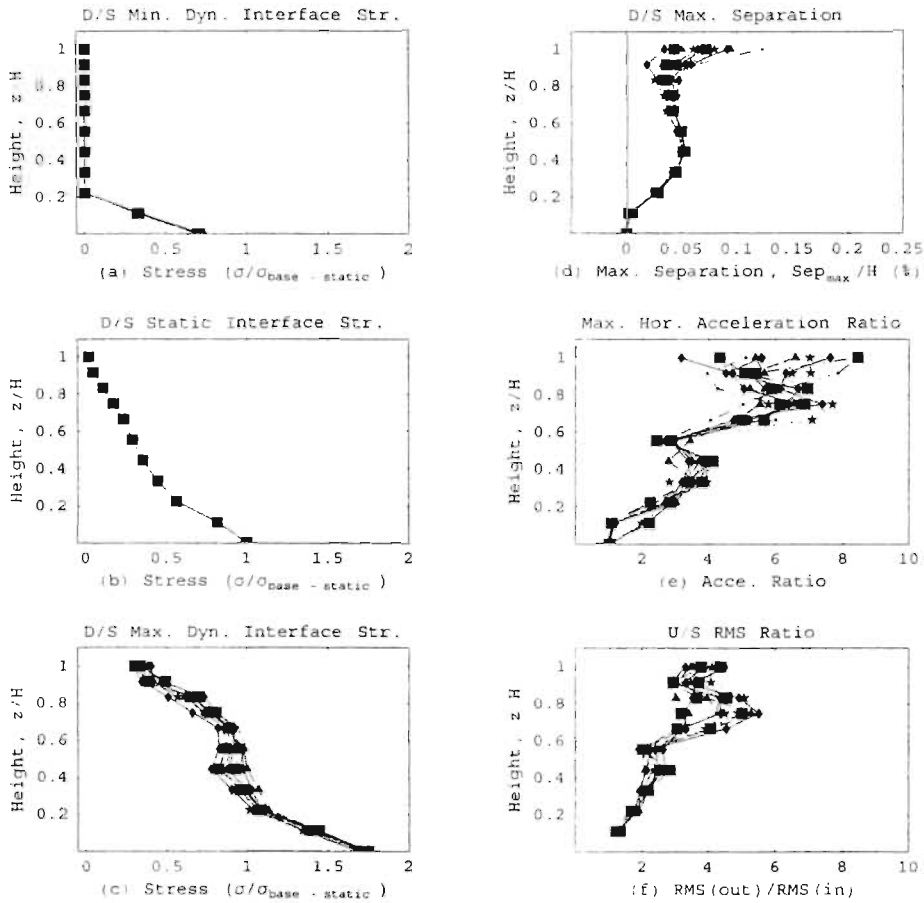

Figure 6.29 Collective graphs of Max. Separation, Acceleration, and interface pressures along the *DOWNSTREAM* Interface at all θ's (11=100)

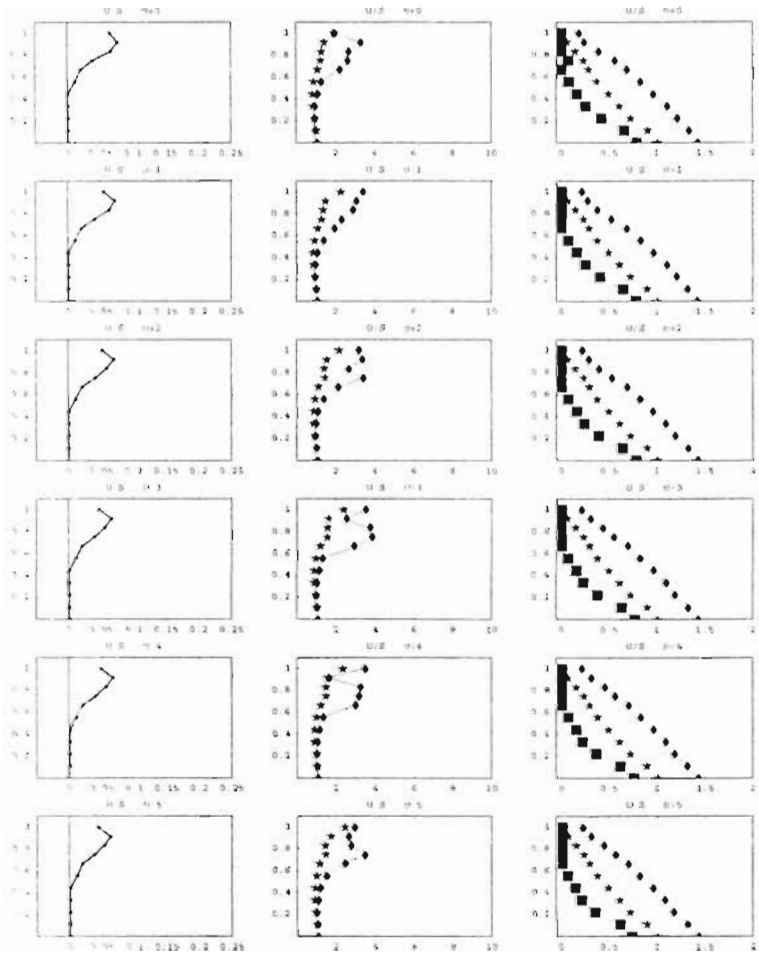

Figure 6.30 Max. Separation, Max. Acceleration, and Nodal Interface Stresses (Max., Static, Min.) along the *UPSTREAM* Interface due to change of θ (in degrees) (H=200)

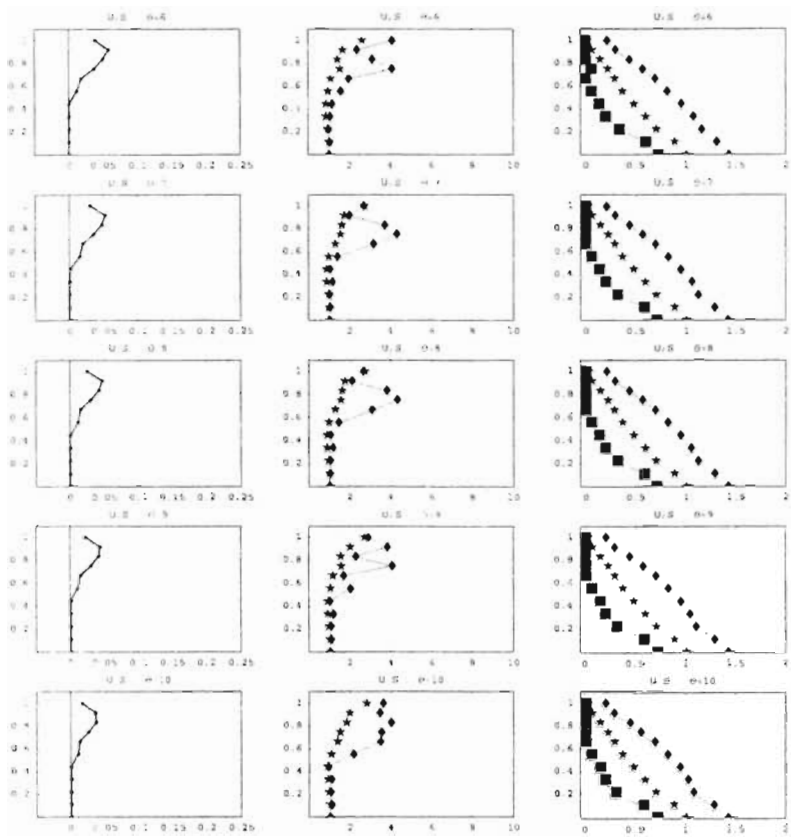

Figure 6.31 (Continued from previous figure) Max. Separation, Max. Acceleration, and Nodal Interface Stresses (Max., Static, Min.) along the *UPSTREAM* Interface due to change of θ (in degrees)(H=200)

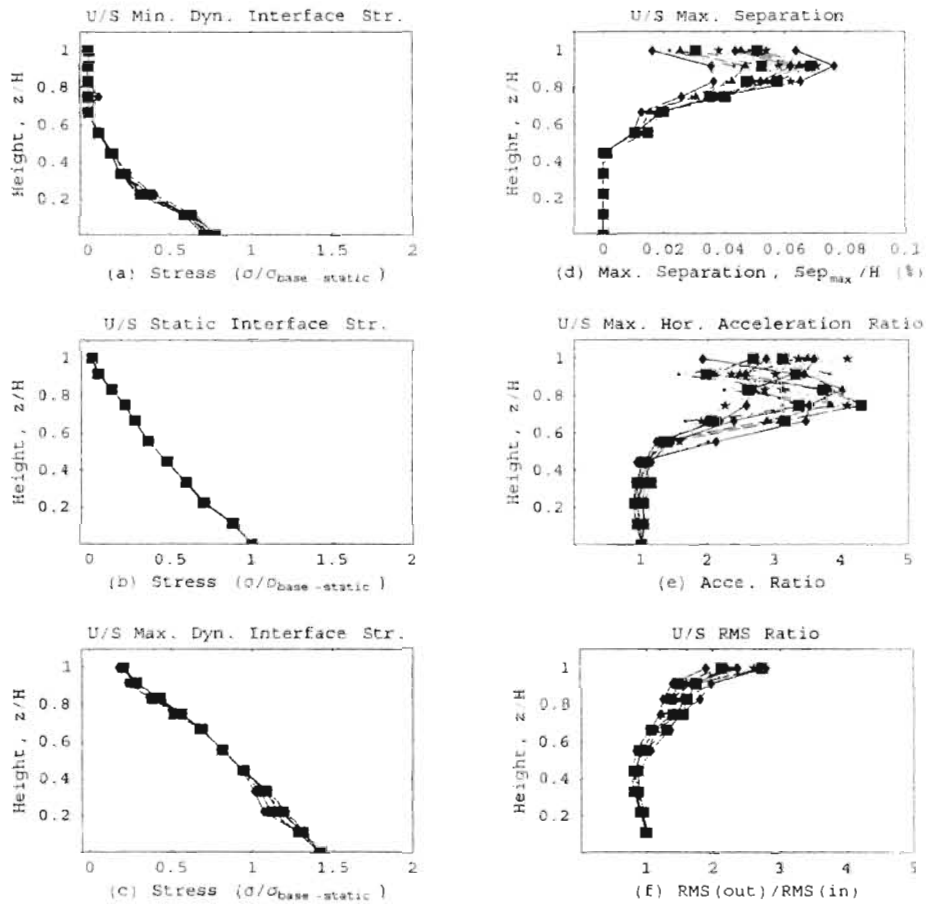

Figure 6.32 Collective graphs of Max. Separation, Acceleration, and interface pressures along the *UPSTREAM* Interface at all θ's (H=200)

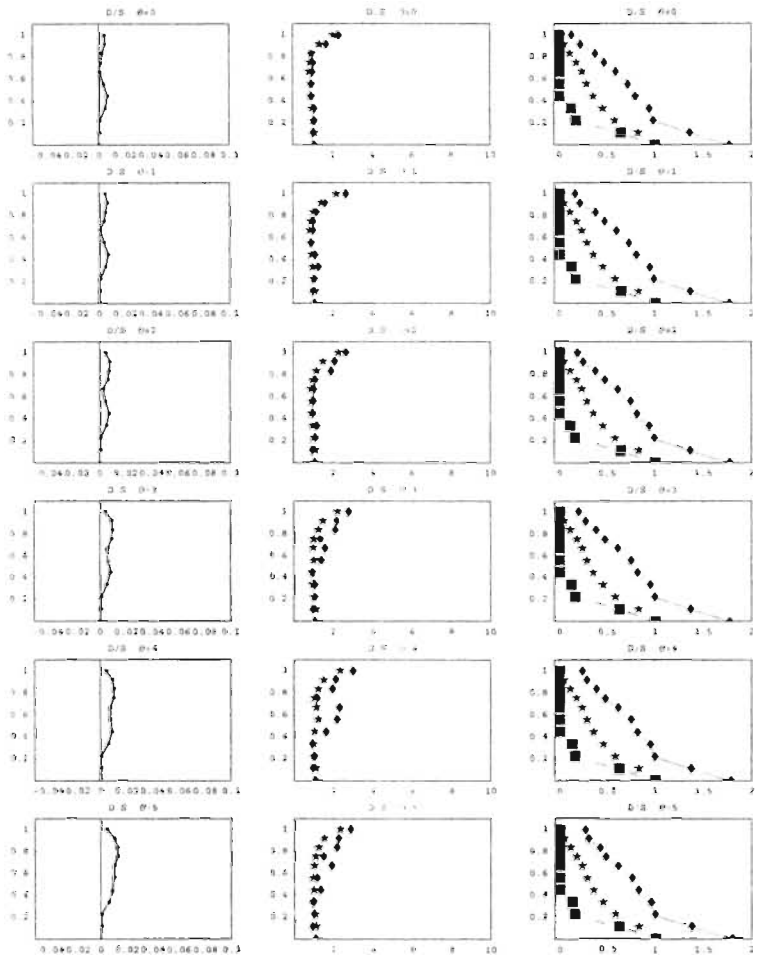

Figure 6.33 Max. Separation, Max. Acceleration, and Nodal Interface Stresses (Max., Static, Min.) along the *DOWNSTREAM* Interface due to change of θ (in degrees)(H=200)

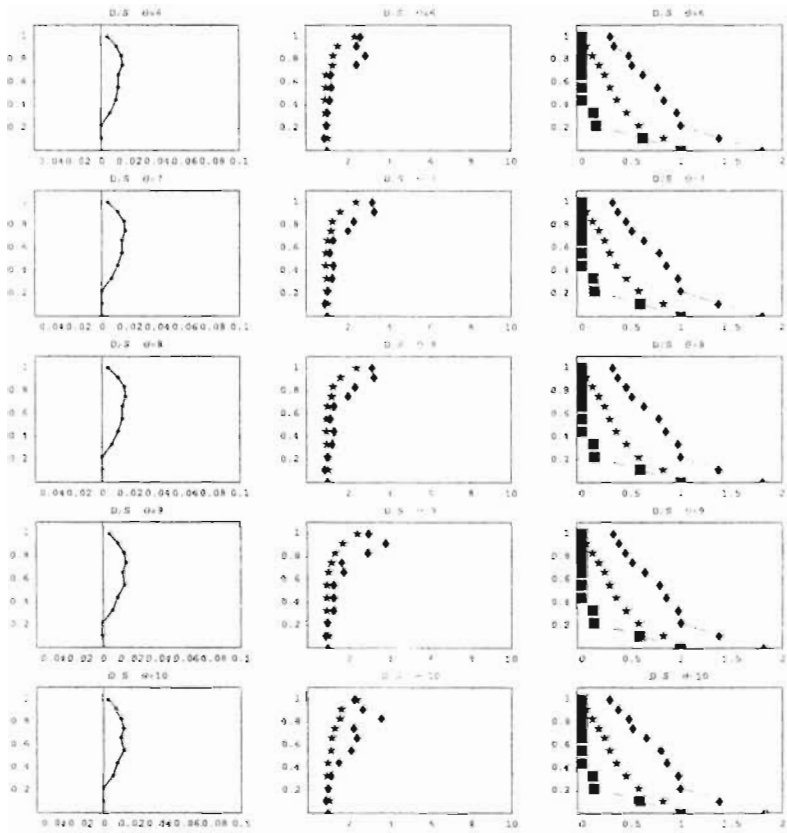

Figure 6.34 (Continued from previous figure) Max. Separation, Max. Acceleration, and Nodal Interface Stresses (Max., Static, Min.) along the *DOWNSTREAM* Interface due to change of θ (in degrees) (H=200)

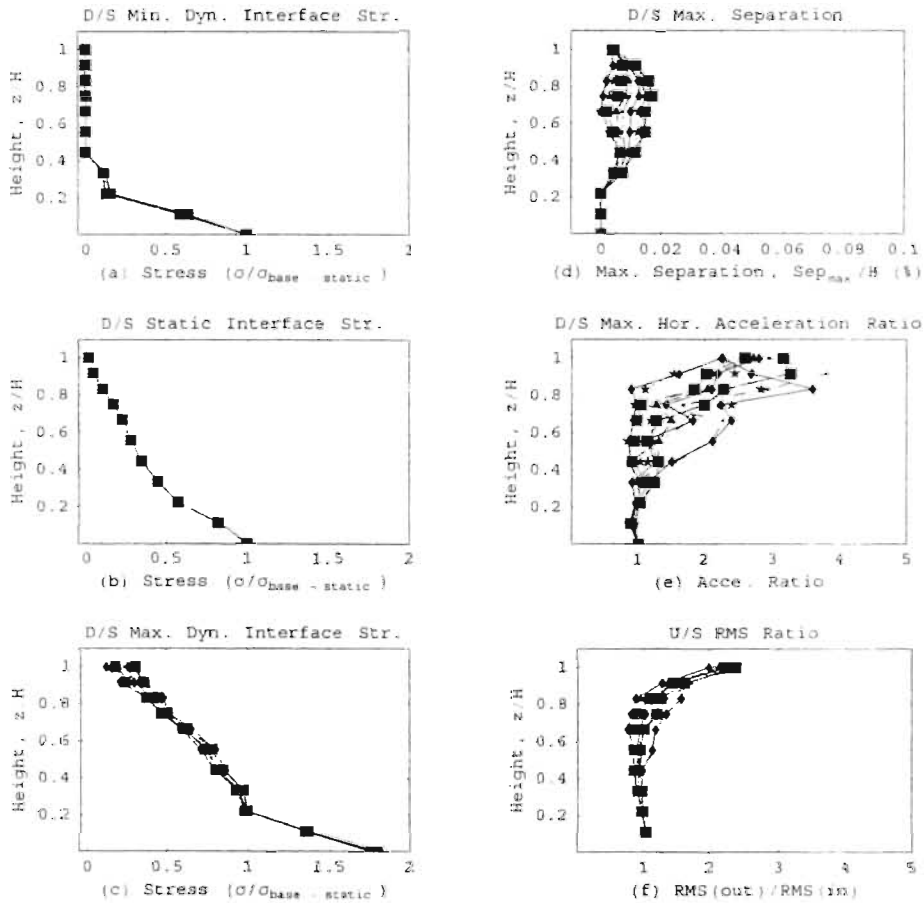

Figure 6.35 Collective graphs of Max. Separation, Acceleration, and interface pressures along the *DOWNSTREAM* Interface at all θ's (H=200)

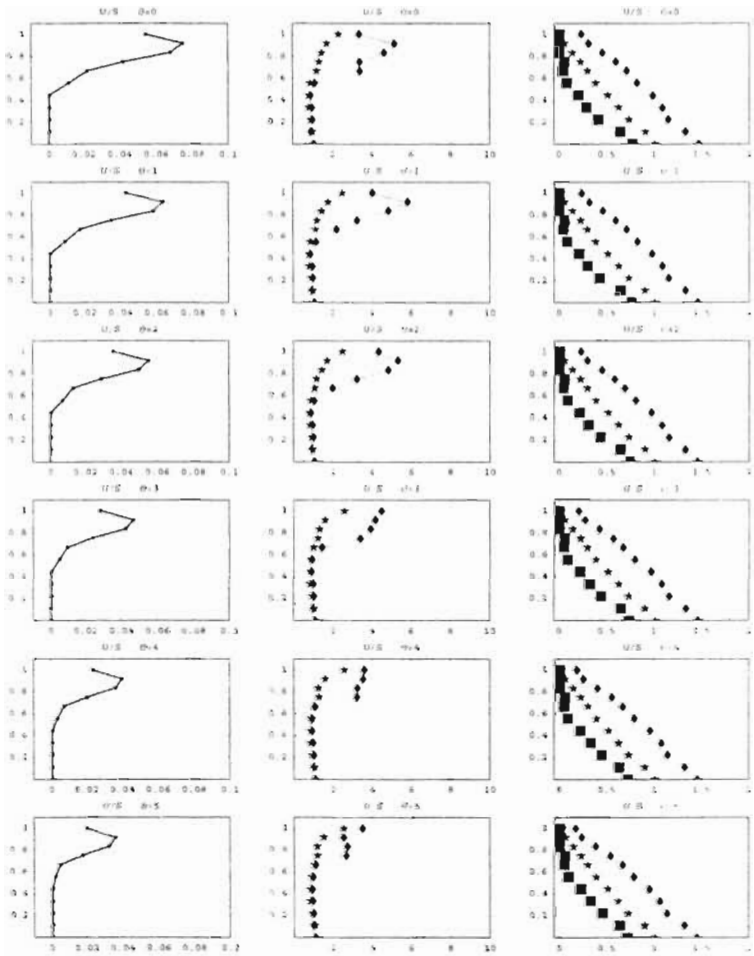

Figure 6.36 Max. Separation, Max. Acceleration, and Nodal Interface Stresses (Max., Static, Min.) along the *UPSTREAM* Interface due to change of θ (in degrees) (H=300)

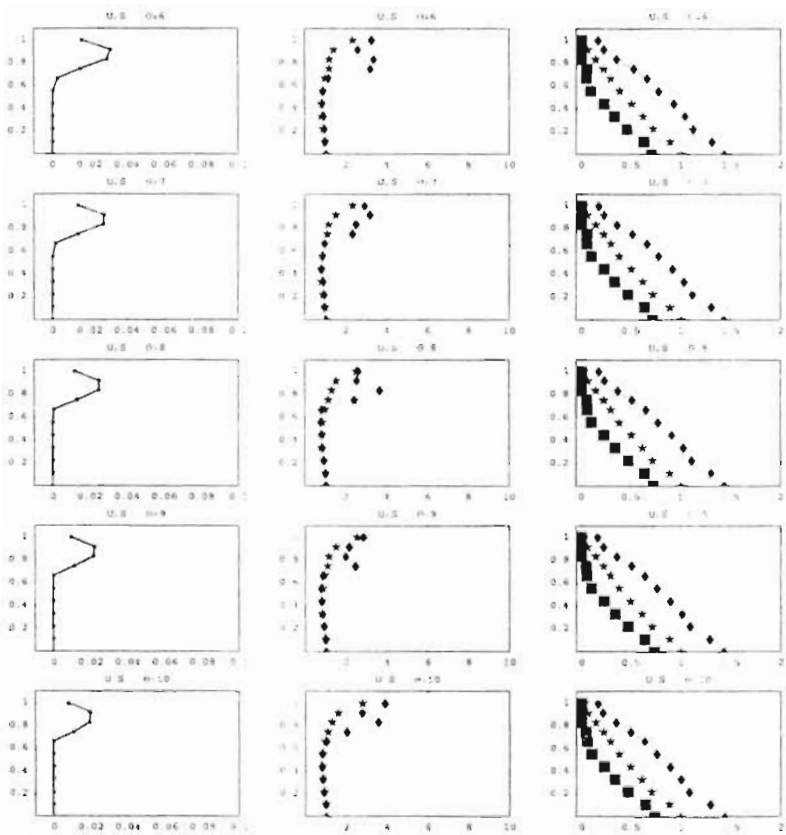

Figure 6.37 (Continued from previous figure) Max. Separation, Max. Acceleration, and Nodal Interface Stresses (Max., Static, Min.) along the *UPSTREAM* Interface due to change of θ (in degrees) (H=300)

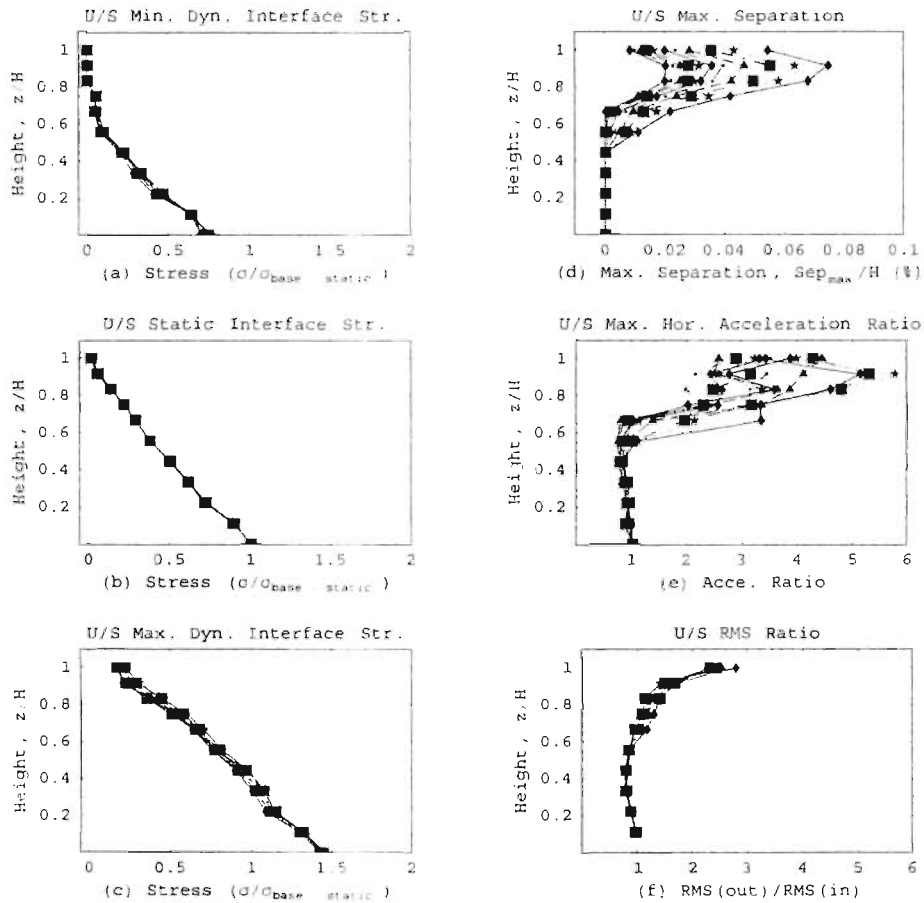

Figure 6.38 Collective graphs of Max. Separation, Acceleration, and interface pressures along the *UPSTREAM* Interface at all θ's (H=300)

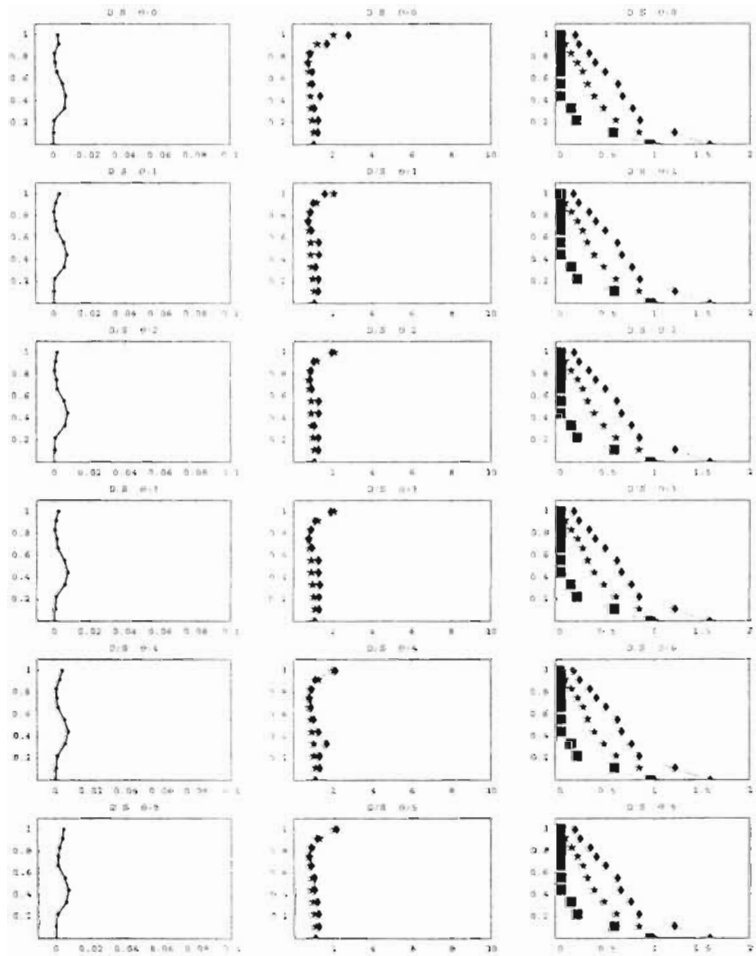

Figure 6.39 Max. Separation, Max. Acceleration, and Nodal Interface Stresses (Max., Static, Min.) along the *DOWNSTREAM* Interface due to change of θ (in degrees) (H=300)

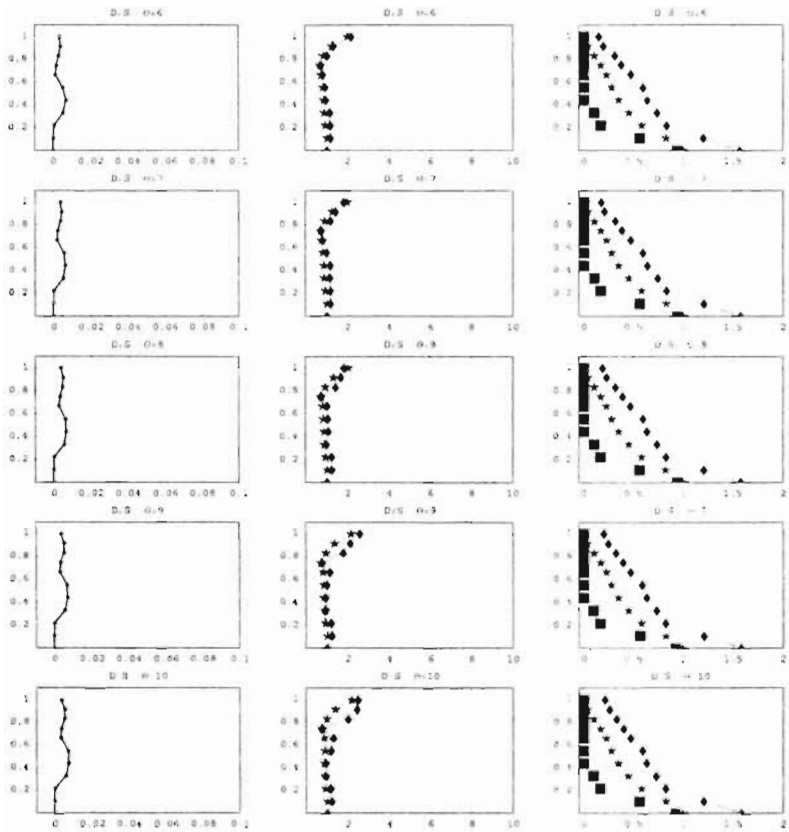

Figure 6.40 (Continued from previous figure) Max. Separation, Max. Acceleration, and Nodal Interface Stresses (Max., Static, Min.) along the *DOWNSTREAM* Interface due to change of θ (in degrees) (H=300)

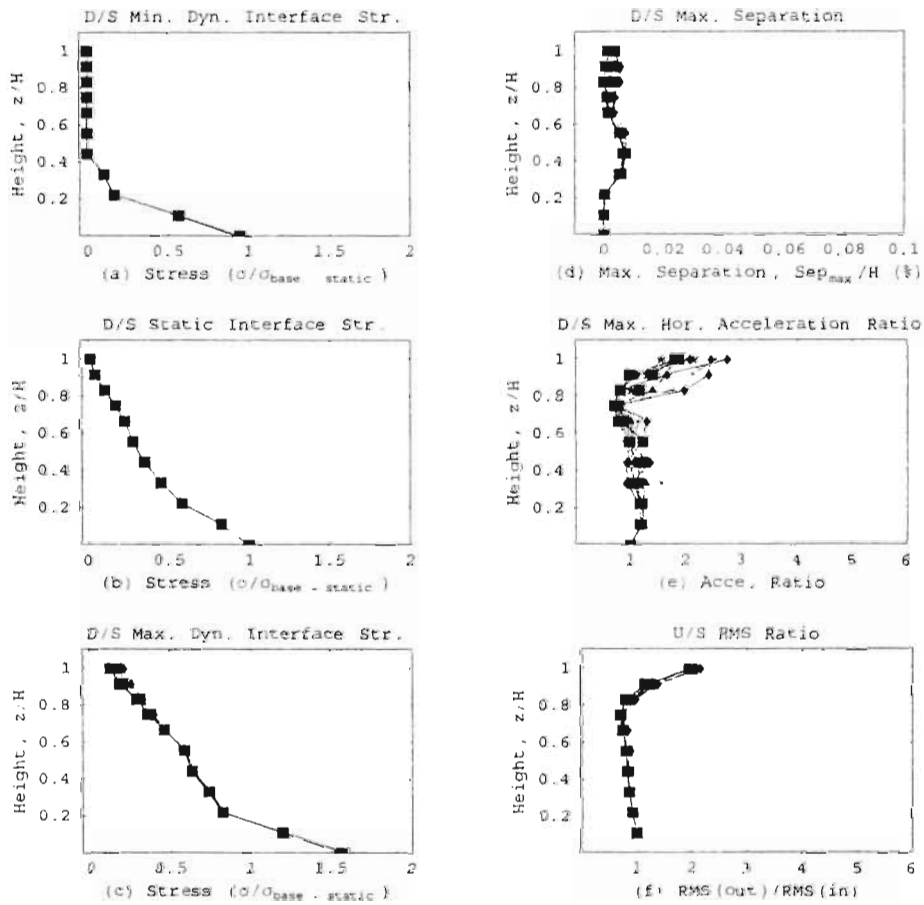

Figure 6.41 Collective graphs of Max. Separation, Acceleration, and interface pressures along the *DOWNSTREAM* Interface at all θ's (H=300)

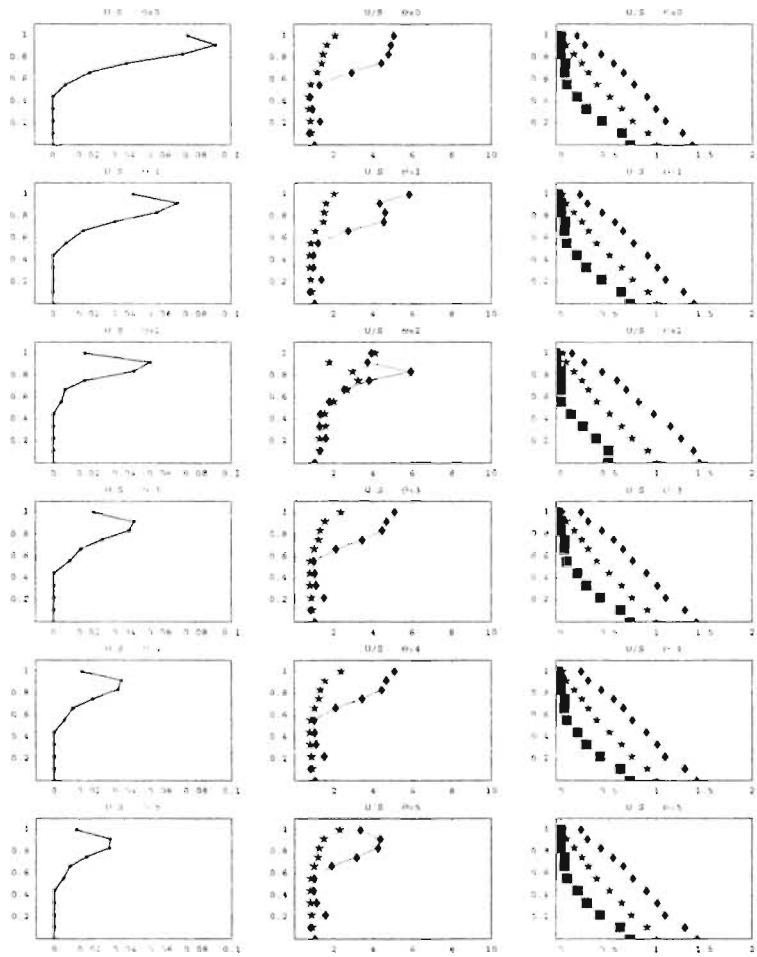

Figure 6.42 Max. Separation, Max. Acceleration, and Nodal Interface Stresses (Max., Static, Min.) along the *UPSTREAM* Interface due to change of θ (in degrees) (H=400)

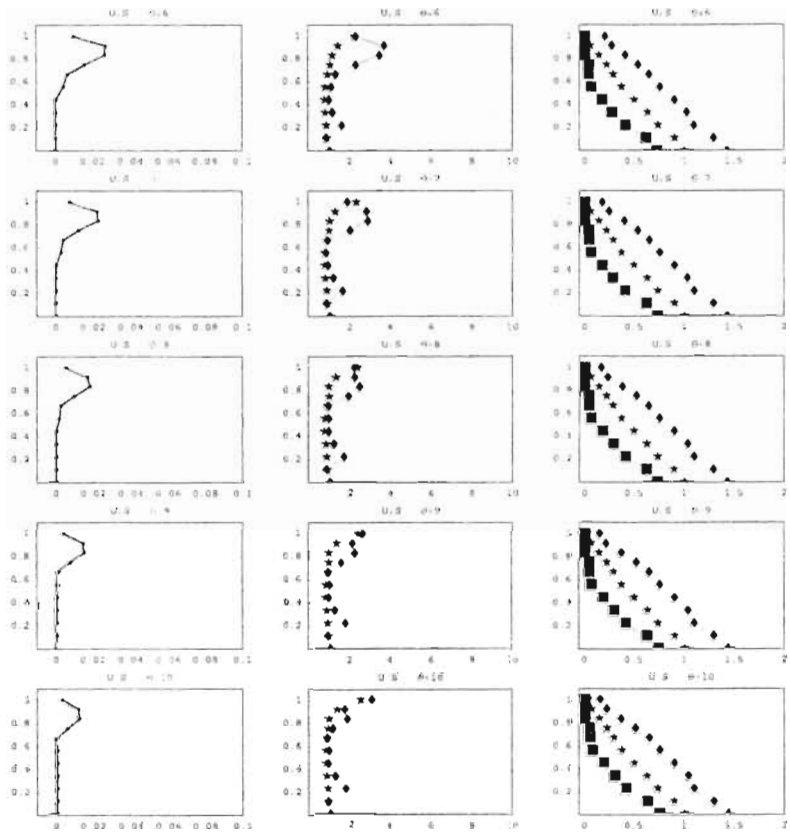

Figure 6.43 (Continued from previous figure) Max. Separation, Max. Acceleration, and Nodal Interface Stresses (Max., Static, Min.) along the *UPSTREAM* Interface due to change of θ (in degrees) (H=400)

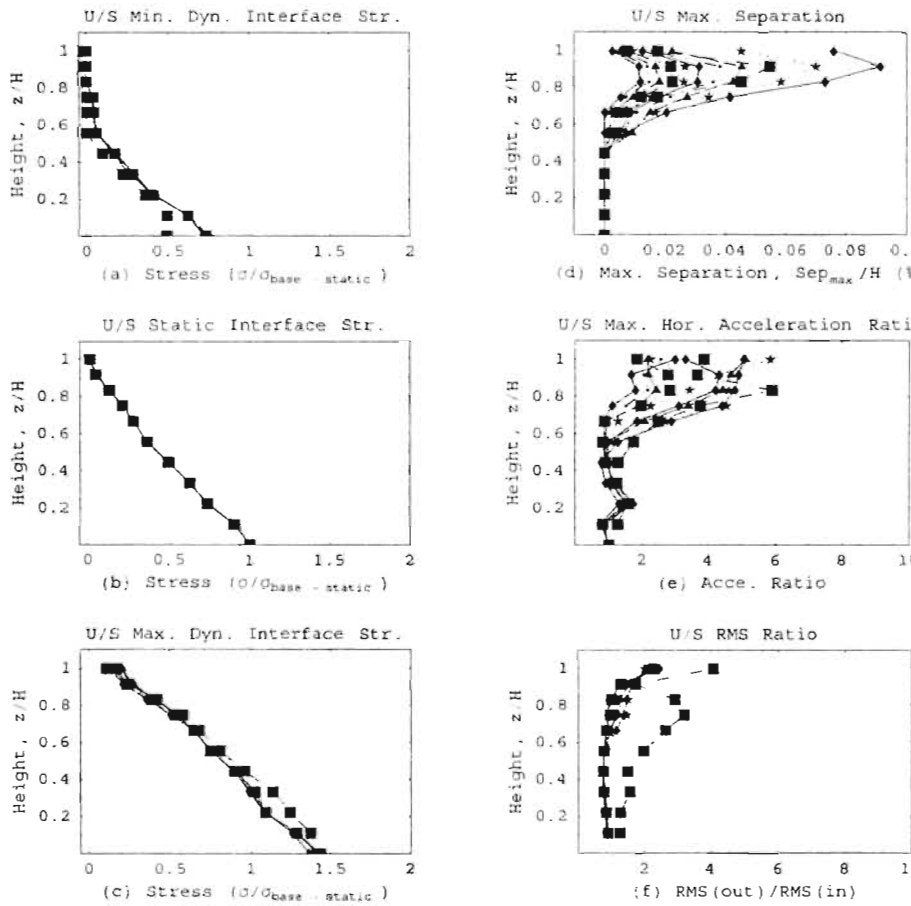

Figure 6.44 Collective graphs of Max. Separation, Acceleration, and interface pressures along the *UPSTREAM* Interface at all θ's (H=400)

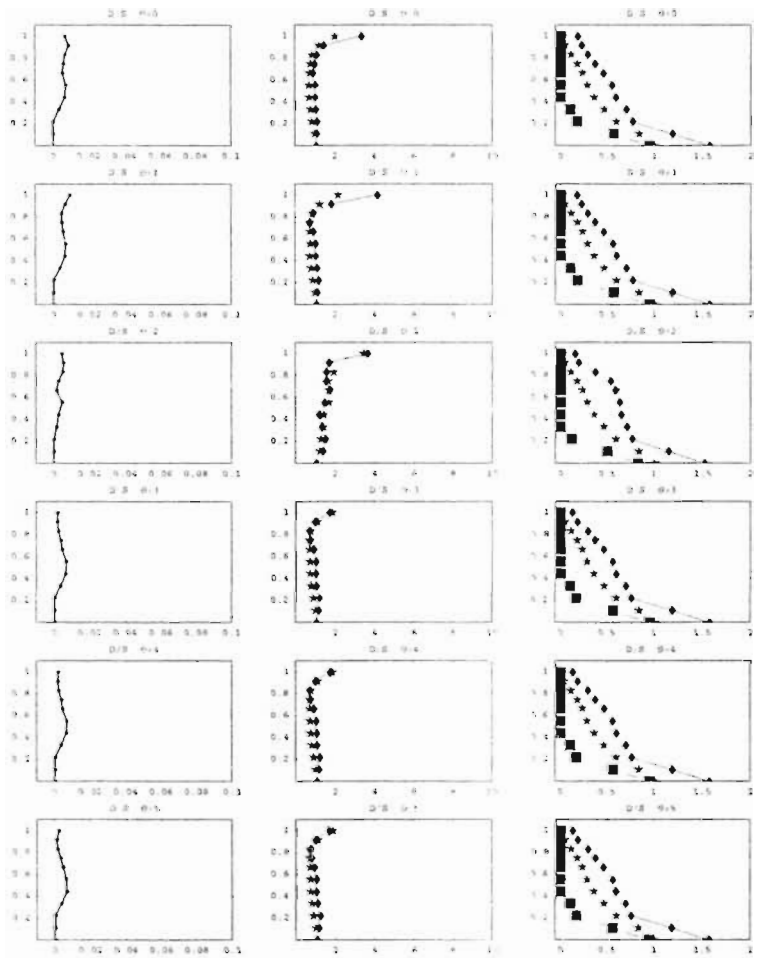

Figure 6.45 Max. Separation, Max. Acceleration, and Nodal Interface Stresses (Max., Static, Min.) along the *DOWNSTREAM* Interface due to change of θ (in degrees) (H=400)

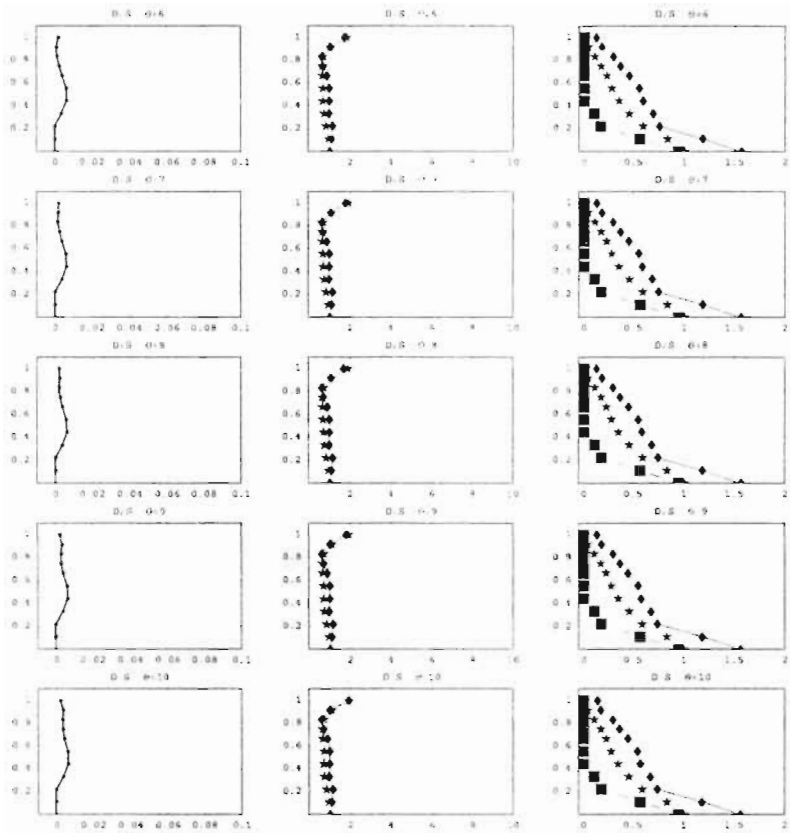

Figure 6.46 (Continued from previous figure) Max. Separation, Max. Acceleration, and Nodal Interface Stresses (Max., Static, Min.) along the *DOWNSTREAM* Interface due to change of θ (in degrees) (H=400)

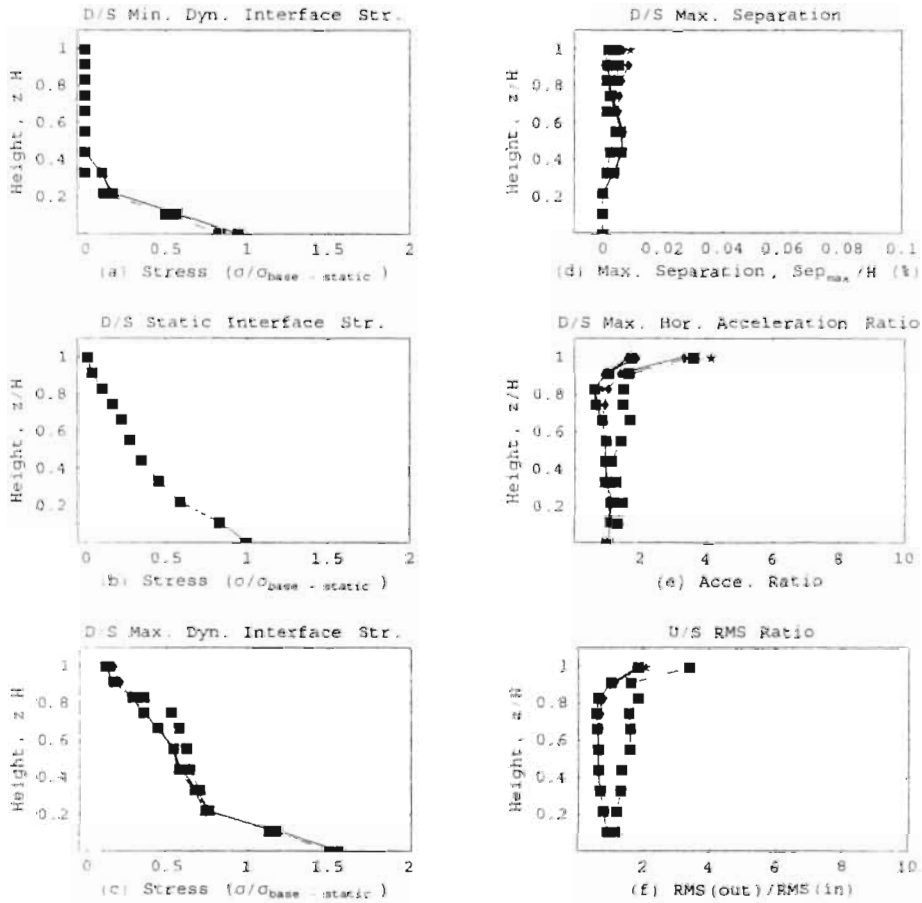

Figure 6.47 Collective graphs of Max. Separation, Acceleration, and interface pressures along the *DOWNSTREAM* Interface at all θ's (H=400)

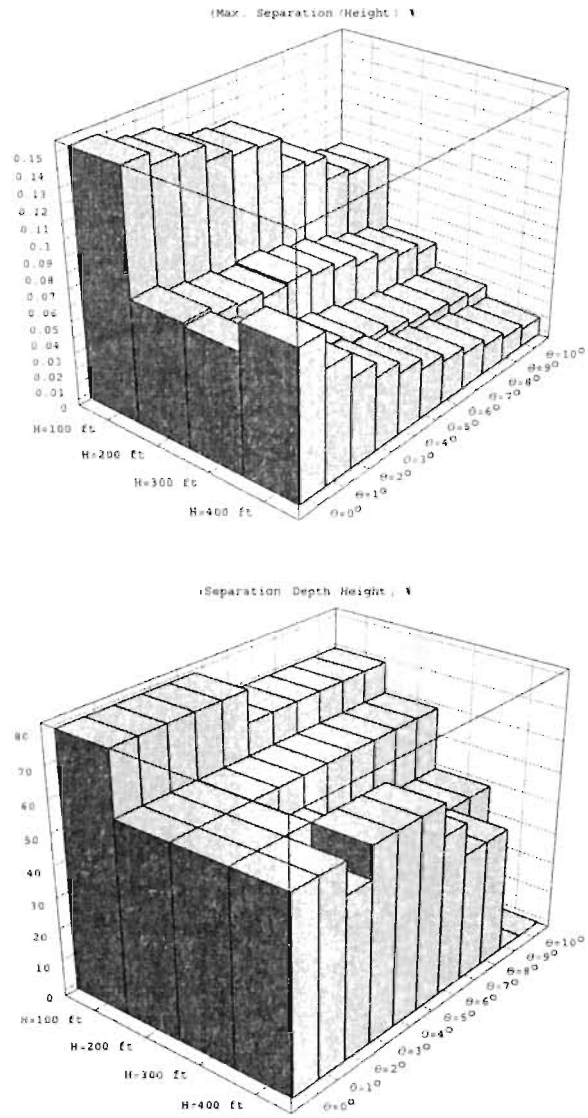

Figure 6.48 Max. Separation and Separation Depth of U/S interface vs θ and Height.

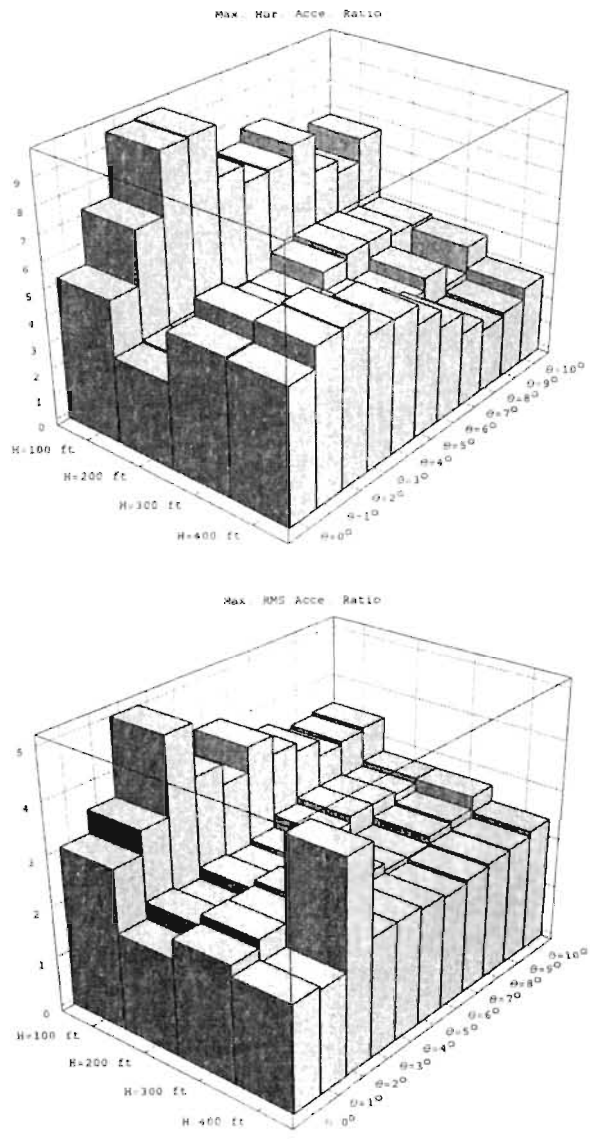

Figure 6.49 Max. Acceleration Ratio and Max. RMS Acceleration Ratio of U/S interface vs θ and Height.

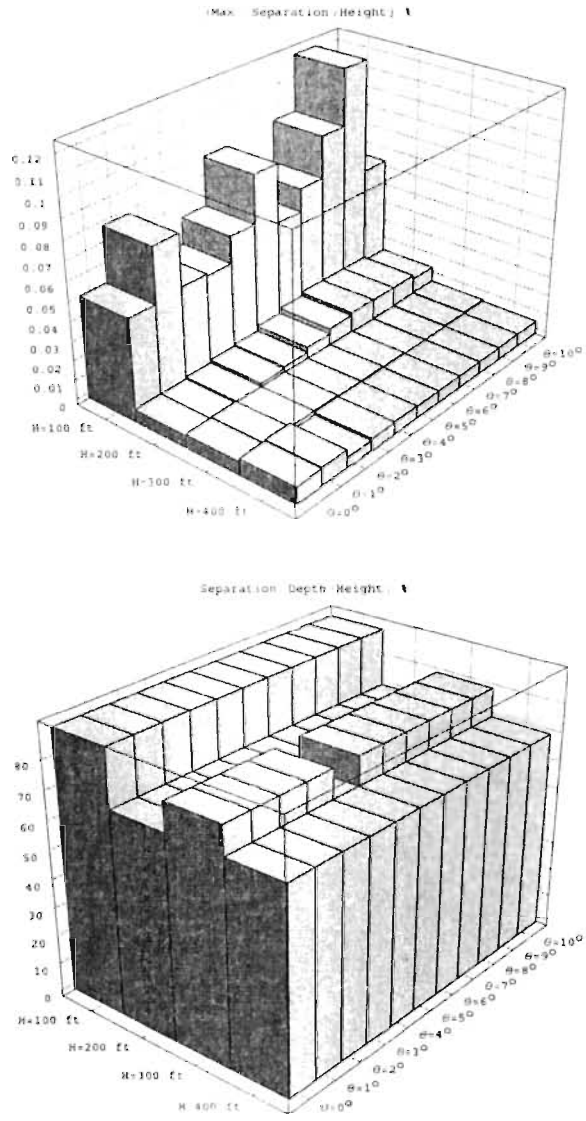

Figure 6.50 Max. Separation and Separation Depth of D/S interface vs θ and Height.

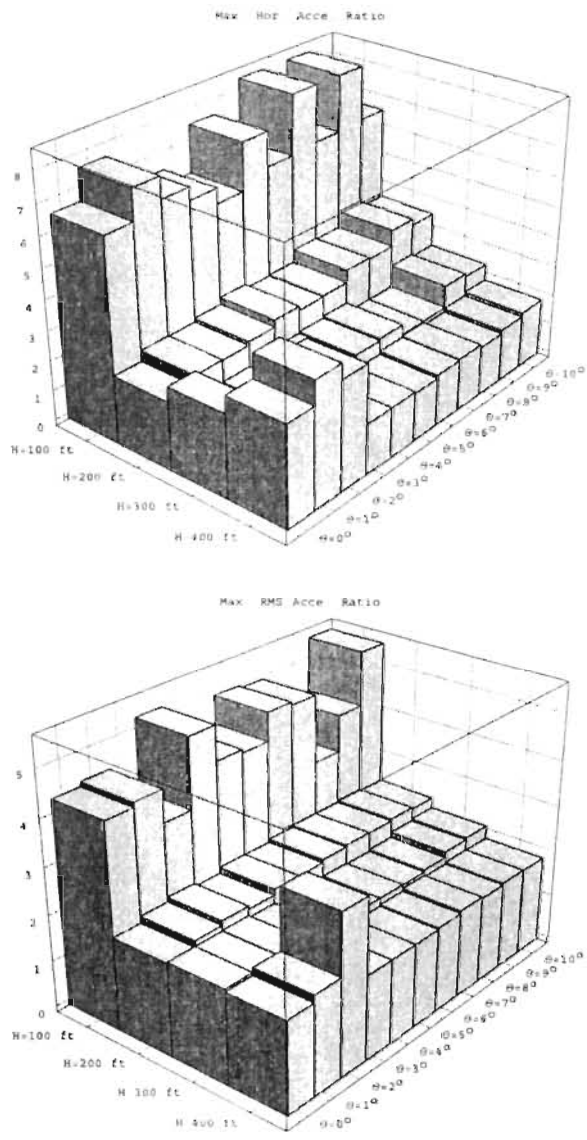

Figure 6.51 Max. Acceleration Ratio and Max. RMS Acceleration Ratio of D/S interface vs θ and Height.

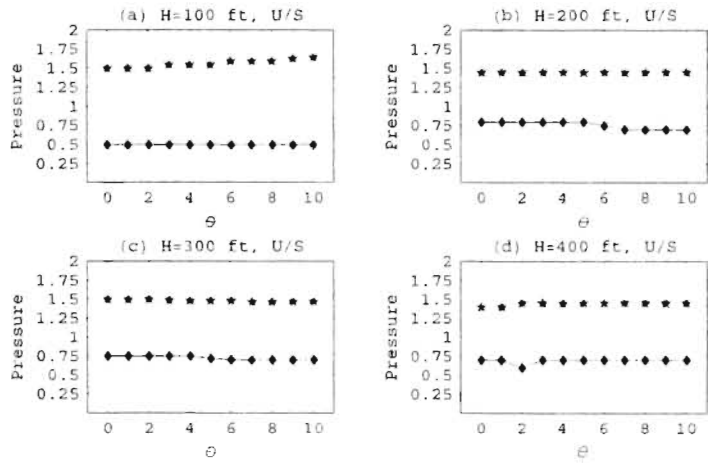

Figure 6.52 The effect of θ on minimum and maximum interface pressures along the U/S interface.

6.4 Effect of Vertical Component of Ground Motion

In order to investigate the influence of vertical component of ground motion, one FE analysis was performed for each dam height using the reference configuration. Vertical component of Koyna Dam Earthquake Record is shown in part (c) of Figure 5.1. It has peak ground acceleration of 0.26 g. The analysis results are compared with ones using horizontal ground motion only.

Figures 6.55, 6.56, 6.57, 6.58 represent the comparisons for dams with heights 100, 200, 300, and 400 ft, respectively. Each figure has 6 plots. First column belongs to U/S interface and second column is for D/S interface. The top graph of each column relates the maximum separation, in feet, to the height (z/H). Second graph represents the

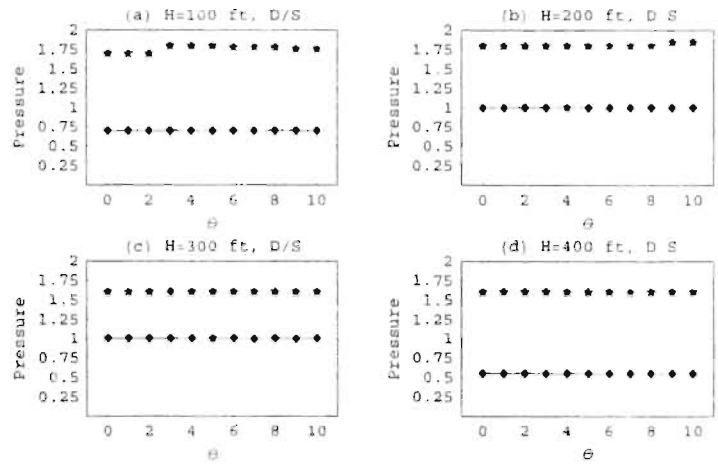

Figure 6.53 The effect of θ on minimum and maximum interface pressures along the D/S interface.

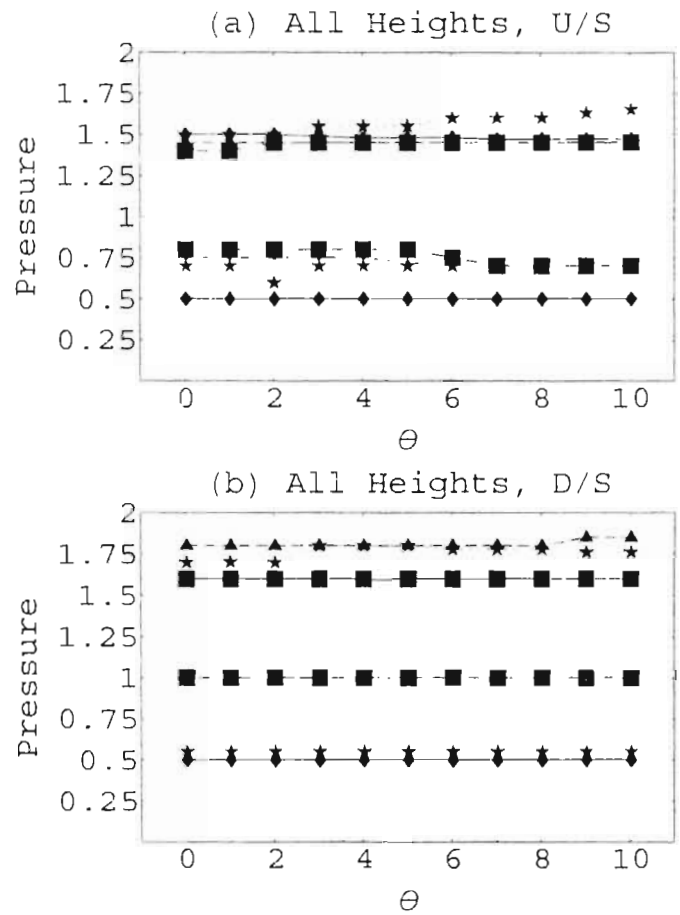

Figure 6.54 Collective graphs of minimum an maximum pressures versus θ for both U/S and D/S interfaces.

maximum acceleration, in g, versus height. Finally, the third one shows maximum interface pressure, in ksf, versus height.

The inclusion of vertical component of ground motion had very little or no effect in interface response as seen in Figures 6.55, 6.56, 6.57, 6.58. Vertical component of ground motion caused some increase in maximum acceleration response of U/S interface of 300 ft high dam (Figure 6.57), and in maximum interface pressure of D/S interface of 400 ft high dam (Figure 6.58).

Based on the conclusion that the effect of vertical ground motion on IBCD is not significant, no more analyses were performed.

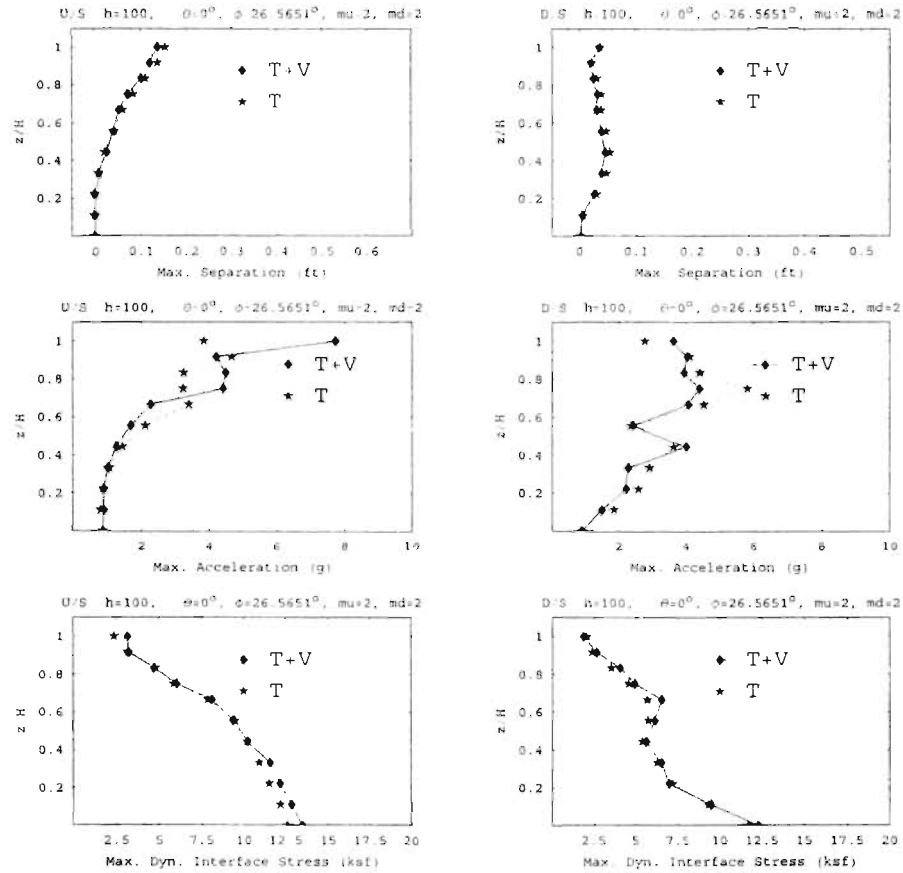

Figure 6.55 Maximum separation, acceleration, and interface stress distribution for both upstream and downstream interfaces under ground shaking with vertical and transverse components (H=100).

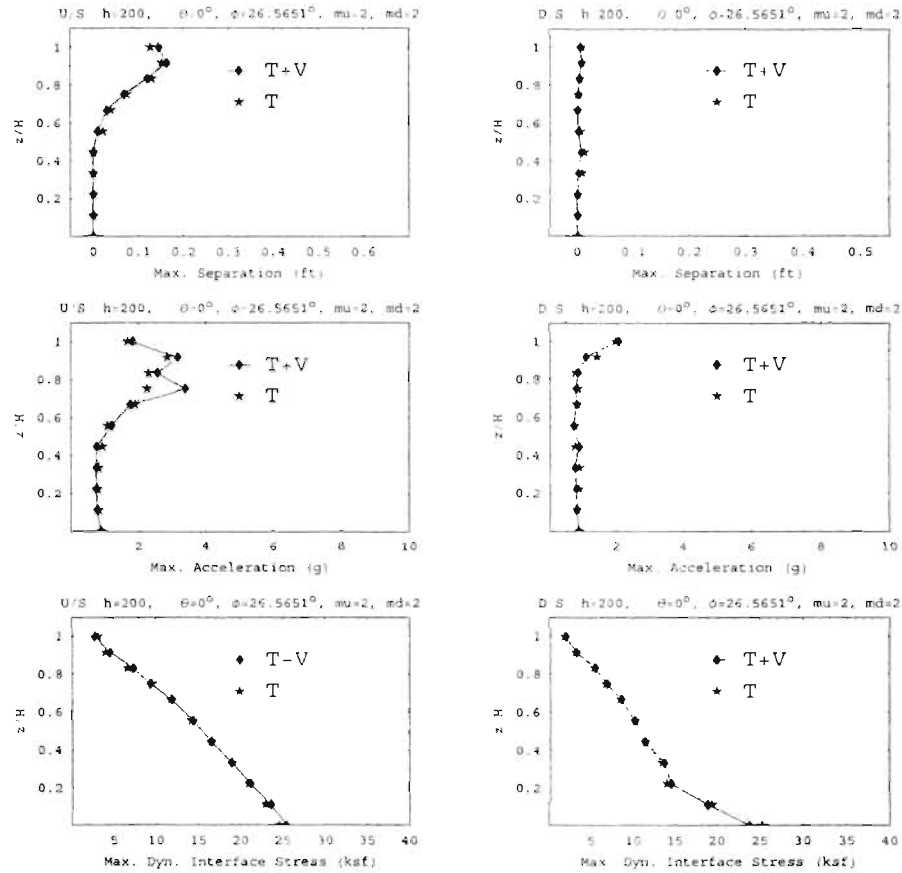

Figure 6.56 Maximum separation, acceleration, and interface stress distribution for both upstream and downstream interfaces under ground shaking with vertical and transverse components (H=200).

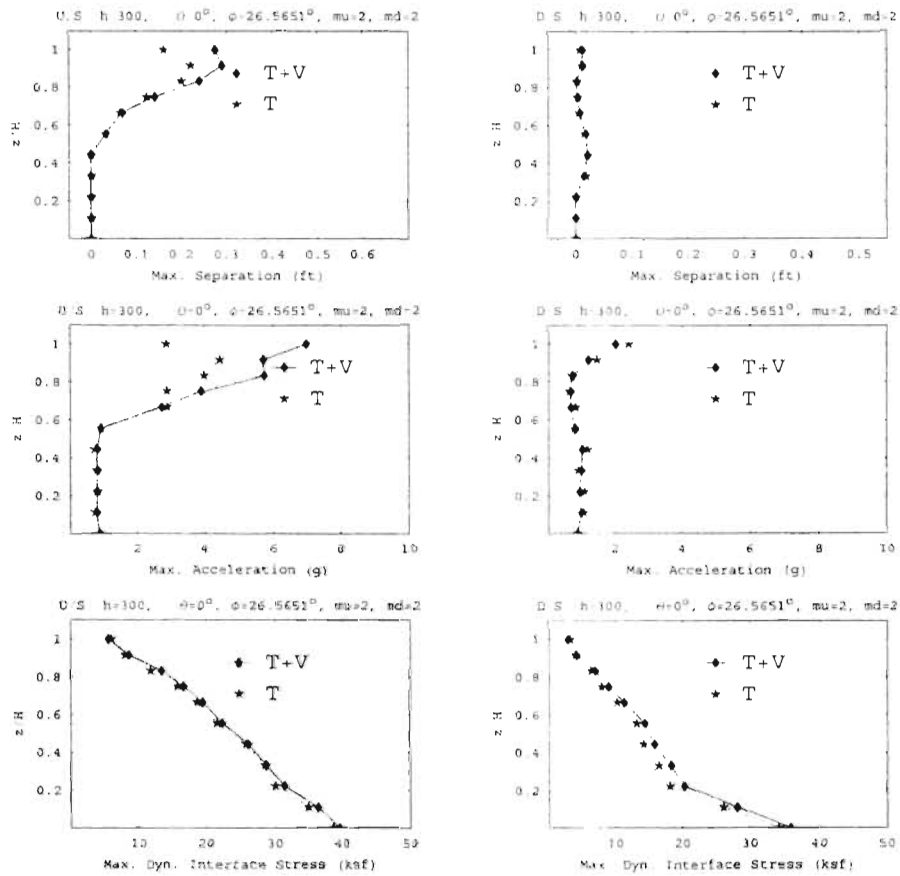

Figure 6.57 Maximum separation, acceleration, and interface stress distribution for both upstream and downstream interfaces under ground shaking with vertical and transverse components (H=300).

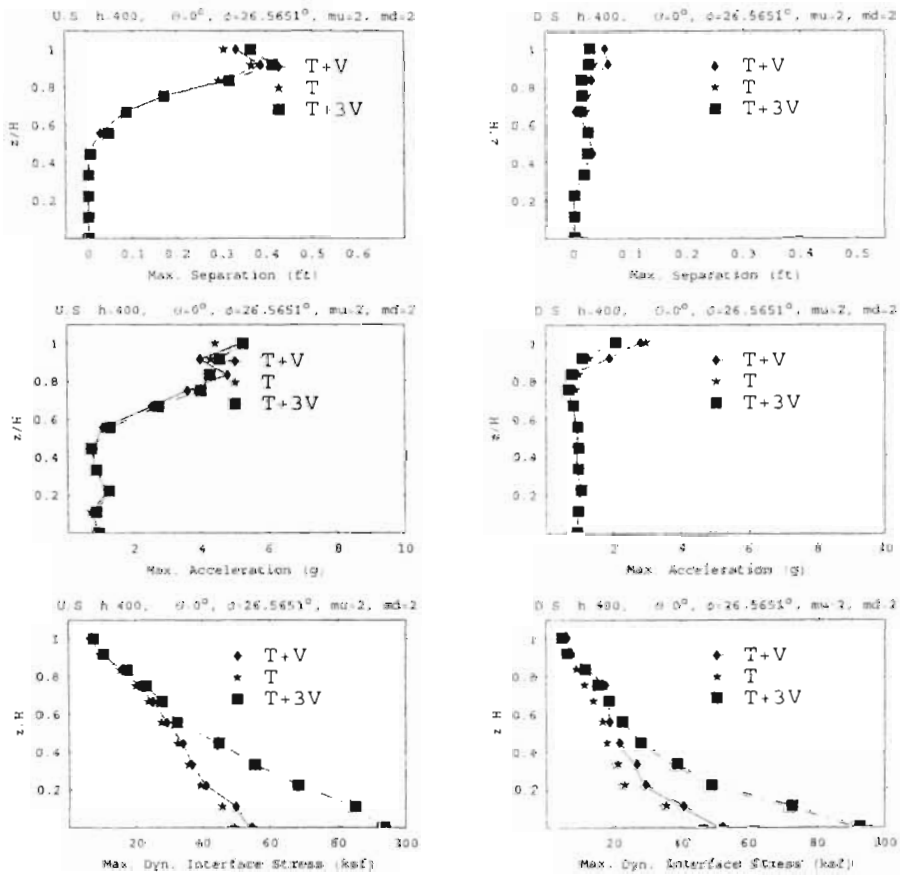

Figure 6.58 Maximum separation, acceleration, and interface stress distribution for both upstream and downstream interfaces under ground shaking with vertical and transverse components (H=400).

6.5 Interpretation of 2-D FE Results

In this section the interpretations of 2-D FE results are presented. Detailed statistical assessment is made in Chapter 9.

Prior to further interpretations typical shapes of maximum separation, maximum acceleration and interface pressure profiles are presented in Figures 6.59, 6.60, and 6.61, respectively. These typical shapes are referenced during the interpretations.

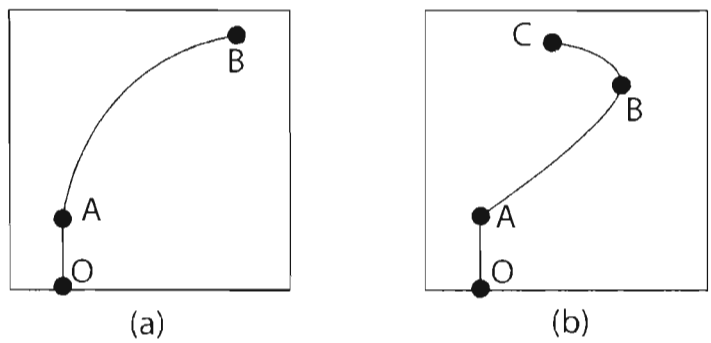

Figure 6.59 Representation of typical maximum separation response of U/S and D/S interfaces.

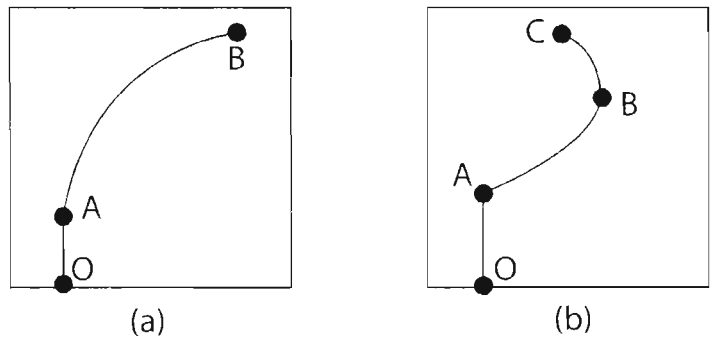

Figure 6.60 Representation of typical maximum acceleration response of U/S and D/S interfaces.

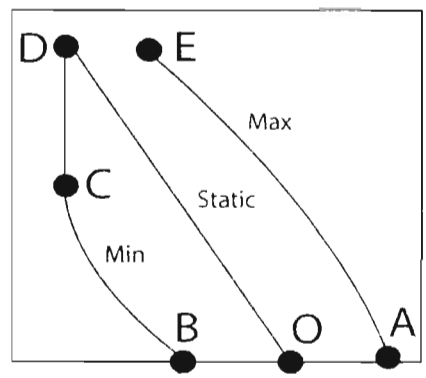

(a)

Upstream Interface Pressure Response

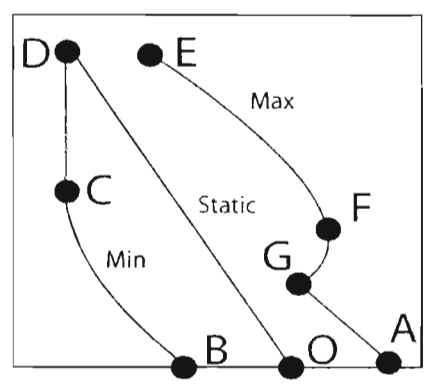

(b)

Downstream Interface Pressure Response

Figure 6.61 Representation of typical interface pressure response of U/S and D/S interfaces.

6.5.1 Maximum Separation

In Figure 6.59 two typical maximum separation response curves are illustrated for each U/S and D/S interface. The magnitudes of response at the dotted points may vary depending on the problem. Downstream interface exhibits more wavy response than upstream interface. This can be explained by the existence of hydrostatic pressure on the upstream slope which has restricting effect on the displacements. Therefore downstream interface has more freedom to move.

H=100 ft

U/S maximum separation reached to 0.157 ft in some cases. Separation depth is as high as 80% of the dam height. The shape of maximum separation profile is similar to part (a) of Figure 6.59, and maximum value occurred at the crest. Change in θ caused decrease in maximum separation. Other parameters had insignificant effect on maximum separation.

D/S maximum separation profile is best described by part (c) of Figure 6.59. Maximum is around 0.06 ft. Separation depth reached almost the full dam height.

H=200 ft

U/S maximum separation reached to 0.16 ft in some cases. The general shape of the profile follows part (b) of Figure 6.59. Change in θ caused decrease in maximum separation. Separation depth is 50% of the dam height.

D/S maximum separation is around 0.04 ft which is much smaller than that of 100 ft high dam. The shape is similar to part (d) of Figure 6.59. Separation depth can be as high as 80%. Change in θ caused a slight increase in maximum separation.

H=300 ft

U/S maximum separation reached to 0.24 ft. Typical shape is similar to part (b) of Figure 6.59. Change in θ caused decrease in maximum separation. Other parameters had insignificant effect on maximum separation. Separation depth may reach to 50%.

D/S maximum separation profile follows the shape part (d) of Figure 6.59 with a very low magnitude of 0.03 ft. None of the parameters had significant effect on D/S maximum separation.

H=400 ft

U/S maximum separation is around 0.36 ft and profile shape is similar to part (b) in Figure 6.59. Maximum value occurred at point B. Change in θ caused decrease in maximum separation and separation depth. Maximum separation depth may reach to 50%. Parameter ϕ had also some decreasing effect on maximum separation.

D/S maximum separation is 0.08 ft. It follows the shape of part (d) of Figure 6.59. Geometric parameters did not have significant effect on separation performance. Separation depth may reach to 80%.

6.5.2 Maximum Acceleration and RMS Acceleration Ratios

Figure 6.60 has also two typical curves of maximum acceleration response for each interface.

H=100 ft

U/S maximum acceleration ratio may be as high as 11 in some cases. The general shape of the profile is similar to part (a) of Figure 6.60, but exhibits quite scatter and zig zag distribution from A to B. There is no significant magnification in region from O to A. In that region no separation was observed. Severe magnifications occurred where there was separation. Parameter θ has some effect on maximum acceleration. On the other hand RMS acceleration ratio profiles show much smoother and more consistent behavior. Maximum RMS acceleration ratio is around 4.

D/S maximum acceleration ratio profile follows the shape of part (d) or (c) in Figure 6.60. It also has scatter and zig zag distribution. Maximum value may be as high as 11. Since separation depth may reach to 100%, acceleration magnification starts from the bottom of the dam. RMS acceleration ratio profiles show smoother and more consistent behavior.

H=200 ft

U/S maximum acceleration ratio value may reach to 10 in some cases. The shape is similar to part (b) of Figure 6.60. Parameters θ and ϕ caused decrease in maximum

acceleration ratio. RMS acceleration ratio profile is again more consistent with a maximum of 3.

D/S maximum acceleration ratio may reach to 4 in some cases. Parameters θ and ϕ caused increase in maximum acceleration ratio. Maximum RMS acceleration ratio is 2.5.

H=300 ft

U/S maximum acceleration ratio reached to 7 in some cases. Parameters θ, ϕ, amd mu had decreasing effect on maximum acceleration ratio. Maximum RMS acceleration ratio is around 2.8.

D/S maximum acceleration ratio is much smaller than that of U/S. The maximum is around 3. Maximum RMS acceleration ratio

H=400 ft

U/S maximum acceleration ratio may reach to as high as 8.5. maximum RMS acceleration ratio is around 4. Parameters θ, μ had decreasing effect on maximum acceleration ratio.

D/S maximum acceleration ratio is again much smaller than that of U/S. The maximum value may reach to 4. Maximum RMS acceleration ratio showed very similar magnification pattern with maximum acceleration ratio profile.

To further investigate the effect of separation on acceleration magnification, 4 more FE runs were performed with all soil cross-section using the `reference configuration` of

each height. Maximum acceleration ratio and RMS acceleration ratio profiles are compared to cases with soil-concrete interface. Figure 6.62 shows the maximum acceleration ratio comparison. In Figure 6.62, first column of plots, parts (a), (c), (e), and (g), represent the U/S maximum acceleration ratio comparison for heights from 100 ft. at the top, to 400 ft, at the bottom. Second column, parts (b), (d), (f), and (h), represent the D/S maximum acceleration comparison. It clearly seen that in parts (d), (f), and (h) of Figure 6.62, which correspond to D/S of 200, 300, and 400 ft high dams, the gap between two curves is not as big as in other parts. It was shown earlier that D/S separation was not significant in 200, 300, and 400 ft cases. Figure 6.63 show the RMS acceleration ratio comparison with the same arrangement with Figure 6.62. Again D/S of 200, 300, 400 ft high dams (parts (d), (f), and (h) of Figure 6.63), show less difference in maximum RMS acceleration profiles.

6.5.3 Interface Pressure

Finally Figure 6.61 shows a typical interface pressure response for each interface. Upstream interface pressure distributions follow almost a linear path whereas maximum interface pressure curve of downstream interface may show severe nonlinearity in the region from G to E. In general, interface pressure increase due to seismic loading is greater at the bottom and less towards the top.

H=100 ft

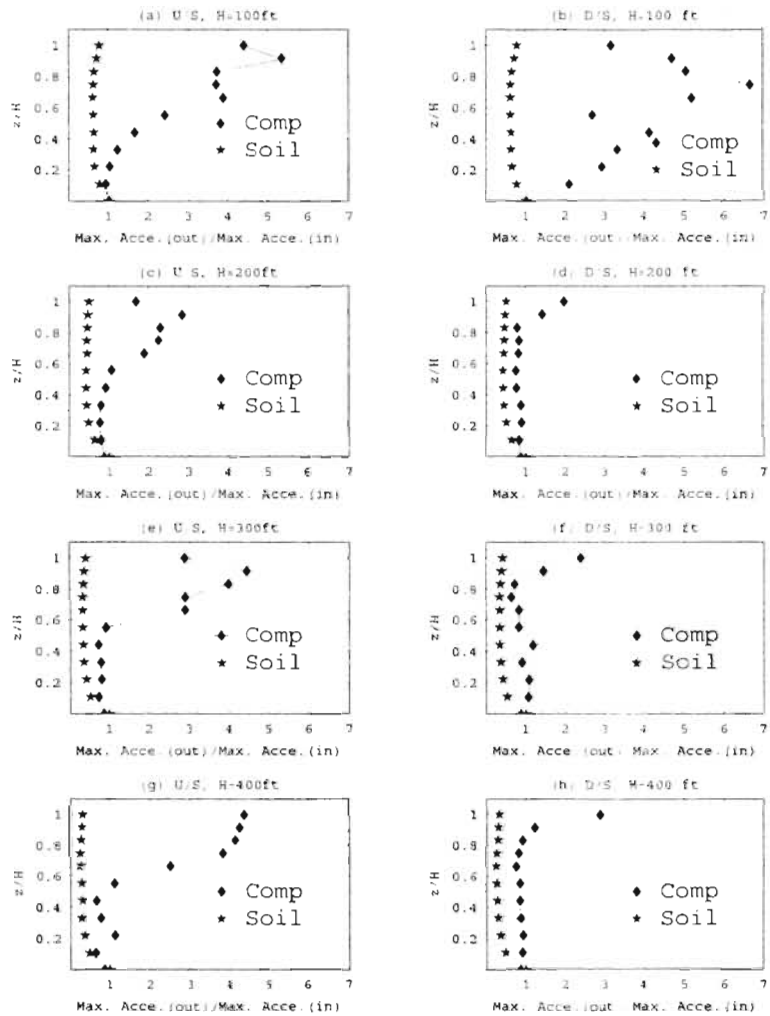

Figure 6.62 Comparison of maximum acceleration ratio with pure soil embankment and composite section.

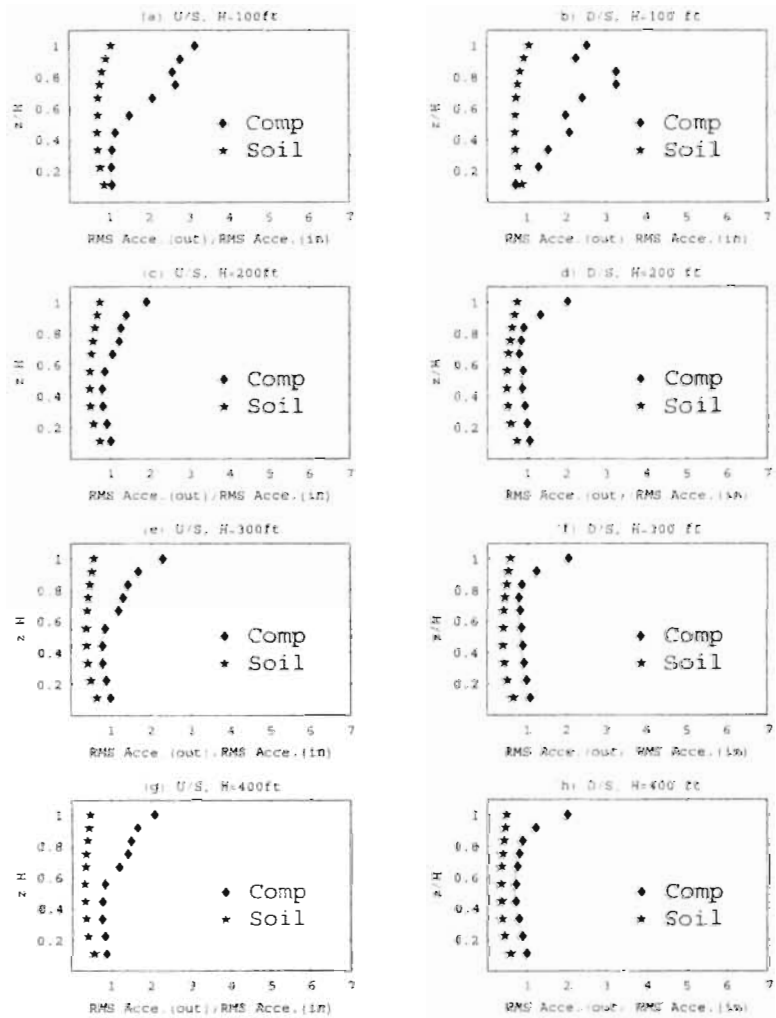

Figure 6.63 Comparison of RMS acceleration ratio with pure soil embankment and composite section.

U/S interface pressure profile was not affected by the geometric parameters. However parameter θ slightly affected maximum interface pressure distribution. Maximum interface pressure at the bottom may reach to 1.7 times the static pressure.

D/S pressure profile has the typical shape of part (b) of Figure 6.61. Maximum interface pressure may also be 1.7 times the static pressure.

H=200 ft

U/S interface pressure profile was not affected by the geometric parameters. Maximum interface pressure is 1.4 times the static pressure.

D/S interface pressure profile was not affected either. Maximum interface pressure is 1.8 times the static pressure.

H=300 ft

In general both U/S and D/S interface pressure profiles were not affected, but *mu*, and *md* caused little changes in U/S, and D/S maximum interface pressure profiles, respectively. Maximum interface pressure is 1.5 and 1.6 times the static interface pressure in U/S and D/S interfaces, respectively.

H=400 ft

Same conditions apply as in H=300 ft case.

6.6 Summary and Conclusions

In this chapter natural vibration characteristics of 2-D composite dams are presented. FE element analysis procedure and data processing are explained. FE results are demonstrated through the series of graphs that relate geometric parameters to performance parameters such as; maximum separation, maximum acceleration ratio, maximum RMS acceleration ratio, and minimum, static, and maximum interface pressures.

Following conclusions can be drawn from 2-D FE parametric study:

- Soil may experience large acceleration magnification upon rebonding.
- Acceleration amplification is dependent on the magnitude of separation; less separation less acceleration amplification.
- Concrete displacements are very small compared to soil displacements along the soil-concrete interface.
- Acceleration magnification along the interface is generally higher in soil than concrete.
- Separation is repetitive.
- Acceleration response of concrete has higher frequency content than soil.
- For all cases presented in this study, maximum dynamic interface pressure at the bottom of the dam is in the range of 1.3-1.8 times the static pressure.

- Dynamic maximum and minimum interface pressures are not affected significantly by geometric controlling parameters used in the analyses.
- The crest of the dam is not necessarily the location of maximum response.
- Height has an important influence on IBCD.
- As height increases the overall effects of geometric parameters decreases.
- If there is no or very small separation maximum accelcration ratio and max RMS acceleration ratio show similar amplification pattern, as shown in Figures 6.44, 6.47, A.63, and A.66.
- As height increases maximum acceleration ratio decreases along both U/S and D/S interfaces.
- Minimum interface pressure and separation profiles are in good agreement.
- Increase in D/S maximum interface pressure is always greater than that of U/S.
- Vertical component of ground motion has little or no effect on IBCD.

7. Elastic Three-Dimensional Finite Element Analysis

7.1 Introduction

The soil-concrete interface area of a composite dam is in fact a three dimensional geometry that deserves attention. Since 3-D FE analyses is quite time consuming and the output is voluminous it has not been possible to perform FE runs as many as 2-D runs.

The geometry of 3-D model, and analysis parameters including material model parameters are discussed in detail in Chapter 5. All 3-D FE analyses were performed on CRAY90 super computer, at San Diego Super Computer Center (SDCS) at the University of California at San Diego. An attempt was made to perform one 3-D analysis on a SGI R4400 computer at the University of Colorado at Denver. Due to the size of the problem it took 7 days to complete only one analysis. Therefore it was strongly necessary to perform the analyses on a faster computer. Each FE run produced 2.5 gigabytes of data.

The behavior of 3-D model has been studied under Koyna Dam Earthquake Record with linear elastic model. The effects of nonlinear soil model and all three components of ground motion were also studied. Maximum separation and acceleration results are

compared with 2-D analysis results. Surface contours of maximum separation at U/S, D/S, and transverse interfaces are presented. All findings are interpreted and compared to 2-D analysis findings where possible.

3-D FE analyses are limited to;

- 4 runs with linear elastic soil model and horizontal ground motion, i.e one run for each height; 100, 200, 300, and 400 ft.
- 1 run with Ramberg-Osgood model and horizontal ground motion for 400 ft high dam.
- 1 run with linear elastic model and all components of ground motion for 400 ft high dam.
- 1 run with Ramberg-Osgood model and all components of ground motion for 400 ft high dam.

In the next sections natural vibration characteristics and FE analyses results of 3-D model are given and results are interpreted.

7.2 Natural Vibration Characteristics

NIKE3D eigenvalue analyses were performed to obtain natural frequency and mode shapes of 3-D composite dam. Table 7.1 lists first natural frequencies of 3-D model and corresponding 2-D model of the composite dams. Natural frequencies of 3-D model are smaller than that of 2-D model. Although it is not possible to make exact comparison

but Mejia [52] reported that when length over height ratio is greater than 6 for an earth dam, the difference in natural frequencies of 2-D and 3-D models may be significant. In the current 3-D composite dam model the lengths of embankment dam and concrete monolith are 7H, and 3H, respectively. Moreover first mode shape of 300 ft high dam is presented in Figure 7.1.

Table 7.1 Natural Frequencies (in Hz) of Dam Models

Height (ft)	3-D	2-D
100	3.564	3.81
200	2.059	2.30
300	1.494	1.68
400	1.167	1.31

7.3 3-D Finite Element Analysis Results

First, one FE analysis for each dam height was performed using linear elastic soil model and 10% Rayleigh damping. Maximum separation and acceleration of both U/S and D/S interfaces were gathered at the maximum cross-section for all heights. This is done for comparison purposes with 2-D model. Figure 7.2, and 7.3 show U/S, and D/S maximum separation and normalized maximum separation, respectively. As shown in Figures 7.2, and 7.3 maximum separation increases with height in both U/S and D/S interfaces. It should also be noted that separation depth reaches the full dam height for all cases presented in Figures 7.2, and 7.3.

Figure 7.4 shows the maximum acceleration ratio (maximum acce. (out)/maximum acce. (in)) of both U/S and D/S interfaces. Maximum acceleration ratio reaches to maximum of 2.5 among all heights. The maximum response takes place at the crest of

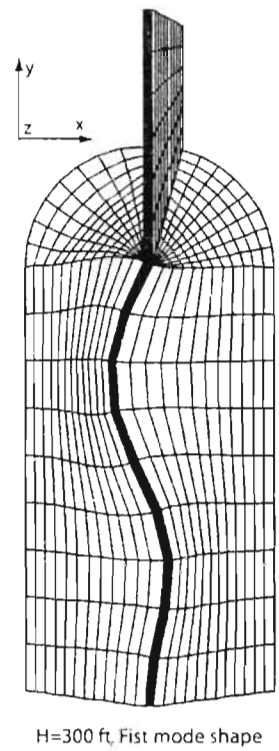

Figure 7.1 First mode shape of 300 ft high composite dam.

300 ft high dam. Figure 7.4 also show the magnification of ground motion during upward propagation.

The maximums of all maximum separation and acceleration response profiles at the maximum cross-section are summarized in Table 7.2, and compared with 2-D model responses. As listed in Table 7.2 maximum accelerations are always lower in 3-D models for the same type of soil model. On the other hand maximum separations of 3-D models are higher than that of 2-D models for higher dams. When elastic soil model is used in 100 and 200 ft high dams maximum separations are higher in 2-D models. When R-O soil model is used in 400 ft high dam the U/S maximum separation is less than 2-D model response and D/S maximum separation is greater than 2-D model response.

Table 7.2 Comparison of 3-D and 2-D results.

H (ft)	UPSTREAM								DOWNSTREAM							
	Max. Acceleration Ratio				Max. Separation (ft)				Max. Acceleration Ratio				Max. Separation (ft)			
	3-D		2-D		3-D		2-D		3-D		2-D		3-D		2-D	
	EL	R-O	EL	R-O	EL	R-O	EL	R-O	EL	R-O	EL	R-O	EL	R-O	EL	R-O
100	1.90	-	18	5.5	0.05	-	0.20	0.15	1.89	-	17	7.0	0.04	-	0.18	0.05
200	2.15	-	9.8	3.5	0.14	-	0.16	0.16	1.99	-	6.8	2.5	0.10	-	0.11	0.01
300	2.40	-	10	5.0	0.32	-	0.40	0.23	2.50	-	5.7	3.0	0.22	-	0.04	0.03
400	2.20	1.26	5.2	5.5	0.52	0.1	0.39	0.36	2.15	1.22	3.4	3.9	0.36	0.28	0.04	0.04

EL=Elastic, R-O=Ramberg-Osgood

Maximum separation surface and contour plots of each interface were also produced after each FE run. Table 7.3 lists the numbers of figures illustrating the maximum separation response of each interface. Both U/S and D/S interfaces showed significant separation whereas transverse interface showed little or no separation. The results are discussed in greater detail later in this chapter.

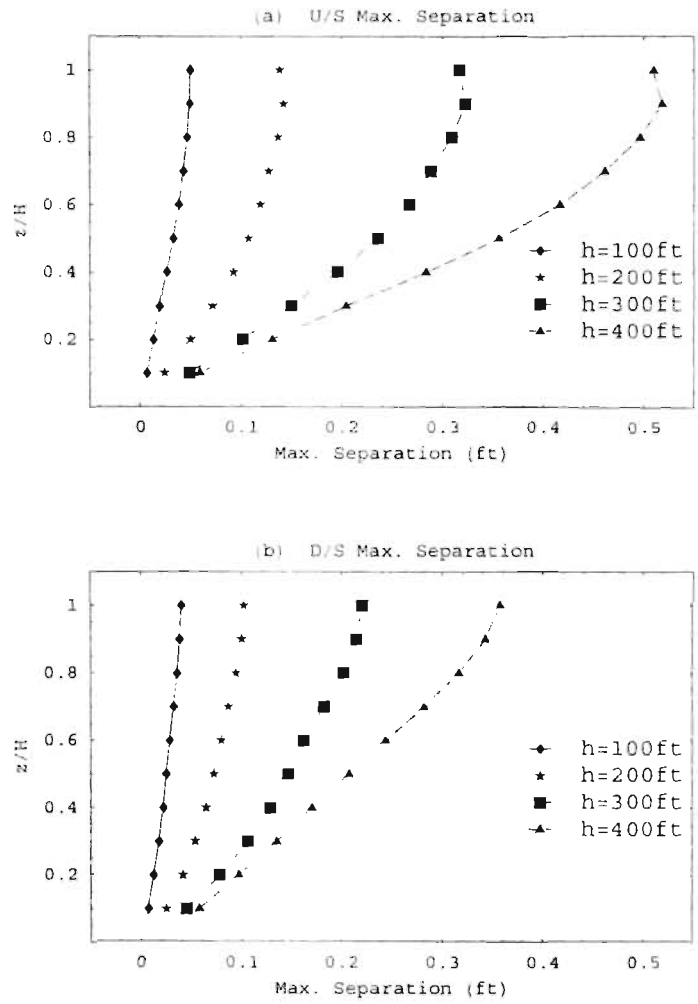

Figure 7.2 Max. Separation along (a) U/S and (b) D/S interfaces at maximum cross-section for all heights (in ft).

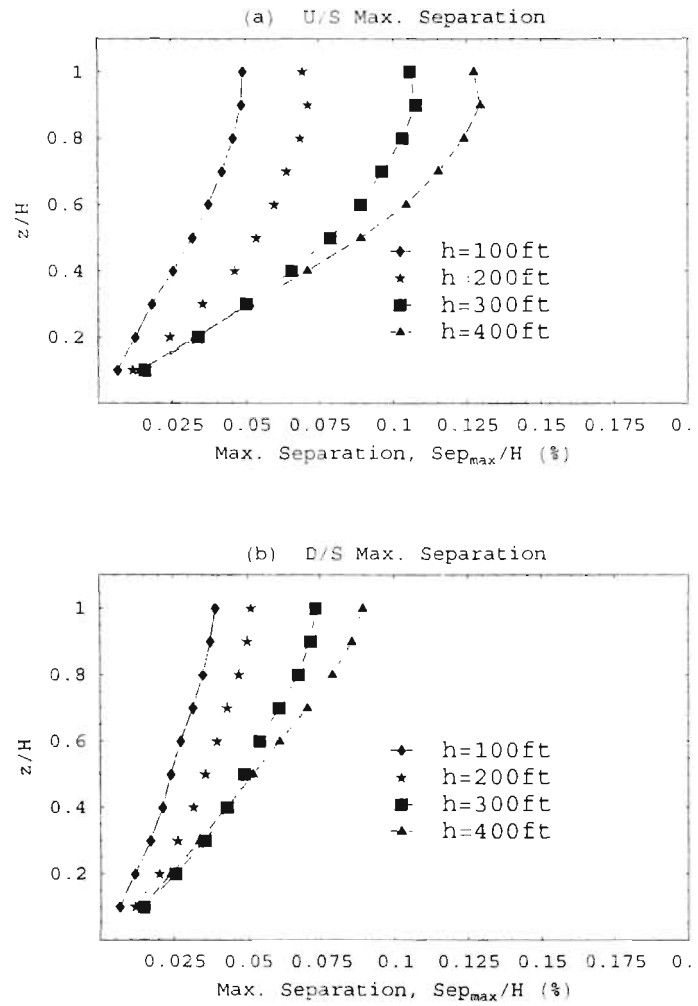

Figure 7.3 Normalized Max. Separation along (a) U/S and (b) D/S interfaces at maximum cross-section for all heights.

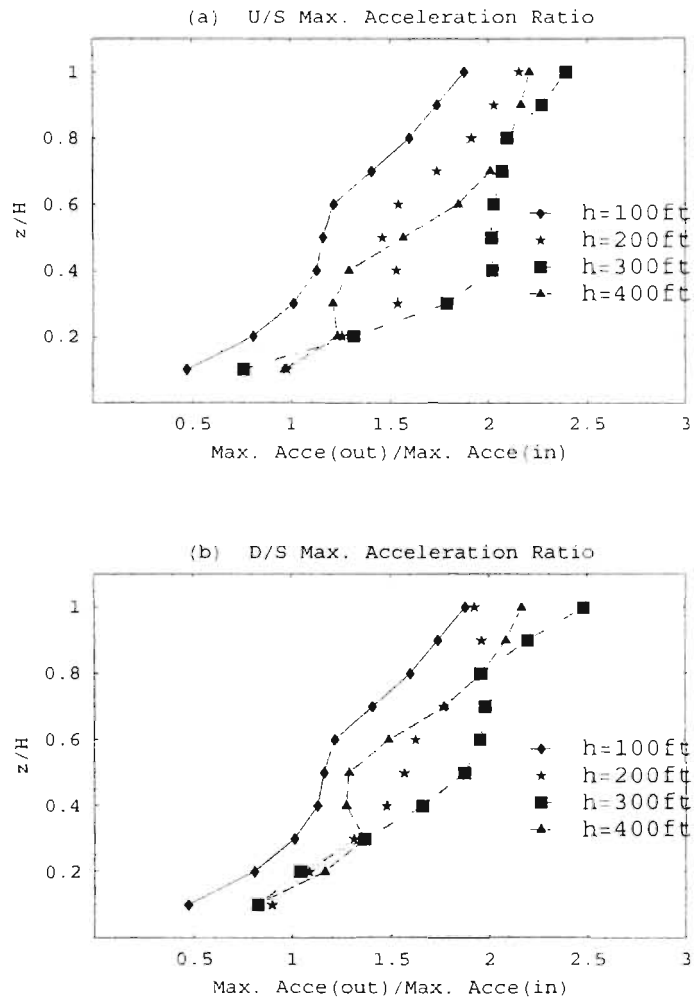

Figure 7.4 Max. Acceleration ratio along (a) U/S and (b) D/S interfaces at maximum cross-section for all heights.

Table 7.3 Numbers of figures illustrating 3-D response.

Height (ft)	Interface	Figure Numbers
100	u/s	7.5
	t	7.6
	d/s	7.7
200	u/s	7.8
	t	7.9
	d/s	7.10
300	u/s	7.11
	t	7.12
	d/s	7.13
400	u/s	7.14
	t	7.15
	d/s	7.16
u/s=upstream, t=transverse, d/s=downstream		

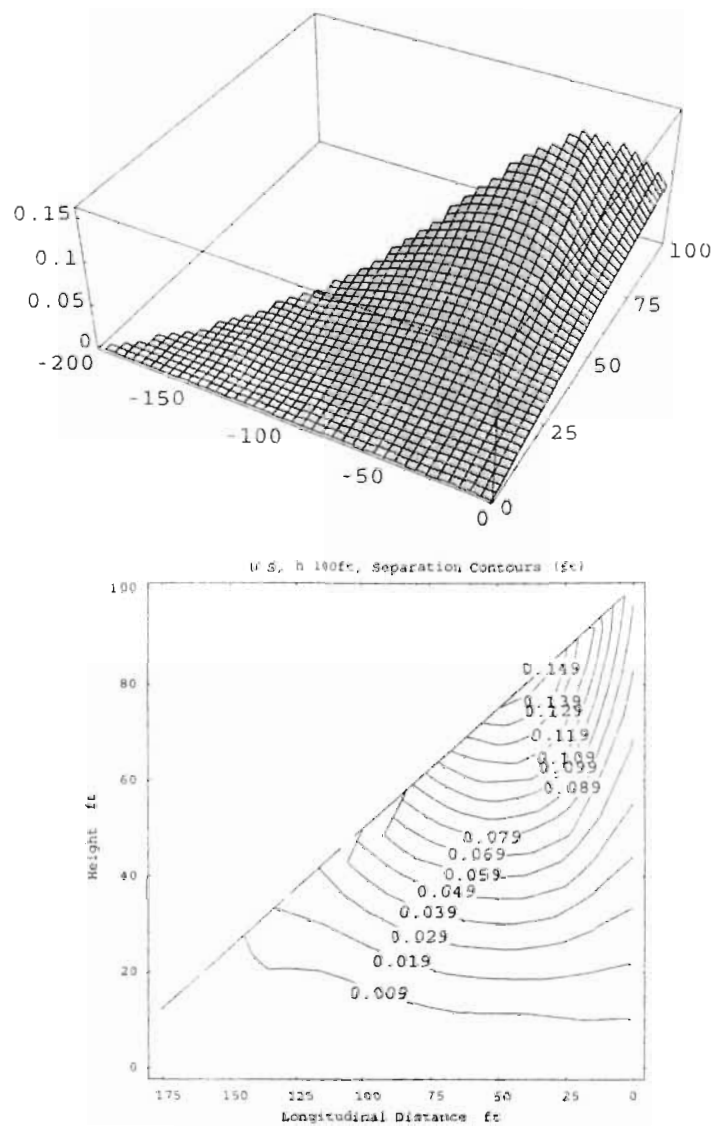

Figure 7.5 Surface and contour plots of maximum separation (in ft) for upstream soil-concrete interface area with elastic soil model (H=100ft).

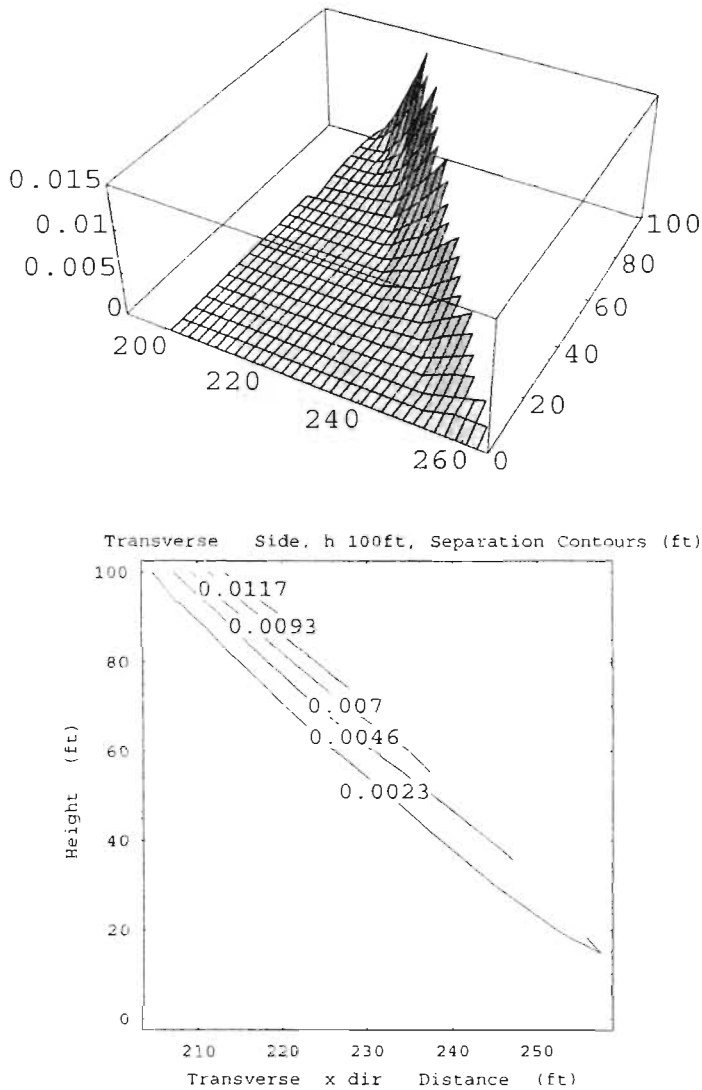

Figure 7.6 Surface and contour plots of maximum separation (in ft) for transverse soil-concrete interface area with elastic soil model (H=100ft).

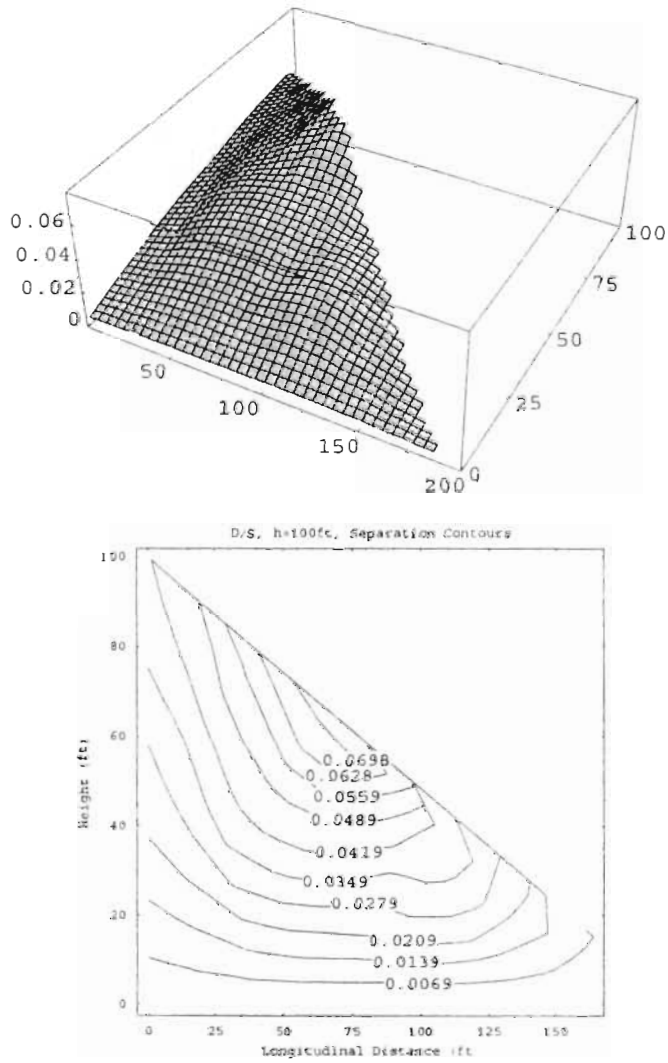

Figure 7.7 Surface and contour plots of maximum separation (in ft) for downstream soil-concrete interface area with elastic soil model (H=100ft).

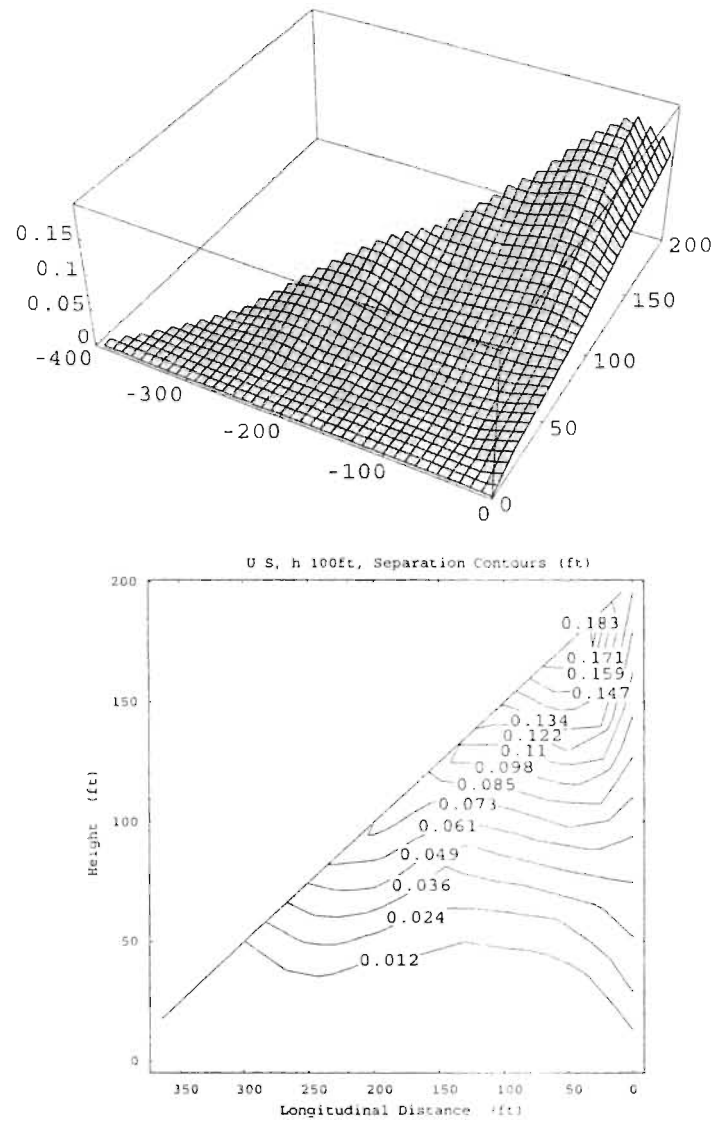

Figure 7.8 Surface and contour plots of maximum separation (in ft) for upstream soil-concrete interface area with elastic soil model (H=200ft).

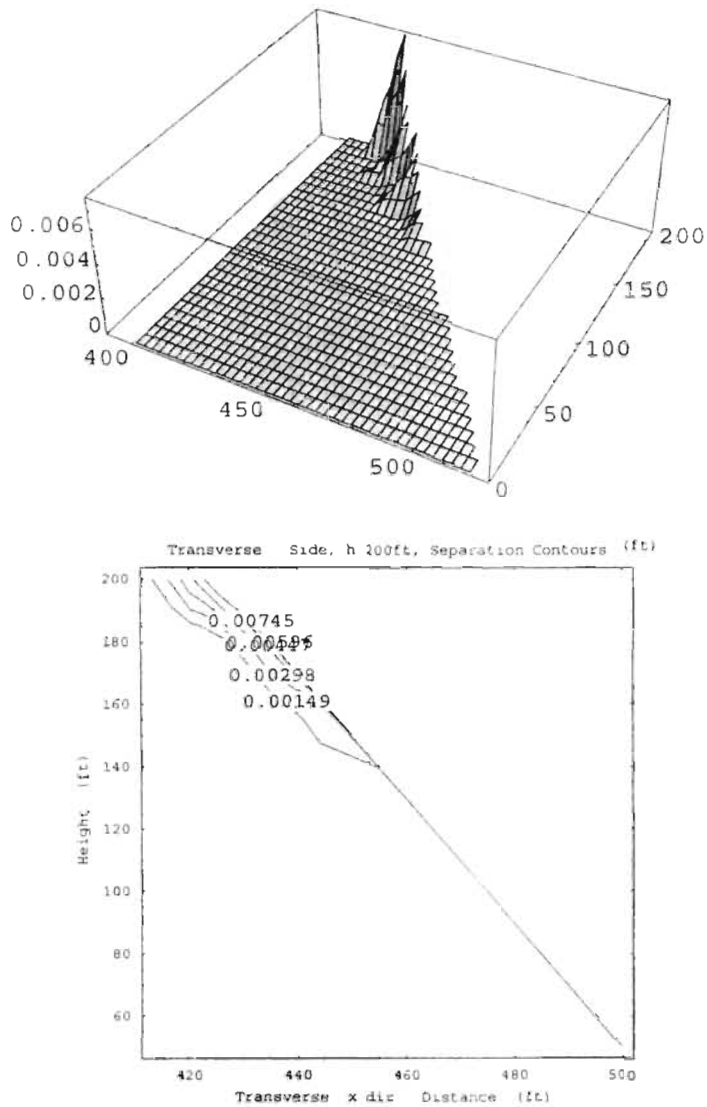

Figure 7.9 Surface and contour plots of maximum separation (in ft) for transverse soil-concrete interface area with elastic soil model (H=200ft).

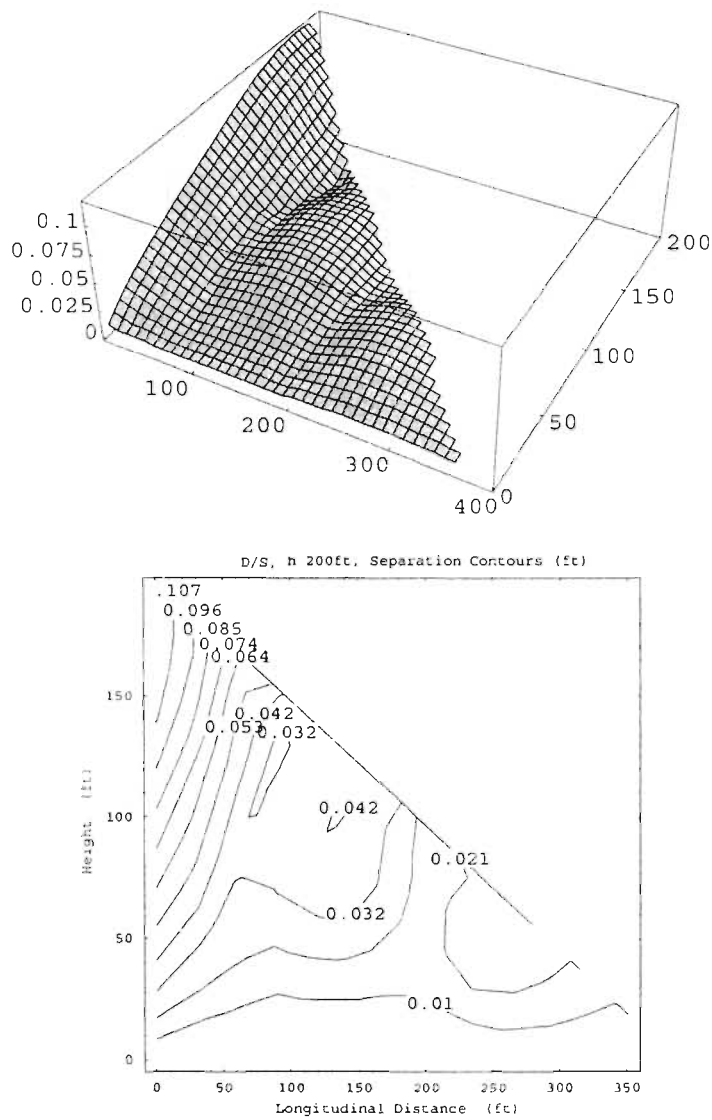

Figure 7.10 Surface and contour plots of maximum separation (in ft) for downstream soil-concrete interface area with elastic soil model (H=200ft).

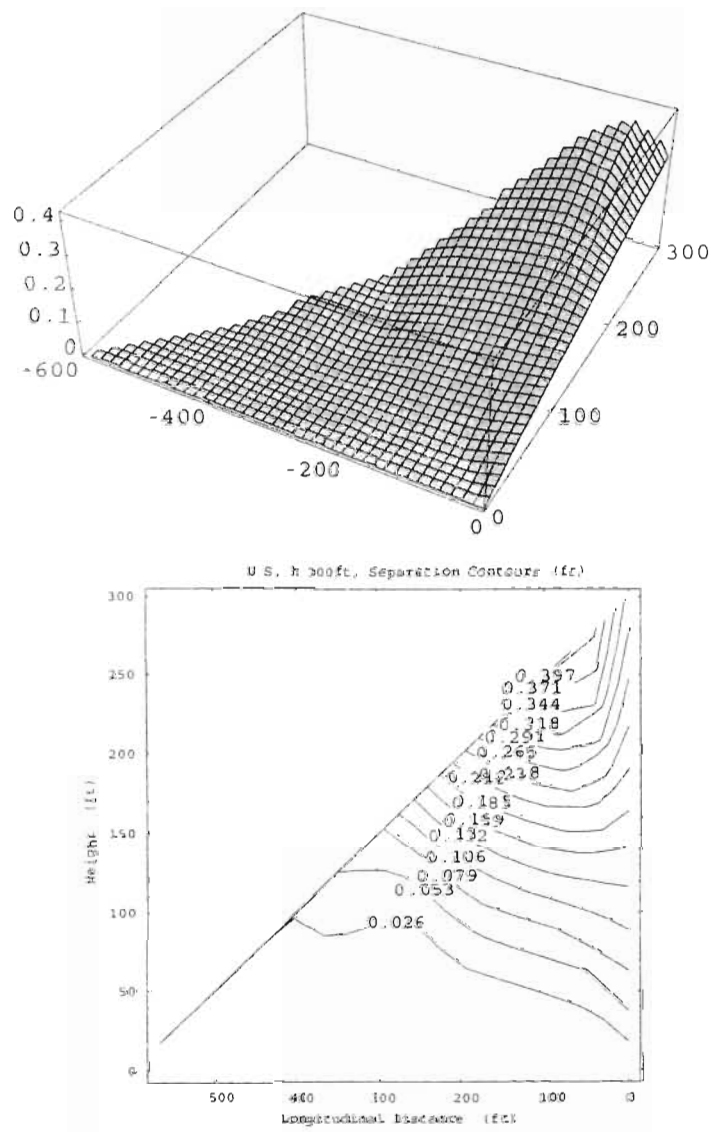

Figure 7.11 Surface and contour plots of maximum separation (in ft) for upstream soil-concrete interface area with elastic soil model (H=300ft).

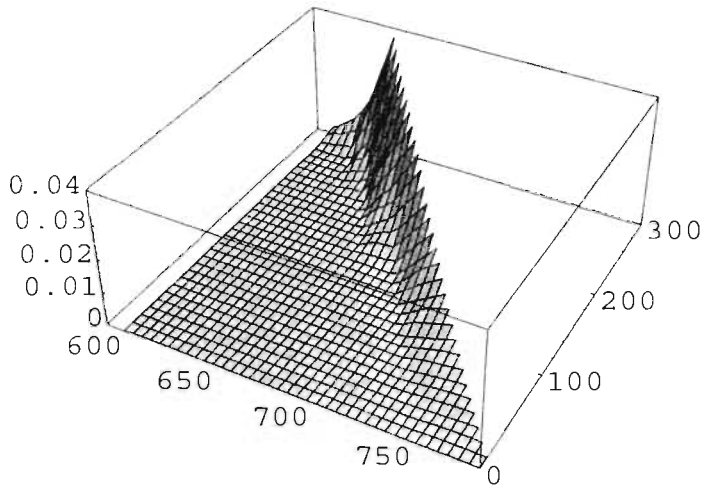

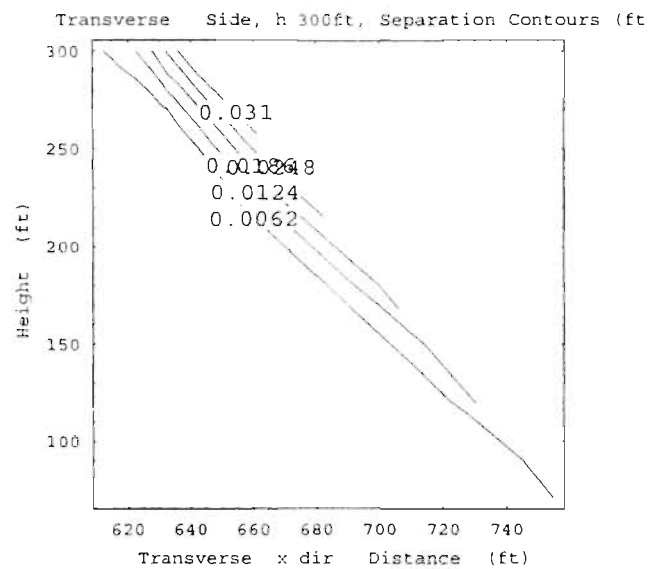

Figure 7.12 Surface and contour plots of maximum separation (in ft) for transverse soil-concrete interface area with elastic soil model (H=300ft).

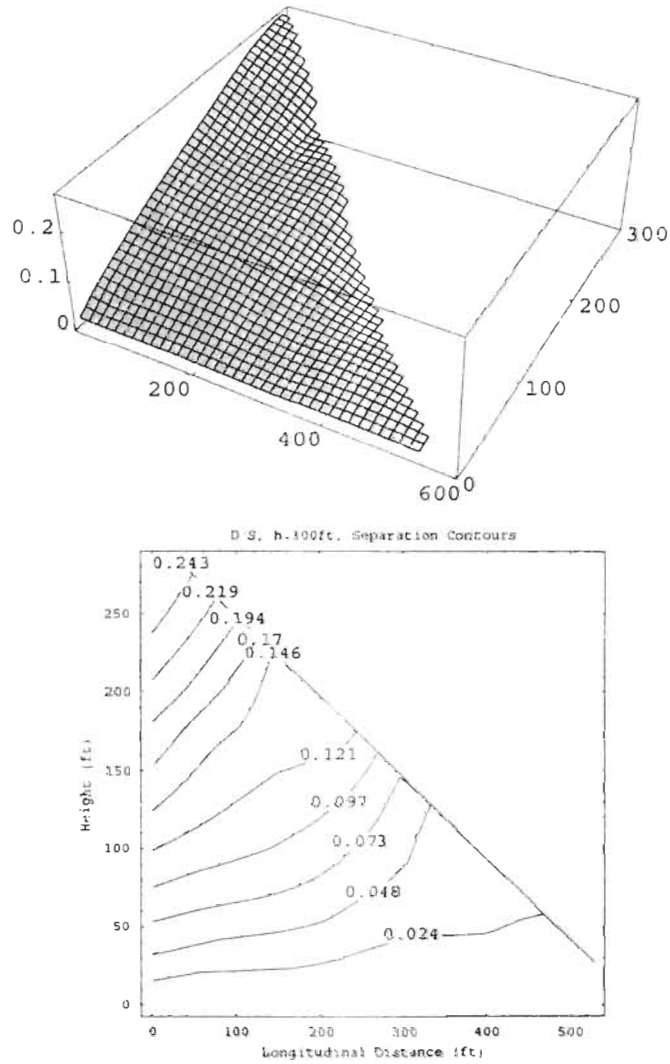

Figure 7.13 Surface and contour plots of maximum separation (in ft) for downstream soil-concrete interface area with elastic soil model (H=300ft).

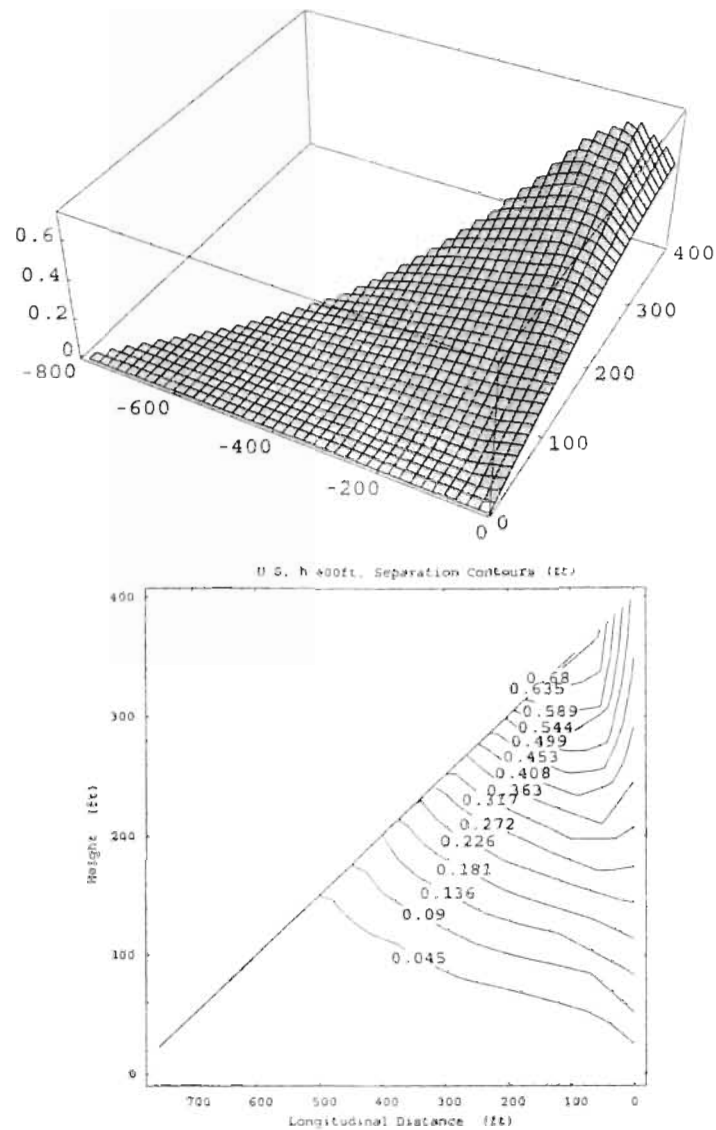

Figure 7.14 Surface and contour plots of maximum separation (in ft) for upstream soil-concrete interface area with elastic soil model (H=400ft).

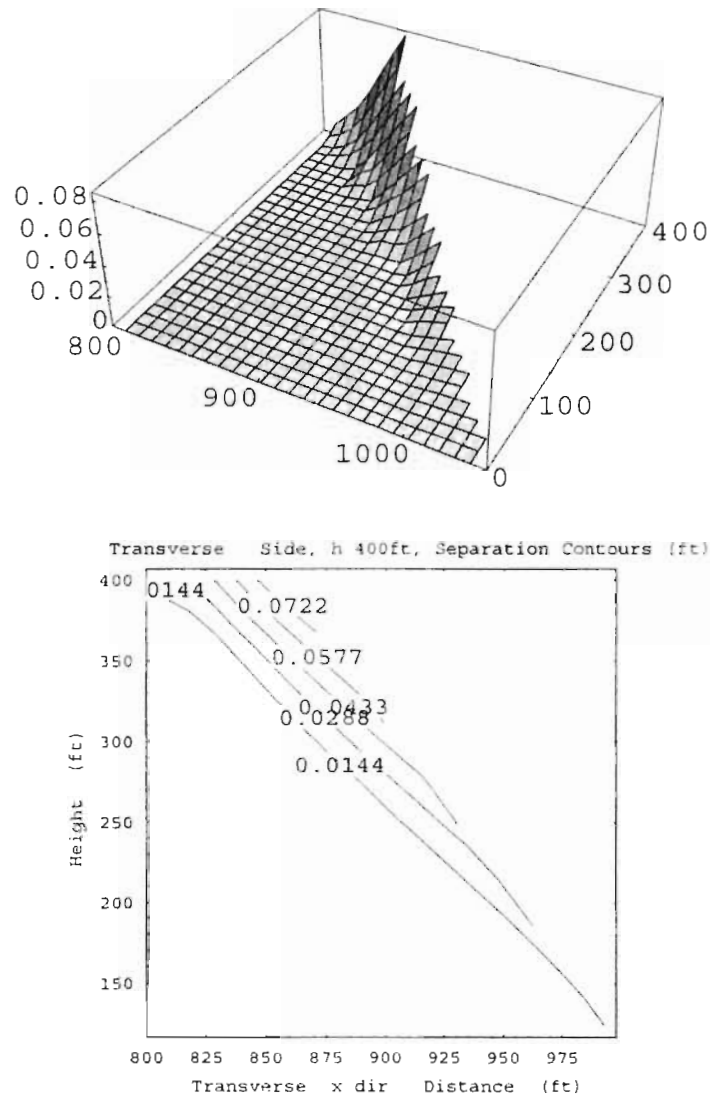

Figure 7.15 Surface and contour plots of maximum separation (in ft) for transverse soil-concrete interface area with elastic soil model (H=400ft).

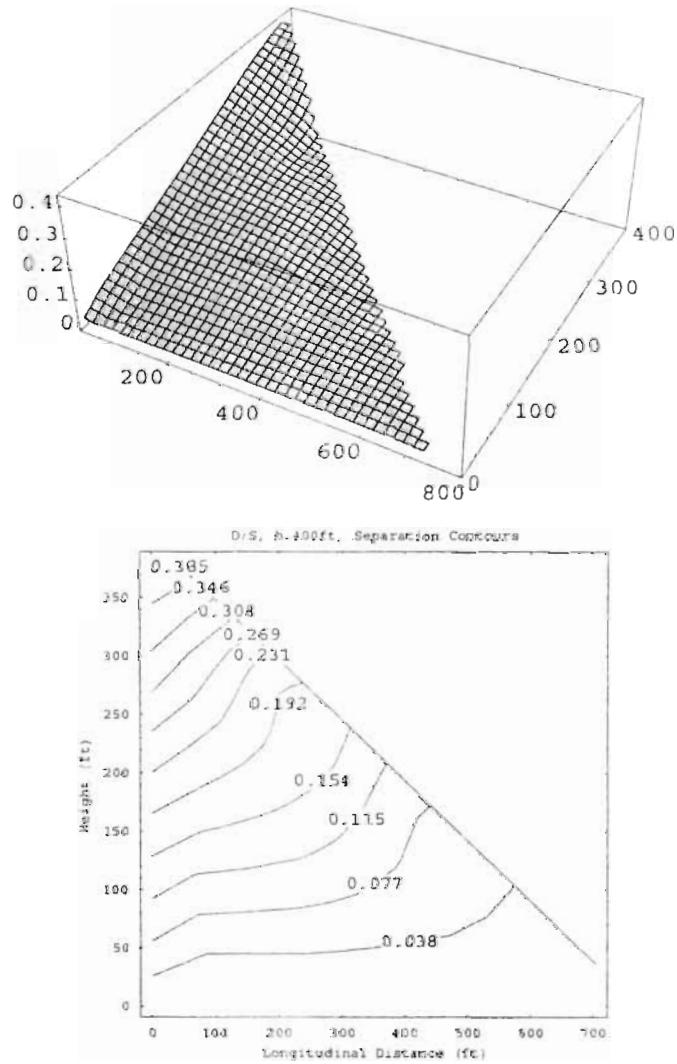

Figure 7.16 Surface and contour plots of maximum separation (in ft) for downstream soil-concrete interface area with elastic soil model (H=400ft).

7.4 Effect of Nonlinear Soil Model

To investigate the effect of nonlinear soil model on interface performance of composite dams, 400 ft high dam was analyzed with Ramberg-Osgood nonlinear soil model. The nonlinear soil parameters are earlier presented in Section 5.4.1.

Maximum separation surface and contour plots are presented in Figures 7.17, 7.18, and 7.19 for U/S, transverse, and D/S interfaces respectively. As shown in contour plots maximum separation and separation depth are decreased. Besides, the transverse interface exhibits no separation. This indicates the model dependent behavior of soil-concrete interface.

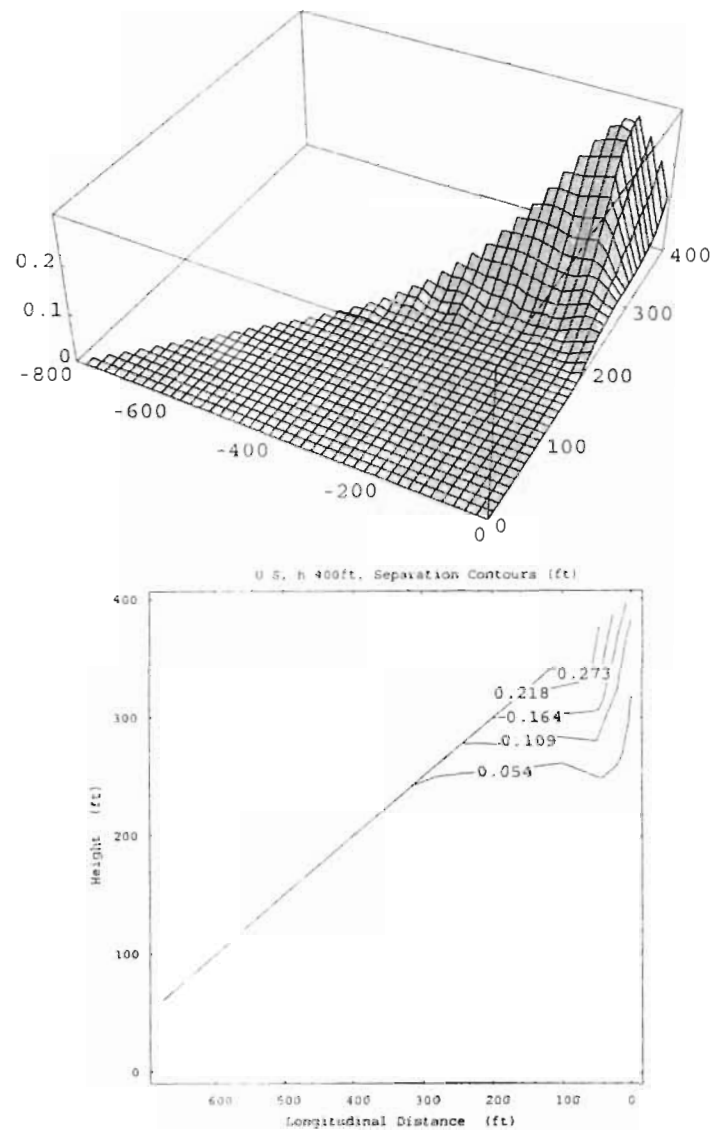

Figure 7.17 Surface and contour plots of maximum separation (in ft) for upstream soil-concrete interface area with R-O soil model (H=400ft).

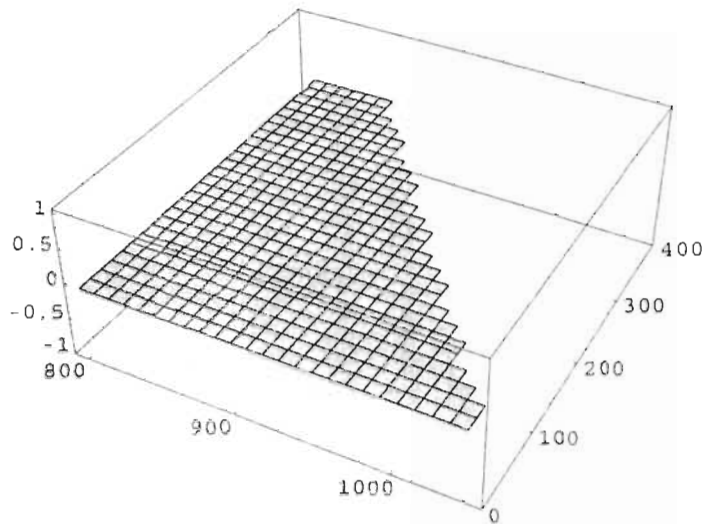

Figure 7.18 Surface and contour plots of maximum separation (in ft) for transverse soil-concrete interface area with R-O soil model (H=100ft).

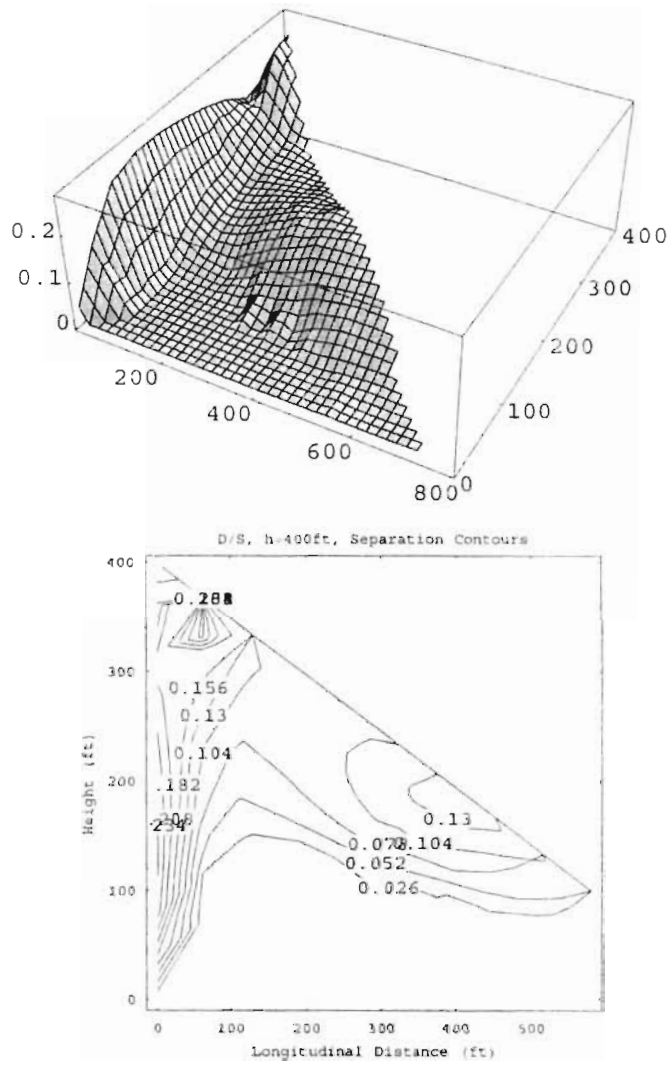

Figure 7.19 Surface and contour plots of maximum separation (in ft) for downstream soil-concrete interface area with R-O soil model (H=400ft).

7.5 Effect of Vertical and Longitudinal Components of Ground Motion

The effect of vertical and longitudinal components of ground motion on interface behavior were investigated. All three components of Koyna Dam Earthquake Record are shown in Figure 5.1.

The effect of additional components of ground motion on maximum separation and separation depth of soil-concrete interfaces were studied by using two different soil model; linear elastic and Ramberg-Osgood nonlinear models. In subsequent sections results are presented for each material model case.

7.5.1 Case I: Linear Elastic Soil Model

Linear elastic soil model parameters are listed earlier in Section 5.4.2. Maximum separation surface and contour plots are presented in Figures 7.20, 7.21, and 7.22 for U/S, transverse, and D/S interfaces respectively. The magnitude of maximum separation increased to 0.73 ft and 0.4 ft in U/S, and D/S interfaces respectively. Additionally transverse interface experienced some separation with a maximum of 0.15 ft.

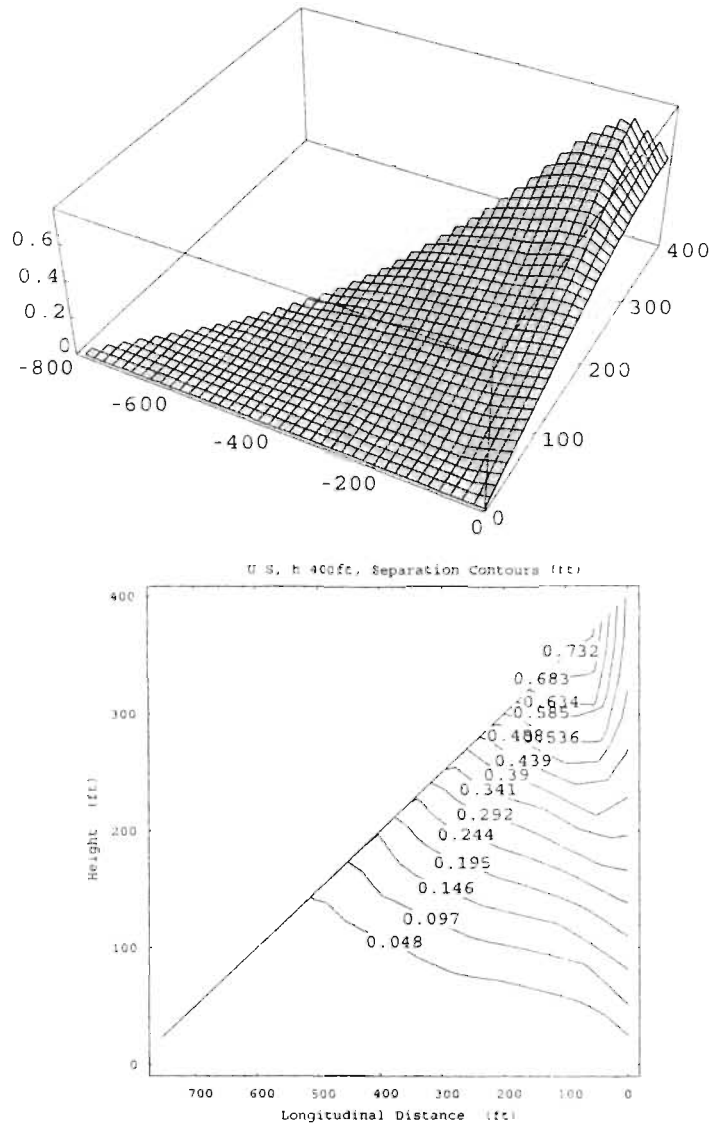

Figure 7.20 Surface and contour plots of maximum separation (in ft) for upstream soil-concrete interface area with elastic soil model and all three ground motion components (H=400ft).

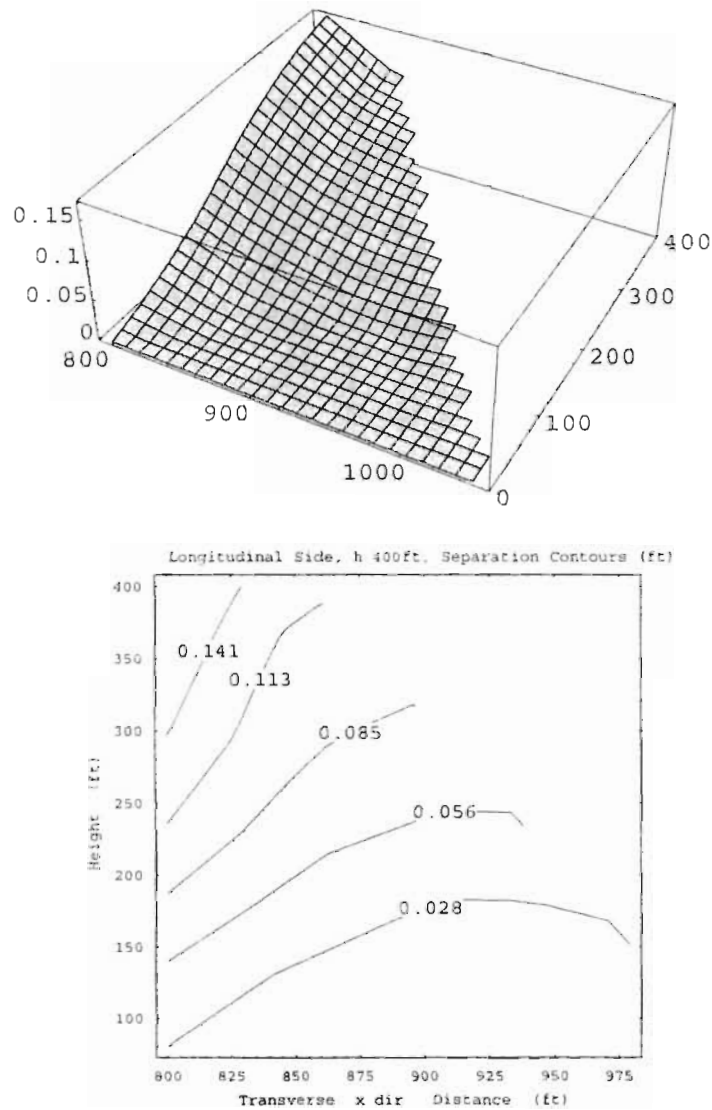

Figure 7.21 Surface and contour plots of maximum separation (in ft) for transverse soil-concrete interface area with elastic soil model and all three ground motion components (H=400ft).

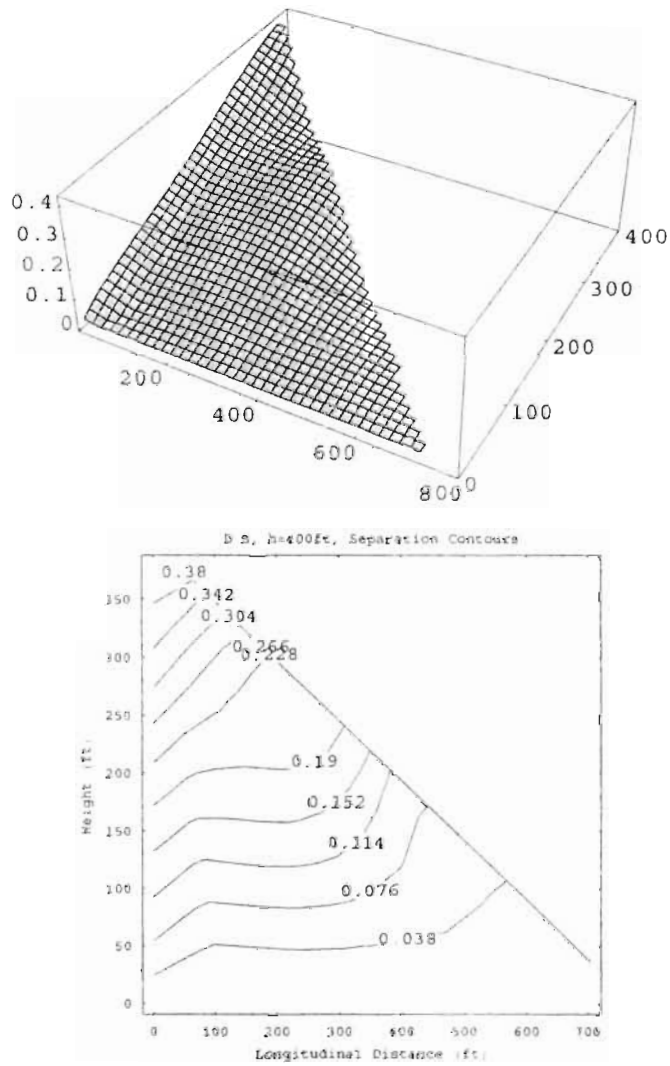

Figure 7.22 Surface and contour plots of maximum separation (in ft) for downstream soil-concrete interface area with elastic soil model and all three ground motion components (H=400ft).

7.5.2 Case II: Ramberg-Osgood Nonlinear Soil Model

Finally, the effect of all three components of ground motion on interface behavior was investigated using Ramberg-Osgood nonlinear model. Maximum separation surface and contour plots are shown in Figures 7.23, 7.24, and 7.25 for U/S, transverse, and D/S interfaces respectively. Compared to the response presented earlier with horizontal ground motion only case shown in Figures 7.17, 7.18, and 7.19, the effect of additional components of ground motion on the interface performance is insignificant.

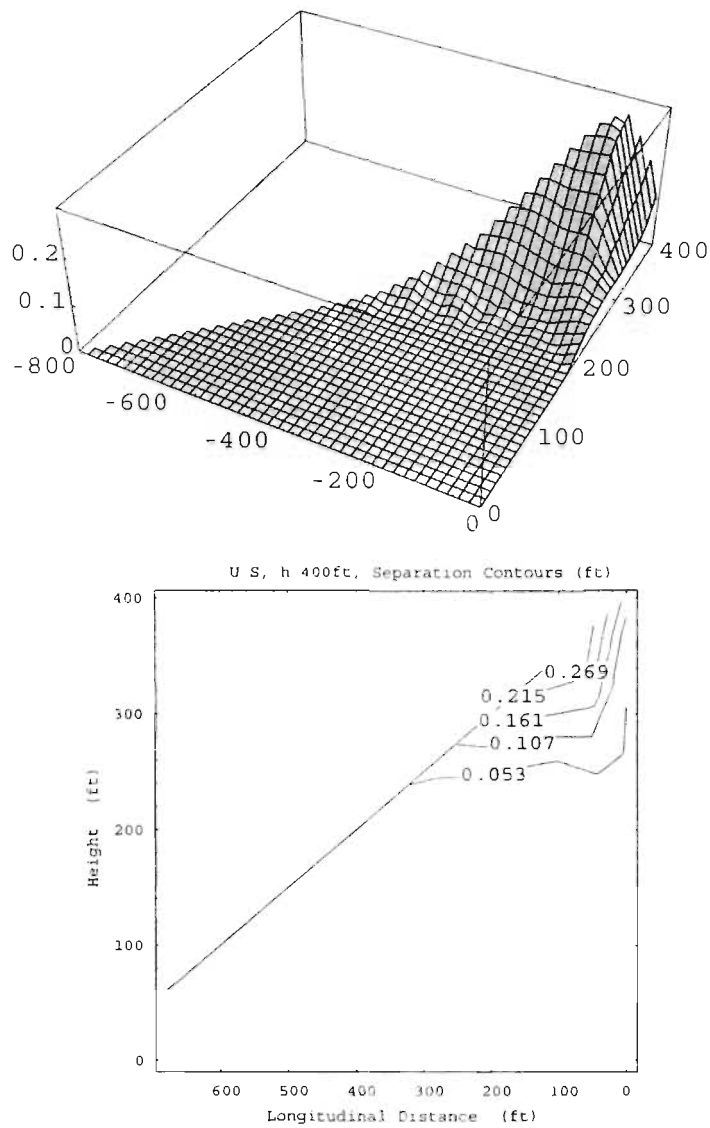

Figure 7.23 Surface and contour plots of maximum separation (in ft) for upstream soil-concrete interface area with R-O soil model and all three ground motion components (H=400ft).

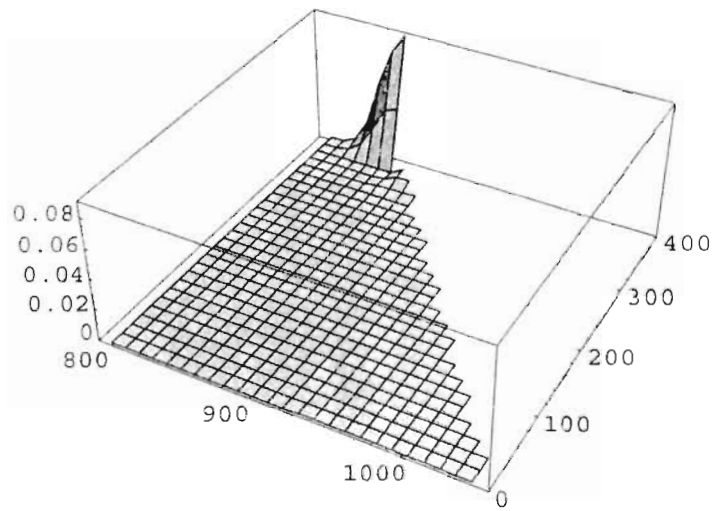

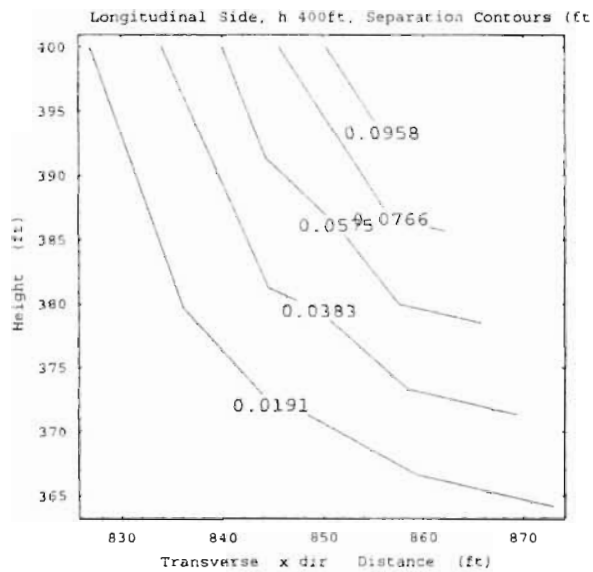

Figure 7.24 Surface and contour plots of maximum separation (in ft) for transverse soil-concrete interface area with R-O soil model and all three ground motion components (H=400ft).

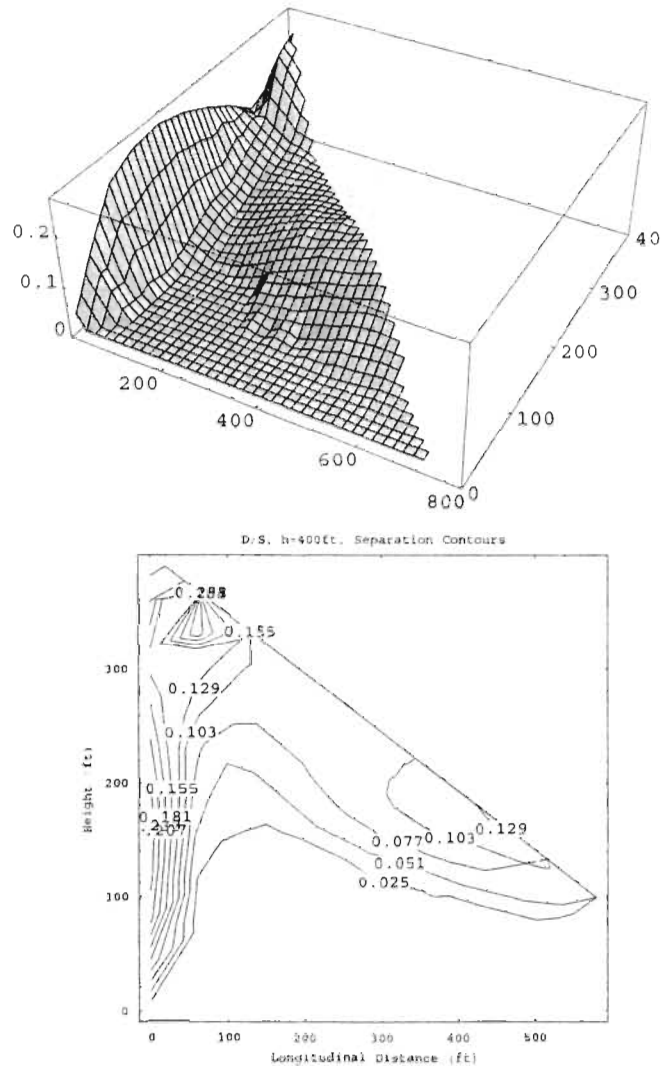

Figure 7.25 Surface and contour plots of maximum separation (in ft) for downstream soil-concrete interface area with R-O soil model and all three ground motion components (H=400ft).

7.6 Interpretation of Results

The interpretation of exploratory 3-D analyses are presented separately for each interface performance parameters; maximum acceleration, maximum separation, and separation depth.

7.6.1 Maximum Acceleration

Maximum acceleration profiles were obtained for U/S and D/S interfaces at the maximum cross-section only, i.e. at the intersection points of transverse interface with each U/S and D/S interfaces. They are shown in Figure 7.4. The maximum acceleration ratio is 2.5 which is substantially less than 2-D model response as compared in Table 7.2. Because of the much larger mass involved in 3-D analysis it is reasonable to have smaller acceleration amplification. It is also worthwhile to mention that acceleration magnification is biggest in 300 ft high dam. This is because the first natural frequency of 300 ft high dam, 1.49 Hz, is very close to predominant frequency of the ground motion, 1.42 Hz. Therefore, resonance may occur in the response of 300 ft high dam.

7.6.2 Maximum Separation

Maximum separation of all interfaces increases with increasing height. In downstream interface maximum separation takes place at the maximum cross-section whereas in upstream interface it occurs at some distance away from the maximum cross-section. The maximum separation reaches to 0.4, and 0.7 ft in D/S and U/S interface.

respectively for 400 ft high dam. Nonlinear soil model has a decreasing effect on the magnitude of the maximum separation of all interfaces. Further, the effect of vertical and longitudinal components of ground motion is insignificant on U/S and D/S interfaces, but significant on transverse interface as shown in Figure 7.21. Maximum separation of transverse interface is always less than 0.08 ft. It should also be noted that, even though it is very small, the transverse interface separation takes place at the D/S corner in general.

7.6.3 Separation Depth

In all cases the separation depth is 100% of the dam height in the U/S, and D/S interfaces at the maximum cross-section, and decreases at distances away from maximum cross-section. Nonlinear soil model has significant decreasing effect on separation depth of U/S interface but no effect on D/S interface response. As shown in Figure 7.17 the separation depth is decreased by 50% in U/S interface.

7.7 Summary and Conclusions

In this chapter 3-D FE analysis results of composite dams are presented. One analysis was performed for each height using linear soil model. Additionally three analyses were performed to demonstrate the effect of nonlinear soil model and all three components of ground motion on the performance of soil-concrete interface. Maximum separation,

separation depth, and maximum acceleration profiles of interfaces are presented. Comparisons are made with 2-D model results where possible.

Finally, the following conclusions are made on the exploratory 3-D FE analyses of composite dams;

- Acceleration amplification along the interfaces is always slightly less than 2-D model acceleration amplification.
- Maximum separations at the maximum cross-section are higher than those of 2-D model.
- Maximum separation increases with increasing height.
- Depth of separation reaches to 100% of the dam height at the maximum cross-section for all cases, except nonlinear soil model case.
- Interface behavior is soil model dependent.
- Using nonlinear soil model causes decrease in maximum separation and separation depth.
- The separation and separation depth are not critical at transverse interface, but the maximum separation reaches to 0.15 ft in case with all three component of ground motion and linear soil model.
- Vertical and longitudinal components of ground motion have significant effect on maximum separation and separation depth for linear elastic soil model case, but insignificant effect for nonlinear soil model case.

- In D/S interface maximum separation takes place at the maximum section, but in U/S interface it occurs some distance away from the maximum section.

8. A Case Study

8.1 Introduction

In this chapter dynamic soil-concrete interface behavior of 180 ft high Folsom Dam located in north-east of Sacramento, California is presented as a case study.

8.2 Folsom Dam

The Left Wing Dam of Folsom Dam is chosen in this study because it is very well documented. As indicated before, the interface separation phenomena was first pointed out in Seismic Stability Evaluation Reports of Folsom Dam. Because of lack of necessary computation tools no numeric analyses were carried out. Therefore, this current work is to confirm the suspicion on the potential interface separation of Folsom Dam.

8.2.1 FLUSH Analyses

The investigation of potential separation along the interface of the upstream side of the Left Wing Dam was first studied by N. Y. Chang and H. H. Chiang at the University of Colorado at Denver in 1989, using the computer code FLUSH [46]. Due to the absence of interface properties allowing separation and frictional sliding, the interface condition was

assumed as hinge or roller connection. Horizontal normal stresses of the elements at the interface are traced to see if tensile stresses are developed during the dynamic analysis. Therefore the occurrence of tensile stress along along the interface indicates the presence of possible separation. Because of the lack of proper interface element, the FLUSH can not provide the amount of separation due to the complexity of the problem. Typical strain dependent shear modulus degradation and damping ratio curves were used. Using horizontal normal stress history output, maximum and minimum stresses are obtained for the boundary elements. Static analyses were also performed using FEADAM. The results from both static and dynamic analyses are then superimposed to obtain the distribution of resultant maximum and minimum horizontal stresses along the boundary. As seen in Figure 8.1, the distribution of superimposed stresses for the case with hinge support indicates the potential for separation along the interface down to a depth of 140 ft, whereas for the case with roller support the separation is almost down to 120 ft. The result indicates possible repeated separation along the upper part of the interface.

8.2.2 NIKE2D Analyses

In FLUSH analyses, because of the lack of proper interface element, the separation potential was investigated only in terms of horizontal stress distribution along the interface. It was necessary to determine maximum separation and separation depth in order to confirm the FLUSH findings and beyond. Therefore, more powerful computer codes are needed, particularly a nonlinear dynamic analysis code with elasto-plastic material models and the interface element allowing sliding, debonding and rebonding.

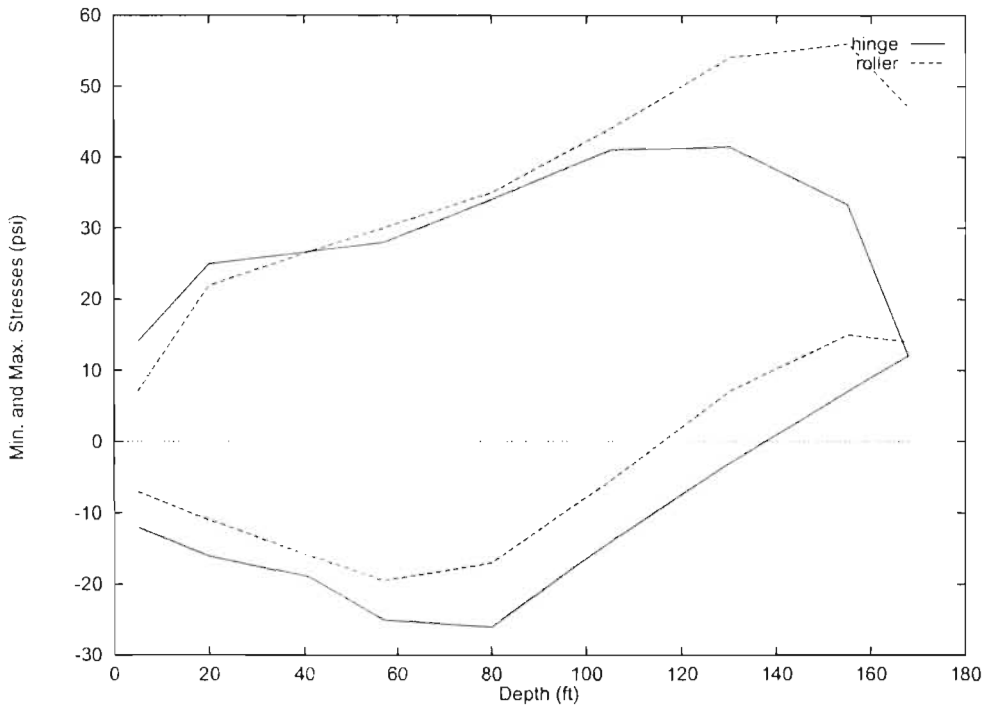

Figure 8.1 FLUSH output of superimposed max. & min. normal stresses along the upstream interface of Left Wing Dam of Folsom Dam for hinge & roller conditions.(Tension is negative)

NIKE2D and NIKE3D developed at the Lawrence Livermore National Laboratory much better satisfy these requirements and they are adopted in the subsequent analysis.

In NIKE2D analyses it was targeted to investigate:

- effect of maximum input ground acceleration on the interface separation,
- distribution of maximum interface normal stresses during shaking.

In the analysis with NIKE2D, by scaling the Original Koyna Dam Earthquake record by 0.75 and 0.5 three different base rock motions are obtained with maximum accelerations 0.87g, 0.65g and 0.44g respectively. These motions are used to study the effect of different maximum accelerations on the interface separation. In the analysis, an elastic model is used for concrete and the R-O model is used for soil. R-O parameters are obtained by the computational procedure proposed by Ueng and Chen [77]. It calculates the R-O parameters using shear modulus and damping ratio versus strain curves. Frictional behavior is modelled with Coulomb friction and frictional constant μ is taken as 0.5 for the soil-concrete interface. Using three different input motions the time histories at different nodes on the soil side along the interface are obtained. Figure 8.2 shows the cross-section of dam and the location of the node # 444 at the time of maximum separation. With original Koyna Dam Earthquake record, maximum separation is found to be around as 0.8 ft at node 444 and depth of separation around 108 ft from the top. At the scaling factor of 0.75 and 0.5, the magnitude of separation and the depth are found to be 0.55 ft and 90 ft and 0.23 ft and 72 ft, respectively.

Figure 8.2 shows the displacement time histories of node # 444 for two different ground motions and it can be seen that separation is repetitive. Finally, Figure 8.2 shows the variation of maximum separations with depth, zero depth at the crest, for three different input ground motions. It shows that doubling the maximum acceleration amplifies the maximum separation about 4 times and deepens the separation by about 50 % (from 72 ft to 108 ft.). All NIKE2D analyses confirmed the suspicion of the interface separation revealed in the FLUSH analyses.

Maximum normal stresses during shaking along the interface are compared with the static normal stress distribution and it is shown in Figure 8.3. According to Figure 8.3 the soil-concrete interface may be subjected to very high stresses during shaking. Static and earthquake induced maximum normal stresses seem to be close to each other below depth 120 ft.

8.3 Comparisons

Maximum separation and separation depth are compared with the parametric study with 200 ft high composite dam as explained in Chapter 6. In the parametric study, the maximum separation and separation depth was found to be 0.156 ft and 120 ft for the `reference configuration` of 200 ft high dam. On the other hand for 180 ft high Folsom Dam, the separation and separation depth was estimated as 0.8 ft and 110 ft, respectively. Separation depth estimates are in good agreement, but maximum separation is overestimated in Folsom Dam case. In NIKE2D analysis of Folsom dam,

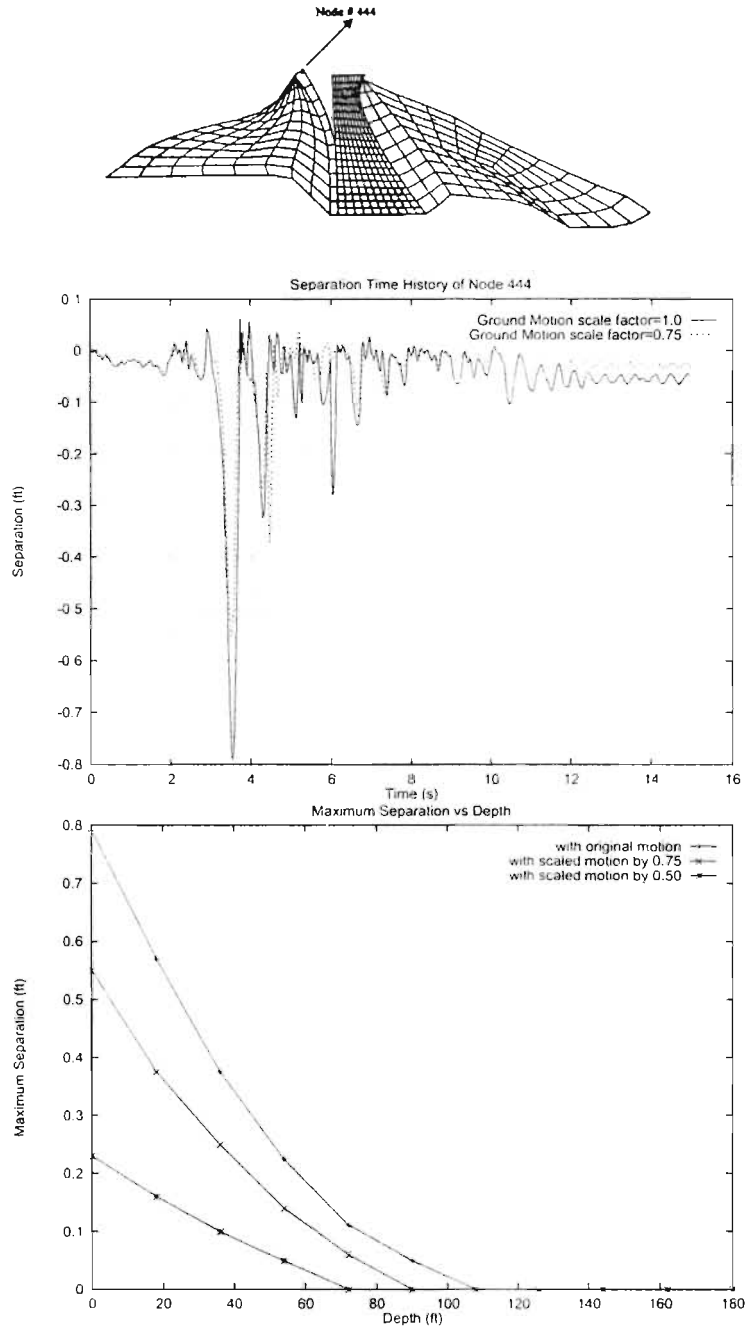

Figure 8.2 Top: Finite element mesh of NIKE2D at the time of maximum separation, Middle: Separation time history of node 444 for original and scaled ground motions, Bottom: Maximum separation versus depth for original and scaled ground motions.

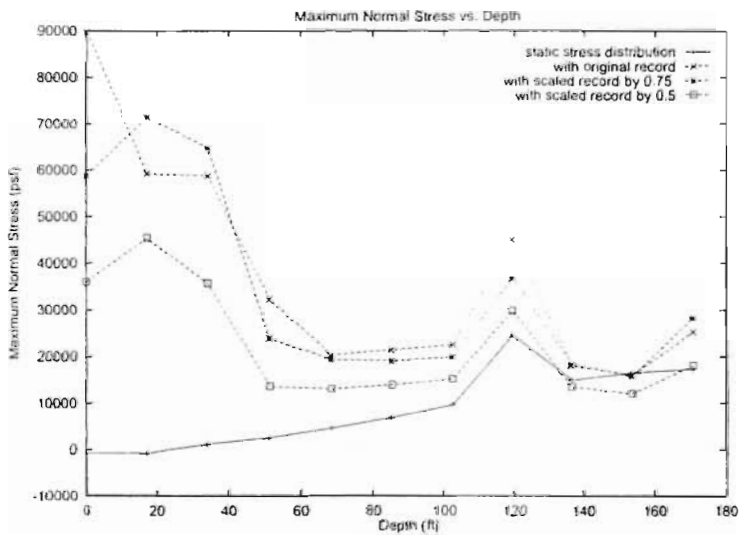

Figure 8.3 Maximum Normal Stress Distribution along the interface.

no Rayleigh damping was used. Damping was incorporated with using nonlinear soil model only. Additionally the geometry of Folsom Dam is also quite different than the hypothetical cross-section used in the parametric study. The existence of foundation trench may affect the dynamic IBCD.

8.4 Summary and Conclusions

As a case study, 180 ft high Folsom dam was analyzed using NIKE2D. The results are presented in terms of maximum separation, separation depth and static, and maximum interface stresses. The results are compared with the parametric FE analysis of 200 ft high composite dam. Good agreement was observed in separation depth. The findings of Folsom Dam case study can be summarized as follows;

- All numerical analysis codes verified the potential separation,
- Separation and separation depth may reach significant values,
- Separation is dependant on maximum input acceleration,
- Upper interface may be subjected to very high normal stresses,
- Separation is repetitive.

9. Statistical Assessment of Parametric Effects

9.1 Introduction

In a parametric study it is necessary to perform statistical assessment to investigate the dependency of structure's response to certain parameters. In this chapter statistical relations between controlling variables, called as independent variables, and maximum interface performance parameters, called as dependent variables, are characterized. Independent variables are:

- θ, the slope angle of the upstream interface,
- ϕ, the slope angle of the downstream interface,
- mu, upstream soil slope,
- md, downstream soil slope,
- H, dam height.

Dependent variables are;

- normalized maximum separation (Max. Sep./H %),
- normalized separation depth (Sep. Depth/H %),
- maximum acceleration ratio (Max. Acce. (out)/Max. Acce. (in)),

- maximum RMS acceleration ratio (Max. RMS Acce. (out)/Max. RMS Acce. (in)).

Maximum separation and separation depth are normalized with dam height and presented in percentage unless it is stated otherwise. Therefore the terms *maximum separation*, and *separation depth* refer to normalized quantities.

The statistical assessment has been performed through the investigation of sample mean, and standard deviation of dependent variables; second-order polynomial best fit models; and squared correlation coefficient, R^2. Since within each dam height every independent variable was varied independently from others, each polynomial model has been formulated with one independent variable. Next correlation matrices have been determined and multiple regression analyses have been performed using all independent variables including the dam height, H.

All statistical parameters are tabulated and plots showing the second-order best fits are presented. Finally all findings are interpreted.

9.2 Basic Statistics and Polynomial Models

The most common types of descriptive statistics are measures of central tendency and variability. The central tendency in a sample of data refers to what is called "sample mean" and it is denoted by $\bar{x}$. The formula for sample mean is given by:

$$\bar{x} = \frac{\sum_{n=1}^{n} x_i}{n} \tag{9.1}$$

where n is the sample size. Sample mean does not summarize all the features of the data. One of the measures of variability is sample standard deviation. The formula for standard deviation is given by:

$$S = \sqrt{\frac{1}{n-1}\sum_{n=1}^{n}(x_i - \bar{x})^2} \tag{9.2}$$

Using S together with $\bar{x}$ gives a fairly good idea of both the amount of spread and the center of the data, respectively.

Polynomial model is a special case of multiple regression model where there is only one independent variable. The statistical second-order polynomial model can be written as:

$$\hat{y} = \hat{a} + \hat{b}x + \hat{c}x^2 \tag{9.3}$$

where $\hat{a}$, $\hat{b}$, and $\hat{c}$ are unknown parameters called regression coefficients, and x is the dependent variable. The best fitting parabola can be estimated with least-squares method in which the sum of squares of deviations of observed points from corresponding points on the fitted parabola are minimized.

To obtain a quantitative measure of how well the second-order model predicts the dependent variable squared multiple correlation coefficient, R^2, can be used. The formula for R^2 is given by:

$$R^2_{(second-order)} = \frac{SSY - SSE_{(second-order)}}{SSY} \tag{9.4}$$

where $SSY = \sum_{n=1}^{n}(y_i - \bar{y})^2$, $SSE = \sum_{n=1}^{n}(y_i - \hat{y})^2)$, $\bar{y}$ is the sample mean, and y_i is the dependent variable. The largest value that R^2 can attain is 1 where there is a very

strong relationship between independent variable and dependent variable. Second-order model was assumed to be adequate for this study. No tests have been performed to check whether a higher order would be better than second-order.

For multiple linear regression analysis the general equation can be written as:

$$\hat{y} = \hat{a}_1 + \hat{a}_2 x_1 + \hat{a}_3 x_2 + ... + \hat{a}_i x_{i-1} \tag{9.5}$$

where a_i is the regression coefficient and x_i is the independent variable.

9.3 Univariate Statistical Assessment

In the next subsections univariate statistical assessment for each dam height is explained. The multivariate statistical analysis is presented in the next section.

9.3.1 Variation and Trend

In this section sample mean and standard deviation of dependent variables are presented in Tables from 9.1 to 9.8. Tables 9.1, and 9.2 show the response of U/S and D/S interfaces of all heights due to change in θ, respectively. Tables 9.3, and 9.4 represent the similar information due to change in ϕ. Tables 9.5, and 9.6 are for the independent variable *mu*, and Tables 9.7, and 9.8 are for *md*. Additionally, in the aforementioned Tables, minimum and maximum ranges are provided together with the general trend of the dependent variables. The trend is characterized by increasing ($\nearrow$), decreasing ($\searrow$), horizontal ($\rightarrow$), parabolic ($\smile$ or $\frown$), and scatter ($\sim$) behavior. The trend

characterization has been done through the plots showing variation of dependent variables. The figure numbers of such plots are listed in Table 9.9 for each independent variable and height. As listed in Table 9.9 the plots related to 100 ft high dam are presented in this section. Others are presented in Appendix A.3. For example, Figures 9.1 and 9.2 show the variation of interface performance parameters due to change in θ for U/S, and D/S interfaces, respectively. Maximum separation, separation depth, maximum acceleration ratio, maximum RMS acceleration ratio are presented in parts (a), (b), (c), and (d) of Figure 9.1, respectively. Same arrangement were followed for other plots in Table 9.9.

9.3.2 Effects of θ Variation

As shown in Table 9.1 increase in θ causes decrease in maximum separation at U/S interfaces of all heights. Separation depth does not change significantly for 100, and 200 ft high dams, but decreases from 60% to 40%, and from 60% to 35% for heights 300 and 400 ft, respectively. Maximum acceleration ratio shows scatter distribution with a mean value of 7.39 for 100 ft high dam. The maximum acceleration ratio mean values are 3.76, 4.03, and 4.16 for 200, 300, and 400 ft high dams, respectively. Additionally increase in θ causes decrease in maximum acceleration for 300 and 400 ft high dams. Maximum RMS acceleration ratio is not affected significantly, and the trend is horizontal for all heights except 200 ft high dam. On the other hand maximum and minimum ranges of maximum RMS acceleration ratio are 3, and 2, respectively for 200

ft high dam indicating an insignificant variation. In general θ has decreasing effect on all U/S performance parameters for dams higher than 200 ft.

Table 9.2 shows the variation of dependent variables of D/S interfaces of all heights due to change in U/S interface angle, θ. In general the effect of θ on D/S performance is not significant. Maximum separation is slightly increased in 100, and 200 ft high dams. Separation depth remains unchanged in all heights, however 300 ft high dam shows a very little change in separation depth with a mean value of 79%, and standard deviation of 3.01. Maximum horizontal acceleration ratio shows different variation for different dams. For example, in 100 ft high dam the mean value, and standard deviation are 7.10 and 0.82, respectively meaning insignificant variation In 400 ft high dam the maximum acceleration ratio decreases from 4.30 to 1.70. Maximum RMS acceleration ratio shows insignificant change due to θ for all heights.

9.3.3 Effects of ϕ Variation

Table 9.3 summarizes the effect of ϕ on U/S interfaces. Change in ϕ has no effect in separation depth for all heights. The maximum separation in 300. and 400 ft high dams is decreased with increasing ϕ. Maximum acceleration ratio shows quite scatter behavior for all dams. It should be noted that the maximum horizontal mean acceleration values are generally higher than θ cases. Maximum RMS acceleration ratios do not show significant change for all heights. In 200 ft high dam RMS acceleration ratio show slight variation in the range from 2 to 3.

Table 9.4 shows the performance of D/S interfaces due to ϕ. ϕ has decreasing effect on maximum separation for 300, and 400 ft high dams, however, mean values are very small as 0.003%, and 0.004% for 300, and 400 ft high dams, respectively. Separation depth is not affected by ϕ for the 400 ft high dam. On the other hand separation depth increases by 10%, and 20% with increasing ϕ in 100, and 200 ft high dams, respectively. Separation depth decreases by 60% in 300 ft high dam. Maximum acceleration ratio decreases in 300, and 400 ft high dams whereas it increases in 200 ft high dam. Maximum RMS acceleration also decreases in 300, and 400 ft high dams. In general ϕ has decreasing effect on all D/S interface performance parameters for 300, and 400 ft high dams.

9.3.4 Effects of *mu* Variation

Table 9.5 shows the effect of *mu* on U/S interfaces. Maximum separation increases in all dams with increasing *mu*. Separation depth decreases by 10% in 100, and 400 ft high dams, and shows no significant change in 200, and 300 ft high dams. Maximum horizontal acceleration ratio decreases in 300, and 400 ft high dams. Maximum RMS ratio also deceases in 100, 300, and 400 ft high dams and is not affected in 200 ft high dam.

Table 9.6 shows the effect of *mu* on D/S interfaces of all heights. It is clearly seen in Table 9.6 that *mu* has insignificant effect on all D/S interface performance parameters.

9.3.5 Effects of *md* Variation

Table 9.7 summarizes the effect of *md* on U/S interfaces. The overall effect of *md* is also insignificant. Increase in *md* causes decrease in separation depth by 10% in 400 ft high dam. Maximum acceleration and RMS acceleration ratios are not affected significantly.

Finally, Table 9.8 shows the variation of D/S interface performance parameters due to change in *md*. Although the mean values are very small (0.008%), *md* causes increase in maximum separation in 200, and 300 ft dams. Separation depth is decreased significantly by 70% and 45% in 300, and 400 ft high dams, respectively. Maximum acceleration ratios decreases with increasing *md* in 100 ft high dam. Maximum acceleration ratio increases in 200 ft high dam and decreases in 400 ft high dam within a very small range. Further, *md* causes decrease in maximum RMS acceleration ratio in 100 ft high dam, and increase in 200, and 300 ft high dams, and no significant change in 400 ft high dam.

Table 9.1 UPSTREAM Response due to θ

UPSTREAM Response due to θ

Maximum Separation (%)(*)

Height	Trend	Range	Mean	Standard Deviation	Comments
100	↘	0.08 0.155	0.119	0.026	
200	↘	0.04 0.08	0.059	0.013	
300	↘	0.02 0.075	0.039	0.018	
400	↘	0.01 0.08	0.038	0.025	

Separation Depth (%)(*)

Height	Trend	Range	Mean	Standard Deviation	Comments
100	→	70 80	74.50	5.220	
200	→	60 60	60.00	0.000	
300	↘	40 60	47.27	9.045	
400	↘	35 60	43.63	22.92	

Maximum Horizontal Acceleration Ratio

Height	Trend	Range	Mean	Standard Deviation	Comments
100	⌒ ~	5.00 10.00	7.39	1.381	Max. at θ=2°, and 3°
200	↗	3.00 4.20	3.76	0.403	
300	↘	3.00 6.00	4.03	0.980	
400	↘	2.20 6.00	4.16	1.31	

Maximum RMS Acceleration Ratio

Height	Trend	Range	Mean	Standard Deviation	Comments
100	→	3.00 5.00	3.76	0.530	
200	↗	2.00 3.00	2.43	0.295	
300	→	2.20 2.80	2.45	0.137	
400	→	2.00 4.00	2.43	0.560	

↗ = increasing, ↘=decreasing, → = horizontal, ⌣ or ⌒ = parabolic, ~ = scatter.
(*) Maximum separation and separation depths are normalized with dam heights and presented in percentage. To convert them into ft they must be multiplied by a factor of H/100, where H is the dam height in ft.

Table 9.2 DOWNSTREAM Response due to θ

DOWNSTREAM Response due to θ

Maximum Separation (%)(⋆)

Height	Trend	Range	Mean	Standard Deviation	Comments
100	↗ ~	0.05 0.12	0.073	0.021	
200	↗	0.005 0.0175	0.012	0.004	
300	→	0.066 0.074	0.007	0.0003	
400	→	0.005 0.01	0.007	0.001	

Separation Depth (%)(⋆)

Height	Trend	Range	Mean	Standard Deviation	Comments
100	→	90 90	90.00	0.00	
200	→	70.00 70.00	70.00	0.00	
300	→	70.00 80.00	79.00	3.01	
400	→	70.00 70.00	70	0.00	

Maximum Horizontal Acceleration Ratio

Height	Trend	Range	Mean	Standard Deviation	Comments
100	→	6.00 8.50	7.10	0.82	
200	↗	2.2 3.5	2.97	0.46	
300	~ →	1.50 2.80	2.08	0.360	
400	↘	1.70 4.30	2.26	0.94	

Maximum RMS Acceleration Ratio

Height	Trend	Range	Mean	Standard Deviation	Comments
100	~	3.50 5.50	4.57	0.60	
200	→	2.00 2.40	2.28	0.14	
300	→	2.00 2.20	2.02	0 069	
400	⌣ ~	1.90 3.50	2.03	0.47	Max. at θ=1°, and 2°

↗ = increasing, ↘=decreasing, → = horizontal, ⌣ or ⌢ = parabolic, ~ = scatter.
(⋆) Maximum separation and separation depths are normalized with dam heights and presented in percentage. To convert them into ft they must be multiplied by a factor of H/100, where H is the dam height in ft.

Table 9.3 UPSTREAM Response due to ϕ

UPSTREAM Response due to ϕ

Maximum Separation (%)(*)

Height	Trend	Range	Mean	Standard Deviation	Comments
100	→	0.140 0.155	0.149	0.003	
200	→	0.079 0.082	0.081	0.002	
300	↘	0.062 0.070	0.064	0.003	
400	↘	0.05 0.09	0.062	0.014	

Separation Depth (%)(*)

Height	Trend	Range	Mean	Standard Deviation	Comments
100	→	80 80	80.00	0.00	
200	→	60 60	60.00	0.00	
300	→	60 60	60.00	0.00	
400	→	60 60	60.00	0.00	

Maximum Horizontal Acceleration Ratio

Height	Trend	Range	Mean	Standard Deviation	Comments
100	⌒ ~	5.50 9.50	7.13	1.55	Max. at ϕ=27°, and 30°
200	↗ ~	3.2 11.0	6.60	3.07	
300	↘	4.00 6.50	5.26	0.66	
400	→ ~	4.50 6.50	5.31	0.58	

Maximum RMS Accceleration Ratio

Height	Trend	Range	Mean	Standard Deviation	Comments
100	→	3.00 5.00	3.81	0.49	
200	↗	2.00 3.00	2.40	0.49	
300	→	2.30 2.50	2.36	0.09	
400	→	1.90 2.2	2.08	0.11	

↗ = increasing, ↘=decreasing, → = horizontal, ⌣ or ⌒ = parabolic, ~ = scatter.
(*) Maximum separation and separation depths are normalized with dam heights and presented in percentage. To convert them into ft they must be multiplied by a factor of H/100, where H is the dam height in ft.

Table 9.4 DOWNSTREAM Response due to ϕ

DOWNSTREAM Response due to ϕ

Maximum Separation (%)(*)

Height	Trend	Range	Mean	Standard Deviation	Comments
100	⌒ ~	0.04 0.06	0.068	0.039	
200	⟋	0.005 0.010	0.008	0.002	
300	⟍	0.002 0.008	0.003	0.002	
400	⟍	0.002 0.01	0.004	0.003	

Separation Depth (%)(*)

Height	Trend	Range	Mean	Standard Deviation	Comments
100	⟋	90 100	98.88	3.33	
200	⟋	70.00 90.00	78.88	7.81	
300	⟍	20.00 80.00	40.00	30.00	
400	→	70.00 70.00	70.00	0.00	

Maximum Horizontal Acceleration Ratio

Height	Trend	Range	Mean	Standard Deviation	Comments
100	⌒ ~	5.50 8.20	7.70	1.89	
200	⟋	2.2 4.0	2.79	0.62	
300	⟍ ~	1.75 3.00	2.00	0.37	
400	⟍ ~	2.00 4.20	2.53	0 91	

Maximum RMS Acceleration Ratio

Height	Trend	Range	Mean	Standard Deviation	Comments
100	~	4.20 7.00	5.43	0.87	
200	→	2.00 2.50	2.16	0.16	
300	⟍	1.75 2.00	1.82	1.12	
400	⟍	1.50 2.00	1.76	0.21	

⟋ = increasing, ⟍=decreasing, → = horizontal, ⌣ or ⌒ = parabolic, ~ = scatter.
(*) Maximum separation and separation depths are normalized with dam heights and presented in percentage. To convert them into ft they must be multiplied by a factor of H/100, where H is the dam height in ft.

Table 9.5 UPSTREAM Response due to mu

UPSTREAM Response due to mu

Maximum Separation (%)(*)

Height	Trend	Range	Mean	Standard Deviation	Comments
100	↗	0.150 0.175	0.166	0.008	
200	↗	0.08 0.011	0.098	0.010	
300	↗	0.07 0.12	0.102	0.017	
400	↗	0.09 0.11	0.105	0.006	

Separation Depth (%)(*)

Height	Trend	Range	Mean	Standard Deviation	Comments
100	↘	80 70	74.44	5.27	
200	→	60 60	60.00	0.00	
300	→	60 60	60.00	0.00	
400	↘	60 50	53.33	5.00	

Maximum Horizontal Acceleration Ratio

Height	Trend	Range	Mean	Standard Deviation	Comments
100	⌒ ~	6.00 12.0	8.92	2.1	Max. at mu=3-3.25
200	⌒	3.2 6.0	4.90	1.13	Max. at mu=3-3.25
300	↘	3.50 7.00	4.44	1.21	
400	↘	2.80 5.20	4.18	0.90	

Maximum RMS Acceleration Ratio

Height	Trend	Range	Mean	Standard Deviation	Comments
100	↘	3.00 3.90	3.29	0.24	
200	→	2.00 2.50	2.16	0.16	
300	↘	1.75 2.50	1.82	1.12	
400	↘	1.20 2.00	1.76	0.21	

↗ = increasing, ↘=decreasing, → = horizontal, ⌣ or ⌒ = parabolic, ~ = scatter.
(*) Maximum separation and separation depths are normalized with dam heights and presented in percentage. To convert them into ft they must be multiplied by a factor of H/100, where H is the dam height in ft.

Table 9.6 DOWNSTREAM Response due to *mu*

DOWNSTREAM Response due to *mu*

Maximum Separation (%)(*)

Height	Trend	Range	Mean	Standard Deviation	Comments
100	→	0.05 0.08	0.055	0.009	
200	→	0.005 0.007	0.006	0.0002	
300	→	0.007 0.008	0.0076	0.0004	
400	→	0.007 0.009	0.0078	0.0007	

Separation Depth (%)(*)

Height	Trend	Range	Mean	Standard Deviation	Comments
100	→	80 100	92.22	4.40	
200	→	70 70	70.00	0.00	
300	→	80 80	80.00	0.00	
400	→	70 70	70.00	0.00	

Maximum Horizontal Acceleration Ratio

Height	Trend	Range	Mean	Standard Deviation	Comments
100	→ ~	6.00 9.50	7.41	1.16	
200	→ ~	2.00 2.70	2.34	0.21	
300	↘	2.40 3.50	2.80	0.32	
400	→ ~	2.10 3.40	2.79	0.38	

Maximum RMS Acceleration Ratio

Height	Trend	Range	Mean	Standard Deviation	Comments
100	→	4.00 5.00	4.48	0.48	
200	→	2.00 2.20	2.08	0.07	
300	→	2.00 2.10	2.08	0.034	
400	→	1.90 2.10	2.00	0.05	

↗ = increasing, ↘=decreasing, → = horizontal, ⌣ or ⌢ = parabolic, ~ = scatter.
(*) Maximum separation and separation depths are normalized with dam heights and presented in percentage. To convert them into ft they must be multiplied by a factor of H/100, where H is the dam height in ft.

Table 9.7 UPSTREAM Response due to *md*

UPSTREAM Response due to *md*

Maximum Separation (%)(*)

Height	Trend	Range	Mean	Standard Deviation	Comments
100	→	0.14 0.16	0.015	0.005	
200	→	0.04 0.08	0.055	0.014	
300	→	0.066 0.070	0.068	0.001	
400	→	0.085 0.095	0.090	0.002	

Separation Depth (%)(*)

Height	Trend	Range	Mean	Standard Deviation	Comments
100	→	70 80	78.88	3.33	
200	→ ~	30 60	52.22	9.71	
300	→	60 60	60.00	0.00	
400	↘	50 60	55.55	5.27	

Maximum Horizontal Acceleration Ratio

Height	Trend	Range	Mean	Standard Deviation	Comments
100	↗	5.50 7.00	6.21	0.29	
200	→ ~	2.80 4.00	3.39	0.35	
300	→	4.1 5.9	5.04	0.43	
400	↗ ~	5.00 7.00	6.31	1.00	

Maximum RMS Acceleration Ratio

Height	Trend	Range	Mean	Standard Deviation	Comments
100	→	3.00 4.00	3.38	0.19	
200	↗	2.00 2.50	2.19	0.16	
300	→	2.00 2.50	2.34	0.13	
400	→	2.00 2.90	2.26	0.19	

↗ = increasing, ↘=decreasing, → = horizontal, ⌣ or ⌢ = parabolic, ~ = scatter.
(*) Maximum separation and separation depths are normalized with dam heights and presented in percentage. To convert them into ft they must be multiplied by a factor of H/100, where H is the dam height in ft.

Table 9.8 DOWNSTREAM Response due to *md*

DOWNSTREAM Response due to *md*

Maximum Separation (%)(*)

Height	Trend	Range	Mean	Standard Deviation	Comments
100	→	0.048 0.050	0.049	0.0009	
200	↗	0.005 0.012	0.008	0.002	
300	↗	0.006 0.011	0.008	0.002	
400	⌒	0.0075 0.015	0.013	0.003	Max. at *mu*=3

Separation Depth (%)(*)

Height	Trend	Range	Mean	Standard Deviation	Comments
100	→	90 90	90.00	0.00	
200	→	60 70	64.44	5.27	
300	↘	10 80	52.22	25.75	
400	↘	25 70	46.66	20.91	

Maximum Horizontal Acceleration Ratio

Height	Trend	Range	Mean	Standard Deviation	Comments
100	↘ ~	4.00 7.00	4.67	0.99	
200	↗	2.30 3.50	2.83	0.32	
300	~	2.4 3.6	3.06	0.46	
400	↘	2.00 3.50	2.68	0.65	

Maximum RMS Acceleration Ratio

Height	Trend	Range	Mean	Standard Deviation	Comments
100	↘	2.30 4.50	2.77	0.71	
200	↗	2.00 2.50	2.26	0.21	
300	↗	2.00 2.50	2.16	0.13	
400	→	1.5 2.1	1.79	0.19	

↗ = increasing, ↘=decreasing, → = horizontal, ⌣ or ⌒ = parabolic, ~ = scatter.
(*) Maximum separation and separation depths are normalized with dam heights and presented in percentage. To convert them into ft they must be multiplied by a factor of H/100, where H is the dam height in ft.

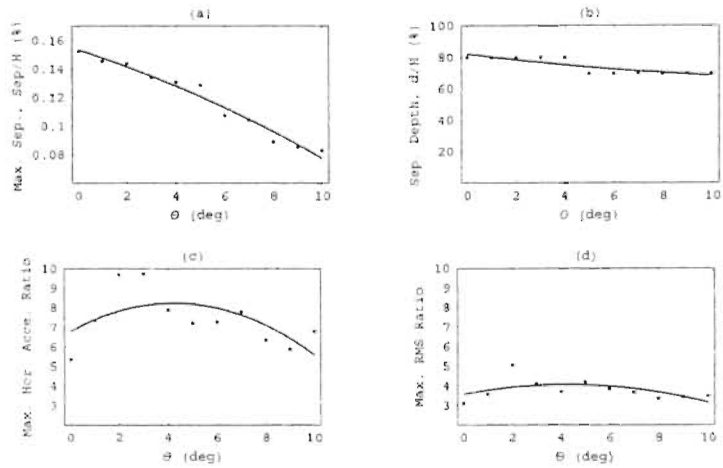

Figure 9.1 Effect of θ on U/S response, H=100 ft.

9.3.6 Polynomial Best Fits

Second-order best-fit coefficients, and R^2 values are summarized in Tables 9.10. and 9.11. Table 9.10 lists the polynomial best fit parameters ($\hat{a}$, $\hat{b}$, and $\hat{c}$), and correlation coefficient R^2 for 100, and 200 ft high dams. Next, the Table 9.11 lists the similar information for 300, and 400 ft high dams. In both Tables, R^2 values greater than 0.80 are typed in bold face. The number of occurrences of R^2 greater than 0.80 is 3, 14, 15, and 10 in 100. 200, 300, and 400 ft high dams. respectively.

In 100 ft high dam, the R^2 values for θ-maximum separation and mu-maximum separation relations along the U/S interface are 0.97 and 0.95, respectively, indicating a very strong relation between the variables. As seen in part (a) of Figure 9.1, maximum

Table 9.9 Numbers of Figures showing variation of independent variables and polynomial best-fit curves.

Height (ft)	Independent Variable	Interface	Figure Number
100	θ	u/s	9.1
		d/s	9.2
	ϕ	u/s	9.3
		d/s	9.4
	mu	u/s	9.5
		d/s	9.6
	md	u/s	9.7
		d/s	9.8
200	θ	u/s	A.79
		d/s	A.80
	ϕ	u/s	A.81
		d/s	A.82
	mu	u/s	A.83
		d/s	A.84
	md	u/s	A.85
		d/s	A.86
300	θ	u/s	A.87
		d/s	A.88
	ϕ	u/s	A.89
		d/s	A.90
	mu	u/s	A.91
		d/s	A.92
	md	u/s	A.93
		d/s	A.94
400	θ	u/s	A.95
		d/s	A.96
	ϕ	u/s	A.97
		d/s	A.98
	mu	u/s	A.99
		d/s	A.100
	md	u/s	A.101
		d/s	A.102
u/s=upstream, d/s=downstream			

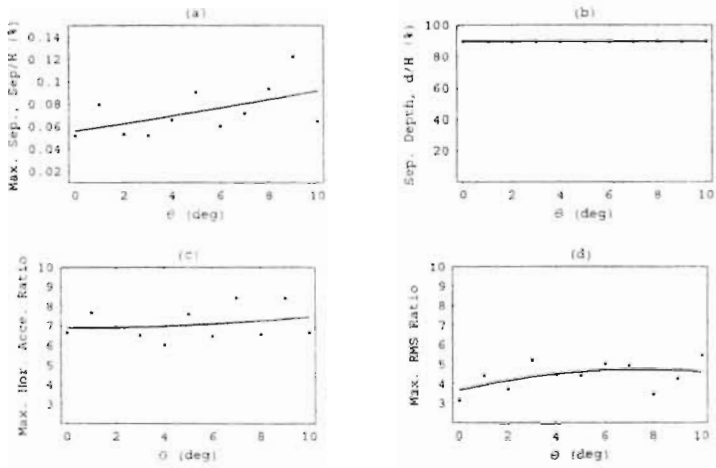

Figure 9.2 Effect of θ on D/S response. H=100 ft.

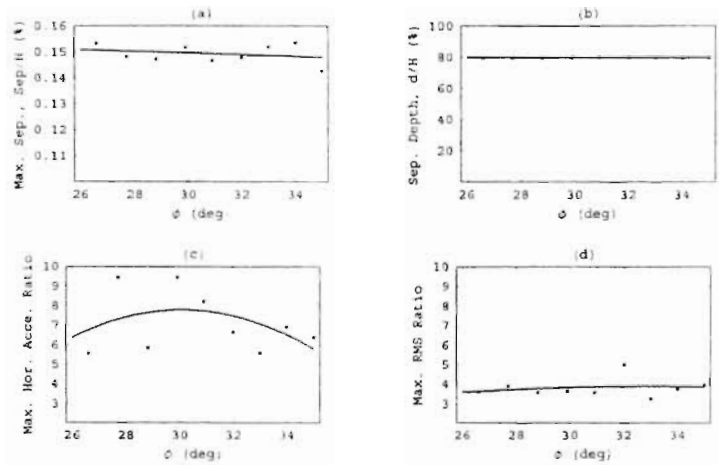

Figure 9.3 Effect of ϕ on U/S response. H=100 ft.

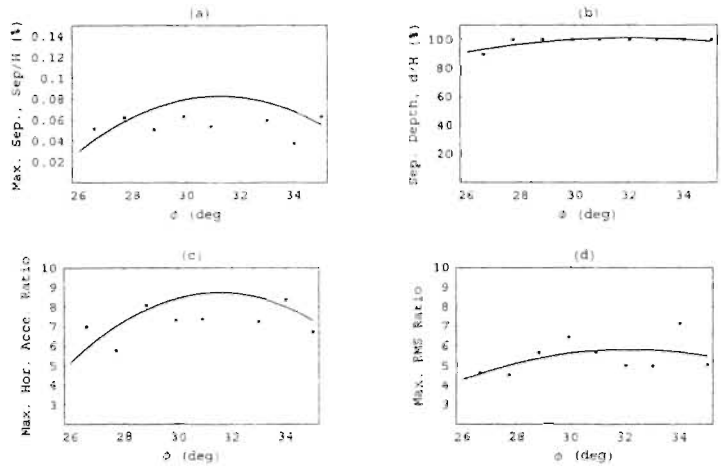

Figure 9.4 Effect of ϕ on D/S response. H=100 ft.

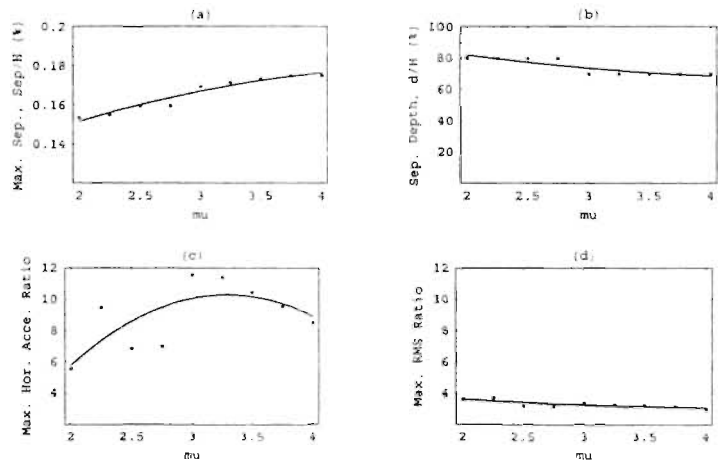

Figure 9.5 Effect of *mu* on U/S response. H=100 ft.

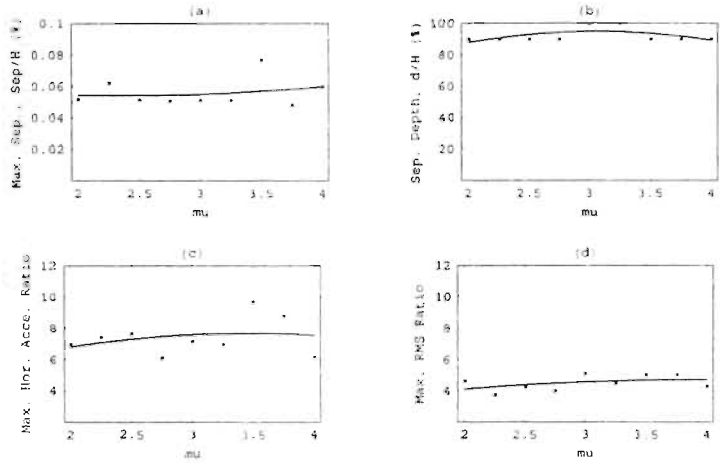

Figure 9.6 Effect of *mu* on D/S response, H=100 ft.

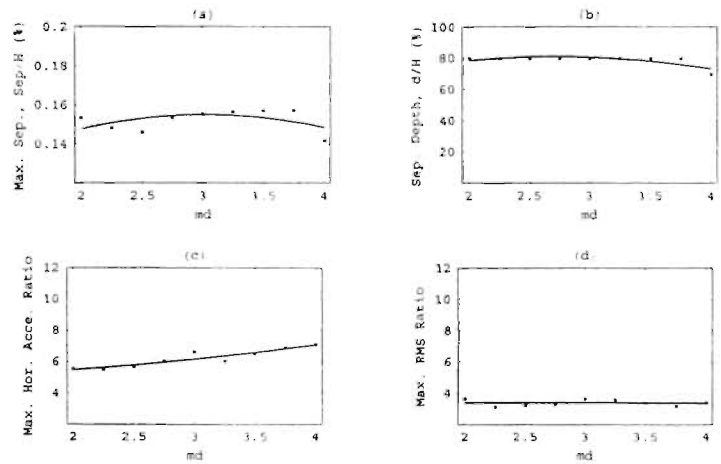

Figure 9.7 Effect of *md* on U/S response, H=100 ft.

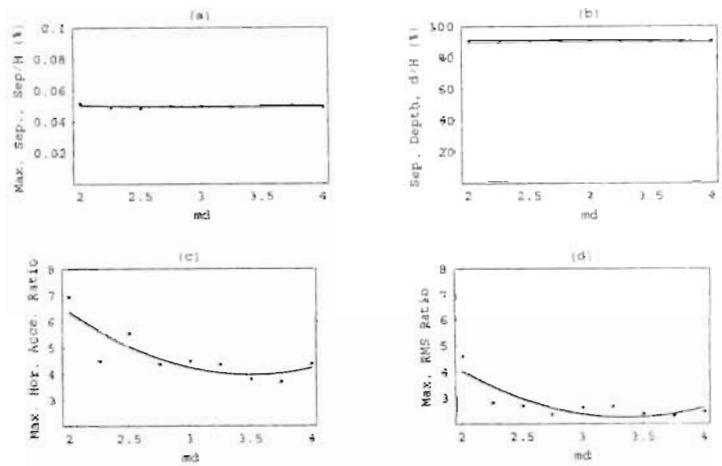

Figure 9.8 Effect of *md* on D/S response, H=100 ft.

separation decreases with increasing θ, and second-degree polynomial best fit curve fits very well to the data. Part (a) of Figure 9.5 also shows the increasing trend of maximum separation and strong relation between *mu* and maximum separation. Additionally, R^2 is 0.87 for *md*-maximum acceleration ratio relation along the U/S interface. Part (c) of Figure 9.7 shows that maximum acceleration ratio increased from 5.5 to 7.0, however maximum RMS acceleration ratio (part (d)of Figure 9.7) does not exhibit a strong *md* dependent distribution.

In 200 ft high dam the R^2 values indicate strong relations between maximum separation and independent variables θ, and ϕ along both U/S and D/S interfaces. In fact the change in maximum separation of D/S interfaces is very small, as shown in parts (a) of Figures A.80, and A.82. There is relatively a bigger change in U/S maximum separation due to θ. As shown in part (a) of Figure A.79, U/S maximum separation decreases from 0.08% (0.16 ft) to 0.04% (0.08 ft) with increasing θ. Further, the change in U/S maximum separation due to ϕ is in the close neighborhood of 0.08% (0.16 ft) as shown in part (a) of Figure A.81. The relation between separation depth and ϕ along the D/S interface is also strong, and shows increasing trend. Finally, Table 9.10 shows several strong relations between maximum RMS acceleration ratios and dependent variables. However all mean values of maximum RMS acceleration are in between 2.08 and 2.43, and the variation is very small.

The second-order best fit coefficients and R^2 values for 300, and 400 ft high dams are presented in Table 9.11. In 300 ft high dam R^2 values again show several strong

relations along both U/S and D/S maximum interface separations. In fact, the maximum separation along the D/S interface is very small and around 0.007% (0.021 ft) for all cases as shown in parts (a) of Figures A.88, A.90, A.92, and A.94. θ has the most significant effect on U/S maximum separation as shown in part (a) of Figure A.87. Maximum separation is decreased from 0.075% (0.225 ft) to 0.02% (0.06 ft) with increasing θ. Additionally, θ has also significant effect on U/S separation depth, and maximum acceleration ratio with R^2 values of 0.89, and 0.97, respectively. Separation depth is decreased from 60% to 40% as shown in part (b) of Figure A.87. Maximum acceleration ratio is decreased from 6 to approximately 4. Another strong relation exists between maximum separation and mu along the U/S interface with an R^2 value of 0.99. As shown in part (a) of Figure A.91 maximum separation is increased from 0.07% (0.21 ft) to 0.118% (0.354 ft) with increasing mu. Additionally D/S separation depth is affected by ϕ, and md, and the trend is decreasing as shown in parts (a) of Figures A.90, and A.94.

In 400 ft high dam θ has also significant effects on U/S interface. As shown in part (a) of Figure A.95, U/S maximum separation decreases from 0.08% (0.32 ft) to 0.02% (0.08 ft). U/S maximum acceleration ratio and separation depth are also significantly decreased with increasing θ. The relation between D/S interface angle, ϕ, and maximum separations of both U/S, and D/S interfaces is also strong and has decreasing effect as shown in parts (a) of Figures A.97, and A.98, respectively. Table 9.11 shows two cases where maximum RMS acceleration ratio are strongly affected by ϕ, and mu, however

the variation is very small, and maximum RMS ratio mean values are in between 1.79 and 2.43.

9.4 Multivariate Statistical Assessment

In the previous section the dam height was not included in the statistical analysis. Since the effect of dam height is critical it is necessary to investigate the statistical significance of dam height on estimating the interface performance parameters. First the correlation matrices have been determined for all variables. They are presented in Tables 9.12, 9.13, 9.14, and 9.15. Tables 9.12, and 9.14 list the information using normalized maximum separation and separation depth for U/S and D/S interfaces, respectively. Tables 9.13, and 9.15 present the correlation coefficients using un-normalized maximum separation and separation depth (in ft) for U/S and D/S interfaces, respectively. Second multiple regression analyses have been performed using all five independent variables. The regression equation used is:

$$\hat{y} = \hat{a} + \hat{b}H + \hat{c}\theta + \hat{d}\phi + \hat{e}(mu) + \hat{f}(md) \tag{9.6}$$

where $\hat{a}, \hat{b}, \hat{c}, \hat{d}, \hat{e}$ and $\hat{f}$ are coefficients. Associated R^2 values are listed in Table are listed in Table 9.16. Third, additional multiple linear regression analysis has been performed with selected independent variables. The variables with high R^2 values were selected from Tables 9.12, 9.13, 9.14, and 9.15. The new R^2 values are presented in Table 9.17. Fourth, second-degree multiple regression analyses have been performed.

Table 9.10 Best Fit Parameters and correlation coefficient for heights 100 and 200 ft.

Height (ft)	Dependent Variable	Independent Variable	Interface	Best Fit Coefficients $\hat{a}$	$\hat{b}$	$\hat{c}$	R^2
100	Maximum Separation (%)(*)	θ	u/s	0.153	-0.006	-0.00021	**0.97**
			d/s	0.056	0.003	0.00003	0.30
		ϕ	u/s	0.152	0.0001	0.0	0.07
			d/s	1.794	0.12	-0.0019	0.12
		mu	u/s	0.101	0.0314	-0.003	**0.95**
			d/s	0.065	-0.009	0.0019	0.05
		md	u/s	0.091	0.0425	-0.007	0.24
			d/s	0.057	0.0052	0.008	0.14
	Separation Depth (%)(*)	θ	u/s	82.24	-1.946	0.058	0.76
			d/s	96	0.0	0.0	0.00
		ϕ	u/s	80	0.0	0.0	0.00
			d/s	-182.21	17.73	-0.277	0.63
		mu	u/s	109.31	-17.06	1.731	0.77
			d/s	35.22	39.108	-6.41	0.33
		md	u/s	45.27	26.42	-4.84	0.62
			d/s	90	0.0	0.0	0.00
	Maximum Horizontal Acceleration Ratio	θ	u/s	6.81	0.672	-0.079	0.36
			d/s	6.894	0.006	0.005	0.06
		ϕ	u/s	68.23	5.05	-0.084	0.18
			d/s	-107.12	7.382	-0.11	0.25
		mu	u/s	-18.89	17.72	-2.69	0.51
			d/s	2.83	2.77	-0.397	0.07
		md	u/s	4.91	0.036	0.127	**0.87**
			d/s	17.01	-7.44	1.06	0.71
	Maximum RMS Ratio	θ	u/s	3.573	0.229	-0.027	0.29
			d/s	4.393	0.029	0.001	0.05
		ϕ	u/s	-2.52	0.388	0.0058	0.03
			d/s	-36.24	2.617	-0.041	0.22
		mu	u/s	3.22	0.128	-0.023	0.00
			d/s	12.99	-6.385	0.95	0.72
		md	u/s	0.152	0.0001	0.0	0.07
			d/s	1.794	0.12	-0.0019	0.12
200	Maximum Separation (%)(*)	θ	u/s	0.074	-0.0015	-0.0002	**0.98**
			d/s	0.004	0.002	0.00008	**0.90**
		ϕ	u/s	0.088	0.01	-0.00015	**0.88**
			d/s	-0.048	0.003	-0.00003	**0.81**
		mu	u/s	-0.058	0.096	-0.014	**0.96**
			d/s	0.006	0.00007	-0.00004	0.17
		md	u/s	0.209	-0.0925	0.0131	0.55
			d/s	-0.011	0.01	-0.0013	**0.87**
	Separation Depth (%)(*)	θ	u/s	60	0.0	0.0	0.00
			d/s	80.21	-0.95	0.1	0.11
		ϕ	u/s	60	0.0	0.0	0.00
			d/s	91.58	-3.42	0.096	**0.87**
		mu	u/s	60	0.0	0.0	0.00
			d/s	70.0	0.00	0.00	0.00
		md	u/s	127.16	-47.26	7.099	0.18
			d/s	99.3	-17.05	1.73	0.70
	Maximum Horizontal Acceleration Ratio	θ	u/s	3.183	0.15	-0.0057	0.68
			d/s	2.394	0.0797	0.00511	**0.89**
		ϕ	u/s	-113.08	6.97	-0.099	0.67
			d/s	16.478	-1.067	0.02	0.67
		mu	u/s	-17.12	14.82	-2.38	0.76
			d/s	3.48	-0.866	0.155	0.12
		md	u/s	1.84	1.525	-0.257	0.27
			d/s	-1.191	2.475	-0.361	0.62
	Maximum RMS Acceleration Ratio	θ	u/s	1.951	0.1241	-0.0039	**0.92**
			d/s	2.933	0.0762	-0.0038	**0.93**
		ϕ	u/s	-4.962	0.324	-0.0027	**0.82**
			d/s	8.559	-0.4634	0.0082	0.75
		mu	u/s	-0.776	1.92	-0.32	0.43
			d/s	2.055	-0.083	-0.03	**0.89**
		md	u/s	0.5	0.932	-0.11	**0.95**
			d/s	1.929	-0.076	0.0599	**0.86**

u/s=upstream, d/s=downstream

(*) Maximum separation and separation depths are normalized with dam heights and presented in percentage. To convert them into ft they must be multiplied by a factor of H/100, where H is the dam height in ft.

Table 9.11 Best Fit Parameters and correlation coefficient for heights 300 and 400 ft.

Height (ft)	Dependent Variable	Independent Variable	Interface	Best Fit Coefficients			R^2
				$\hat{a}$	$\hat{b}$	$\hat{c}$	
300	Maximum Separation (%)(*)	θ	u/s	0.073	-0.01	0.0005	0.99
			d/s	0.0072	-0.0001	-0.00001	0.20
		ϕ	u/s	0.192	-0.0076	0.0001	0.93
			d/s	0.115	-0.0067	0.0001	0.99
		mu	u/s	-0.1175	0.128	-0.0175	0.99
			d/s	0.001	0.003	-0.0005	0.91
		md	u/s	0.061	0.007	-0.0014	0.96
			d/s	0.0009	0.002	0.0	0.75
	Separation Depth (%)(*)	θ	u/s	63.91	-5.368	0.291	0.89
			d/s	80.21	0.958	0.104	0.11
		ϕ	u/s	60	0.0	0.0	0.00
			d/s	1724.1	-101.35	1.50	0.80
		mu	u/s	60	0.0	0.0	0.00
			d/s	80.00	0.00	0.00	0.00
		md	u/s	60	0.0	0.0	0.00
			d/s	122.75	-12.37	-3.55	0.80
	Maximum Horizontal Acceleration Ratio	θ	u/s	5.64	-0.65	0.042	0.97
			d/s	2.31	-0.2	0.022	0.35
		ϕ	u/s	-10.39	1.17	-0.0215	0.49
			d/s	29.69	-1.74	0.027	0.53
		mu	u/s	16.36	-6.85	0.918	0.66
			d/s	2.51	0.61	-0.16	0.64
		md	u/s	3.743	0.751	-0.1	0.06
			d/s	-0.66	2.28	-0.33	0.27
	Maximum RMS Ratio	θ	u/s	2.41	-0.0215	0.0044	0.38
			d/s	2.051	-0.044	0.0055	0.82
		ϕ	u/s	-3.945	0.432	-0.007	0.58
			d/s	5.36	-0.18	0.002	0.95
		mu	u/s	5.5	-2.16	0.29	0.89
			d/s	1.38	0.47	-0.074	0.86
		md	u/s	2.88	-0.52	0.11	0.59
			d/s	1.588	0.218	-0.0089	0.82
400	Maximum Separation (%)(*)	θ	u/s	0.086	-0.0149	0.0008	0.98
			d/s	0.008	-0.0008	0.00007	0.49
		ϕ	u/s	0.761	0.041	0.0006	0.97
			d/s	0.082	-0.04	0.000049	0.88
		mu	u/s	0.152	0.0001	0.0	0.07
			d/s	0.0136	-0.003	0.00034	0.75
		md	u/s	0.064	0.022	-0.0041	0.97
			d/s	-0.05	0.042	-0.0067	0.72
	Separation Depth (%)(*)	θ	u/s	53.99	6.251	-1.188	0.89
			d/s	70.00	0.00	0.00	0.00
		ϕ	u/s	60.0	0.0	0.0	0.00
			d/s	70.00	0.00	0.00	0.00
		mu	u/s	111.463	-34.05	4.67	0.81
			d/s	70.0	0.0	0.0	0.00
		md	u/s	60.69	3.722	1.7316	0.76
			d/s	130.66	-28.0	0.00	0.84
	Maximum Horizontal Acceleration Ratio	θ	u/s	5.85	-0.285	-0.0007	0.83
			d/s	4.0	-0.68	0.048	0.73
		ϕ	u/s	-22.67	1.803	-0.028	0.15
			d/s	36.82	-1.97	0.0277	0.73
		mu	u/s	9.68	-2.69	0.274	0.64
			d/s	5.397	-2.03	0.37	0.25
		md	u/s	-0.19	2.588	-0.452	0.39
			d/s	5.48	-1.103	0.054	0.68
	Maximum RMS Acceleration Ratio	θ	u/s	2.45	0.027	-0.0046	0.02
			d/s	2.35	-0.091	0.003	0.13
		ϕ	u/s	-2.09	0.25	-0.0037	0.33
			d/s	0.477	0.156	-0.003	0.92
		mu	u/s	4.63	-1.76	0.236	0.92
			d/s	1.498	0.293	-0.039	0.68
		md	u/s	1.026	0.642	-0.073	0.51
			d/s	5.04	-2.201	0.359	0.53

u/s=upstream, d/s=downstream
(*) Maximum separation and separation depths are normalized with dam heights and presented in percentage. To convert them into ft they must be multiplied by a factor of H/100, where H is the dam height in ft.

Table 9.12 Correlation matrix of normalized variables for U/S interface.

	H	θ	ϕ	mu	md	MS(*)	SD(*)	MAR	MRMSR
H	1	0	0	0	0	-0.61	-0.66	-0.43	-0.69
θ	0	1	-0.23	-0.23	-0.23	-0.47	-0.38	-0.23	0.18
ϕ	0	-0.23	1	-0.2	-0.2	-0.03	0.14	0.22	0.13
mu	0	-0.23	-0.2	1	-0.2	0.38	-0.01	0.04	-0.32
md	0	-0.23	-0.2	-0.2	1	0.01	-0.03	0	0.04
MS(*)	-0.61	-0.47	-0.03	0.38	0.01	1	0.77	0.61	0.49
SD(*)	-0.66	-0.38	0.14	-0.01	-0.03	0.77	1	0.56	0.57
MAR	-0.43	-0.23	0.22	0.04	0	0.61	0.56	1	0.64
MRMSR	-0.69	0.18	0.13	-0.32	0.04	0.49	0.57	0.64	1

H=Height, MS=Maximum Separation, SD=Separation Depth, MAR=Maximum Acceleration Ratio, MRMSR=Maximum RMS Acceleration Ratio (*)=Percent of dam height.

The equation used is:

$$\hat{y} = \hat{a} + \hat{b}x + \hat{c}x^2 + \hat{d}H \tag{9.7}$$

where x is the independent variable, and H is the dam height. The multiple correlation coefficients are listed in Table 9.18. Finally all R^2 values obtained from all regression models were compared. The best regression equations were selected by considering the simplicity of models and the high R^2 values. The selected regression equations are listed in Tables 9.19, and 9.20 for U/S, and D/S interfaces, respectively.

Inclusion of dam height in the multiple linear regression decreased the R^2 values compared to univariate regression analysis performed for each dam height separately. Table 9.20 also shows that downstream concrete angle has statistically insignificant effect on D/S interface performance.

Table 9.13 Correlation matrix of un-normalized variables for U/S interface.

	H	θ	ϕ	mu	md	MS(*)	SD(*)	MAR	MRMSR
H	1	0	0	0	0	0.57	0.97	-0.43	-0.69
θ	0	1	-0.23	-0.23	-0.23	-0.52	-0.12	-0.23	0.18
ϕ	0	-0.23	1	-0.2	-0.2	-0.07	0.04	0.22	0.13
mu	0	-0.23	-0.2	1	-0.2	0.43	-0.02	0.04	-0.32
md	0	-0.23	-0.2	-0.2	1	0.04	0.02	0	0.04
MS(*)	0.57	-0.52	-0.07	0.43	0.04	1	0.65	-0.01	-0.5
SD(*)	0.97	-0.12	0.04	-0.02	0.02	0.65	1	-0.33	-0.63
MAR	-0.43	-0.23	0.22	0.04	0	-0.01	-0.33	1	0.64
MRMSR	-0.69	0.18	0.13	-0.32	0.04	-0.5	-0.63	0.64	1

H=Height, MS=Maximum Separation, SD=Separation Depth, MAR=Maximum Acceleration Ratio, MRMSR=Maximum RMS Acceleration Ratio (*)=In feet.

Table 9.14 Correlation matrix of normalized variables for D/S interface.

	H	θ	ϕ	mu	md	MS(*)	SD(*)	MAR	MRMSR
H	1	0	0	0	0	-0.7	-0.54	-0.7	-0.71
θ	0	1	-0.23	-0.23	-0.23	0.11	0.12	-0.01	0.06
ϕ	0	-0.23	1	-0.2	-0.2	0	-0.08	0.03	0.08
mu	0	-0.23	-0.2	1	-0.2	-0.03	0.12	0.05	0.04
md	0	-0.23	-0.2	-0.2	1	-0.01	-0.4	-0.1	-0.15
MS(*)	-0.7	0.11	0	-0.03	-0.01	1	0.54	0.9	0.79
SD(*)	-0.54	0.12	-0.08	0.12	-0.4	0.54	1	0.56	0.57
MAR	-0.7	-0.01	0.03	0.05	-0.1	0.9	0.56	1	0.91
MRMSR	-0.71	0.06	0.08	0.04	-0.15	0.79	0.57	0.91	1

H=Height, MS=Maximum Separation, SD=Separation Depth, MAR=Maximum Acceleration Ratio, MRMSR=Maximum RMS Acceleration Ratio (*)=Percent of dam height.

Table 9.15 Correlation matrix of un-normalized variables for D/S interface.

	H	θ	ϕ	mu	md	MS(*)	SD(*)	MAR	MRMSR
H	1	0	0	0	0	-0.44	-0.54	-0.7	-0.71
θ	0	1	-0.23	-0.23	-0.23	0.13	0.12	-0.01	0.06
ϕ	0	-0.23	1	-0.2	-0.2	-0.12	-0.08	0.03	0.08
mu	0	-0.23	-0.2	1	-0.2	-0.05	0.12	0.05	0.04
md	0	-0.23	-0.2	-0.2	1	0.09	-0.4	-0.1	-0.15
MS(*)	-0.44	0.13	-0.12	-0.05	0.09	1	0.4	0.8	0.64
SD(*)	-0.54	0.12	-0.08	0.12	-0.4	0.4	1	0.56	0.57
MAR	-0.7	-0.01	0.03	0.05	-0.1	0.8	0.56	1	0.91
MRMSR	-0.71	0.06	0.08	0.04	-0.15	0.64	0.57	0.91	1

H=Height, MS=Maximum Separation, SD=Separation Depth, MAR=Maximum Acceleration Ratio, MRMSR=Maximum RMS Acceleration Ratio (*)=In ft.

Table 9.16 R^2 values of regression models in the form of $\hat{y} = \hat{a} + \hat{b}H + \hat{c}\theta + \hat{d}\phi + \hat{e}(mu) + \hat{f}(md)$.

DV		$R^2(\%)$	
		U/S	D/S
MS	Norm	67.4	49.2
	Un-Norm	71.4	22.3
SD	Norm	59.7	47.3
	Un-Norm	95.1	47.3
MAR		26.8	49.3
MRMSR		59.3	53.8

DV= Dependent Var., MS= Max. Sep., SD= Sep. Depth, MAR= Max. Acce. Ratio, MRMSR= Max. RMS Acce. Ratio.

Table 9.17 R^2 values of linear regression models with selected independent variables.

		Norm		Un-Norm	
DV		U/S	D/S	U/S	D/S
MS	IV	H, θ, mu	H	H, θ, mu	H, θ, ϕ
	$R^2(\%)$	66.7	47.9	69.8	21.1
SD	IV	H, θ, ϕ	H, md	H	H, md
	$R^2(\%)$	56.8	44.6	93.2	44.6
MAR	IV	H, θ, ϕ	H	H, θ, ϕ	H
	$R^2(\%)$	26.8	48.2	26.8	48.2
MRMSR	IV	H, mu	H	H, θ, mu	H
	$R^2(\%)$	57.1	50.8	58.3	50.5

DV= Dependent Var., IV= Independent Var., MS= Max. Sep., SD= Sep. Depth, MAR= Max. Acce. Ratio, MRMSR= Max. RMS Acce. Ratio.

Table 9.18 R^2 values of second-degree linear regression models in the form of $\hat{y} = \hat{a} + \hat{b}x + \hat{c}x^2 + \hat{d}H$.

DV	IV	$R^2(\%)$	
		U/S	D/S
MS	H, θ	60.4	49.5(*)
	H, ϕ	33.3	48.4(*)
	H, mu	53.6	48.4(*)
	H, md	33.1	45.0(*)
SD	H, θ	95.1	30.6
	H, ϕ	93.4	29.5
	H, mu	93.3	30.9
	H, md	93.3	44.7
MAR	H, θ	23.9	48.3
	H, ϕ	23.0	48.4
	H, mu	19.5	48.5
	H, md	18.6	49.1
MRMSR	H, θ	51.1	51.2
	H, ϕ	48.5	51.7
	H, mu	57.6	51.0
	H, md	47.1	54.0

(*)= Normalized, DV= Dependent Var., IV= Independent Var., MS= Max Sep., SD= Sep. Depth, MAR= Max. Acce. Ratio, MRMSR= Max. RMS Acce. Ratio.

Table 9.19 Best multivariate regression models selected for U/S interface performance parameters.

$R^2(\%)$	DV		$\hat{a}$		$\hat{b}$		$\hat{c}$		$\hat{d}$	
69.8	MS(*)	=	-0.36	+	0.0049	H	- 0.015	θ	+ 0.058	mu
93.2	SD(*)	=	19.51	+	0.521	H				
26.8	MAR	=	2.99	-	0.0065	H	- 0.116	θ	+ 0.126	ϕ
57.1	MRMSR	=	4.62	-	0.0044	H	- 0.433	mu		

(*)= Un-Normalized

Table 9.20 Best multivariate regression models selected for D/S interface performance parameters.

$R^2(\%)$	DV		$\hat{a}$		$\hat{b}$			$\hat{c}$			$\hat{d}$	
60.4	MS(⋆)	=	0.0627	-	0.00016	H						
44.6	SD(⋆)	=	127.41	-	0.09	H	-	14.13	md			
49.1	MAR	=	7.5	-	0.965	md	+	0.114	md^2	-	0.011	H
54.0	MRMSR	=	8.724	-	3.039	md	+	0.481	md^2	-	0.0074	H

(⋆)=Normalized

9.5 Summary and Conclusions

This chapter discusses the statistical relations between controlling parameters and interface performance parameters. Standard deviation, mean, and minimum and maximum ranges of interface performance parameters for each dam height are presented. Additionally, second-order polynomial best fit curves and correlation coefficients are also presented. Multiple regression analyses have been performed including the dam height as one of the independent variable and related R^2 values are tabulated. Following conclusions are drawn from the statistical assessment of parametric effects.

- U/S maximum separation is strongly dependent on U/S interface angle, θ for all heights. Increase in θ causes decrease in maximum separation. The related correlation coefficients are all greater than 0.82.
- U/S maximum separation is also significantly affected by U/S soil slope, mu. Increase in mu causes increase in U/S maximum separation.
- θ has strong decreasing effect on U/S depth of separation and maximum horizontal acceleration ratio for 300 and 400 ft high dams. The related R^2 values are greater than 0.83.

- The decreasing effect of ϕ on all D/S interface performance parameters is more evident in 300, and 400 ft high dams.
- In most cases maximum RMS ratio shows more consistent dependency on controlling parameters than maximum horizontal acceleration ratio.
- More strong relations are found between controlling parameters and interface performance parameters in 300, and 400 ft high dams than shorter dams.
- U/S, and D/S soil slopes have insignificant effect on performance parameters of opposite sides.
- In most cases second-order polynomial best fit curves are found to be adequate in modelling the variation of interface performance parameters.
- Dam height has been found to have strong effect on estimating the interface performance parameters.
- Including dam height in the multiple regression model caused decrease in R^2 values compared to single variable regression models, but they can still be considered as acceptable.

10. Summary, Conclusions and Recommendations

10.1 Summary

The interface stability of a composite dam under earthquake shaking is quite critical to its seismic safety. In the evaluation of the seismic stability of a composite dam, besides others, the main problem is the dynamic interaction between concrete gravity dam and soil embankment. The wrap-around sections are the transitional sections of a dam where it changes from concrete dam to embankment wing dams. This study covers both 2-D and 3-D modelling of interface area, elastic-plastic material model, effect of different geometric configurations of the interface on the separation, separation depth, horizontal acceleration, and earthquake induced stresses along the both upstream and downstream interfaces.

Literature survey has revealed that nobody has conducted any research attempt on Interface Behavior of Composite Dams (IBCD), except some preliminary numerical analyses. Therefore IBCD research is in its early stages, and this thesis is the first detailed research performed to study dynamic IBCD. Through the nonlinear finite element analyses, quite a bit of research effort has been devoted to the study of IBCD, and an inordinately amount of data was generated. To gain a good insight into the IBCD problem, the results have been interpreted carefully.

In the following paragraphs a brief summary of each chapter is provided, and next sections present the conclusions drawn from dynamic IBCD study, and finally recommendations for future work are discussed.

In Chapter 2 findings from the literature survey on composite dams, soil-concrete interface models, numerical analysis codes to analyze IBCD, constitutive soil models, and pore pressure generation models are discussed.

Chapter 3 describes the softwares used in 2-D, and 3-D parametric FE analyses. Pre and post processors, and NIKE3D [47] are presented. TrueGrid [83] and GRIZ [72] have been used as the pre-processor and post-processor, respectively. Theoretical background of NIKE3D, its interface algorithm, and solution strategy are discussed.

Chapter 4 discusses the principles of dynamic centrifuge testing with emphasis on composite dams, and NIKE3D simulation of Stadler's [73] retaining wall centrifuge test. Wall deflection, earth pressure, and horizontal accelerations of both soil and wall are compared with experimental measurements. Moreover, horizontal acceleration of soil along the wall-soil interface is presented. Although it was not possible to make direct comparisons of amount of separation along the wall-soil interface, calculated zero interface pressures were in good agreement with the measured data. Zero interface stresses are indication of possible separation and in all NIKE3D analysis results zero interface pressure and maximum separation regions match very well. Therefore NIKE3D

is proven to be a reliable numerical analysis tool to assess the separation potential along a soil-concrete interface.

Chapter 5 summarizes the input parameters used in the FE analyses, and discusses them in detail. Input parameters include; input ground motion, 2-D and 3-D FE mesh, numerical damping, material, and interface model parameters.

Chapter 6 presents the natural vibration characteristics of 2-D composite dams, and 2-D parametric nonlinear FE analyses that have been performed to assess the potential for the interface separation, and the influence of the height, upstream slope angle, upstream embankment slope, downstream interface slope and the downstream embankment slope on interface performance parameters such as: magnitude of interface separation, separation depth, maximum acceleration, maximum RMS acceleration ratio and static, minimum dynamic, and maximum dynamic interface pressures. Results are demonstrated through a series of graphs that relate geometric parameters to interface performance parameters.

Chapter 7 presents the study on the behavior of 3-D model under Koyna Dam Earthquake Record with linear elastic model. The effects of nonlinear soil model and all three components of ground motion are also presented. Maximum separation and acceleration results are compared with 2-D analysis results. Surface contours of maximum separation at U/S, D/S, and longitudinal interfaces are presented. All findings are interpreted and compared to 2-D analysis findings where possible.

Chapter 8 explains a case study of 180 ft high Folsom dam which was analyzed using NIKE2D. The results are presented in terms of maximum separation, separation depth and static, and maximum interface stresses along the upstream interface. The results are compared with the parametric FE analysis of 200 ft high composite dam. Good agreement was observed in separation depth.

Chapter 9 characterizes the statistical relations between controlling variables, called as independent variables, and maximum interface performance parameters, called as dependent variables. The statistical assessment has been performed through the investigation of sample mean, and standard deviation of dependent variables; second-order polynomial best fit models; and squared correlation coefficient, R^2.

10.2 Conclusions

The stability of the soil-concrete interface in composite dams under seismic load was studied extensively using the computer code, NIKE3D, developed at the Lawrence Livermore National Laboratory. The code performance in studying the interface behavior is calibrated using the centrifuge test results on a retaining wall with a dry sand backfill. The comparison of results shows that the code is effective as a study tool for the interface behavior of composite dams under seismic shaking.

Dynamic analyses were performed on the composite dams under Koyna earthquake shaking using only one set material properties. The findings from the extensive plane-strain analyses are concluded as follows:

- The soil-concrete interface can separate and close during a seismic event. The separation/closure phenomenon is repetitive and can take place anywhere along the interface.
- The maximum separation and the maximum depth of separation where the gap occurs increase with the dam height. The maximum separation also increases with the separation depth, and maximum soil response acceleration ratio, and decreases with the respective upstream or downstream slope of concrete face.
- During the upward propagation the ground motion amplifies. In the incident of interface separation, the embankment ground motion amplification is even more severe. This subsequently results in a very high interface earth pressure upon the separation closure.
- The maximum dynamic earth pressure is about 1.3 to 1.8 times the static earth pressure.

Since the wrapped-around section of a composition dam is in general three-dimensional, three-dimensional analyses were also carried out to investigate the potential difference between the plane-strain and three-dimensional simulations. The findings are summarized as follows:

- Applying only the maximum horizontal component in the transverse direction, three-dimensional effects using elastic soil model yield much smaller maximum embankment acceleration for all dams, but larger separation for higher dams along both upstream and downstream interfaces. The maximum separation also

found to increase with the dam height. The separation, in all cases, can occur throughout the complete depth of the dam while not simultaneously. No significant interface problem along the transverse interface.

- When Ramberg-Osgood soil is used, the separation and separation depth significantly decreases compared to the case with elastic soil. This shows the significant soil model dependency of the interface behavior.

The simultaneous imposition of all three components of ground motion to the 400 ft high dam with elastic soil causes significant increase in the separation along all three interfaces and the separation takes place throughout the whole depth while not simultaneously.

10.3 Recommendations for Further Study

While the study is extensive, it is preliminary. Much work is needed to gain further insight into the problem of soil-concrete interface behavior in composite dams. Since many composite dams of over 100 feet height exist in the world and many in seismically active areas, it is important to put this aspect of dam safety to rest through vigorous study. It is recommended to pursue further research in the following areas:

- Only elastic and Ramberg-Osgood models were used. The analysis results showed a strong soil model dependency of the interface behavior. It is recommended to investigate the soil model effect further.

- The best way to calibrate the effectiveness of a computer code in simulating the interface behavior in dam is by the way of centrifugal modelling. It is recommended to perform centrifugal tests to provide the datum for checking the validity of the computer codes and soil models.
- The preliminary three-dimensional analysis shows the significant effect of imposing all three components of ground motion on the interface behavior of composite dams, it is recommended to investigate further the effect of the imposition of all three components of ground motion and earthquake magnitudes on the interface behavior.
- To allow the problem to be manageable in this stage of study, while knowing it is extremely important, the pore water pressure was never considered. The saturated soils in the upstream area will cumulate excess pore water pressure during the seismic shaking, it is strongly recommended to study the impact of the excess pore water pressure on the interface behavior under seismic shaking. This can be accomplished via uncoupled formulation, partially coupled formulation or coupled Biot formulation.
- In this study the reservoir hydrodynamic effects was not considered. Instead, the hydrostatic water pressure was applied along the upstream slope. It is recommended to include the full hydrodynamic effect in the future study.

NOTATION INDEX

- U/S: Downstream
- D/S: Upstream
- `IBCD`: Interface Behavior of Composite Dams
- θ: Upstream interface angle
- ϕ: Downstream interface angle
- mu: Upstream soil slope
- mu: Downstream soil slope
- H: Height
- `reference configuration`: The geometric configuration when θ=0.0°, ϕ=26.6°, mu=2.0, and md=2.0.
- RMS: Root mean square
- γ: Unit weight
- ρ: Density
- E: Young's modulus
- G: Shear Modulus
- V_s: Shear wave velocity
- K: Bulk Modulus
- μ: Friction coefficient

- ν: Poisson's ratio
- σ: Stress
- τ: Shear stress
- w: Frequency
- T: Period
- u: Displacement
- $\dot{u}$: Velocity
- $\ddot{u}$: Acceleration
- ϵ_v: Volumetric strain
- g: Gravitational acceleration
- $\mathbf{K}$: Stiffness matrix
- $\mathbf{M}$: Mass matrix
- $\mathbf{C}$: Damping matrix
- $\mathbf{F}$: Force Matrix
- NID: National Inventory of Dams
- DV: Dependent Variable
- IV: Independent Variable
- MS: Maximum Separation
- SD: Separation Depth
- MAR: Maximum Acceleration Ratio
- MRMSR: Maximum RMS Acceleration Ratio

A. APPENDIX Figures

A.1 Free Vibrational Behavior

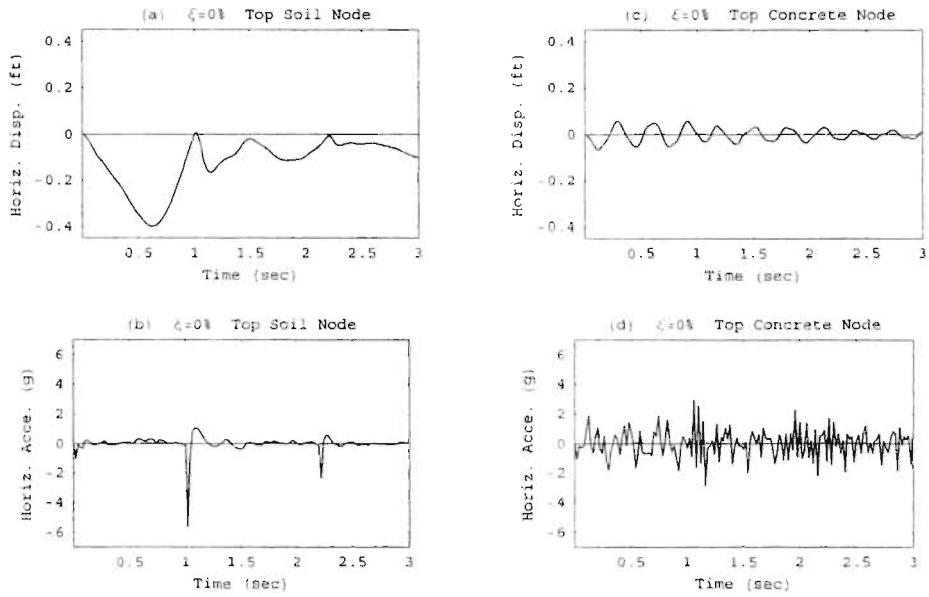

Figure A.1 Horizontal displacement and acceleration time histories of soil and concrete nodes at the crest, $\xi = 0\%$ (H=300).

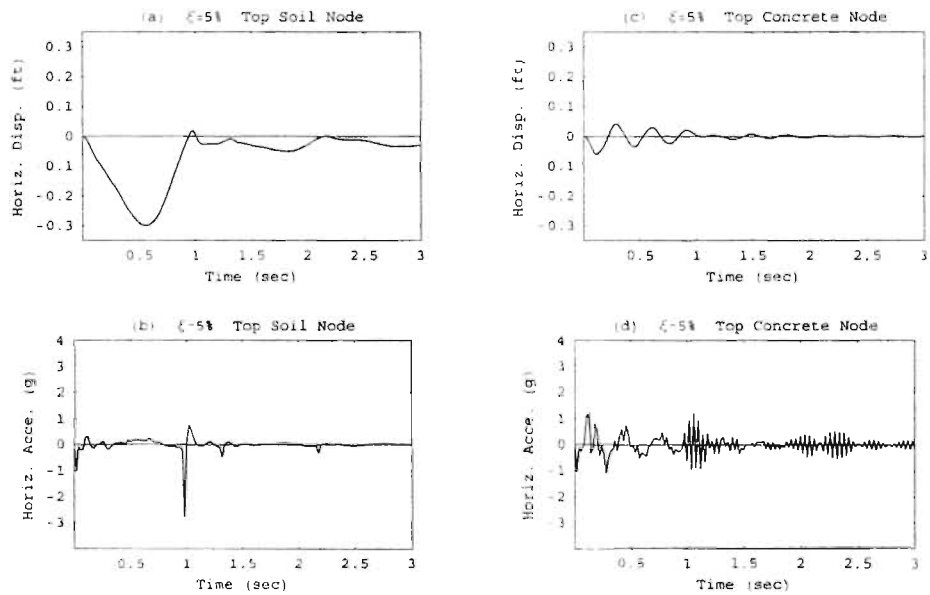

Figure A.2 Horizontal displacement and acceleration time histories of soil and concrete nodes at the crest, $\xi = 5\%$ (H=300).

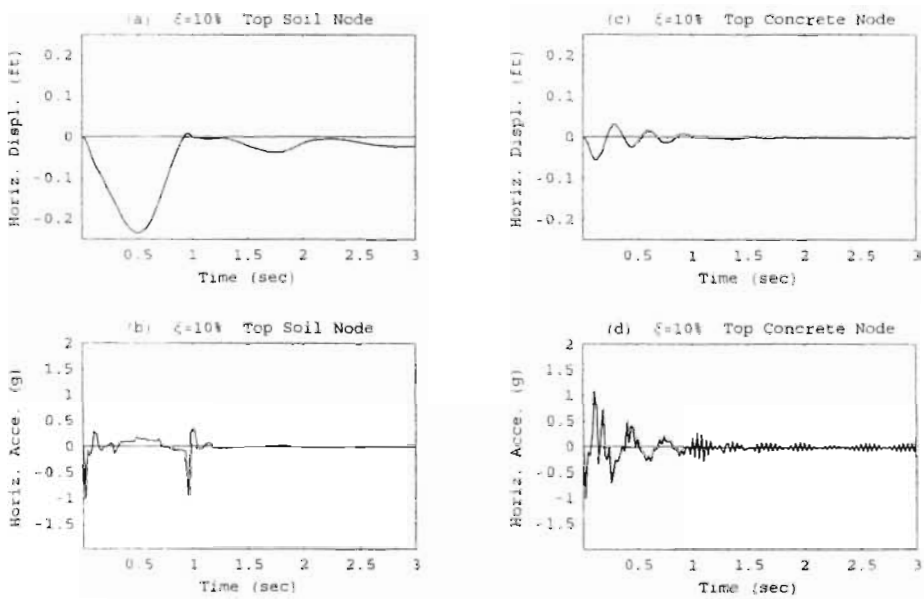

Figure A.3 Horizontal displacement and acceleration time histories of soil and concrete nodes at the crest, $\xi = 10\%$ (H=300).

A.2 2-D FE Results

A.2.1 H=100ft

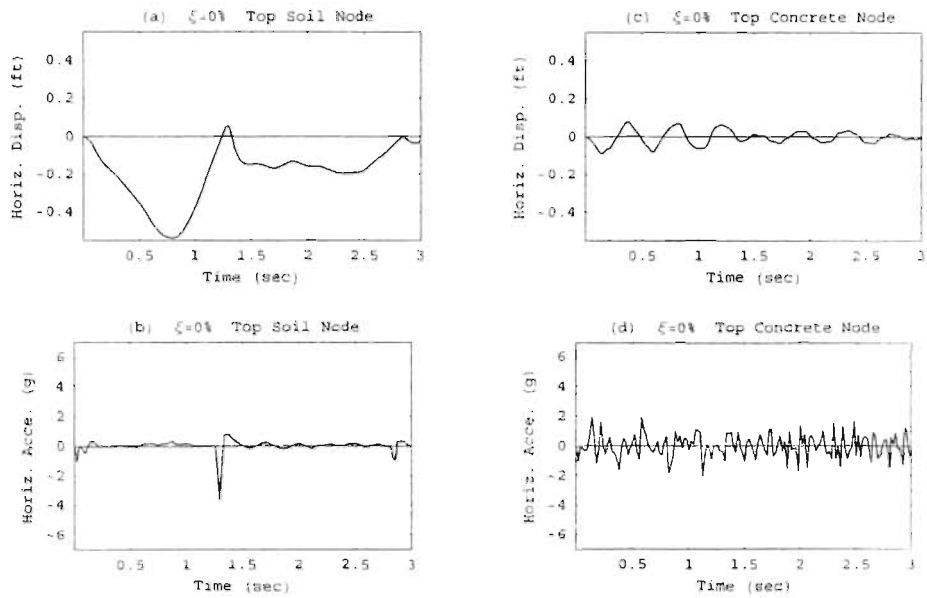

Figure A.4 Horizontal displacement and acceleration time histories of soil and concrete nodes at the crest, $\xi = 0\%$ (H=400).

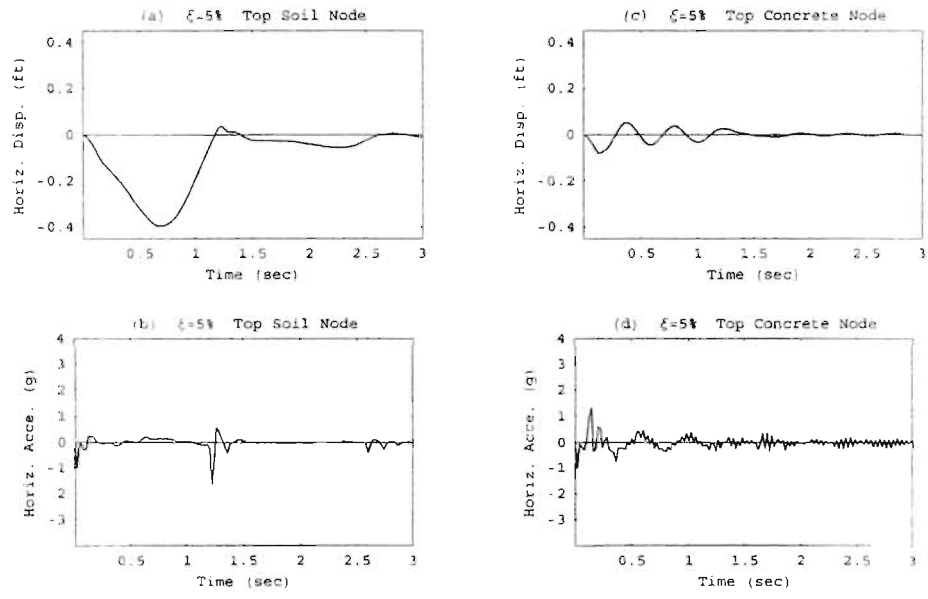

Figure A.5 Horizontal displacement and acceleration time histories of soil and concrete nodes at the crest, $\xi = 5\%$ (H=400).

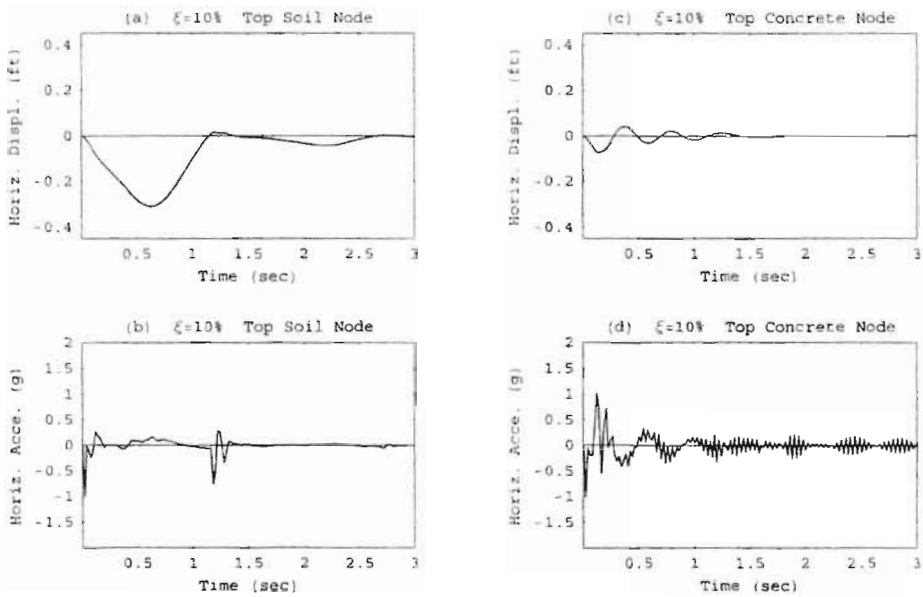

Figure A.6 Horizontal displacement and acceleration time histories of soil and concrete nodes at the crest, $\xi = 10\%$ (H=400).

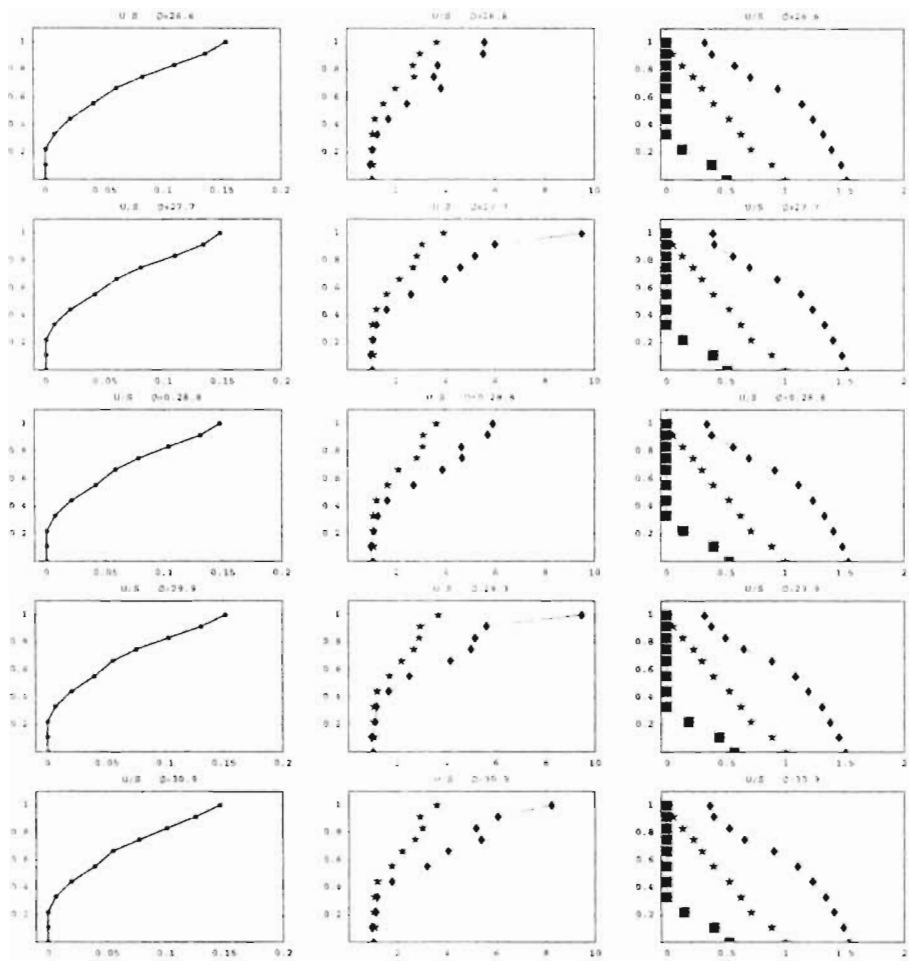

Figure A.7 Max. Separation, Max. Acceleration, and Nodal Interface Stresses (Max., Static, Min.) along the *UPSTREAM* Interface due to change of ϕ (in degrees) (H=100).

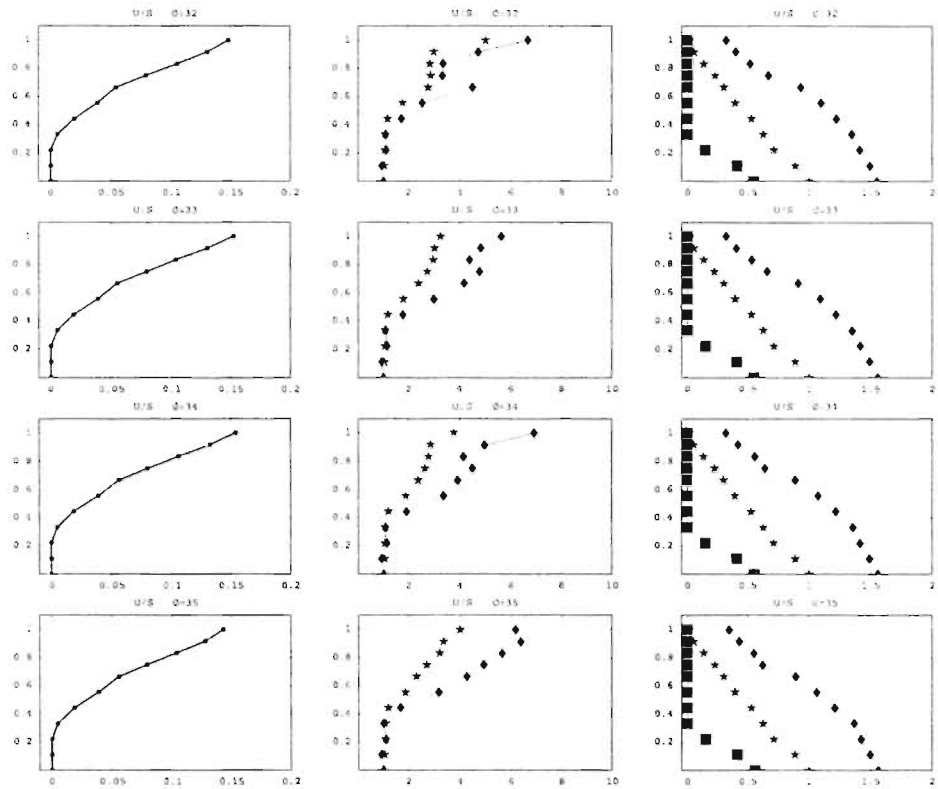

Figure A.8 (Continued from previous figure) Max. Separation, Max. Acceleration, and Nodal Interface Stresses (Max., Static, Min.) along the *UPSTREAM* Interface due to change of ϕ (in degrees) (H=100).

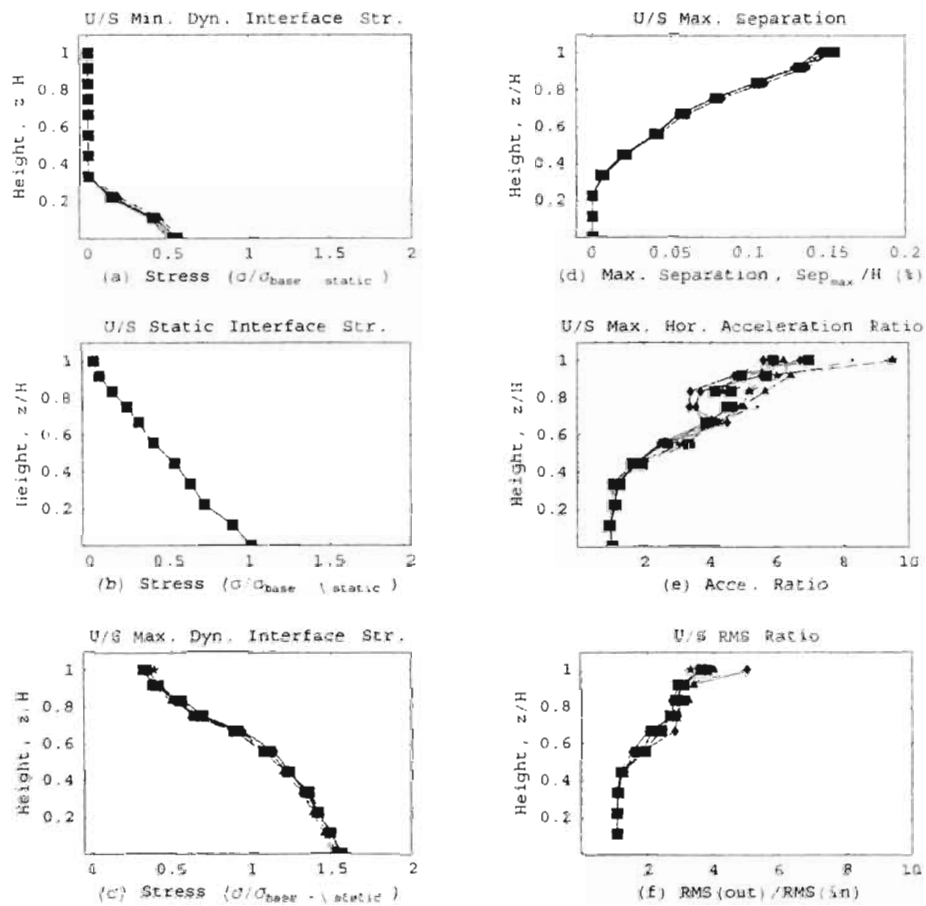

Figure A.9 Collective graphs of Max. Separation, Acceleration, and interface pressures along the *UPSTREAM* Interface at all ϕ's (H=100).

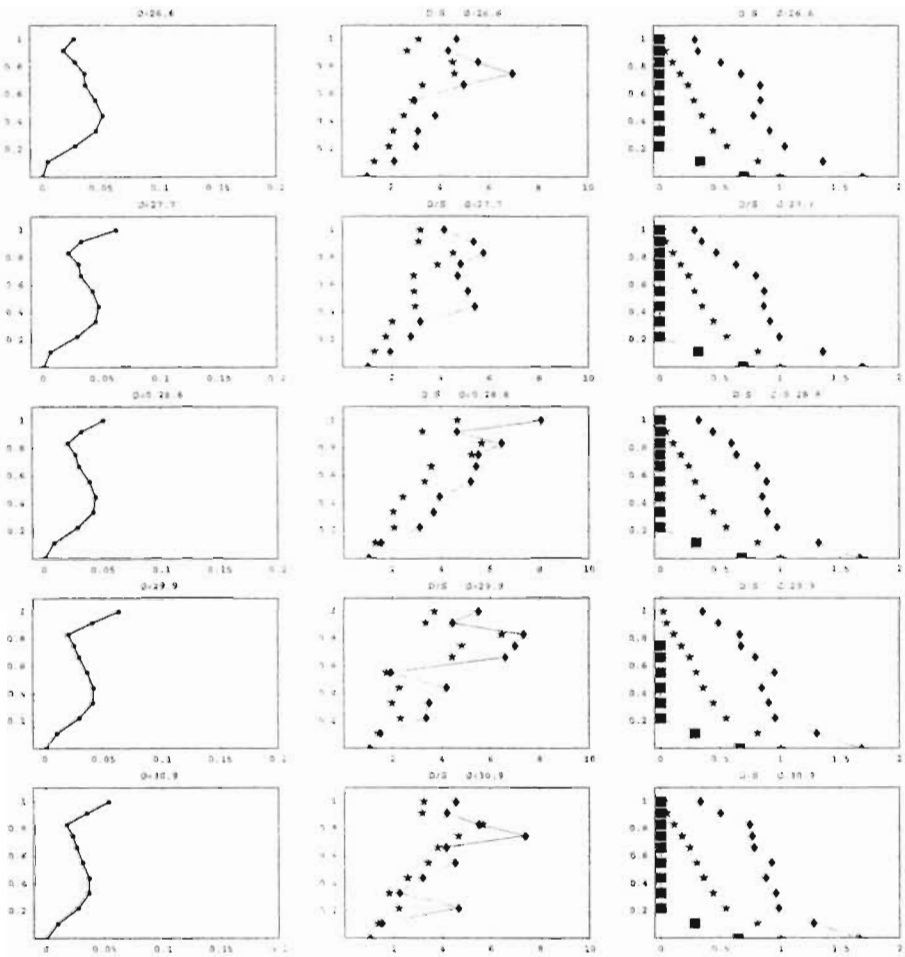

Figure A.10 Max. Separation, Max. Acceleration, and Nodal Interface Stresses (Max., Static, Min.) along the *DOWNSTREAM* Interface due to change of ϕ (in degrees) (H=100).

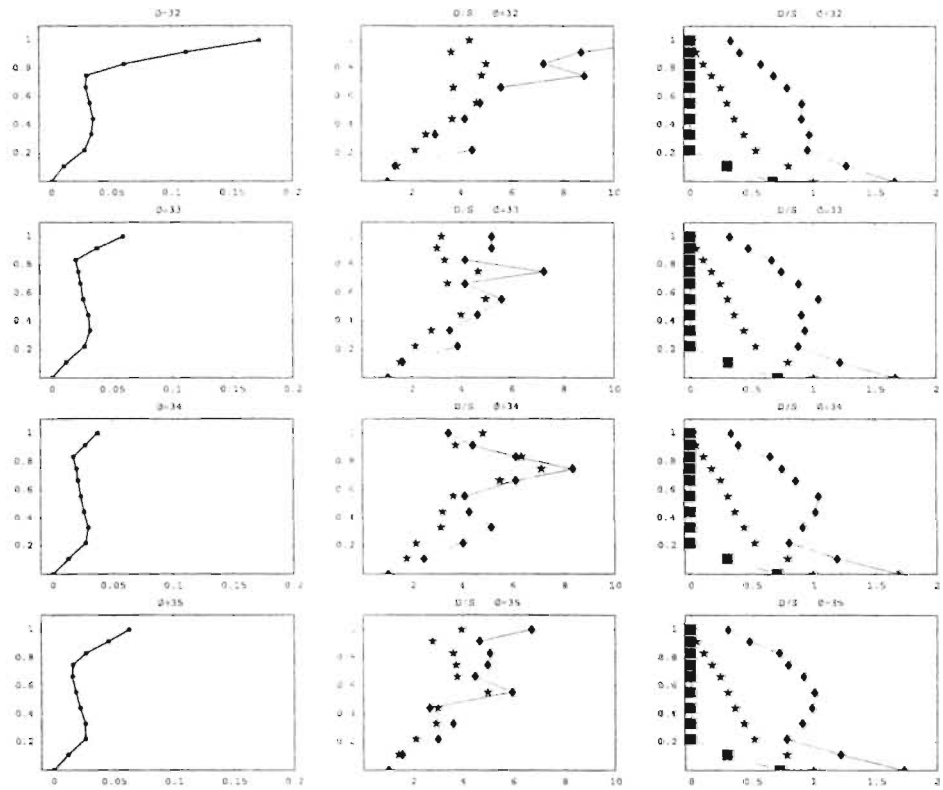

Figure A.11 (Continued from previous figure) Max. Separation, Max. Acceleration, and Nodal Interface Stresses (Max.. Static. Min.) along the *DOWNSTREAM* Interface due to change of ϕ (in degrees) (H=100).

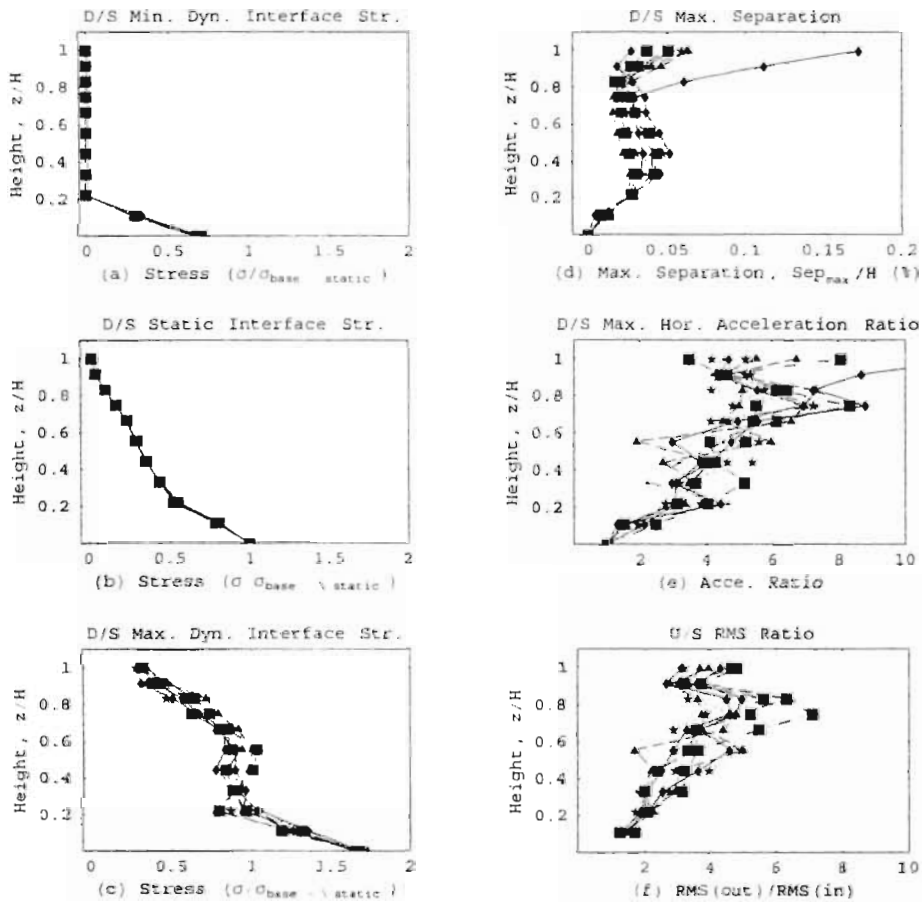

Figure A.12 Collective graphs of Max. Separation, Acceleration, and interface pressures along the *DOWNSTREAM* Interface at all ϕ's (H=100).

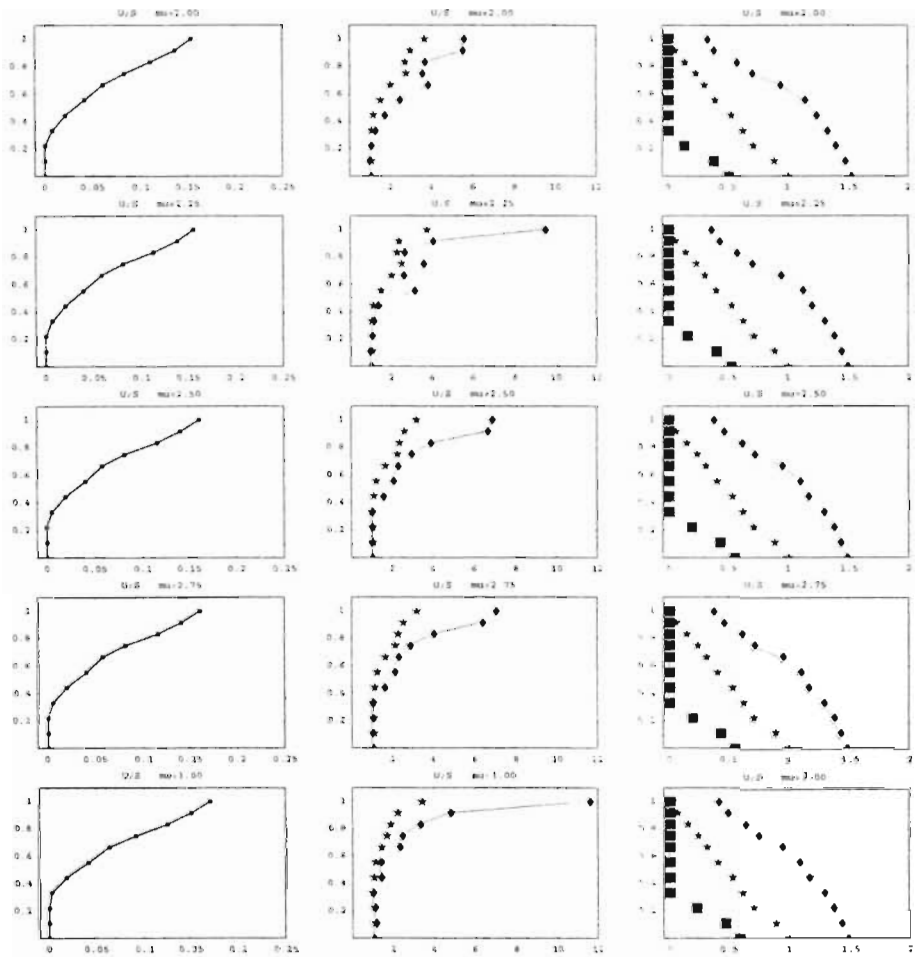

Figure A.13 Max. Separation, Max. Acce., and Nodal Interface Stresses (Max., Static, Min.) along the *UPSTREAM* Interface due to change of mu (H=100).

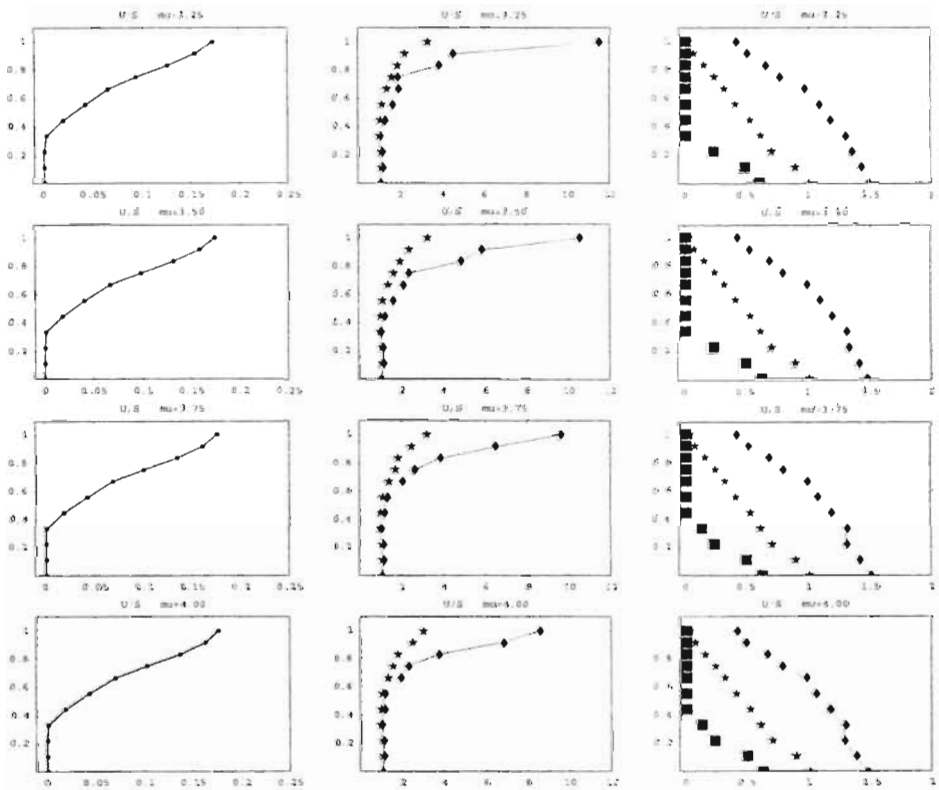

Figure A.14 (Continued from previous figure) Max. Separation, Max. Acceleration, and Nodal Interface Stresses (Max., Static, Min.) along the *UPSTREAM* Interface due to change of mu (H=100).

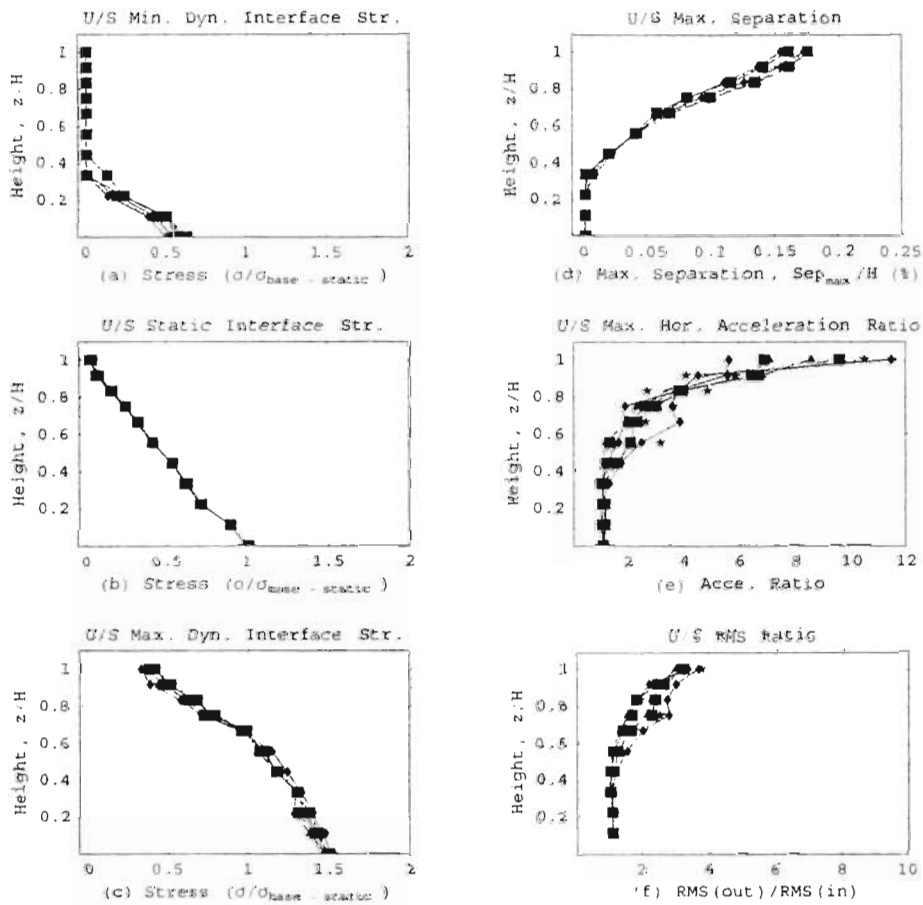

Figure A.15 Collective graphs of Max. Separation, Acceleration, and interface pressures along the *UPSTREAM* Interface at all *mu*'s (H=100).

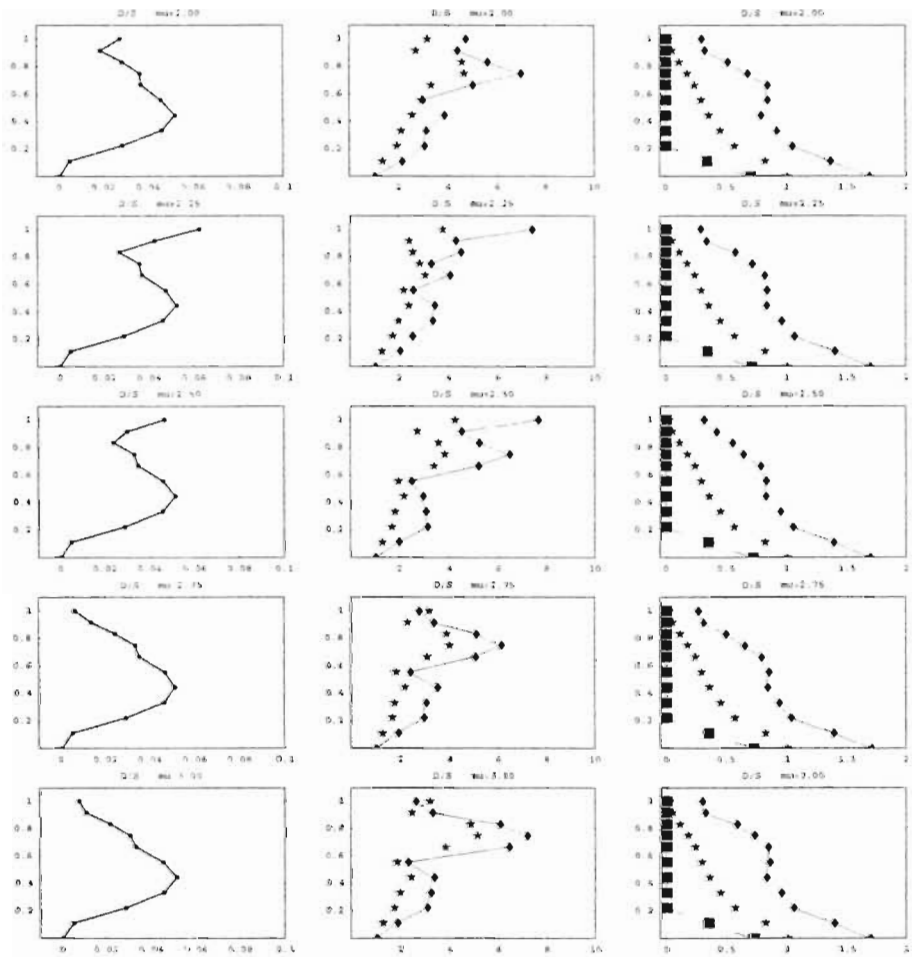

Figure A.16 Max. Separation, Max. Acce., and Nodal Interface Stresses (Max., Static, Min.) along the *DOWNSTREAM* Interface due to change of mu (H=100)

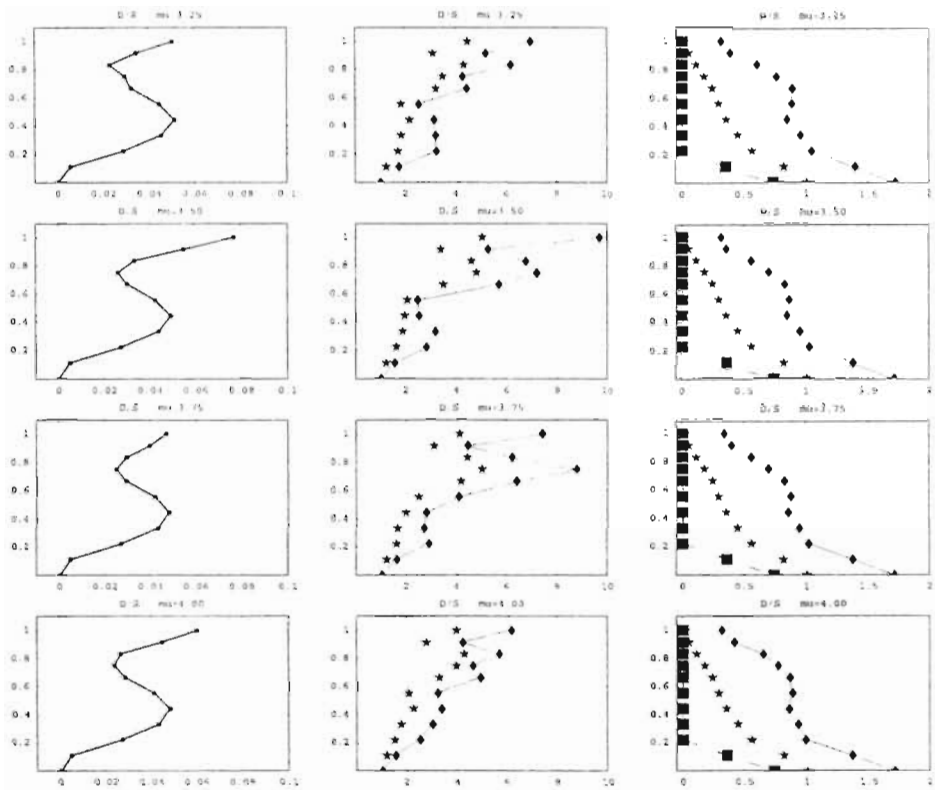

Figure A.17 (Continued from previous figure) Max. Separation, Max. Acceleration, and Nodal Interface Stresses (Max., Static, Min.) along the *DOWNSTREAM* Interface due to change of *mu* (H=100).

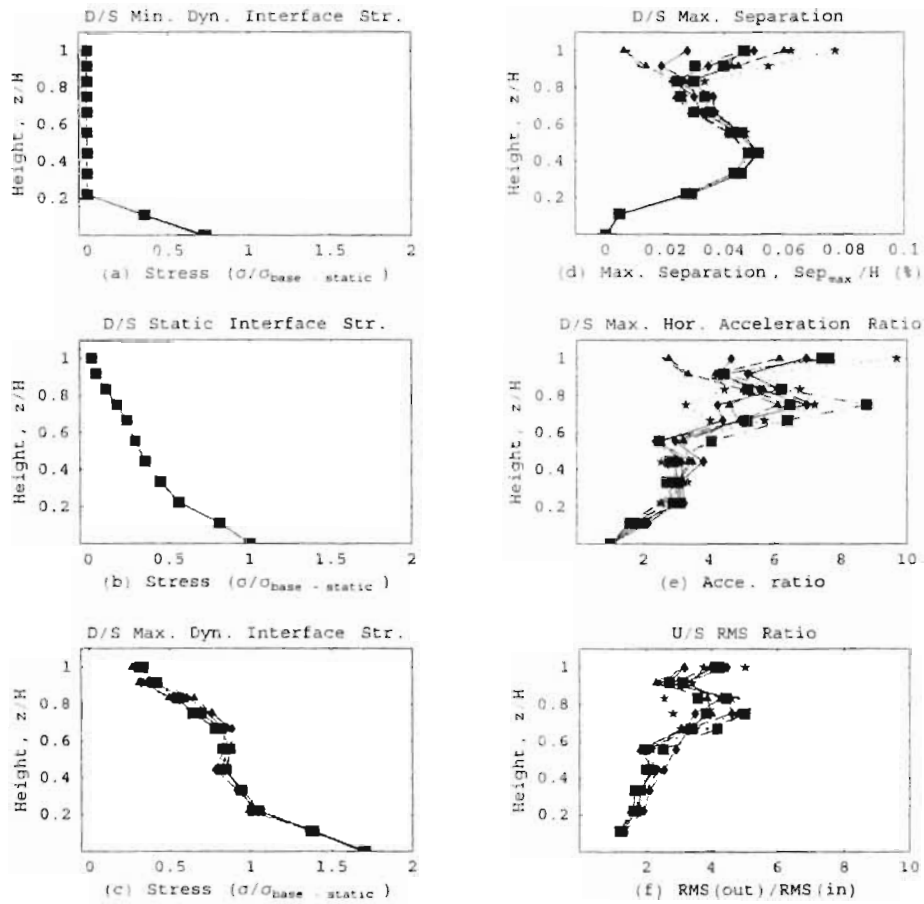

Figure A.18 Collective graphs of Max. Separation, Acceleration, and interface pressures along the *DOWNSTREAM* Interface at all *mu*'s (H=100).

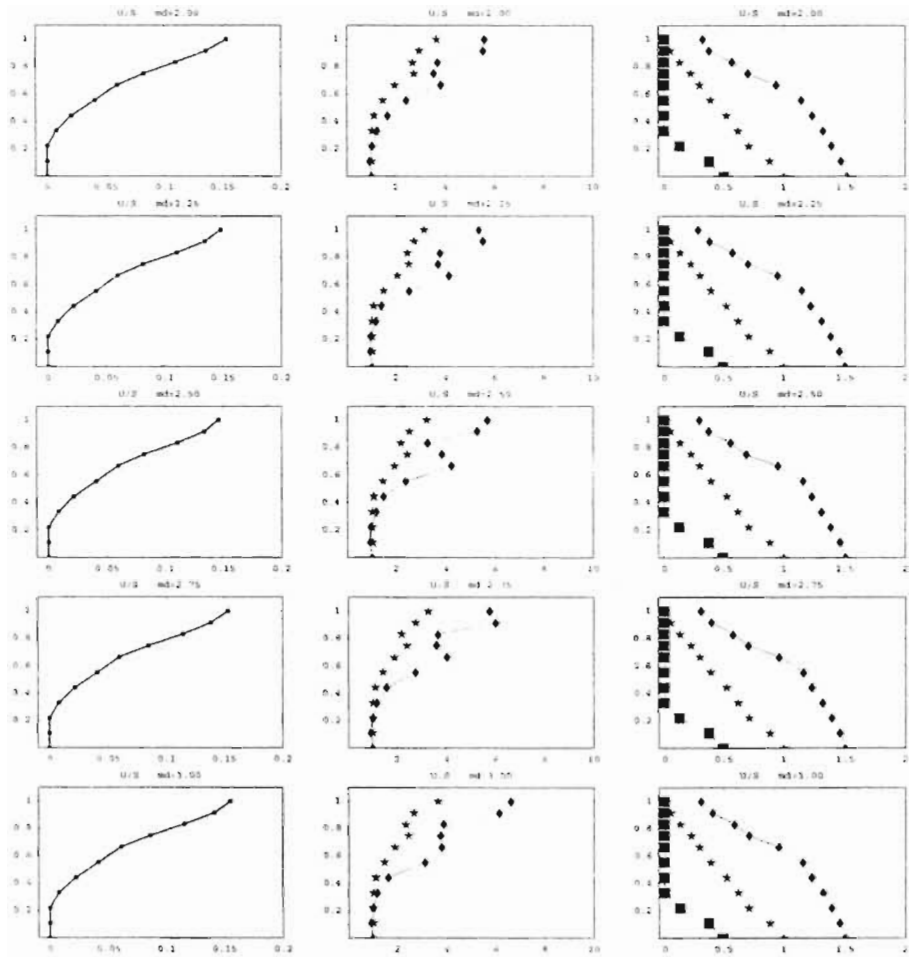

Figure A.19 Max. Separation, Max. Acce., and Nodal Interface Stresses (Max., Static, Min.) along the *UPSTREAM* Interface due to change of *md* (H=100).

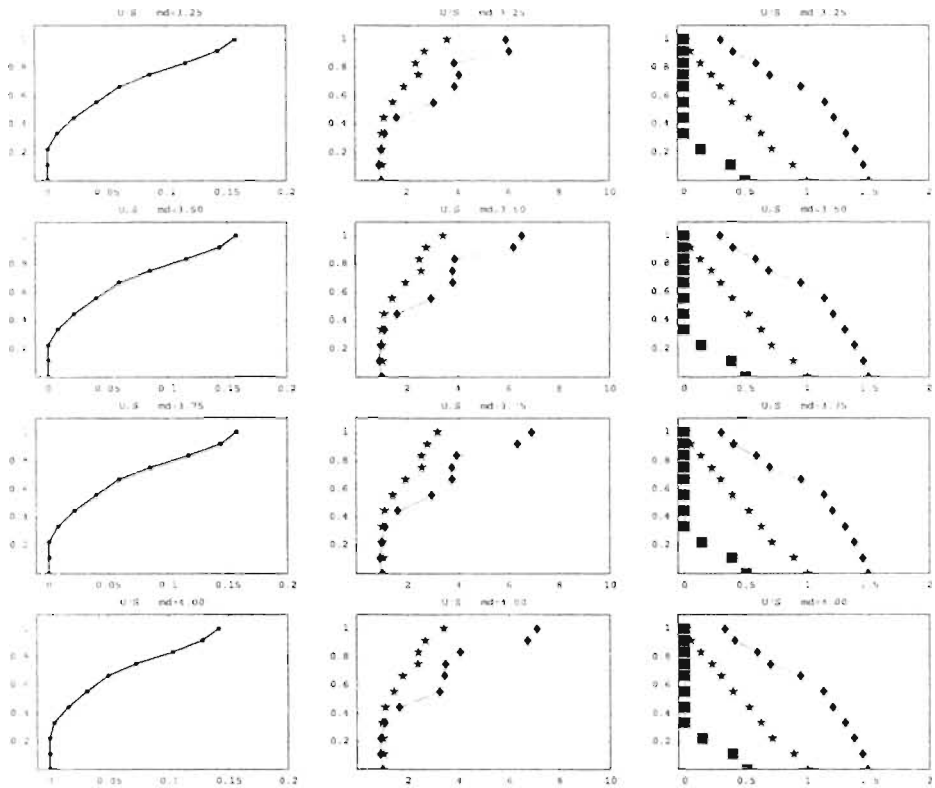

Figure A.20 (Continued from previous figure) Max. Separation, Max. Acceleration, and Nodal Interface Stresses (Max., Static, Min.) along the *UPSTREAM* Interface due to change of *md* (H=100).

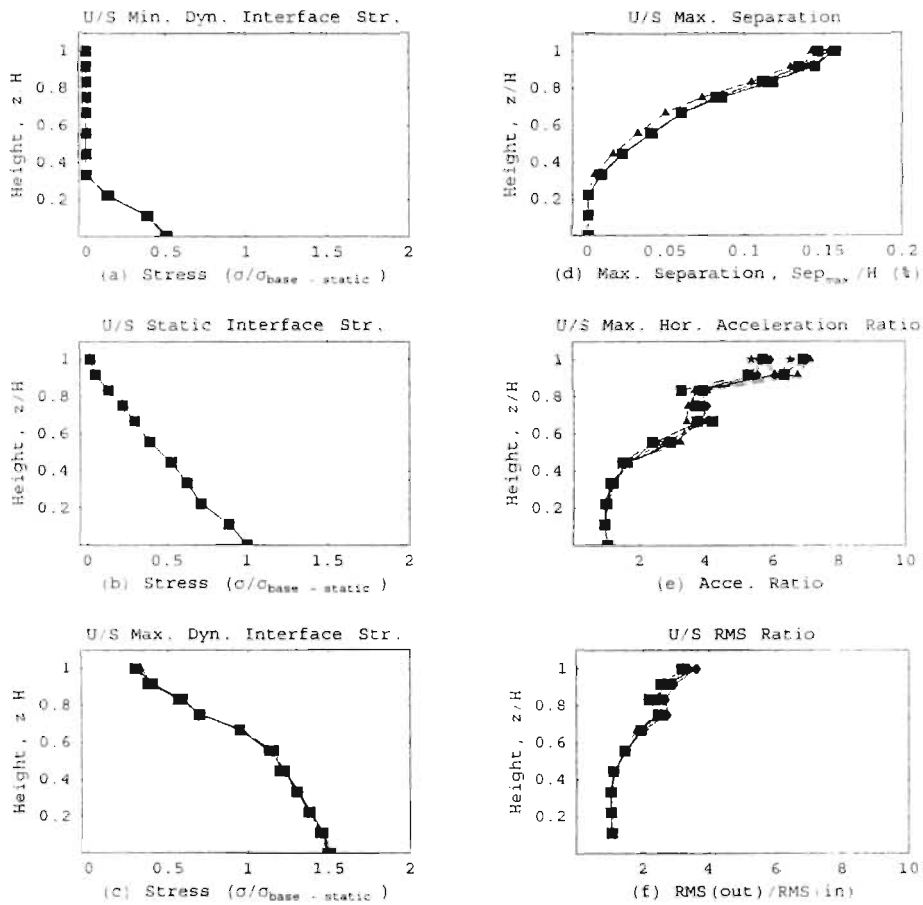

Figure A.21 Collective graphs of Max. Separation, Acceleration, and interface pressures along the *UPSTREAM* Interface at all *md*'s (H=100)

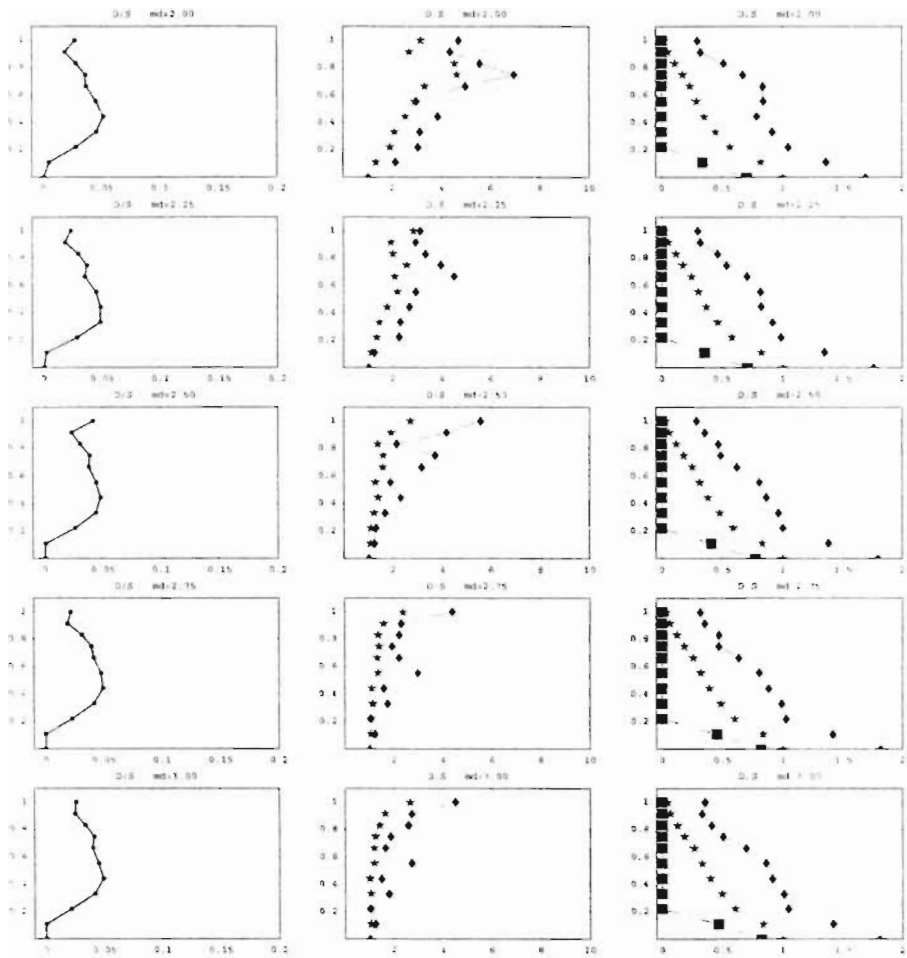

Figure A.22 Max. Separation, Max. Acceleration, and Nodal Interface Stresses (Max., Static, Min.) along the *DOWNSTREAM* Interface due to change of *md* (H=100).

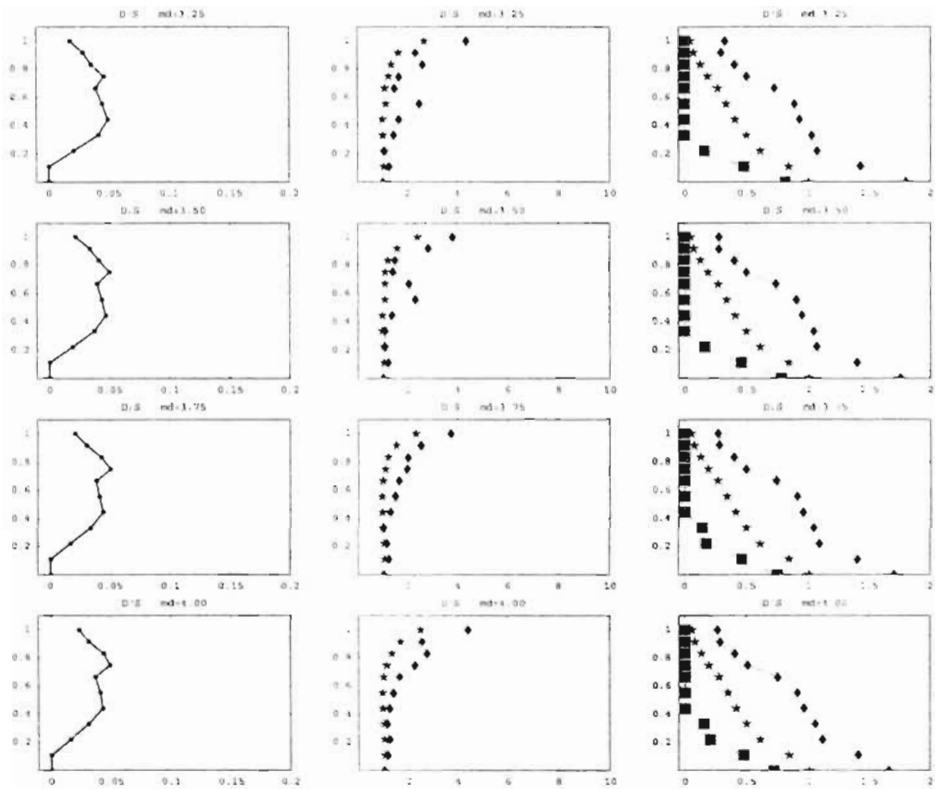

Figure A.23 (Continued from previous figure) Max. Separation, Max. Acceleration, and Nodal Interface Stresses (Max., Static, Min.) along the *DOWNSTREAM* Interface due to change of *md* (H=100).

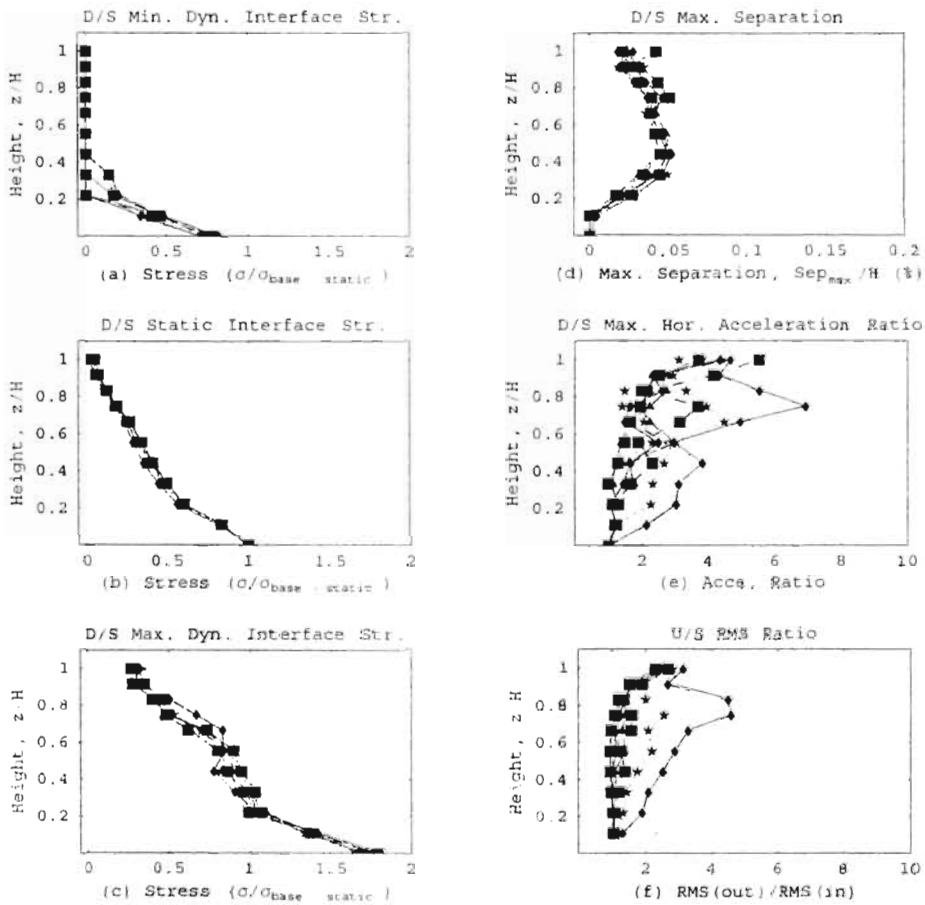

Figure A.24 Collective graphs of Max. Separation, Acceleration, and interface pressures along the *DOWNSTREAM* Interface at all *md*'s (II=100).

A.2.2 H=200ft

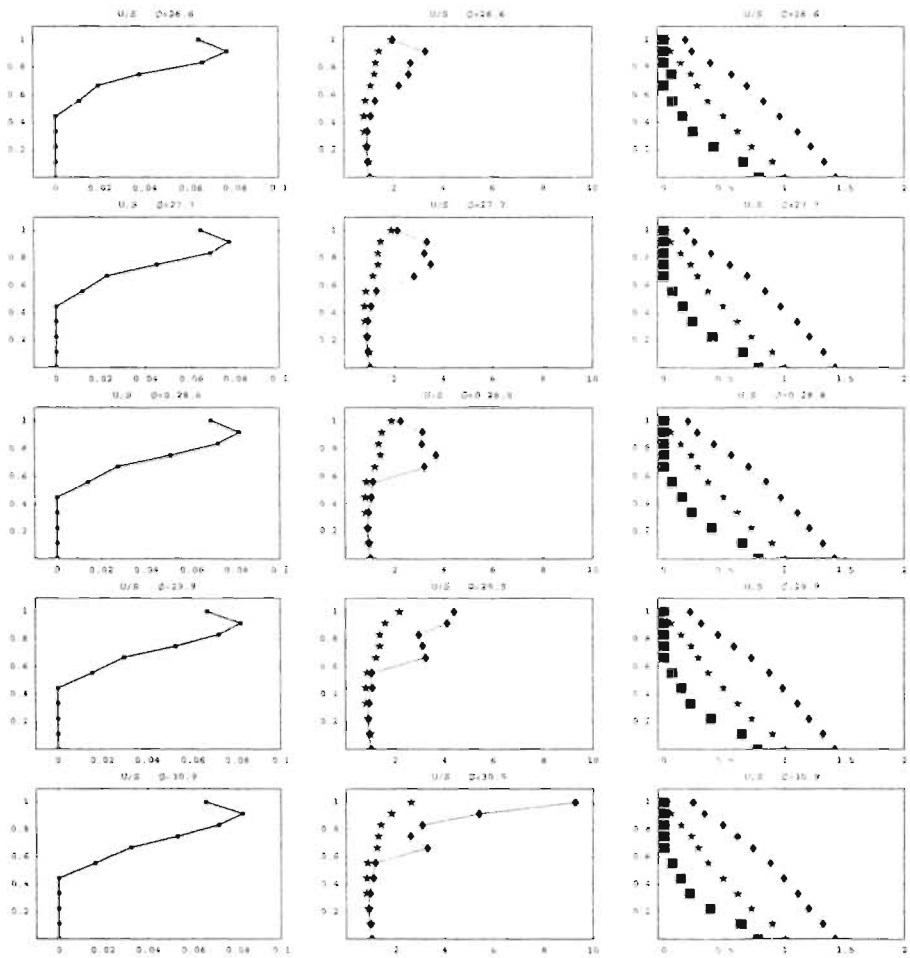

Figure A.25 Max. Separation, Max. Acceleration, and Nodal Interface Stresses (Max., Static, Min.) along the *UPSTREAM* Interface due to change of φ (in degrees) (H=200).

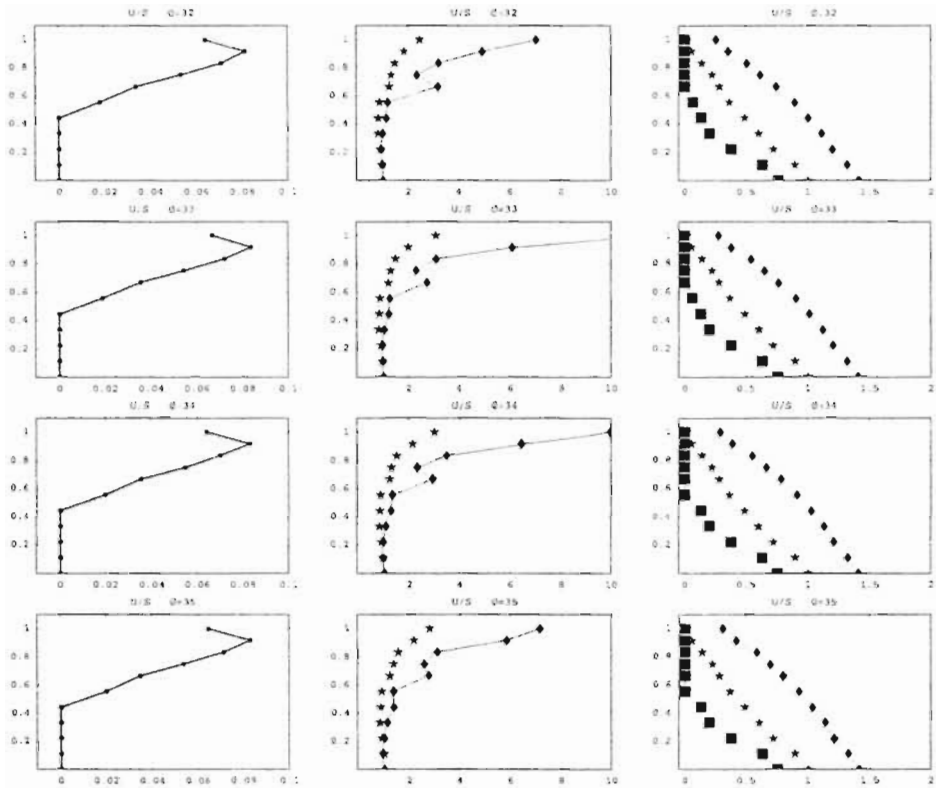

Figure A.26 (Continued from previous figure) Max. Separation, Max. Acceleration, and Nodal Interface Stresses (Max., Static, Min.) along the *UPSTREAM* Interface due to change of ϕ (in degrees) (H=200).

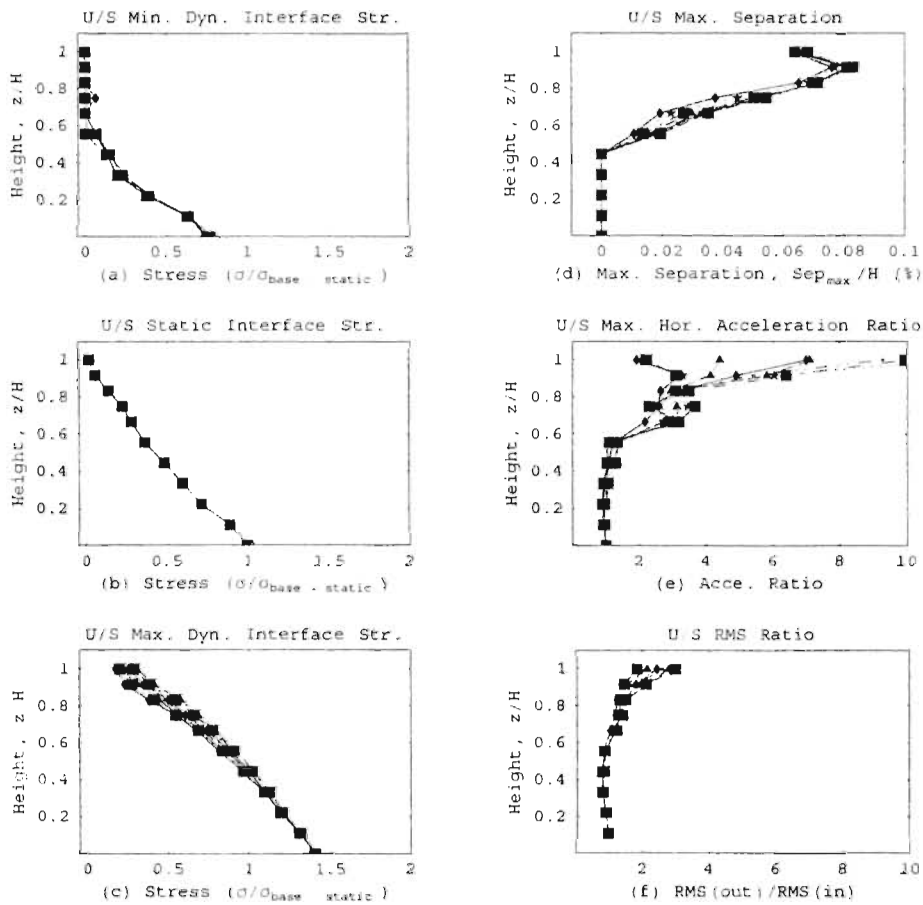

Figure A.27 Collective graphs of Max. Separation, Acceleration, and interface pressures along the *UPSTREAM* Interface at all ϕ's (H=200).

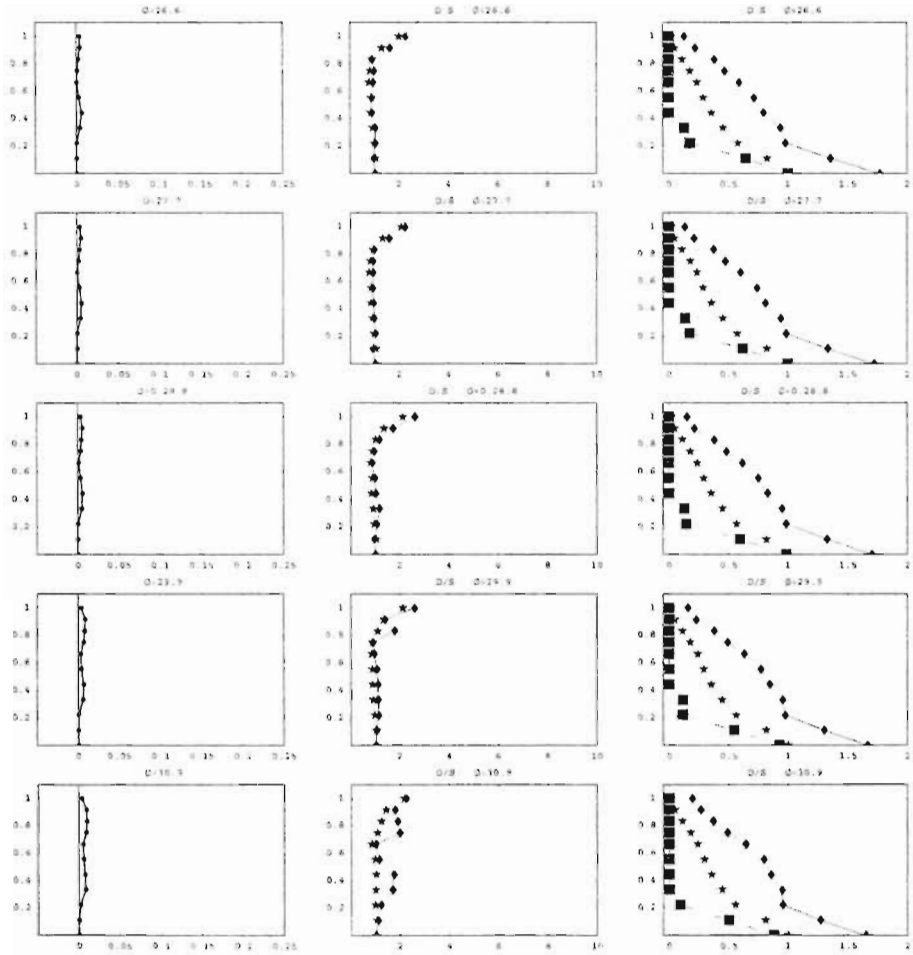

Figure A.28 Max. Separation. Max. Acceleration, and Nodal Interface Stresses (Max., Static, Min.) along the *DOWNSTREAM* Interface due to change of ϕ (in degrees) (H=200).

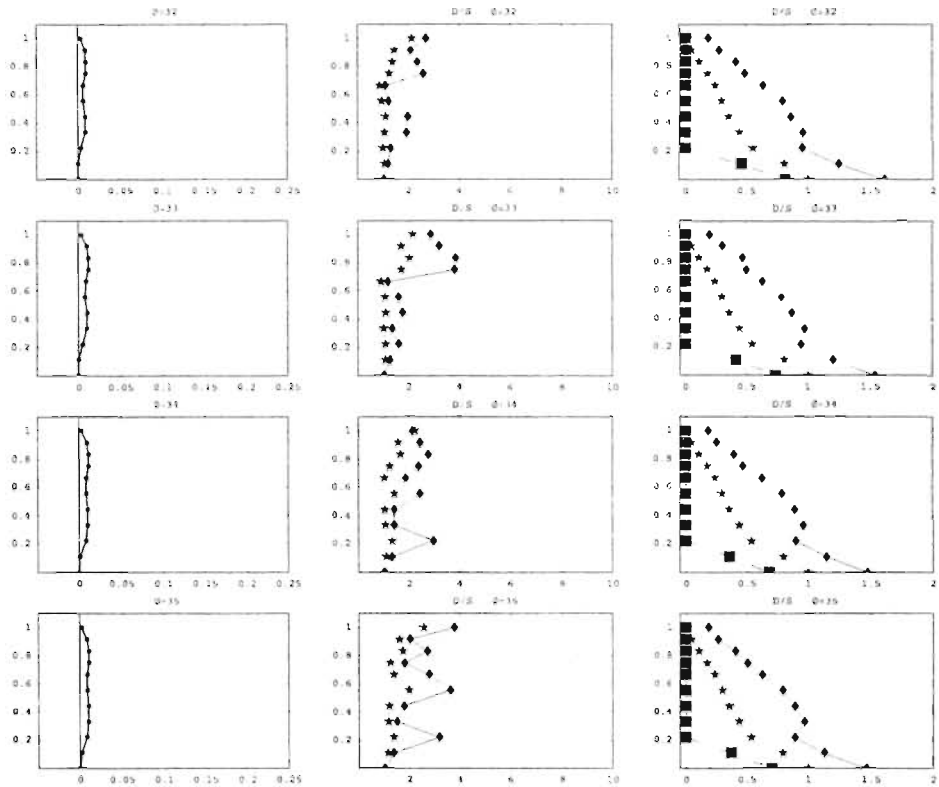

Figure A.29 (Continued from previous figure) Max. Separation, Max. Acceleration, and Nodal Interface Stresses (Max., Static, Min.) along the *DOWNSTREAM* Interface due to change of ϕ (in degrees) (H=200).

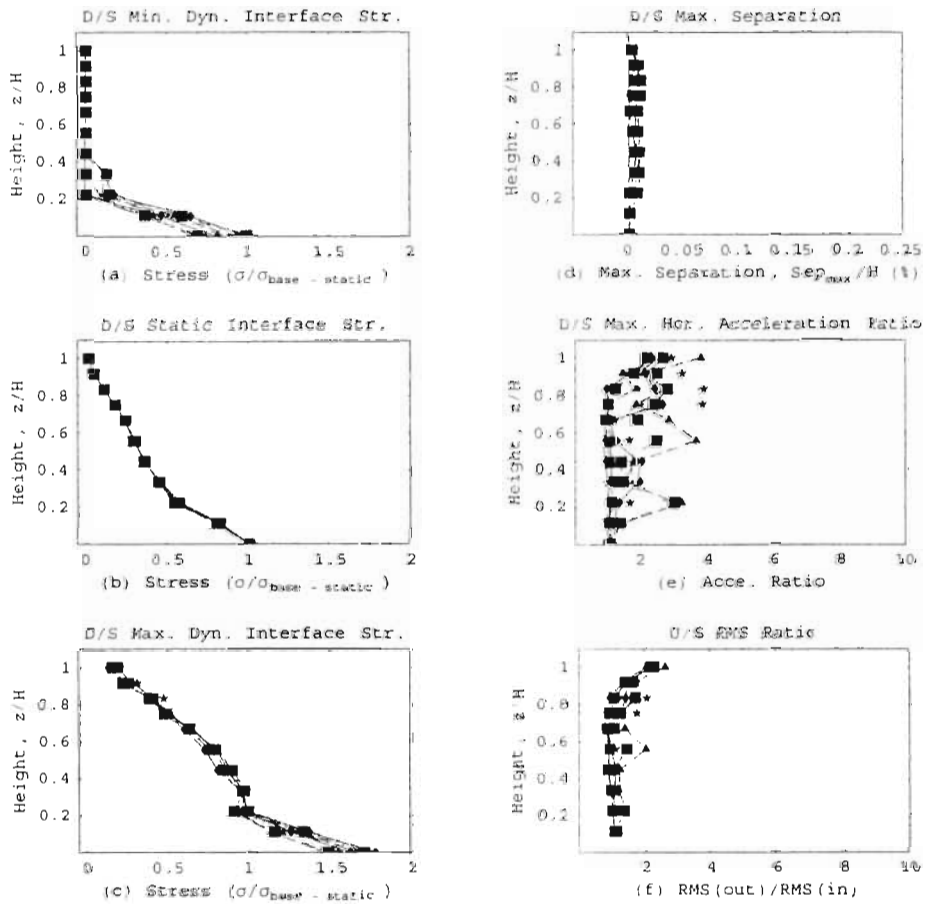

Figure A.30 Collective graphs of Max. Separation, Acceleration, and interface pressures along the *DOWNSTREAM* Interface at all φ's (H=200).

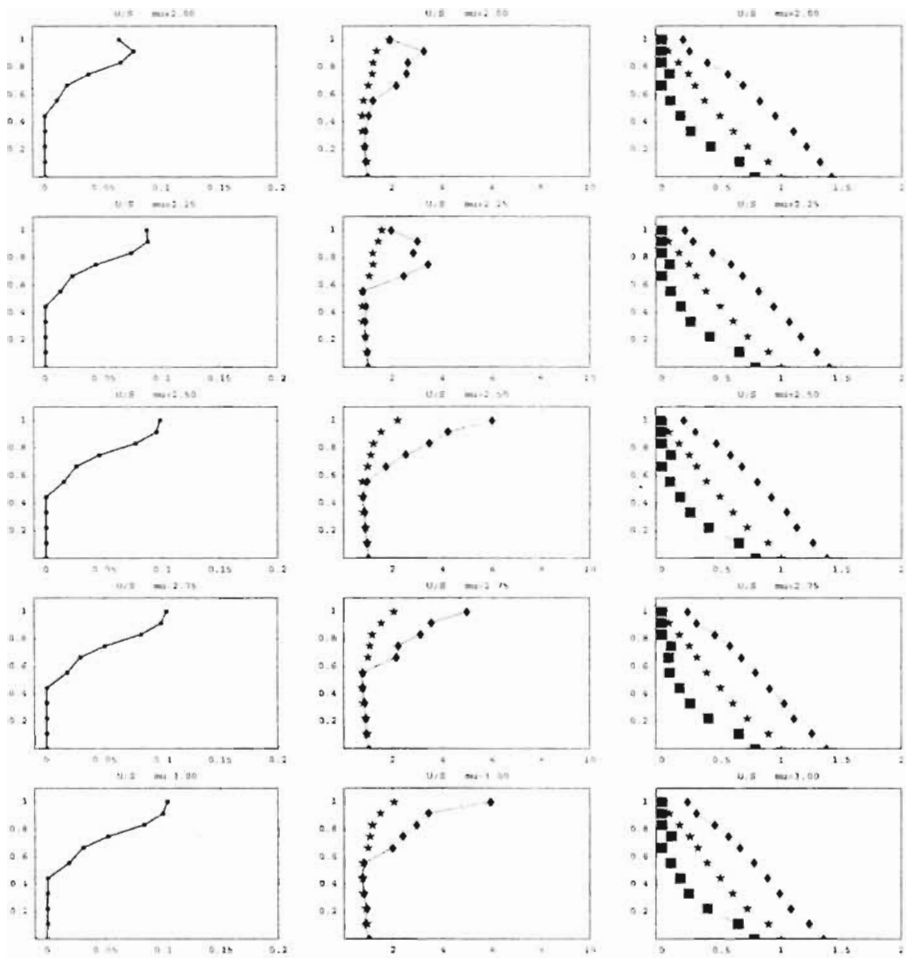

Figure A.31 Max. Separation, Max. Acceleration, and Nodal Interface Stresses (Max., Static, Min.) along the *UPSTREAM* Interface due to change of *mu* (H=200).

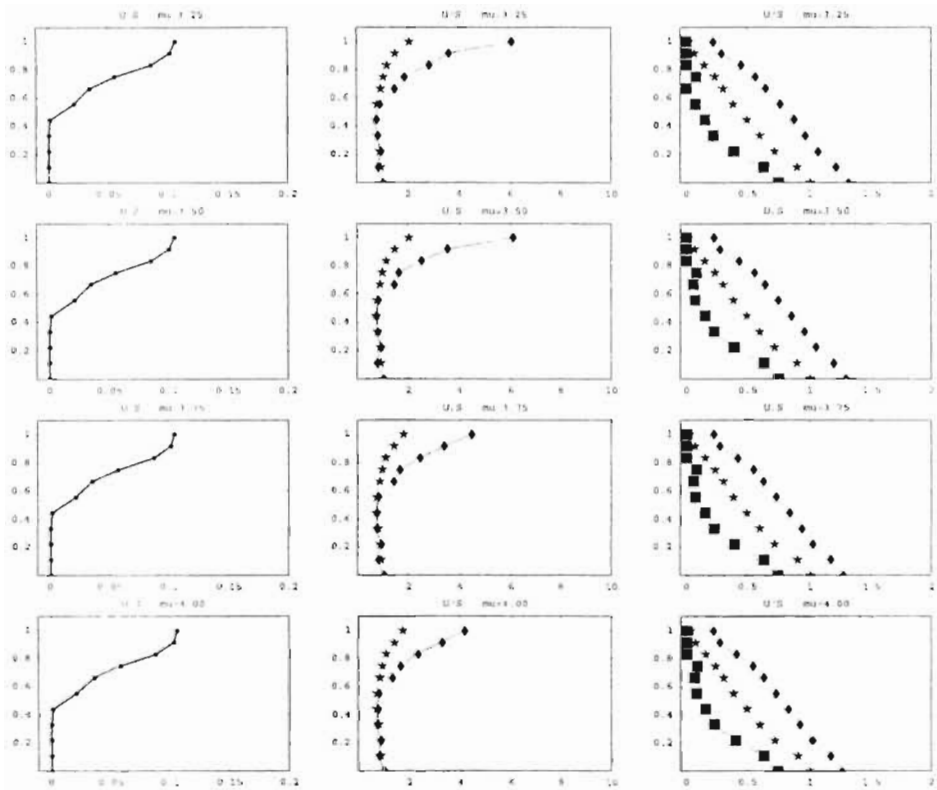

Figure A.32 (Continued from previous figure) Max. Separation. Max. Acceleration, and Nodal Interface Stresses (Max., Static, Min.) along the *UPSTREAM* Interface due to change of mu (H=200).

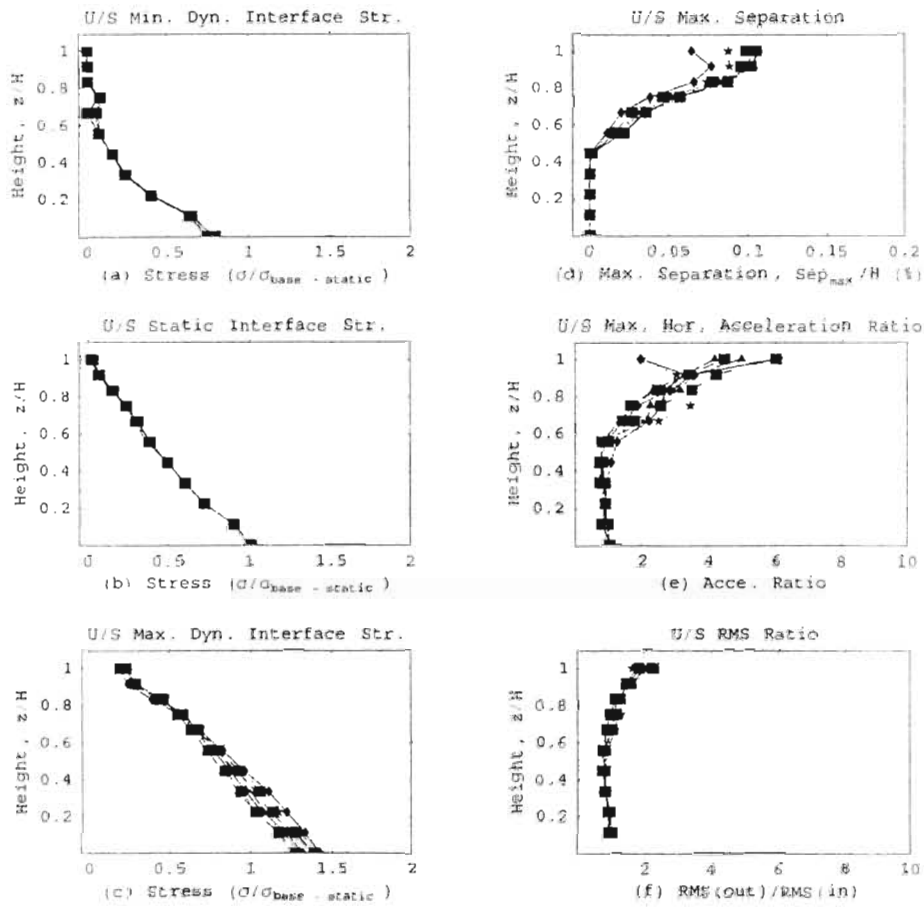

Figure A.33 Collective graphs of Max. Separation, Acceleration, and interface pressures along the *UPSTREAM* Interface at all mu's (H=200).

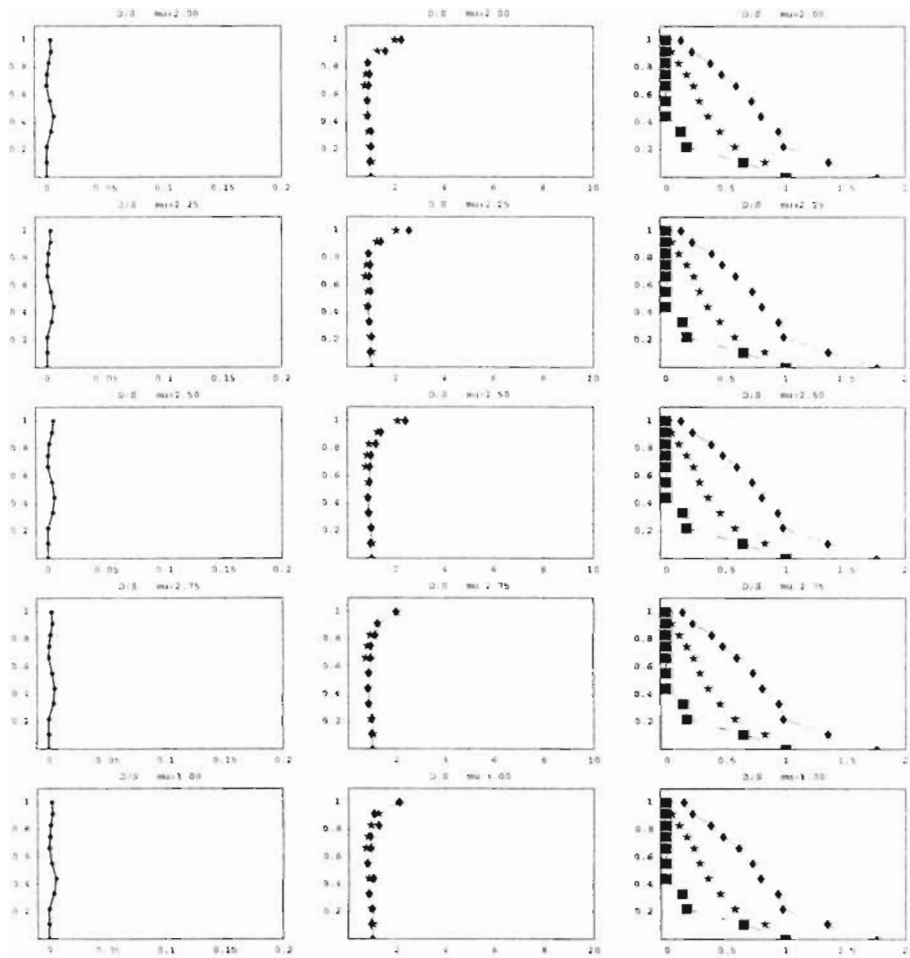

Figure A.34 Max. Separation, Max. Acceleration, and Nodal Interface Stresses (Max., Static, Min.) along the *DOWNSTREAM* Interface due to change of *mu* (H=200).

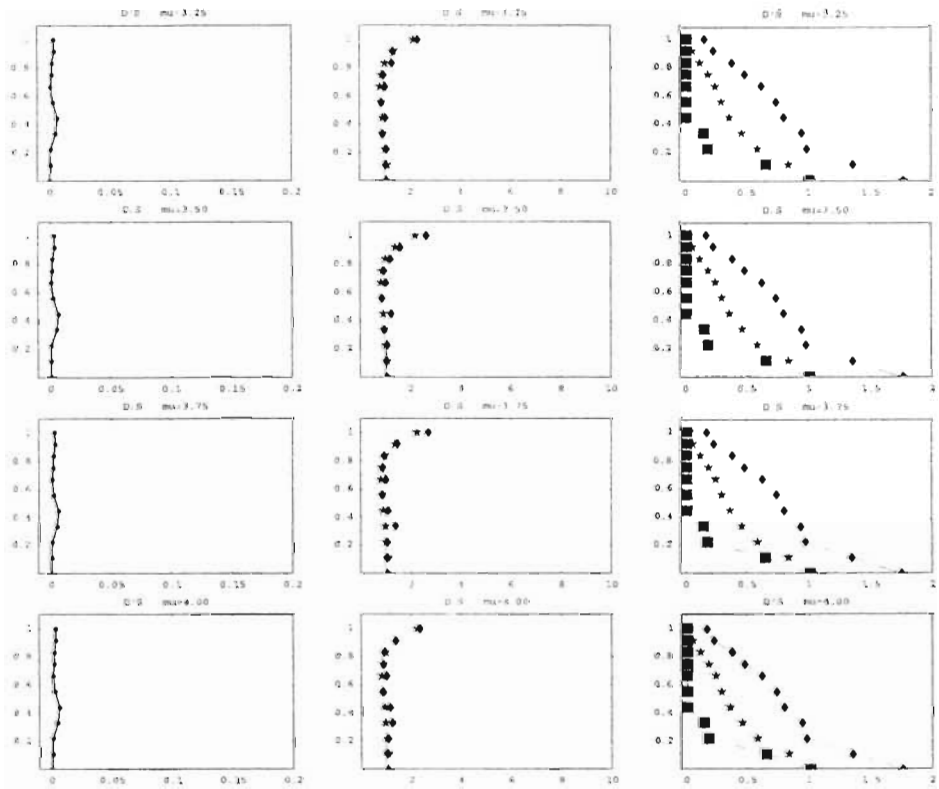

Figure A.35 (Continued from previous figure) Max. Separation, Max. Acceleration, and Nodal Interface Stresses (Max., Static. Min.) along the *DOWNSTREAM* Interface due to change of *mu* (H=200).

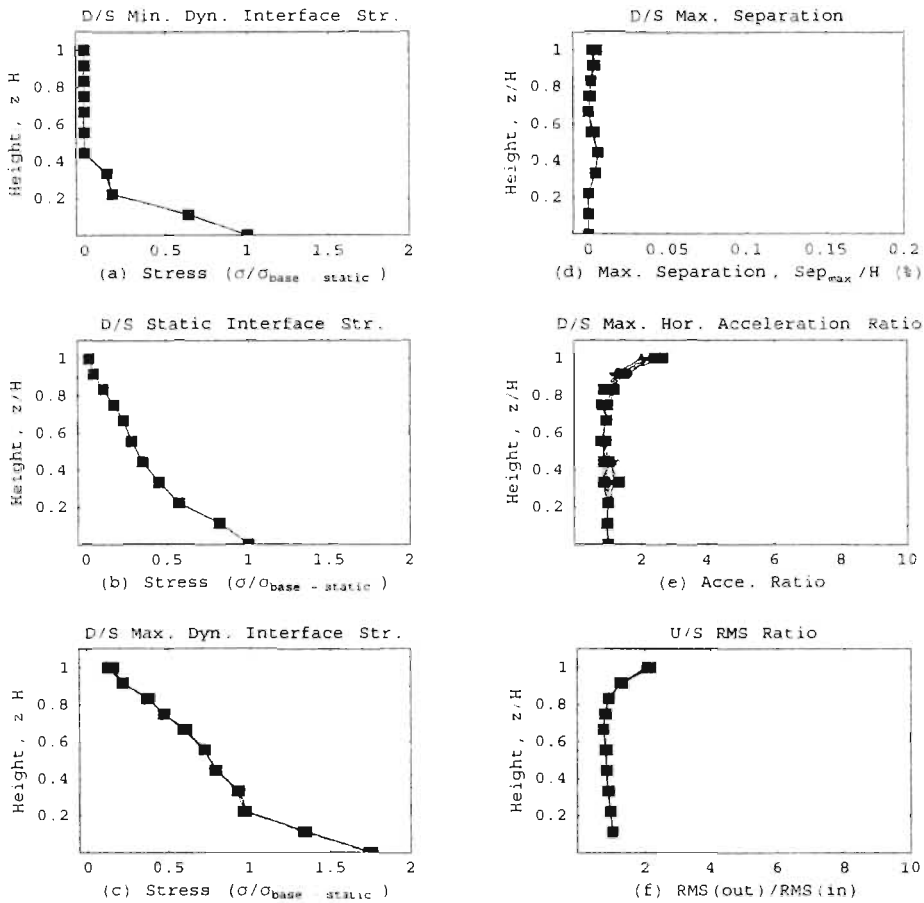

Figure A.36 Collective graphs of Max. Separation, Acceleration, and interface pressures along the *DOWNSTREAM* Interface at all *mu*'s (H=200).

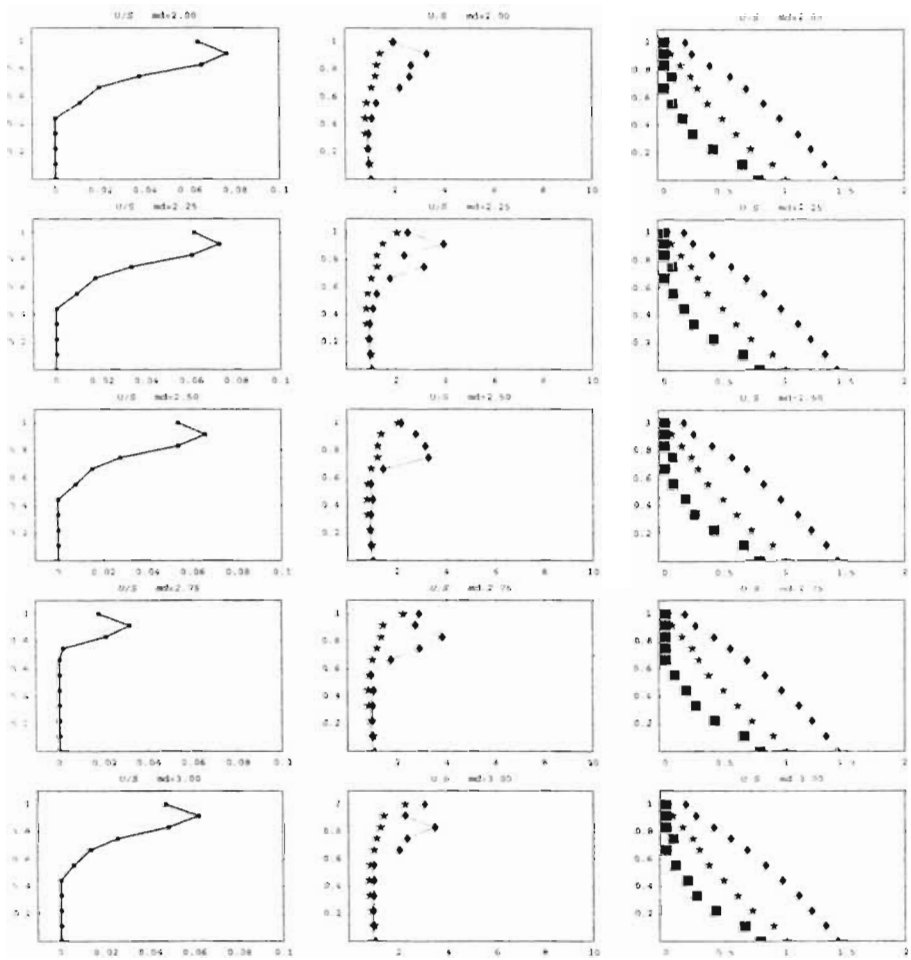

Figure A.37 Max. Separation, Max. Acceleration, and Nodal Interface Stresses (Max., Static, Min.) along the *UPSTREAM* Interface due to change of *md* (H=200).

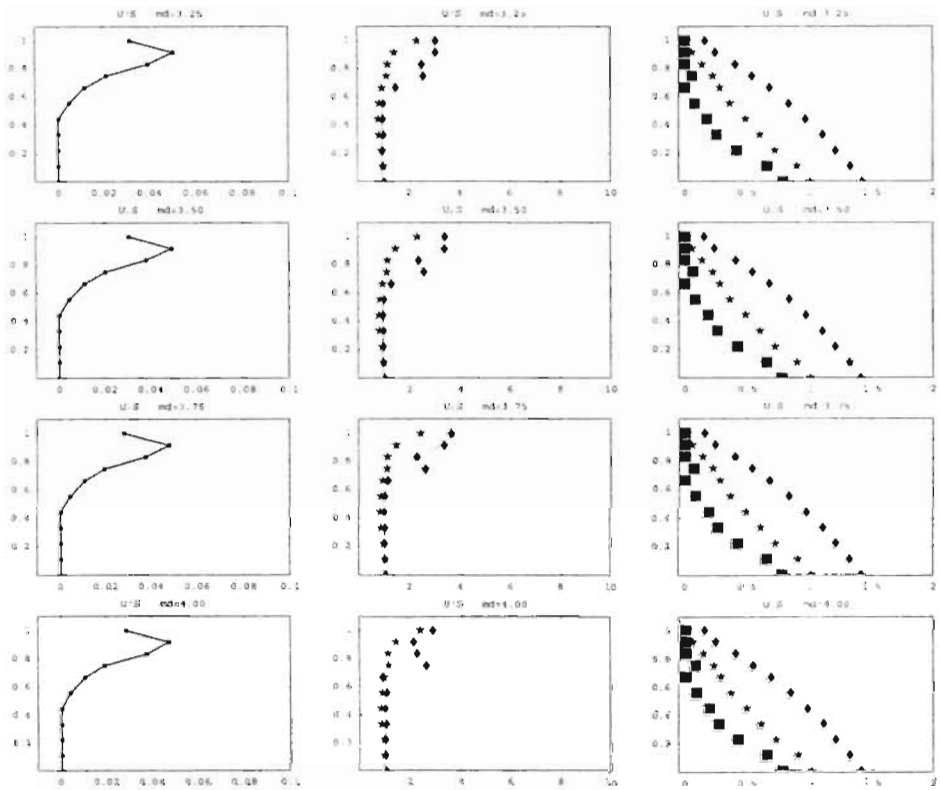

Figure A.38 (Continued from previous figure) Max. Separation. Max. Acceleration, and Nodal Interface Stresses (Max., Static, Min.) along the *UPSTREAM* Interface due to change of *md* (H=200).

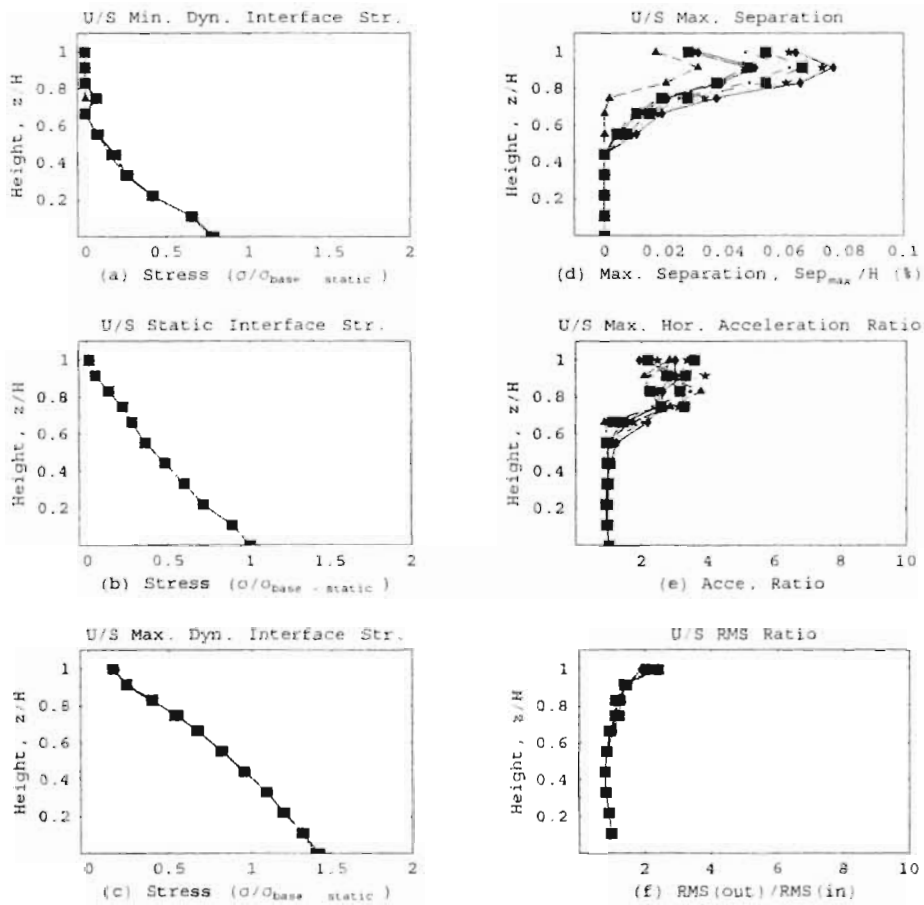

Figure A.39 Collective graphs of Max. Separation, Acceleration, and interface pressures along the *UPSTREAM* Interface at all *md*'s (H=200).

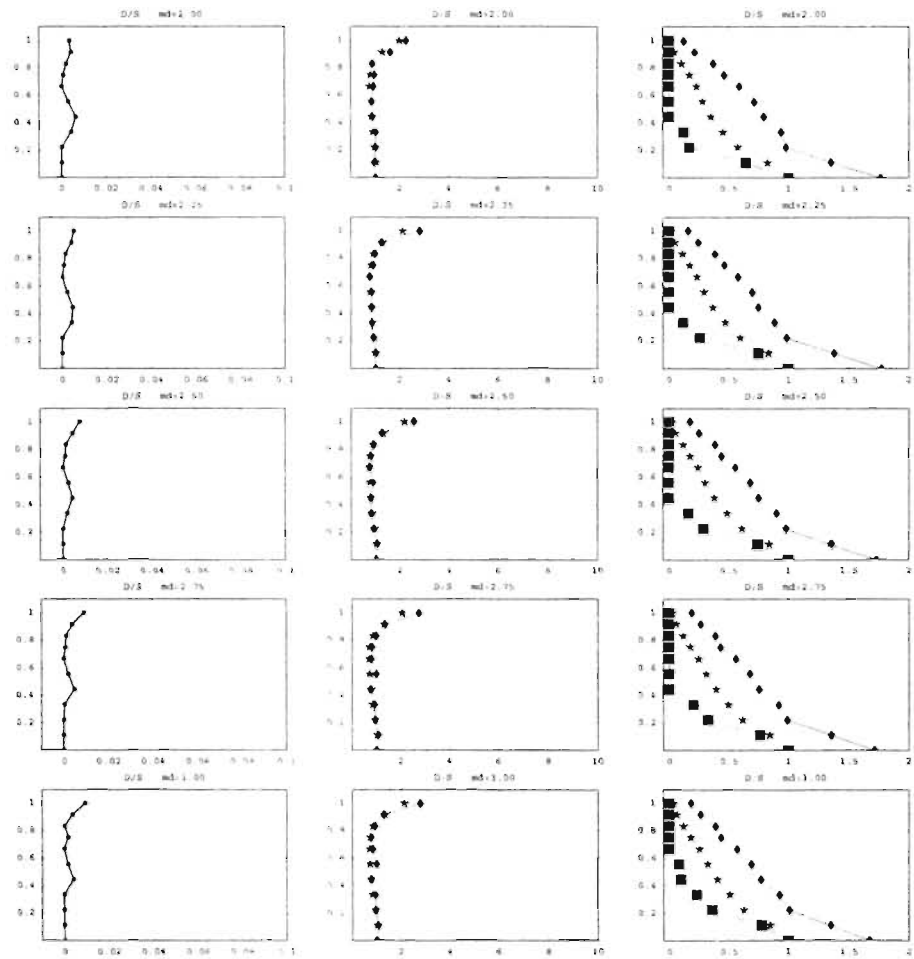

Figure A.40 Max. Separation, Max. Acceleration, and Nodal Interface Stresses (Max., Static, Min.) along the *DOWNSTREAM* Interface due to change of *md* (H=200).

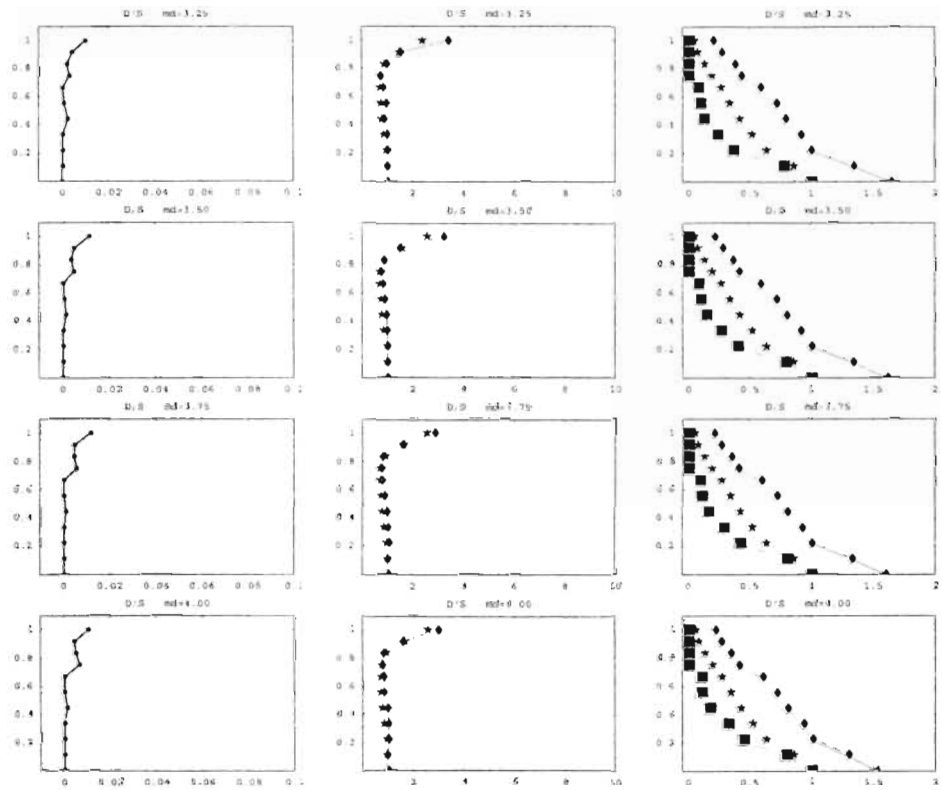

Figure A.41 (Continued from previous figure) Max. Separation, Max. Acceleration, and Nodal Interface Stresses (Max., Static, Min.) along the *DOWNSTREAM* Interface due to change of *md* (H=200).

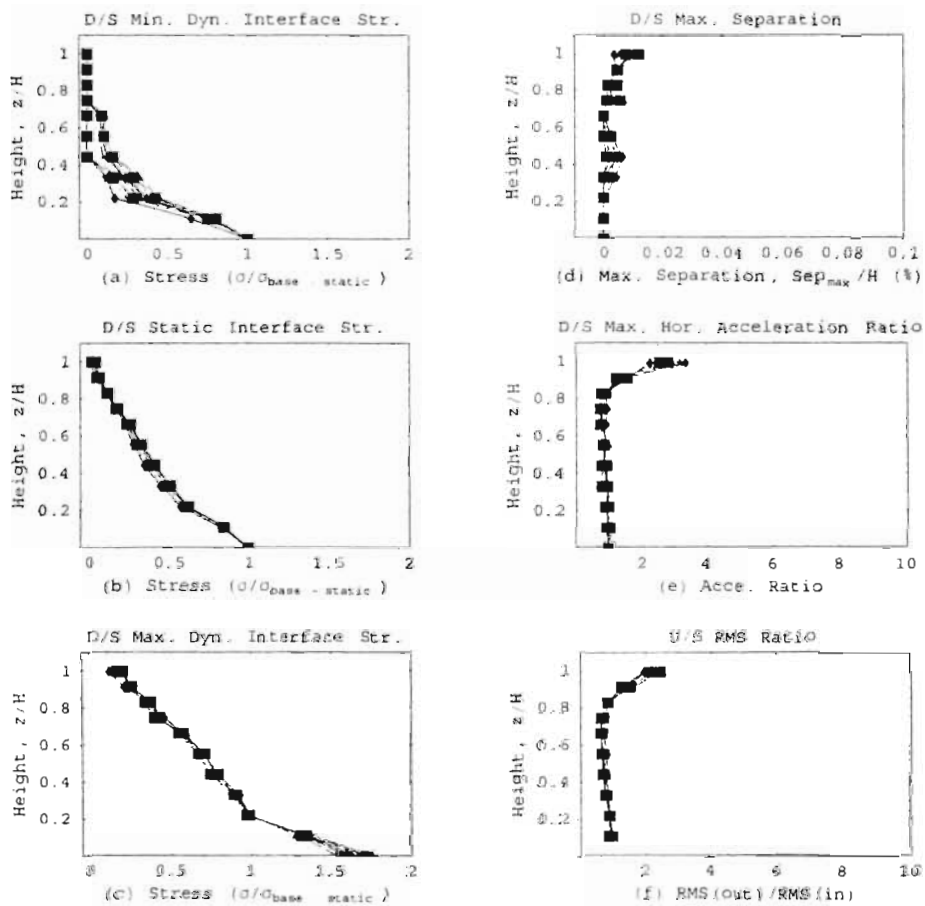

Figure A.42 Collective graphs of Max. Separation, Acceleration, and interface pressures along the *DOWNSTREAM* Interface at all *md*'s (H=200).

A.2.3 H=300ft

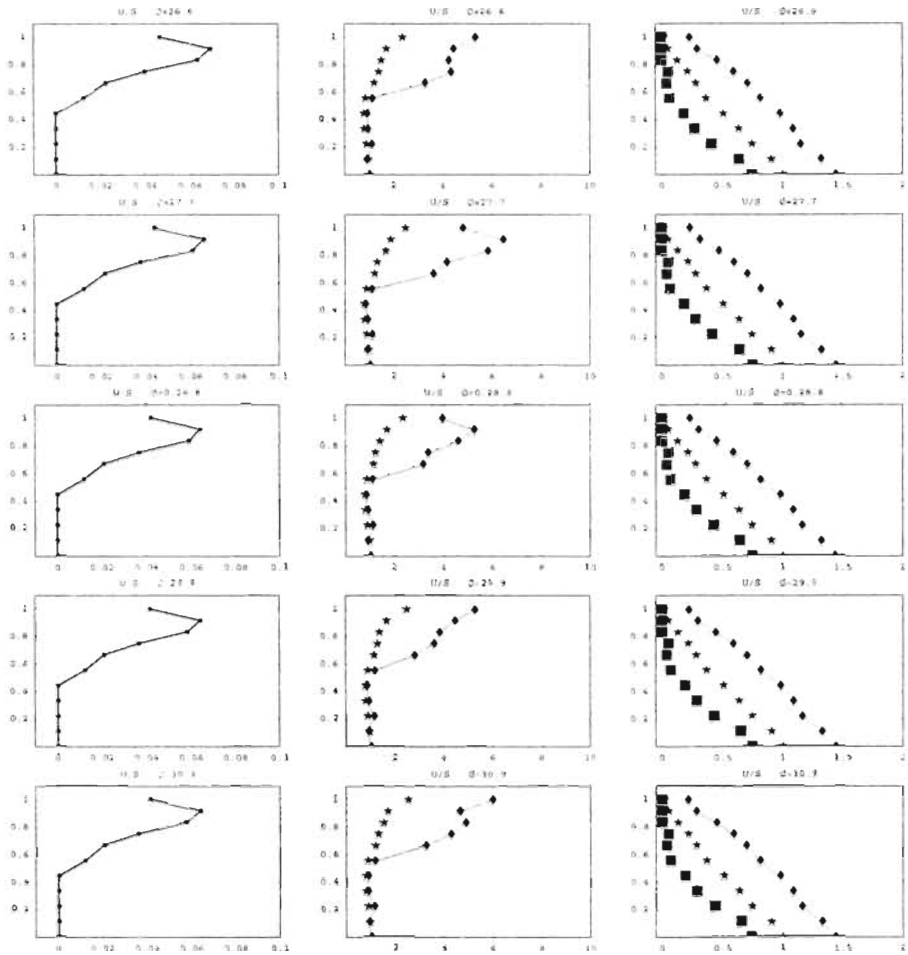

Figure A.43 Max. Separation, Max. Acceleration, and Nodal Interface Stresses (Max., Static, Min.) along the *UPSTREAM* Interface due to change of $\dot{\phi}$ (in degrees) (H=300).

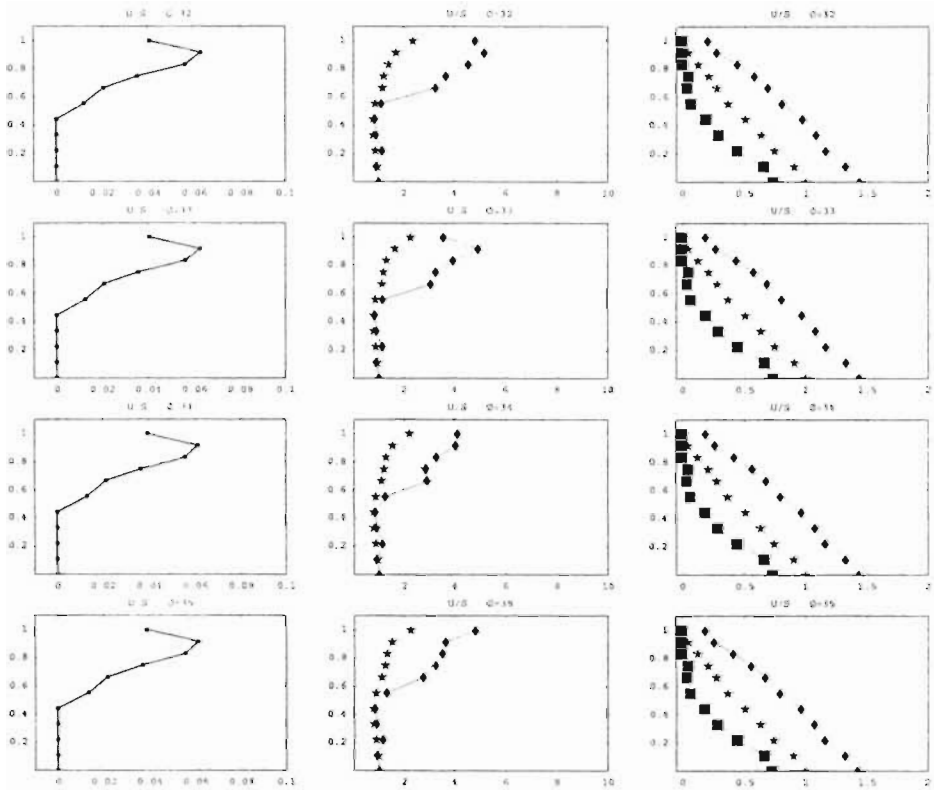

Figure A.44 (Continued from previous figure) Max. Separation, Max. Acceleration, and Nodal Interface Stresses (Max., Static, Min.) along the *UPSTREAM* Interface due to change of ϕ (in degrees) (H=300).

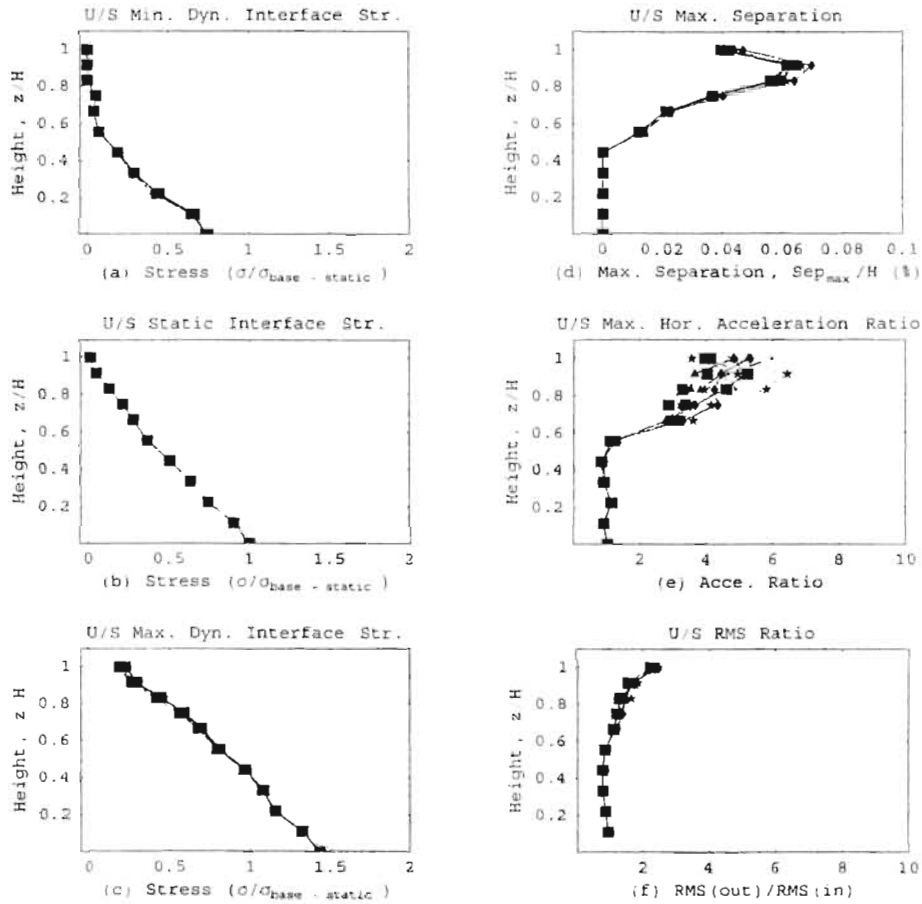

Figure A.45 Collective graphs of Max. Separation. Acceleration, and interface pressures along the *UPSTREAM* Interface at all ϕ's (H=300).

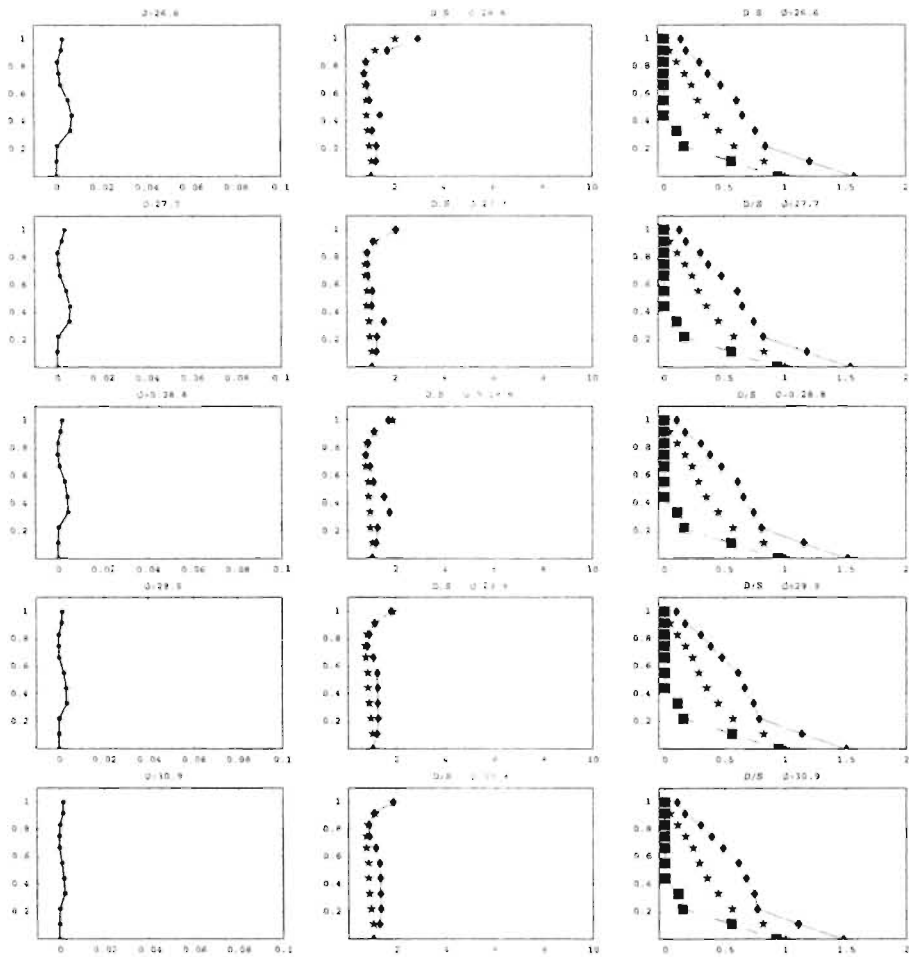

Figure A.46 Max. Separation, Max. Acceleration, and Nodal Interface Stresses (Max., Static, Min.) along the *DOWNSTREAM* Interface due to change of ϕ (in degrees) (H=300).

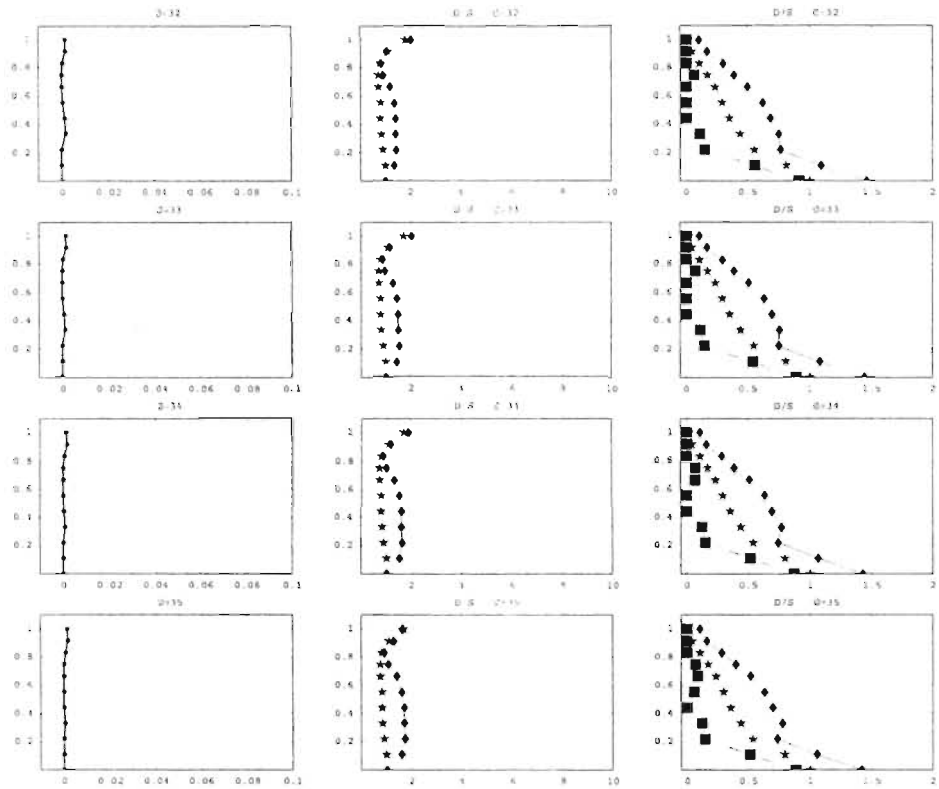

Figure A.47 (Continued from previous figure) Max. Separation, Max. Acceleration, and Nodal Interface Stresses (Max., Static, Min.) along the *DOWNSTREAM* Interface due to change of ϕ (in degrees) (H=300).

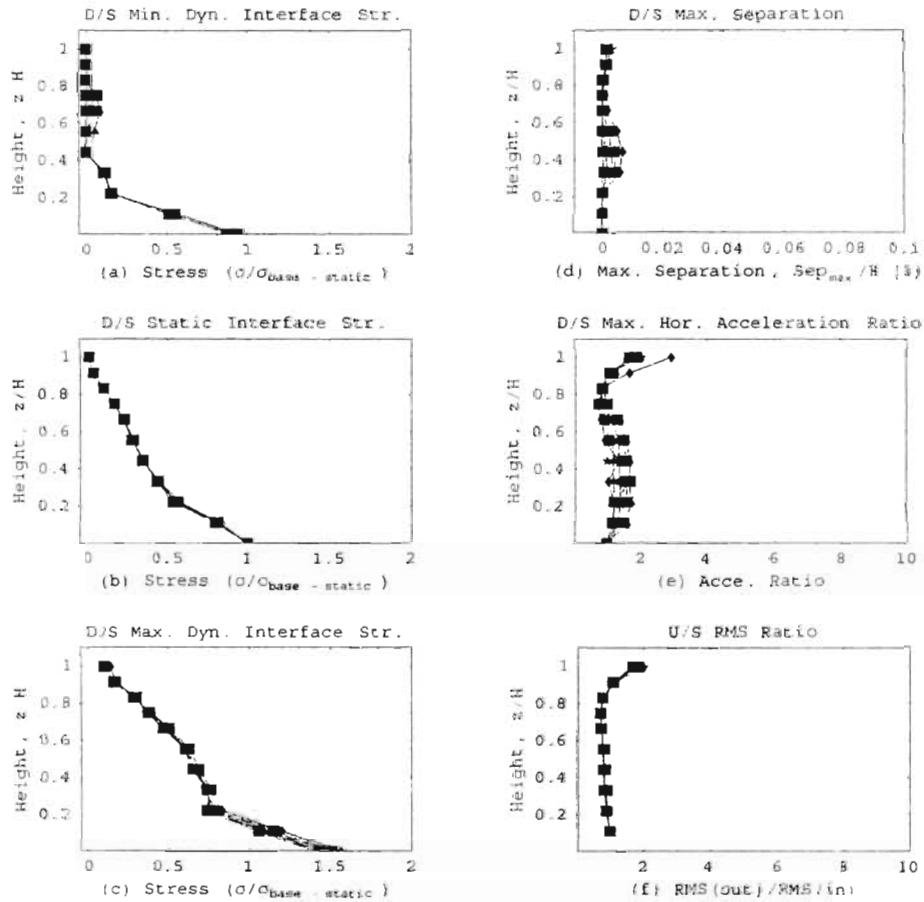

Figure A.48 Collective graphs of Max. Separation, Acceleration, and interface pressures along the *DOWNSTREAM* Interface at all φ's (H=300)

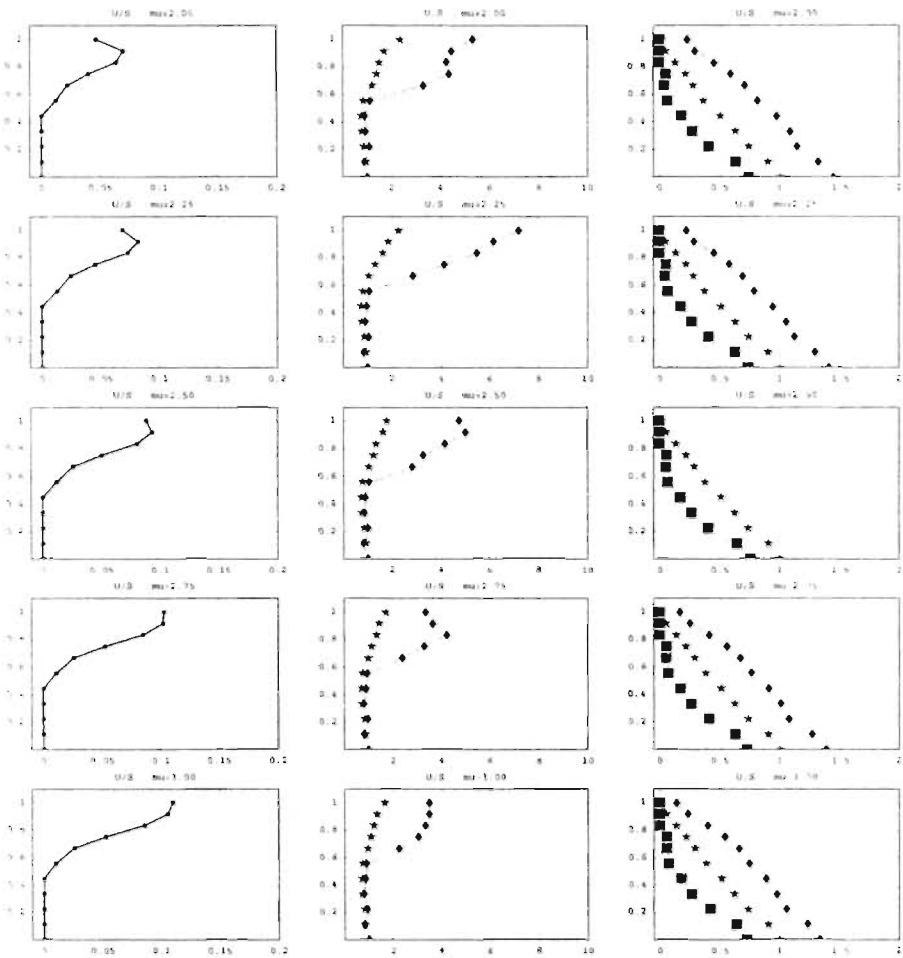

Figure A.49 Max. Separation, Max. Acceleration, and Nodal Interface Stresses (Max., Static, Min.) along the *UPSTREAM* Interface due to change of *mu* (H=300).

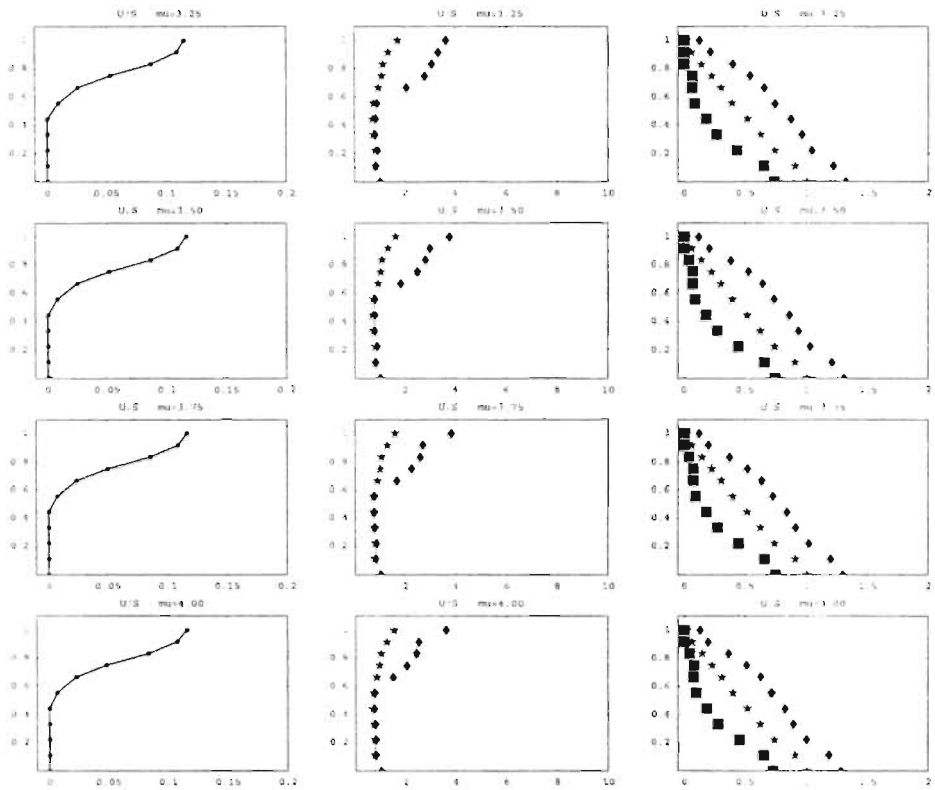

Figure A.50 (Continued from previous figure) Max. Separation, Max. Acceleration, and Nodal Interface Stresses (Max., Static, Min.) along the *UPSTREAM* Interface due to change of *mu* (H=300).

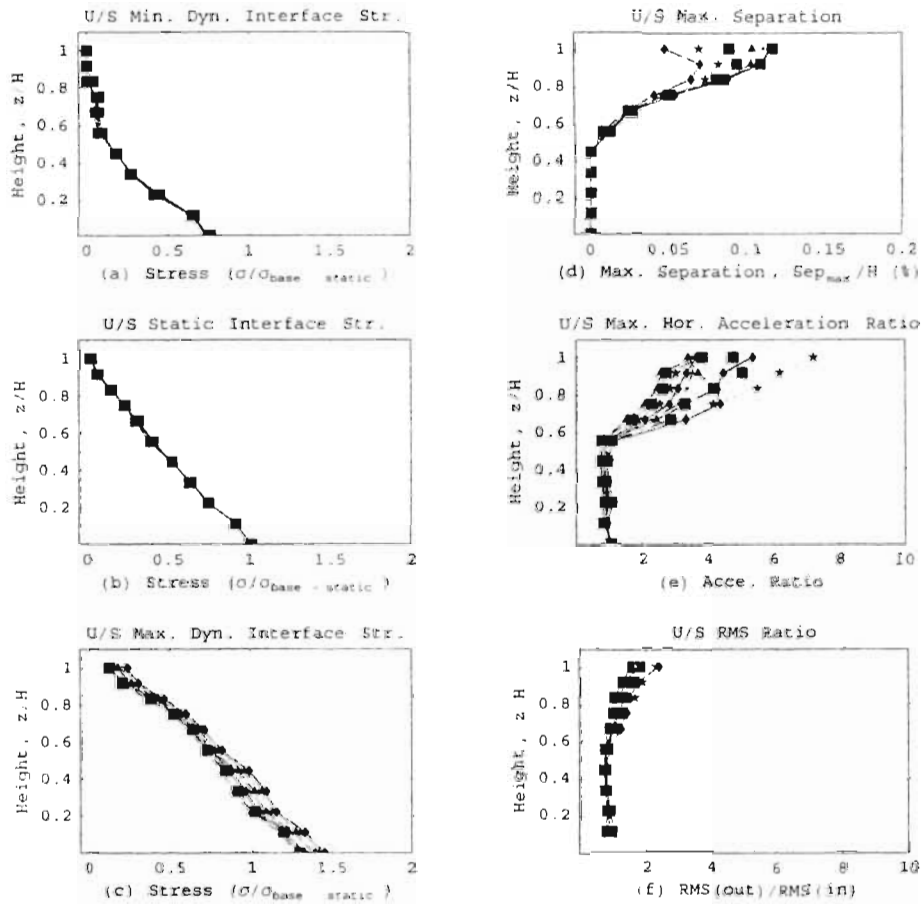

Figure A.51 Collective graphs of Max. Separation, Acceleration, and interface pressures along the *UPSTREAM* Interface at all *mu*'s (H=300).

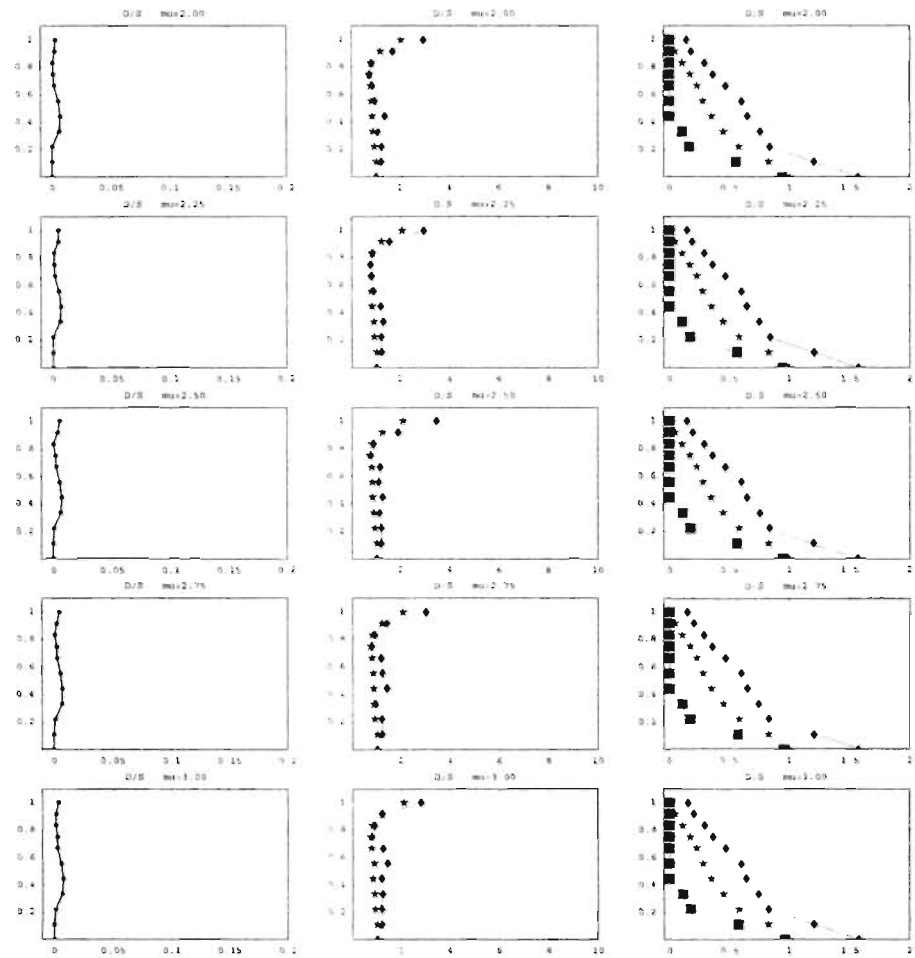

Figure A.52 Max. Separation. Max. Acceleration, and Nodal Interface Stresses (Max., Static, Min.) along the *DOWNSTREAM* Interface due to change of *mu* (H=300).

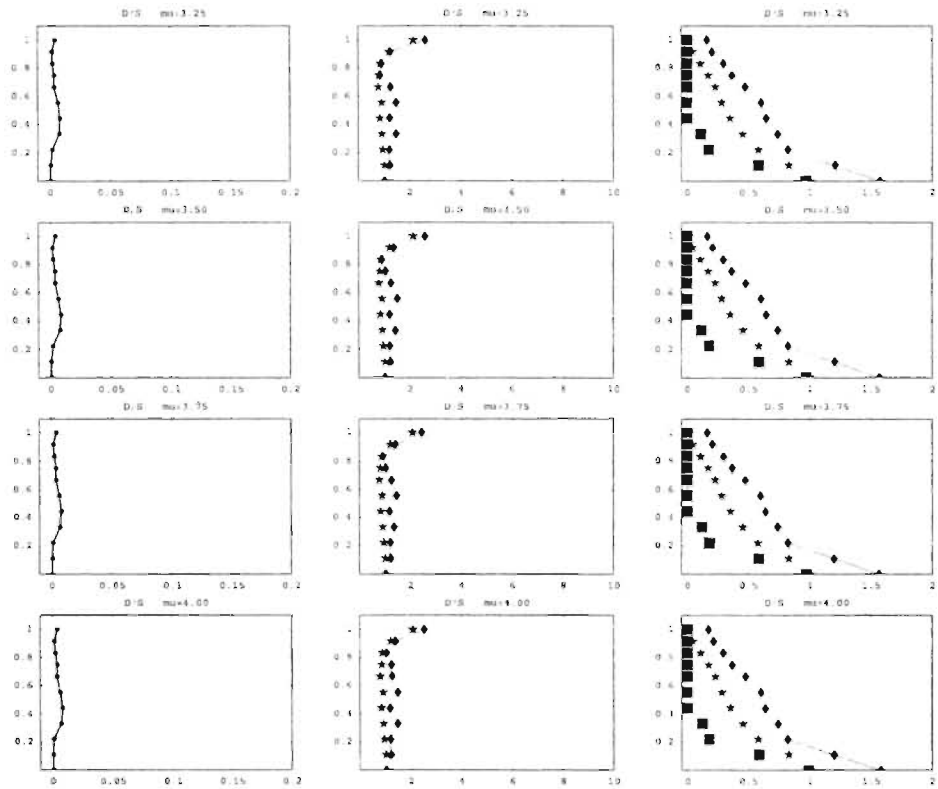

Figure A.53 (Continued from previous figure) Max. Separation, Max. Acceleration, and Nodal Interface Stresses (Max., Static, Min.) along the *DOWNSTREAM* Interface due to change of *mu* (H=300).

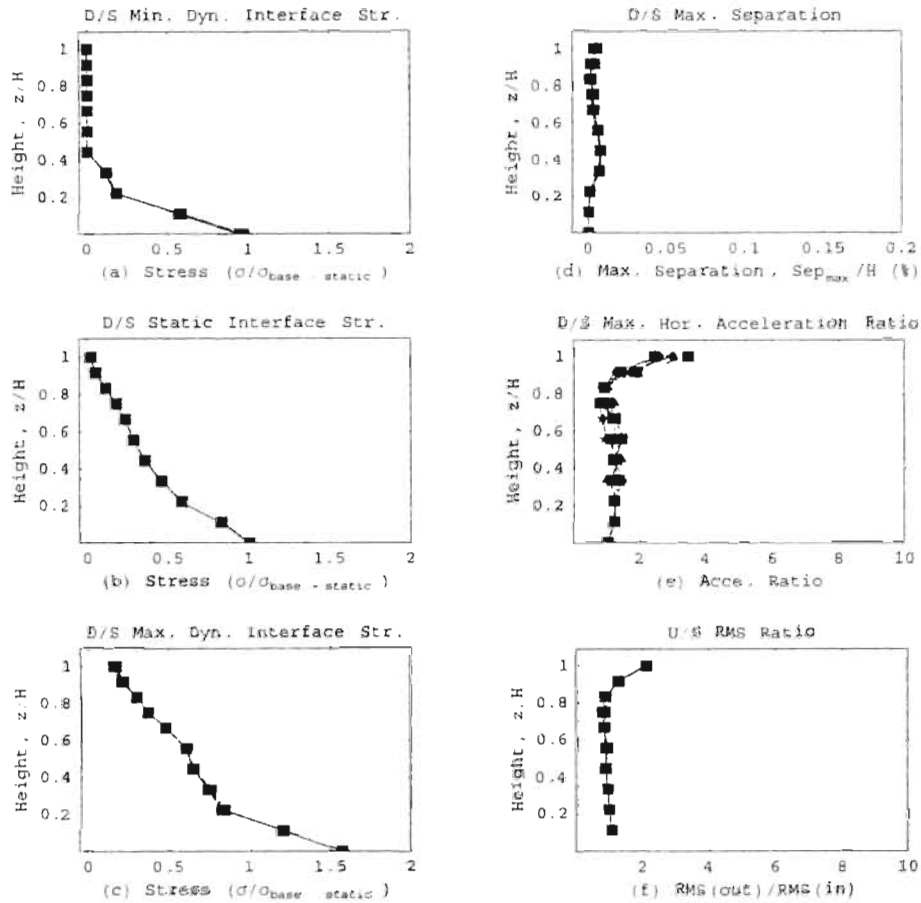

Figure A.54 Collective graphs of Max. Separation, Acceleration, and interface pressures along the *DOWNSTREAM* Interface at all *mu*'s (H=300).

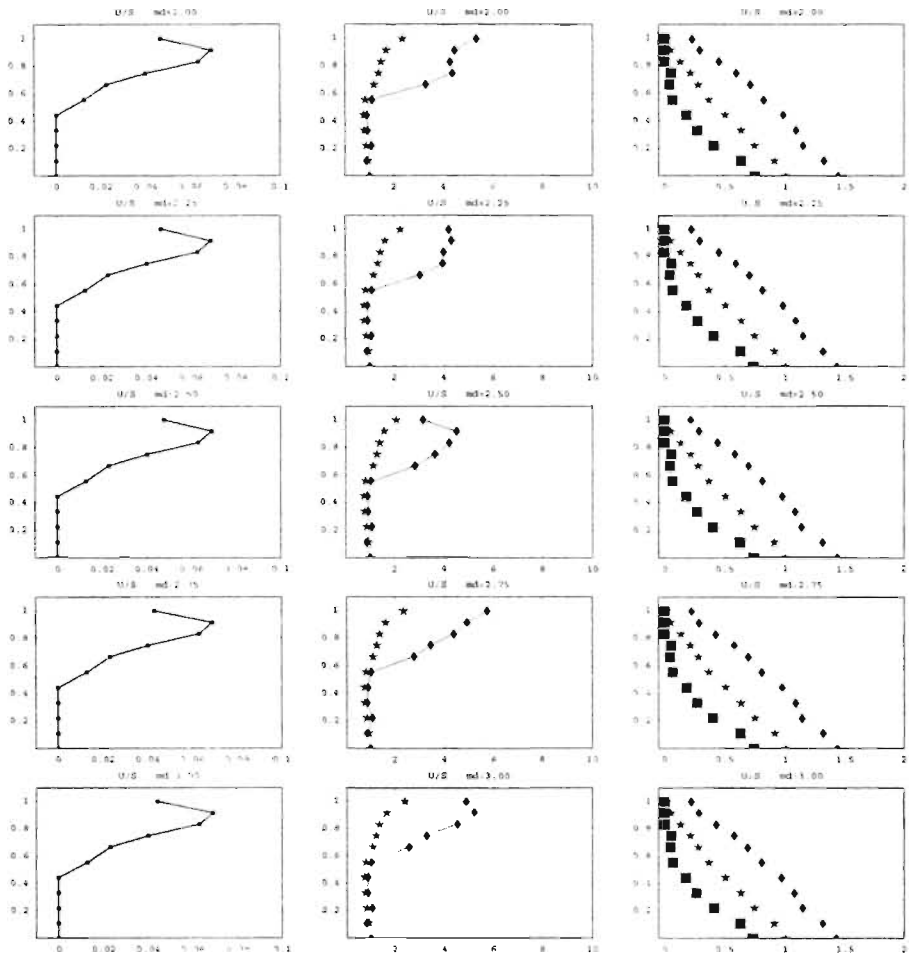

Figure A.55 Max. Separation, Max. Acceleration, and Nodal Interface Stresses (Max., Static, Min.) along the *UPSTREAM* Interface due to change of *md* (H=300).

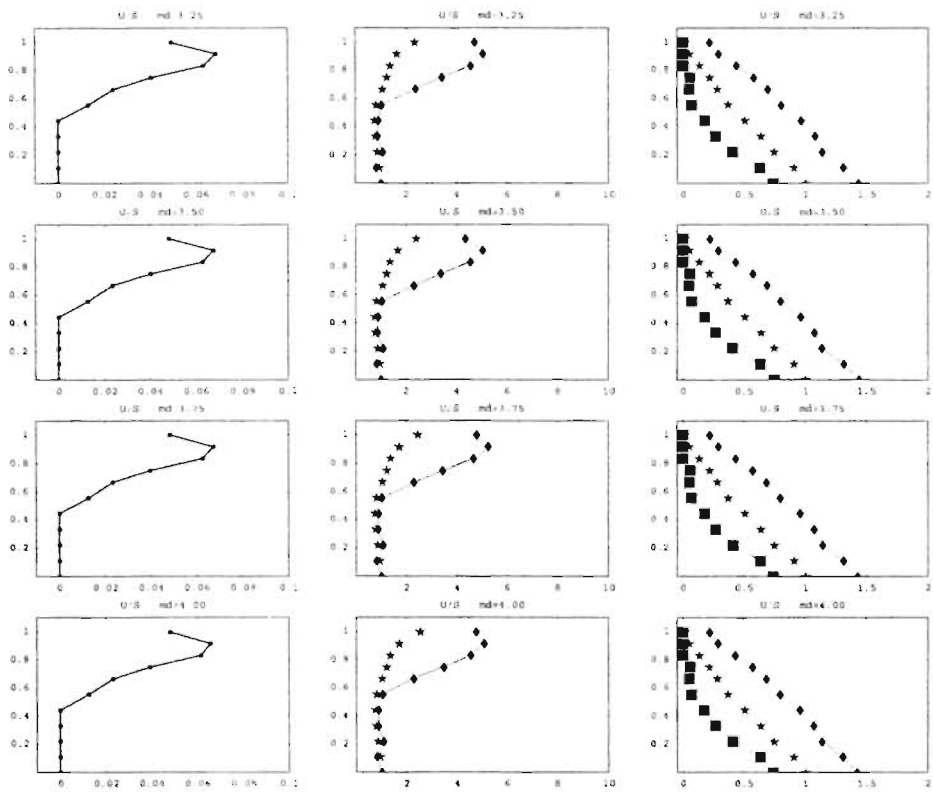

Figure A.56 (Continued from previous figure) Max. Separation, Max. Acceleration, and Nodal Interface Stresses (Max., Static, Min.) along the *UPSTREAM* Interface due to change of *md* (H=300).

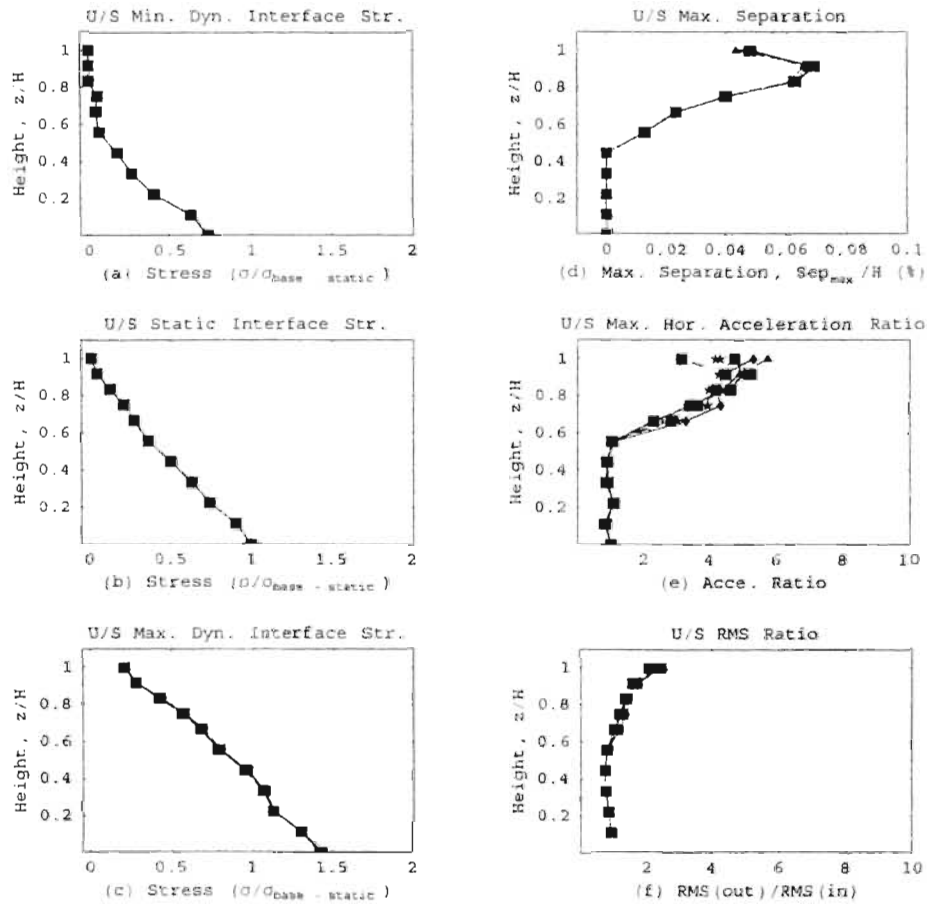

Figure A.57 Collective graphs of Max. Separation, Acceleration, and interface pressures along the *UPSTREAM* Interface at all *md*'s (H=300).

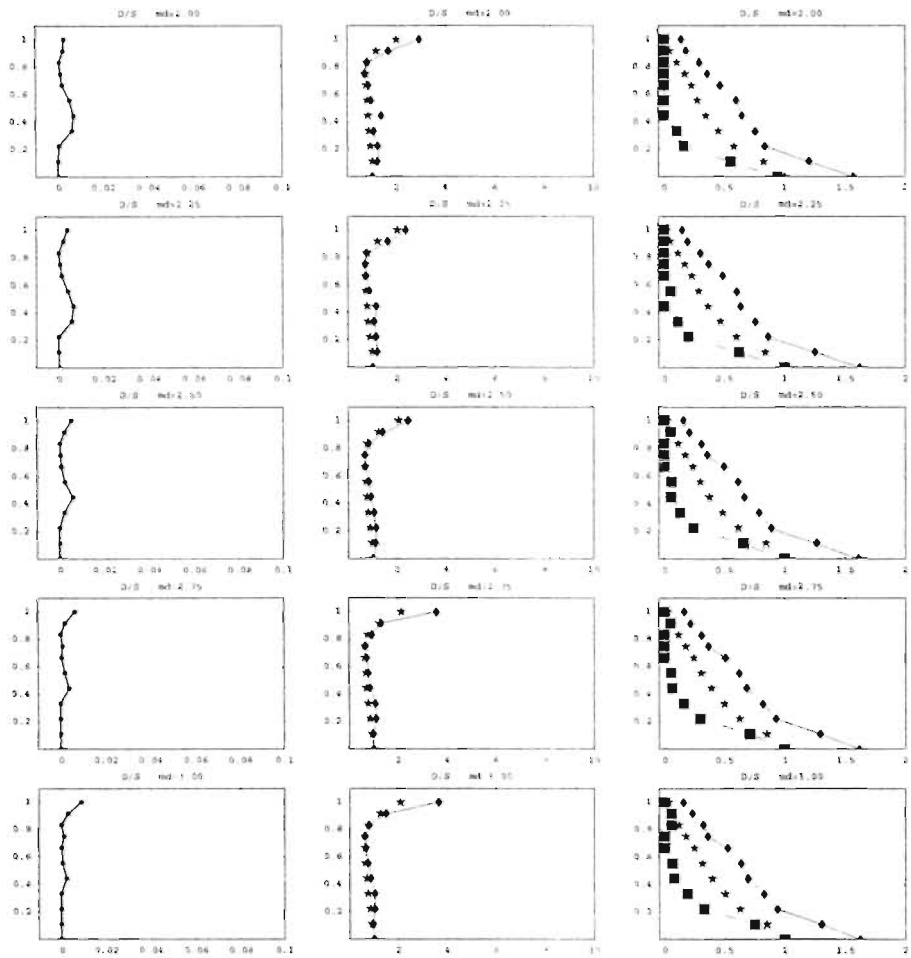

Figure A.58 Max. Separation, Max. Acceleration, and Nodal Interface Stresses (Max., Static, Min.) along the *DOWNSTREAM* Interface due to change of *md* (H=300).

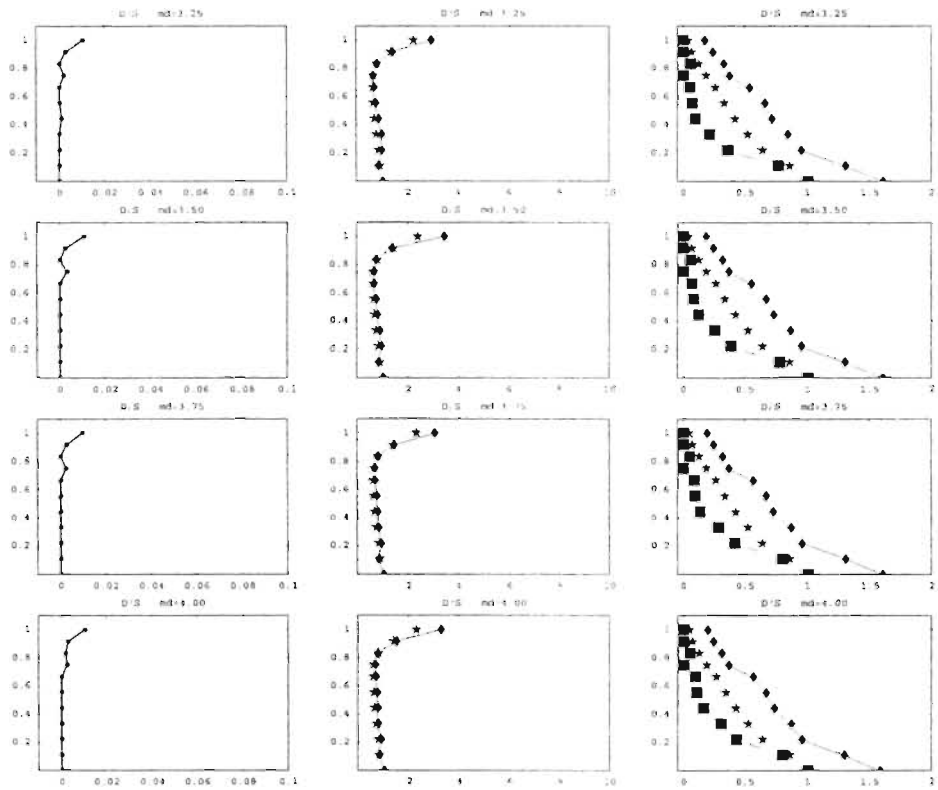

Figure A.59 (Continued from previous figure) Max. Separation, Max. Acceleration, and Nodal Interface Stresses (Max., Static, Min.) along the *DOWNSTREAM* Interface due to change of *md* (H=300).

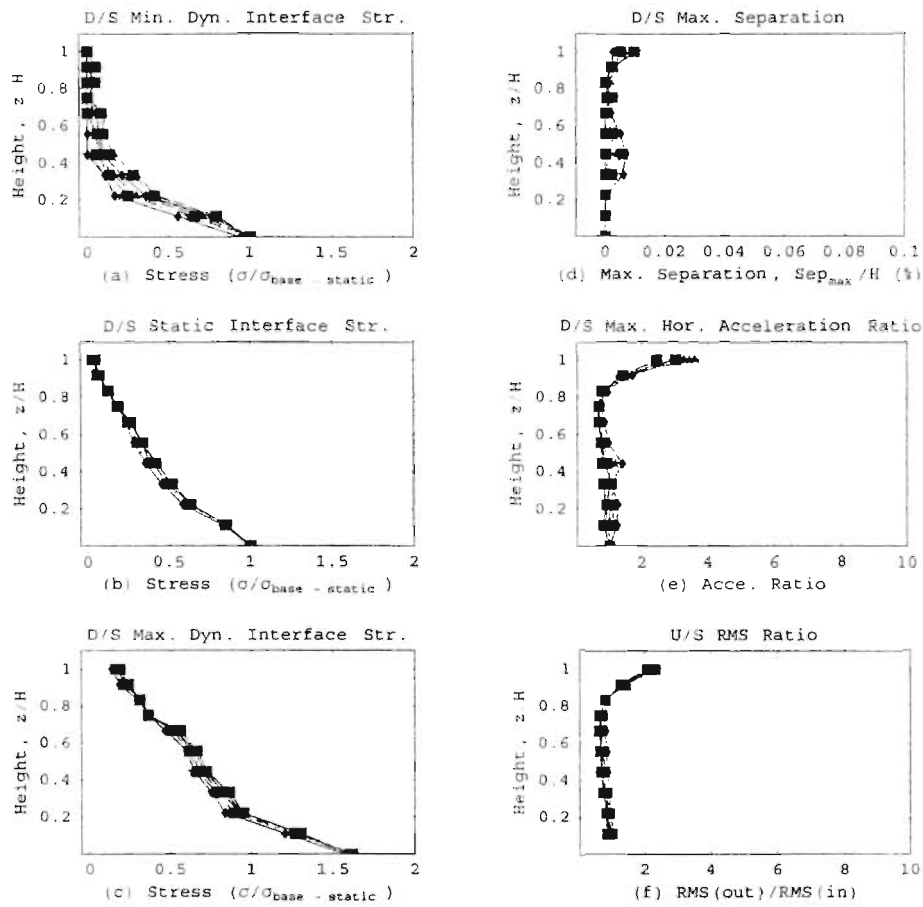

Figure A.60 Collective graphs of Max. Separation. Acceleration, and interface pressures along the *DOWNSTREAM* Interface at all *md*'s (H=300).

A.2.4 H=400ft

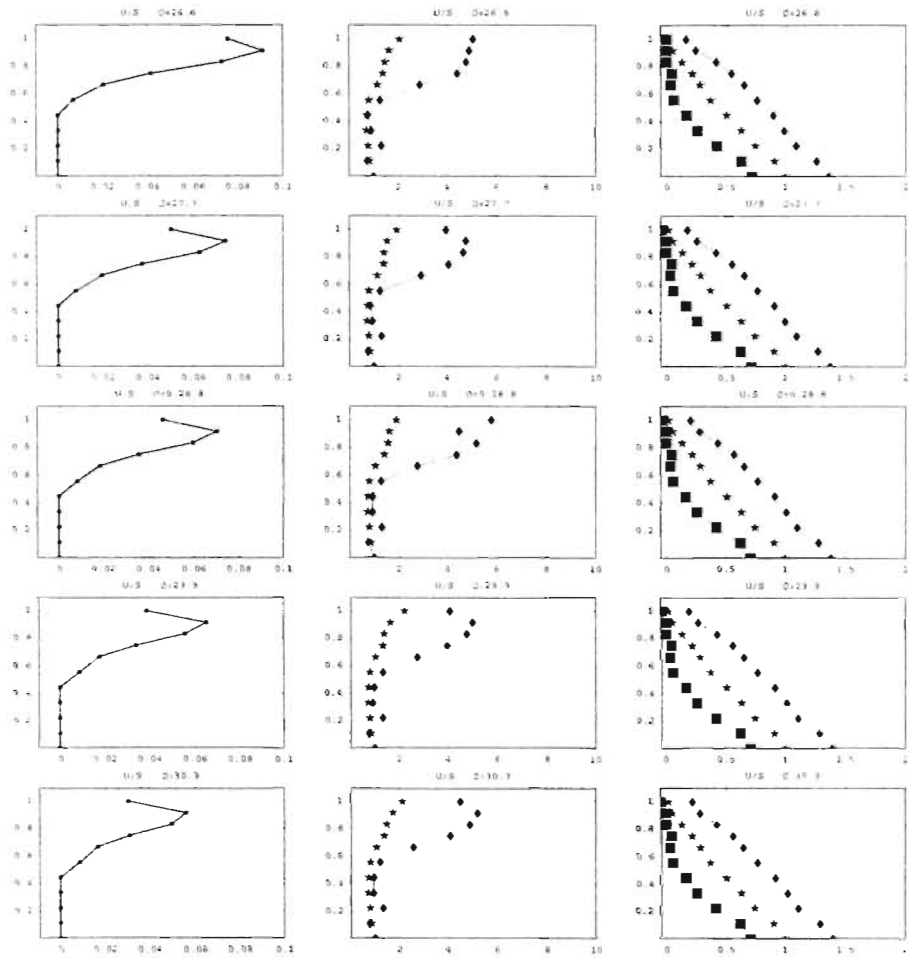

Figure A.61 Max. Separation, Max. Acceleration, and Nodal Interface Stresses (Max., Static, Min.) along the *UPSTREAM* Interface due to change of ϕ (in degrees) (H=400).

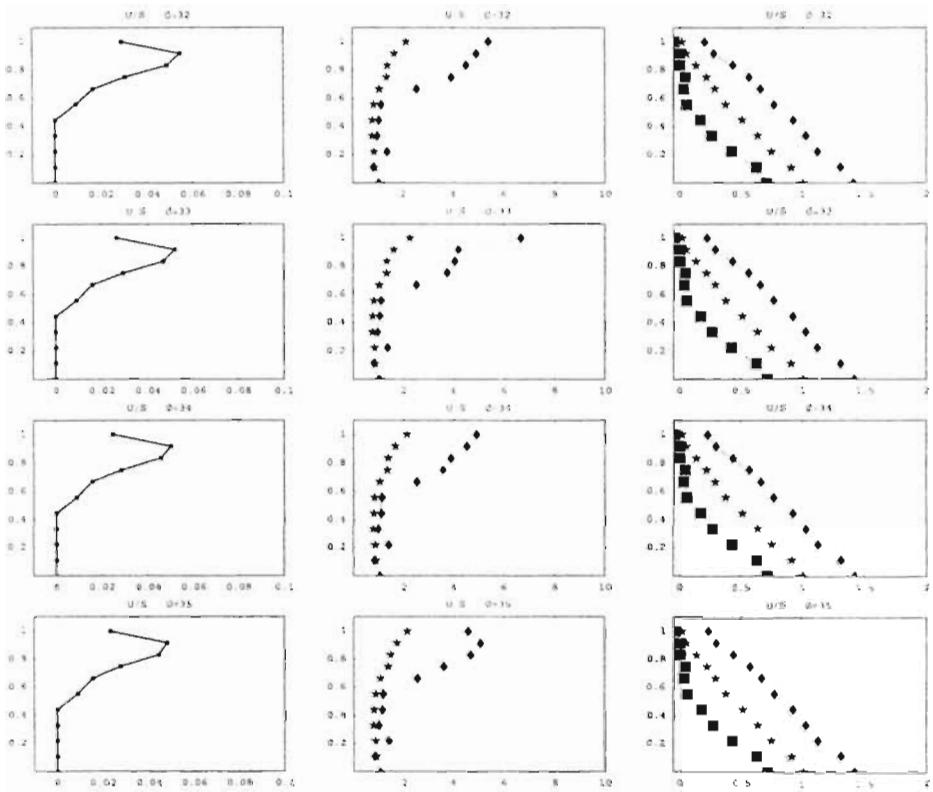

Figure A.62 (Continued from previous figure) Max. Separation, Max. Acceleration, and Nodal Interface Stresses (Max., Static, Min.) along the *UPSTREAM* Interface due to change of ϕ (in degrees) (H=400).

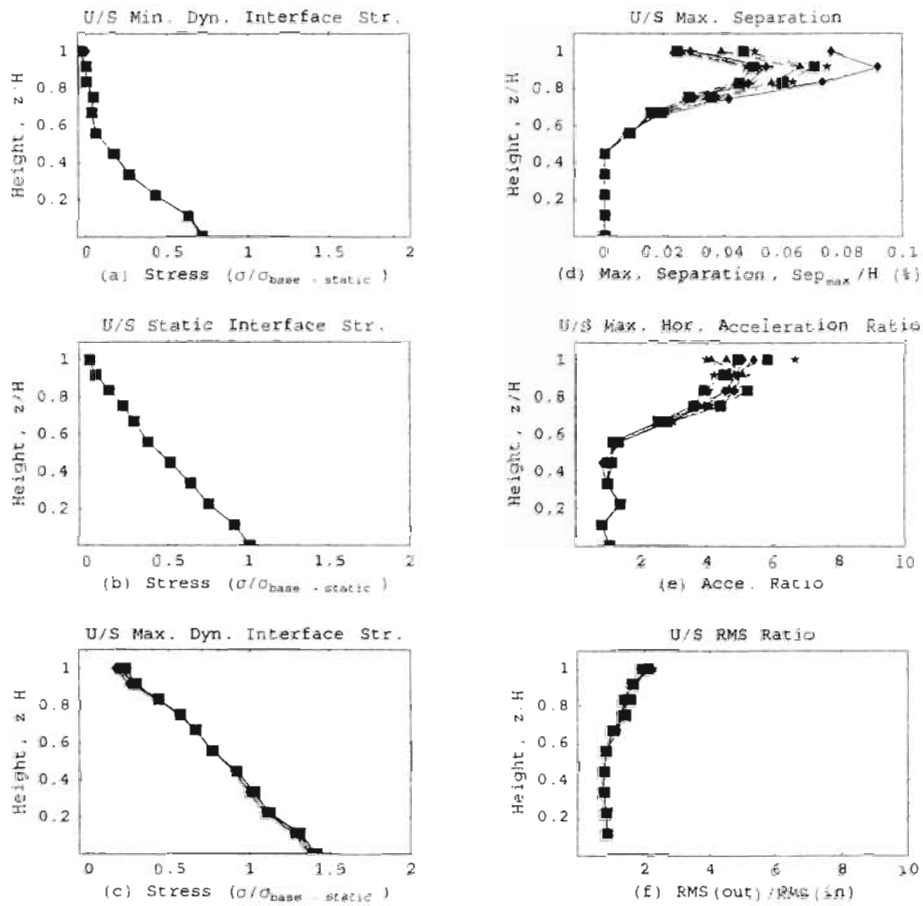

Figure A.63 Collective graphs of Max. Separation, Acceleration, and interface pressures along the *UPSTREAM* Interface at all ϕ's (H=400).

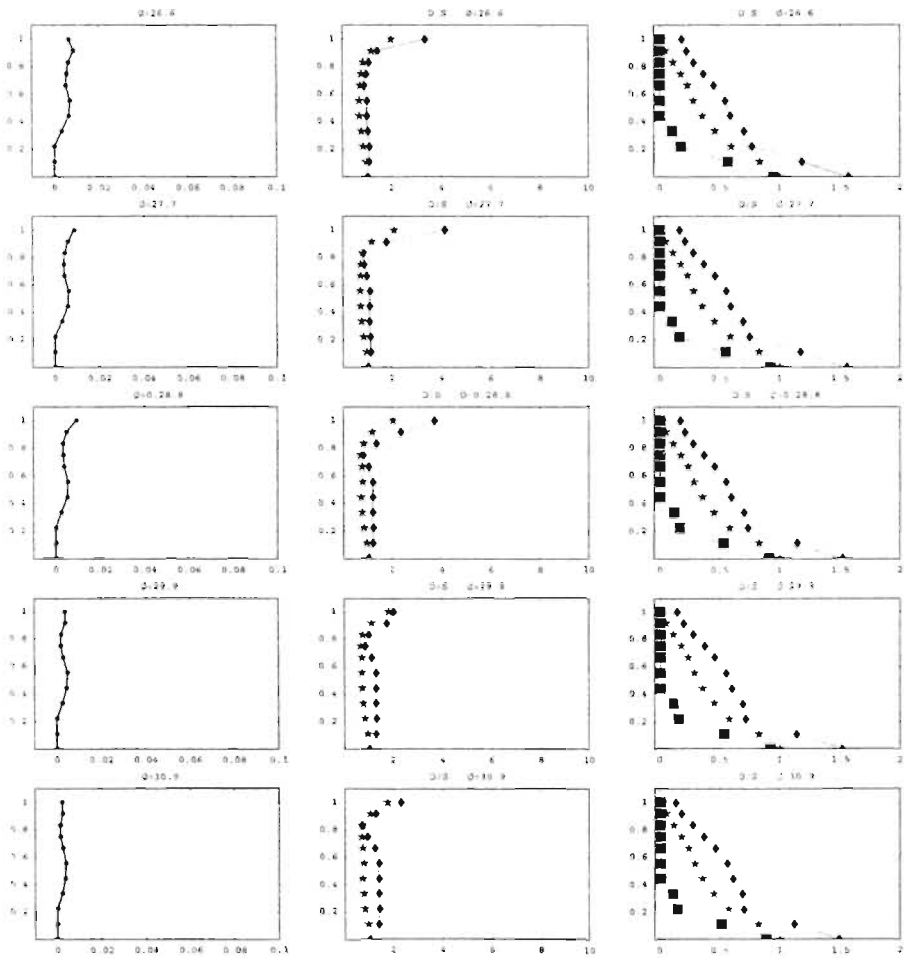

Figure A.64 Max. Separation, Max. Acceleration, and Nodal Interface Stresses (Max., Static, Min.) along the *DOWNSTREAM* Interface due to change of ϕ (in degrees) (H=400).

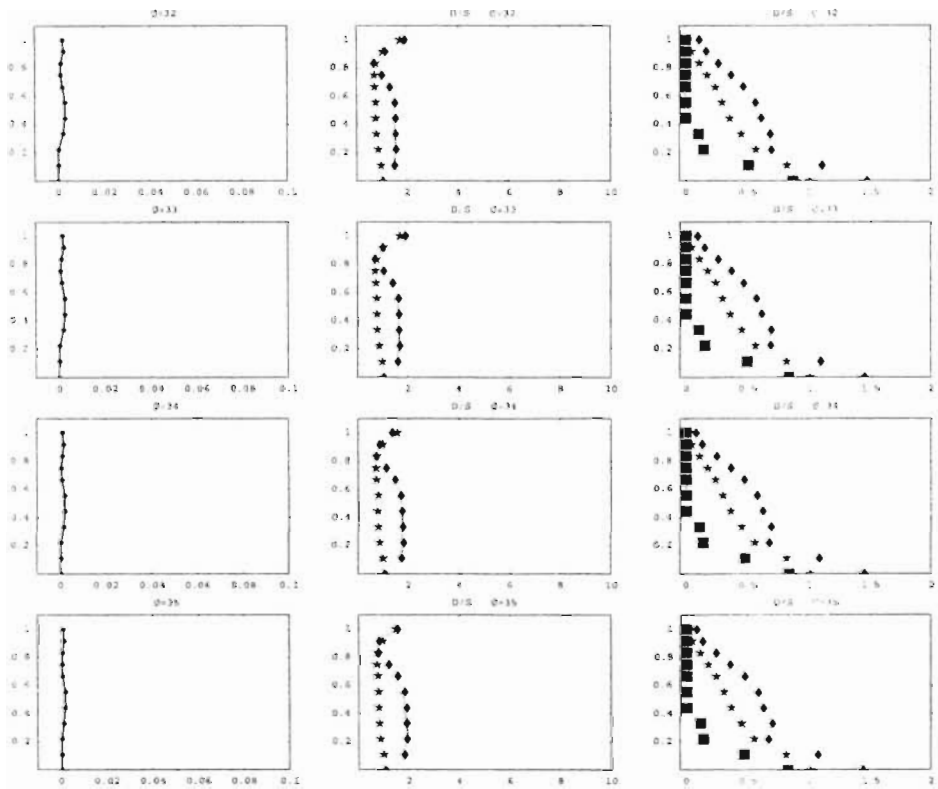

Figure A.65 (Continued from previous figure) Max. Separation, Max. Acceleration, and Nodal Interface Stresses (Max., Static, Min.) along the *DOWNSTREAM* Interface due to change of ϕ (in degrees) (H=400).

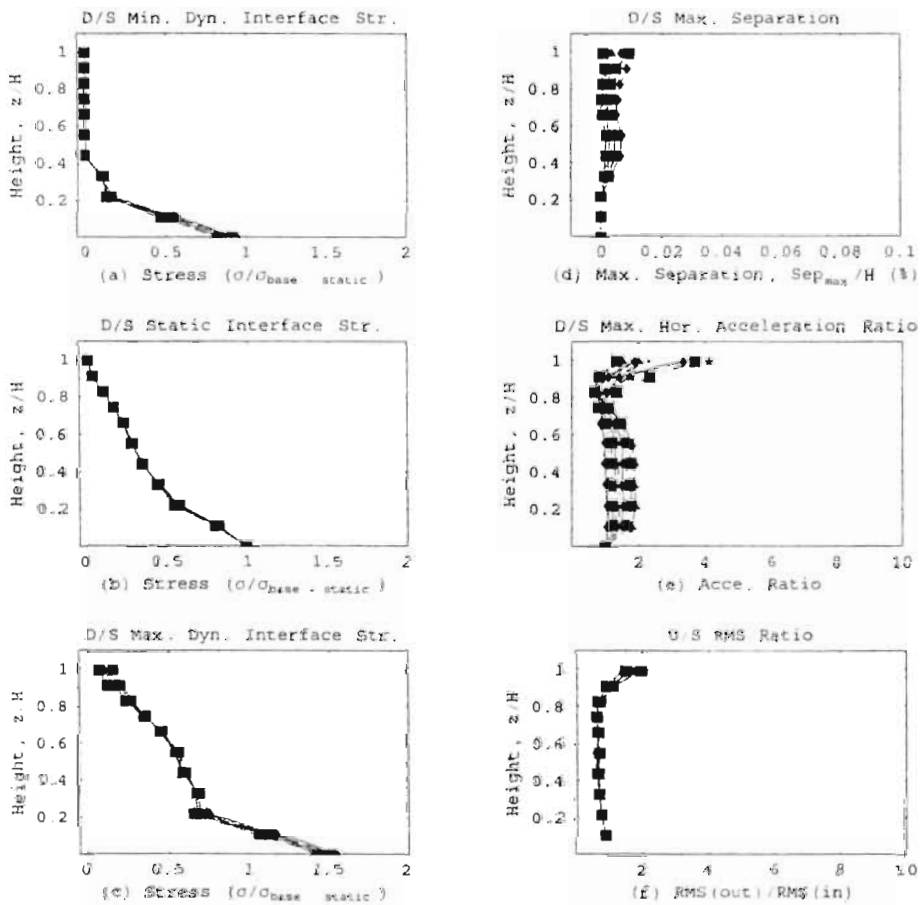

Figure A.66 Collective graphs of Max. Separation, Acceleration, and interface pressures along the *DOWNSTREAM* Interface at all ϕ's (H=400).

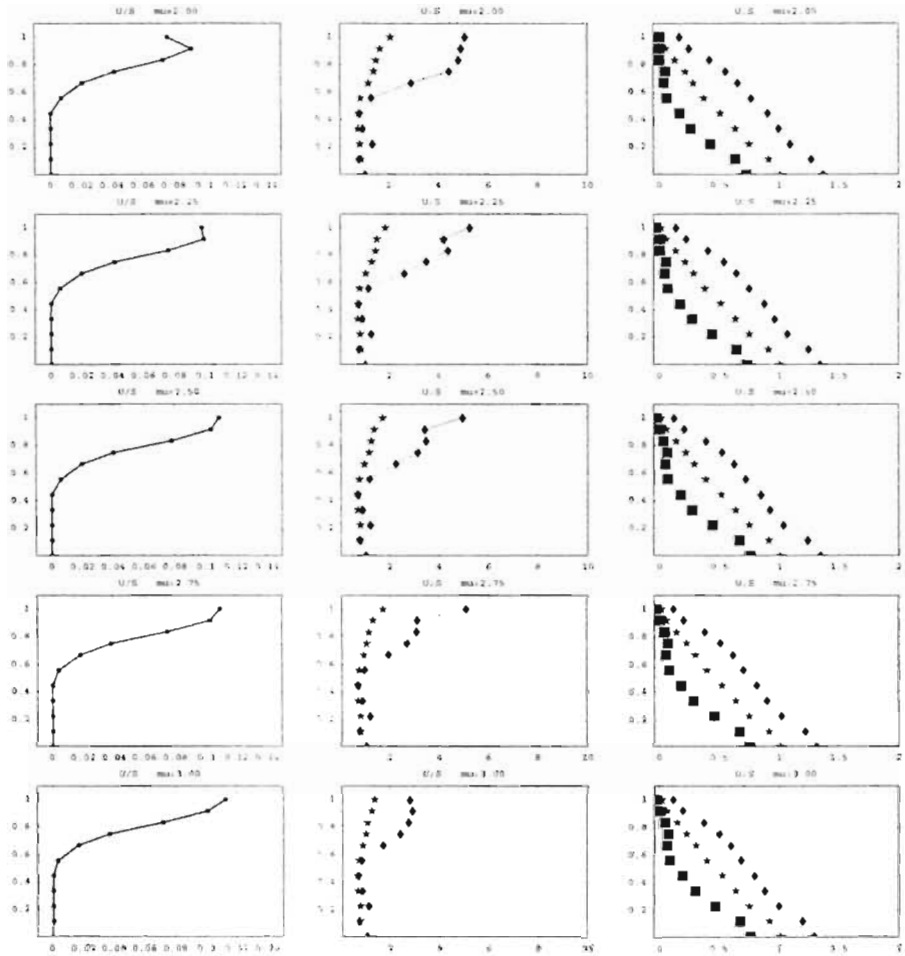

Figure A.67 Max. Separation. Max. Acceleration, and Nodal Interface Stresses (Max., Static, Min.) along the *UPSTREAM* Interface due to change of *mu* (H=400).

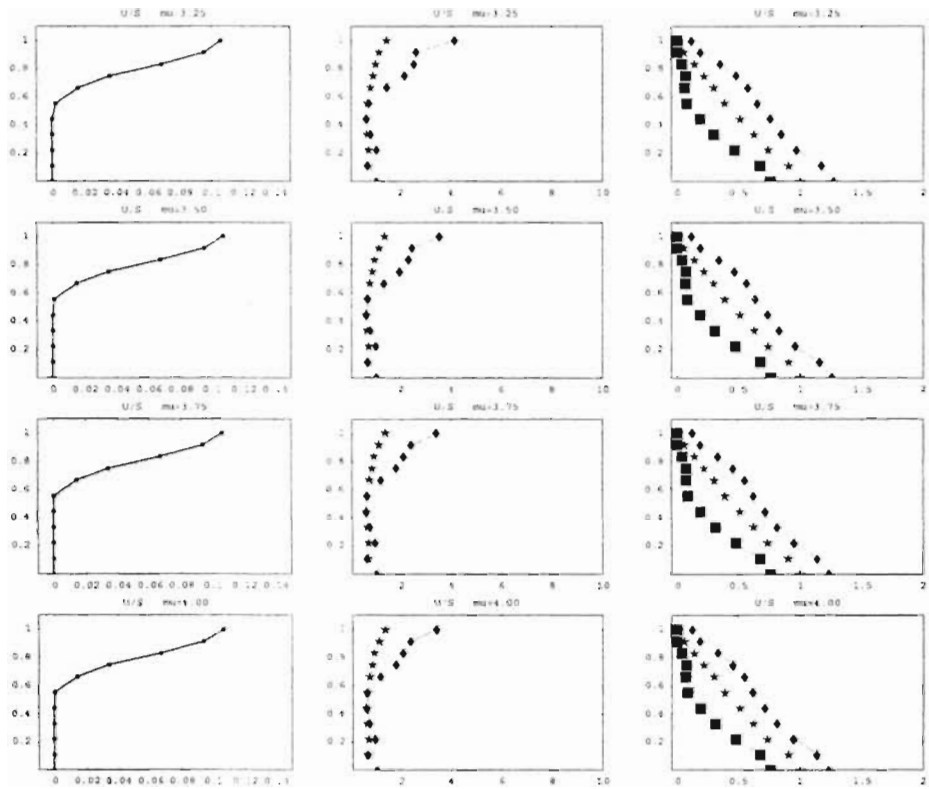

Figure A.68 (Continued from previous figure) Max. Separation, Max. Acceleration, and Nodal Interface Stresses (Max., Static, Min.) along the *UPSTREAM* Interface due to change of *mu* (H=400).

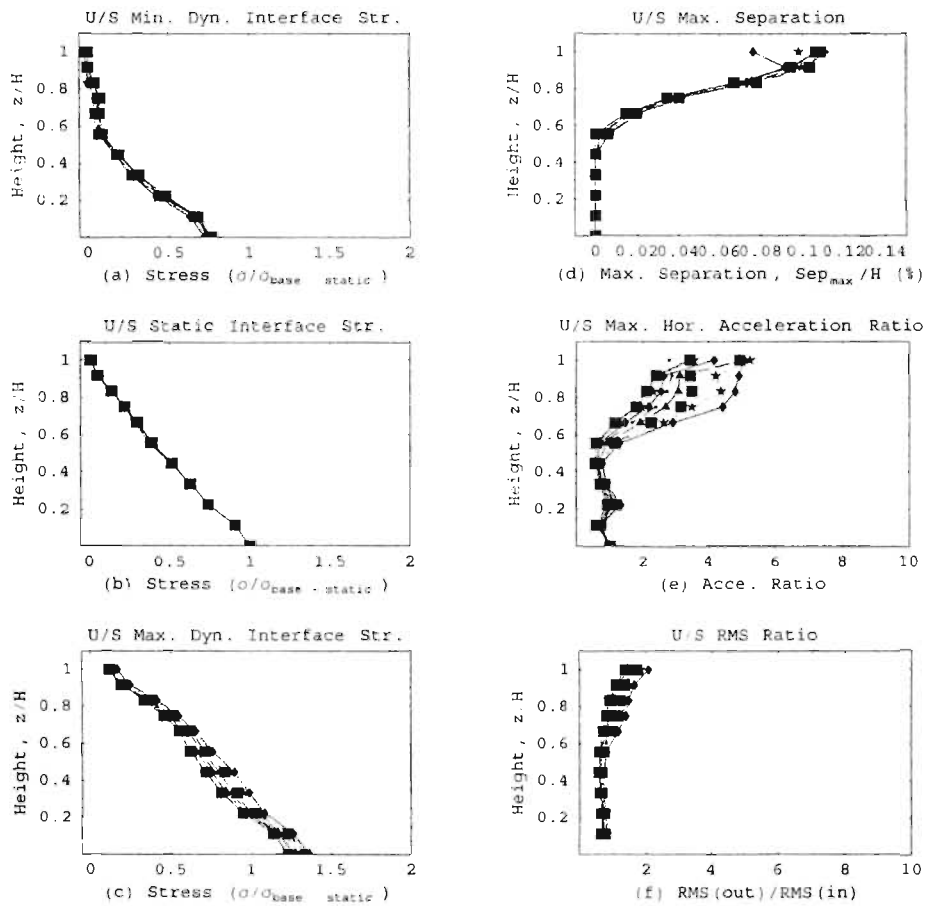

Figure A.69 Collective graphs of Max. Separation, Acceleration, and interface pressures along the *UPSTREAM* Interface at all *mu*'s (H=400).

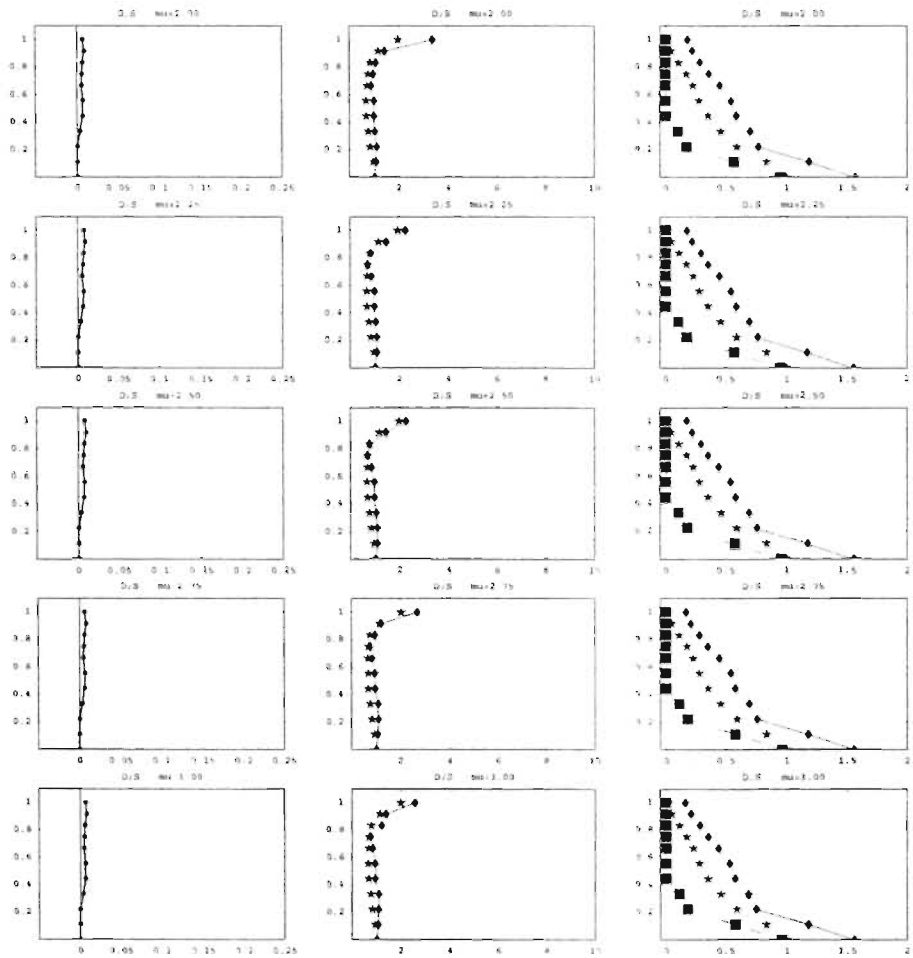

Figure A.70 Max. Separation, Max. Acceleration, and Nodal Interface Stresses (Max., Static, Min.) along the *DOWNSTREAM* Interface due to change of *mu* (H=400).

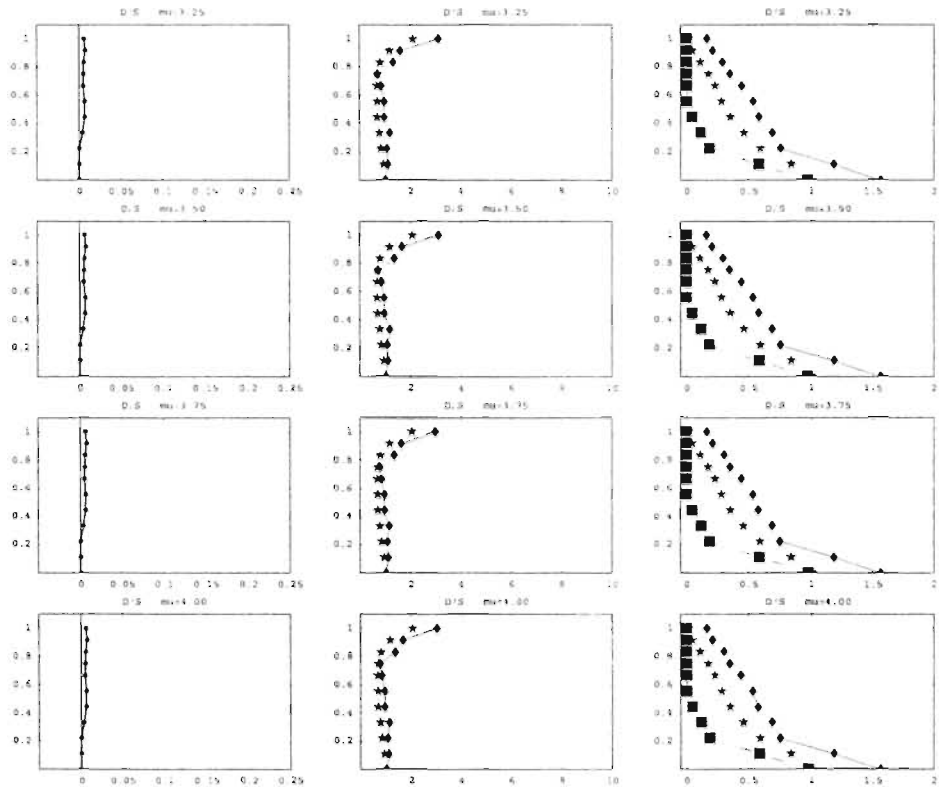

Figure A.71 (Continued from previous figure) Max. Separation, Max. Acceleration, and Nodal Interface Stresses (Max., Static, Min.) along the *DOWNSTREAM* Interface due to change of *mu* (H=400).

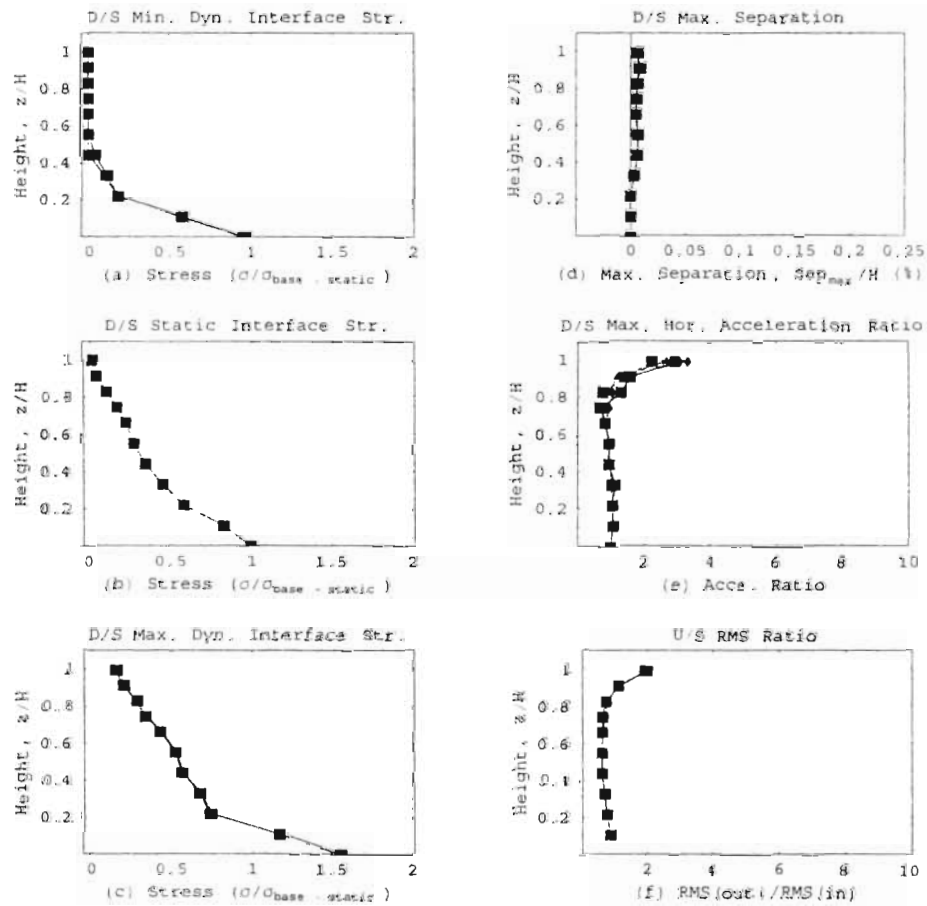

Figure A.72 Collective graphs of Max. Separation, Acceleration, and interface pressures along the *DOWNSTREAM* Interface at all *mu*'s (H=400).

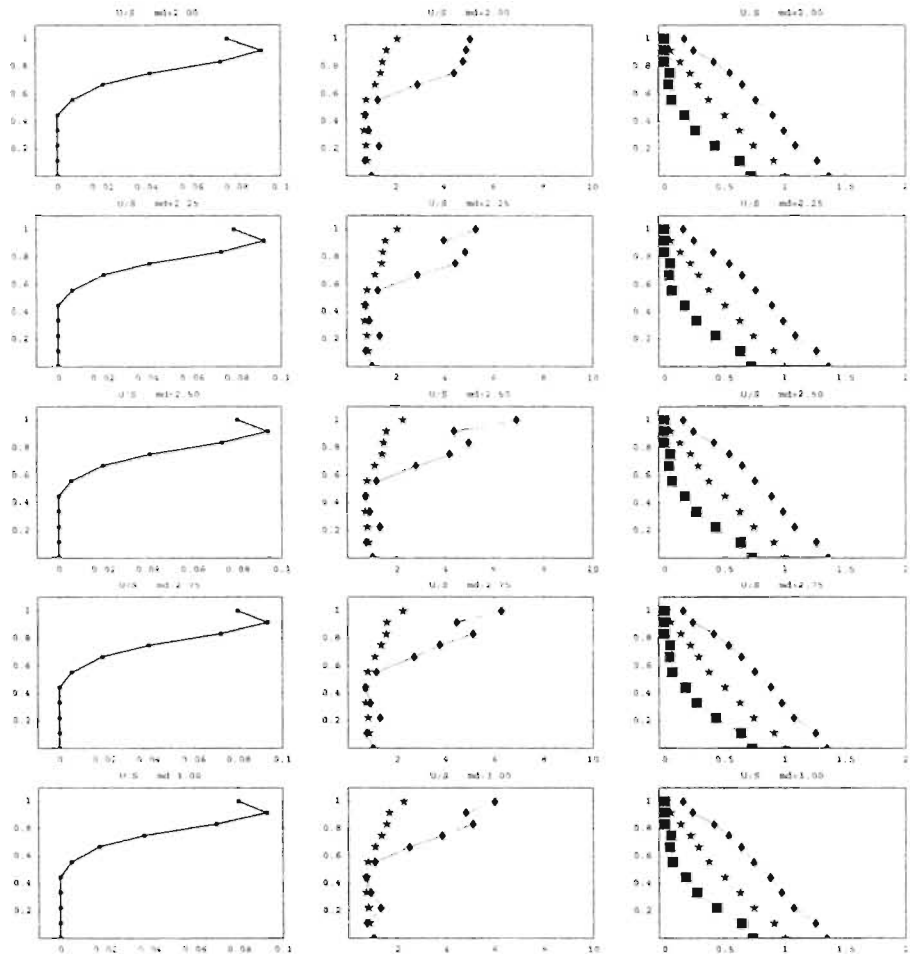

Figure A.73 Max. Separation, Max. Acceleration, and Nodal Interface Stresses (Max., Static, Min.) along the *UPSTREAM* Interface due to change of *md* (H=400).

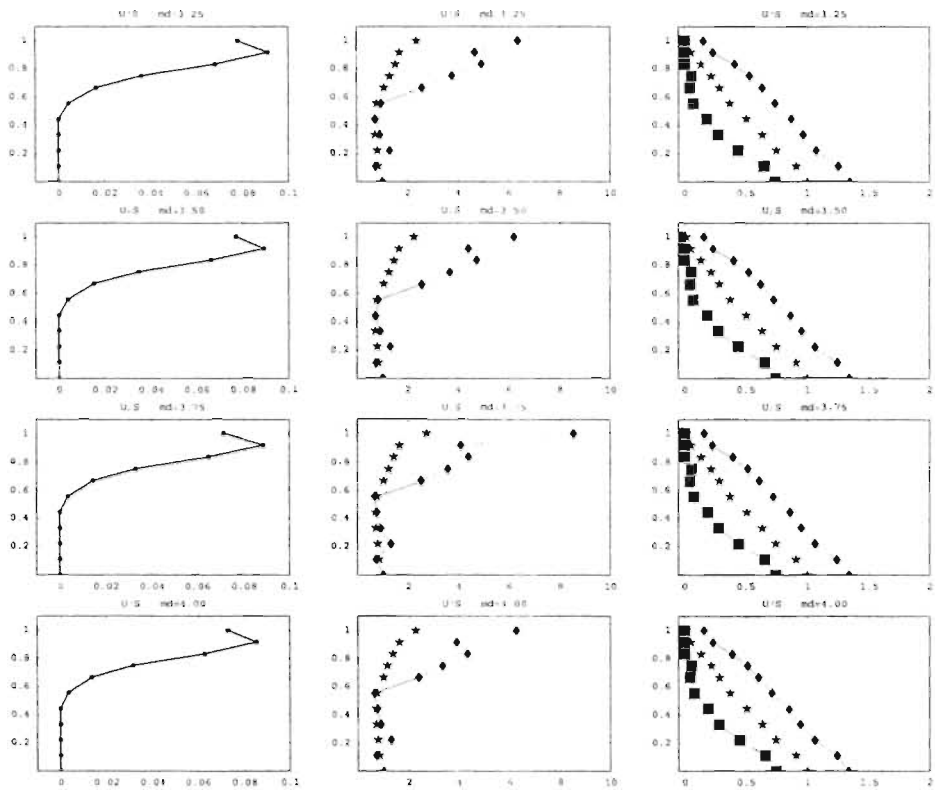

Figure A.74 (Continued from previous figure) Max. Separation, Max. Acceleration, and Nodal Interface Stresses (Max., Static, Min.) along the *UPSTREAM* Interface due to change of *md* (H=400).

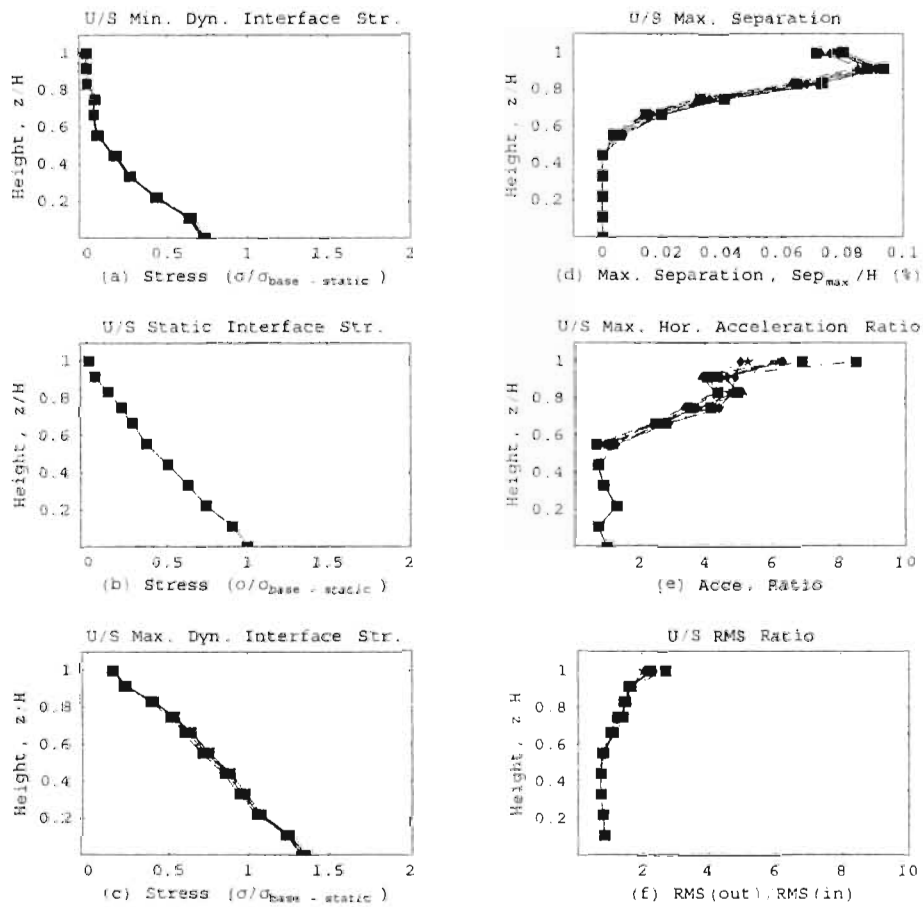

Figure A.75 Collective graphs of Max. Separation, Acceleration, and interface pressures along the *UPSTREAM* Interface at all *md*'s (H=400).

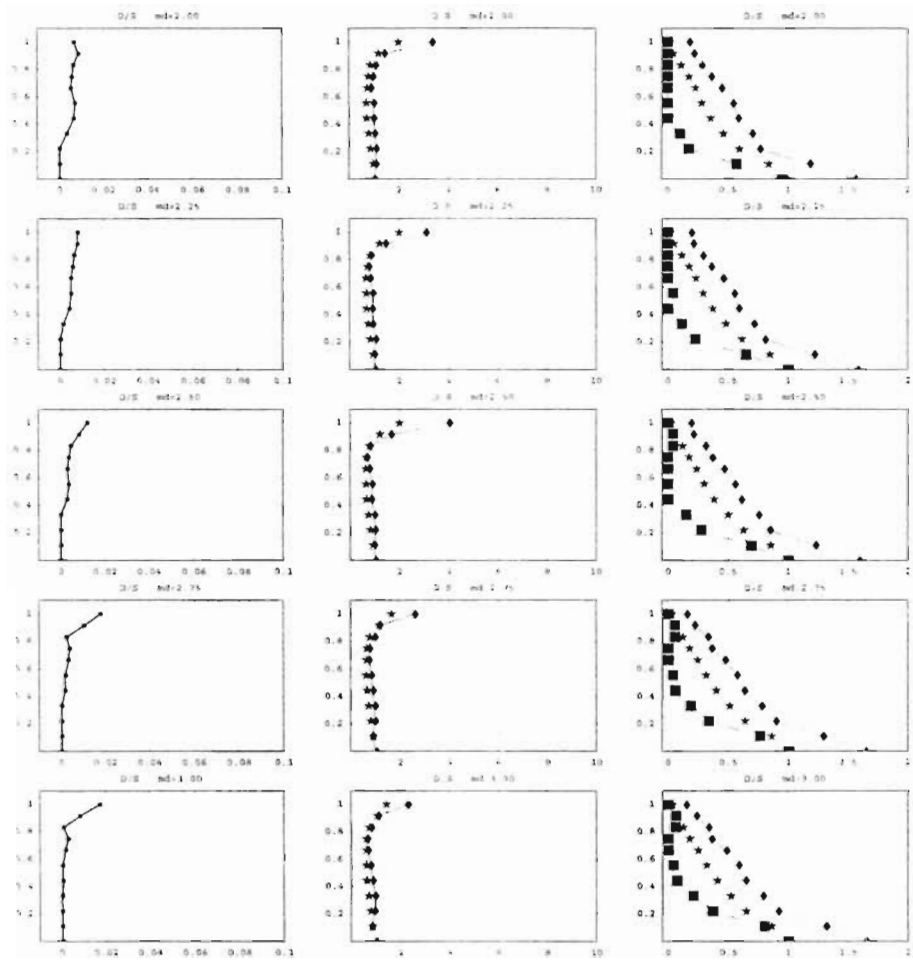

Figure A.76 Max. Separation, Max. Acceleration, and Nodal Interface Stresses (Max., Static, Min.) along the *DOWNSTREAM* Interface due to change of *md* (H=400).

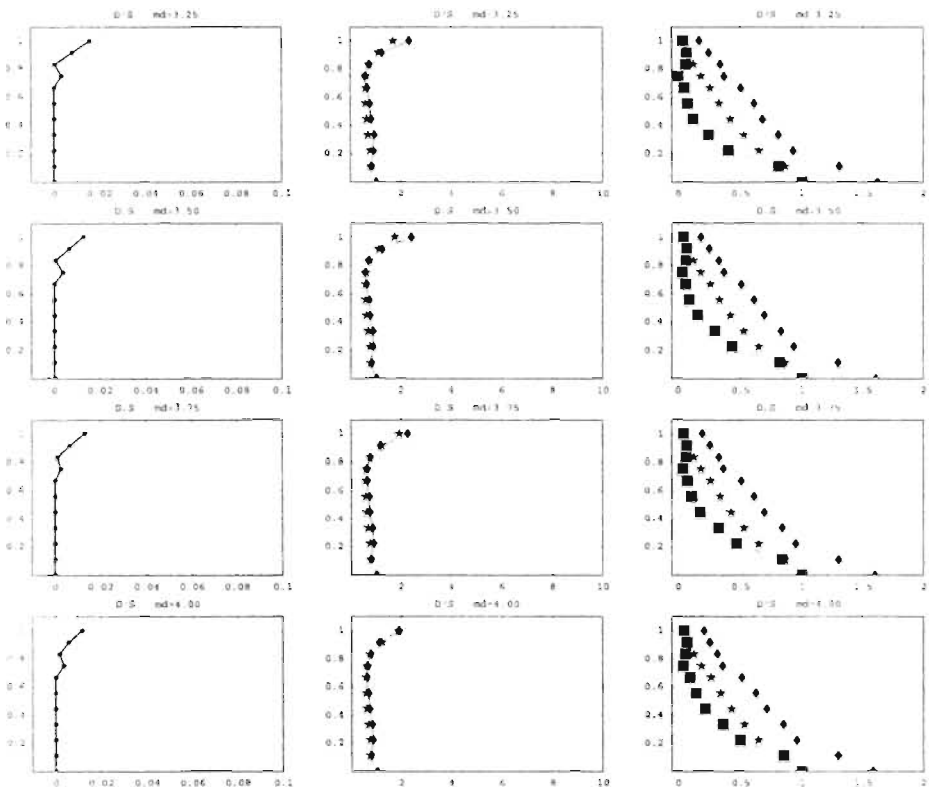

Figure A.77 (Continued from previous figure) Max. Separation, Max. Acceleration, and Nodal Interface Stresses (Max., Static, Min.) along the *DOWNSTREAM* Interface due to change of *md* (H=400).

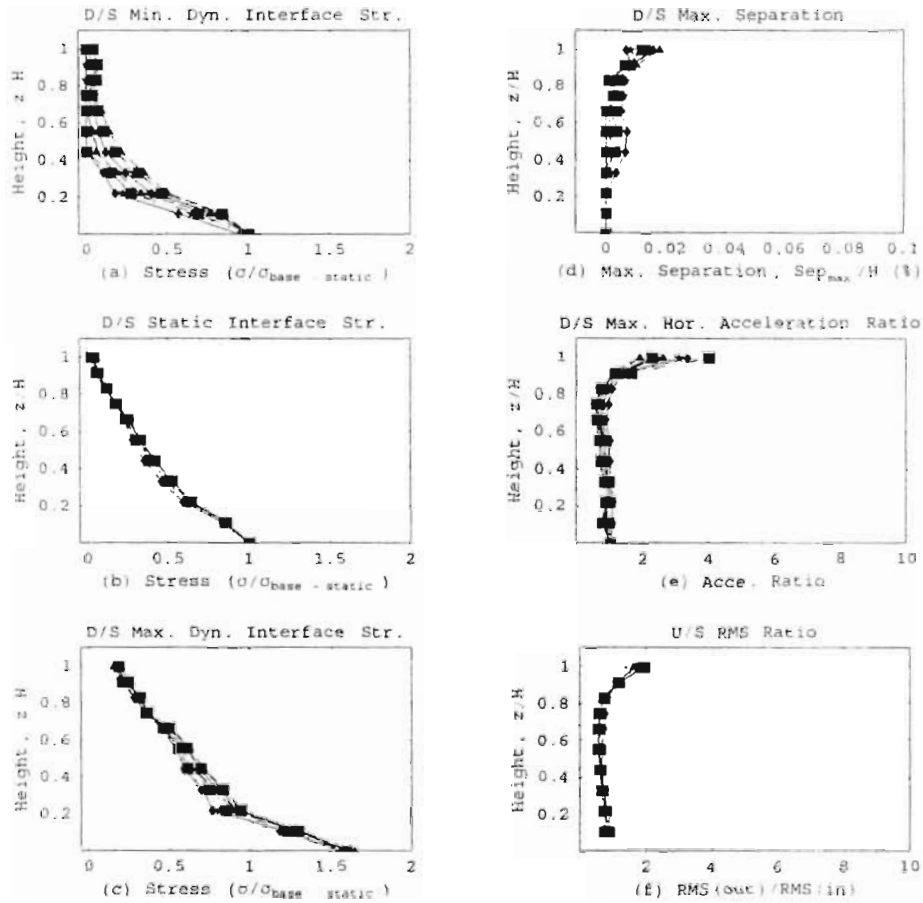

Figure A.78 Collective graphs of Max. Separation, Acceleration, and interface pressures along the *DOWNSTREAM* Interface at all *md*'s (H=400).

A.3 Polynomial Best Fit Curves

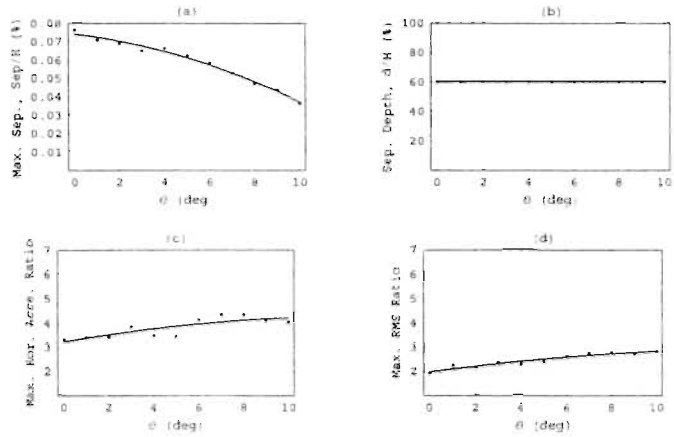

Figure A.79 Effect of θ on U/S response, H=200 ft.

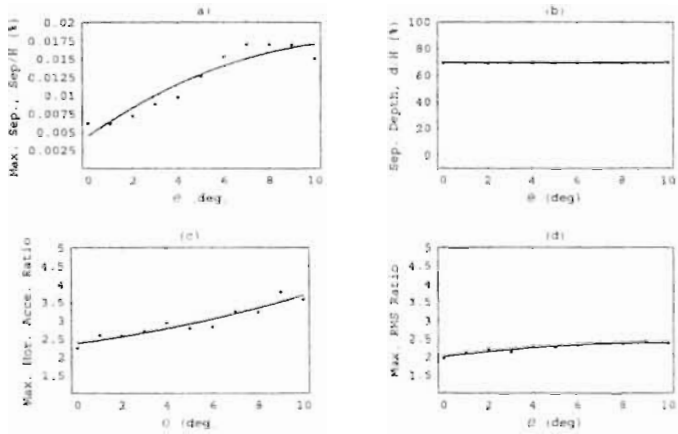

Figure A.80 Effect of θ on D/S response, H=200 ft.

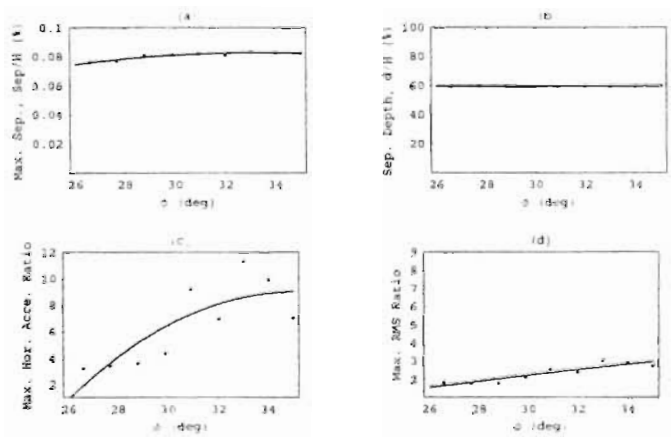

Figure A.81 Effect of ϕ on U/S response, H=200 ft.

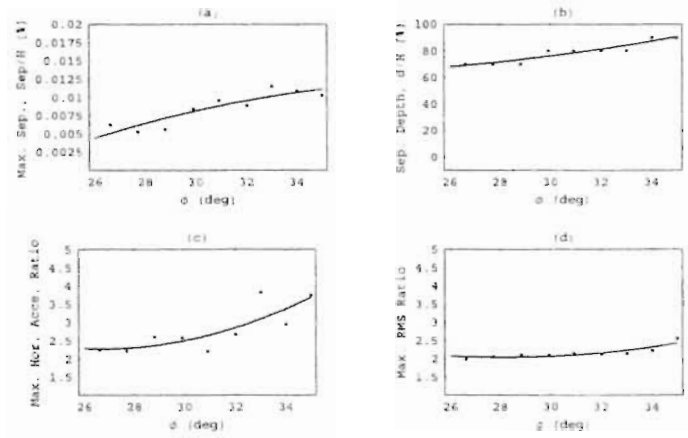

Figure A.82 Effect of ϕ on D/S response, H=200 ft.

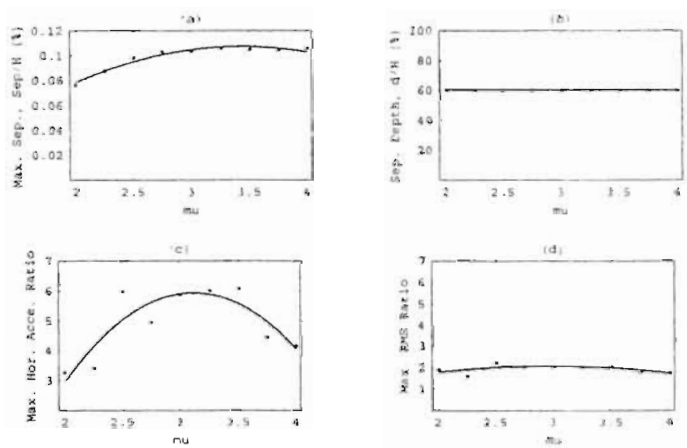

Figure A.83 Effect of *mu* on D/S response, H=200 ft.

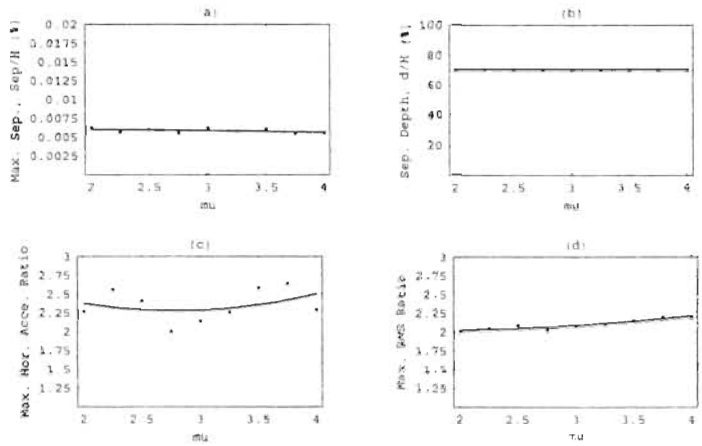

Figure A.84 Effect of *mu* on D/S response, H=200 ft.

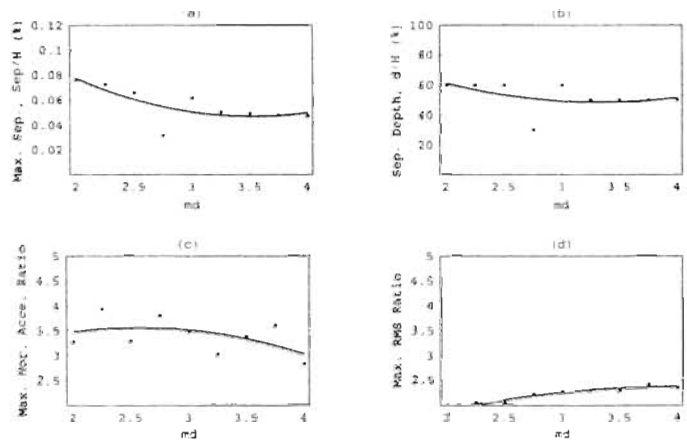

Figure A.85 Effect of *md* on U/S response, H=200 ft.

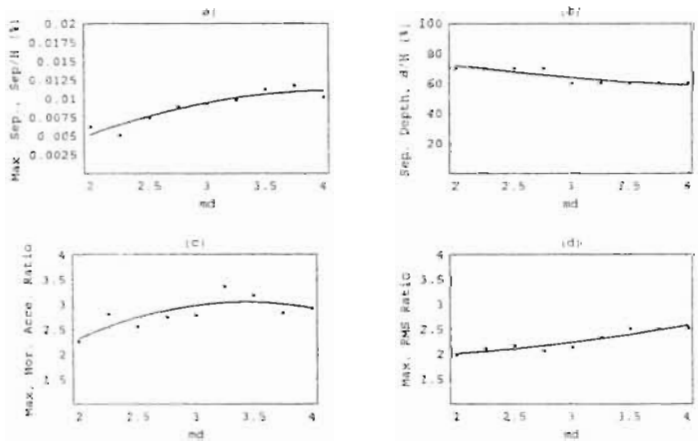

Figure A.86 Effect of *md* on D/S response, H=200 ft.

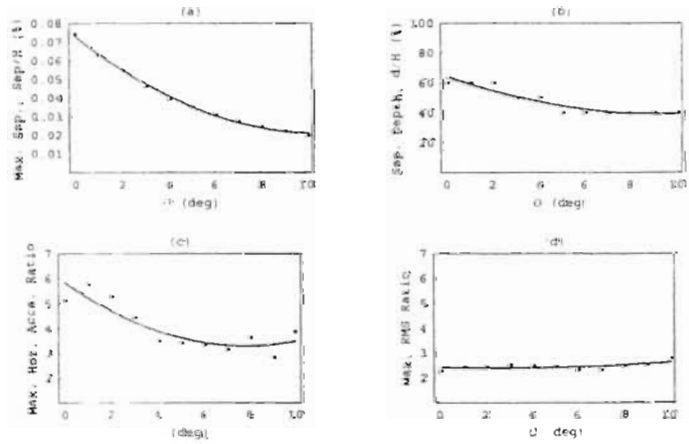

Figure A.87 Effect of θ on U/S response, H=300 ft.

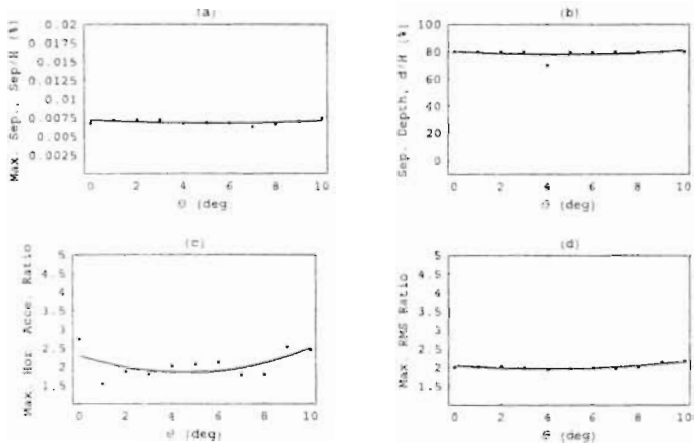

Figure A.88 Effect of θ on D/S response, H=300 ft.

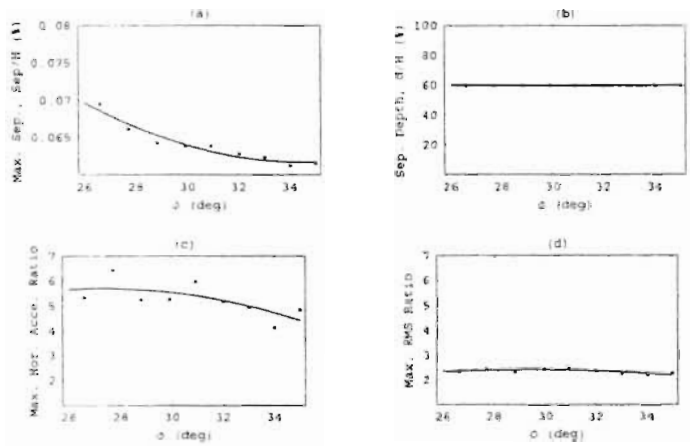

Figure A.89 Effect of ϕ on D/S response, H=300 ft.

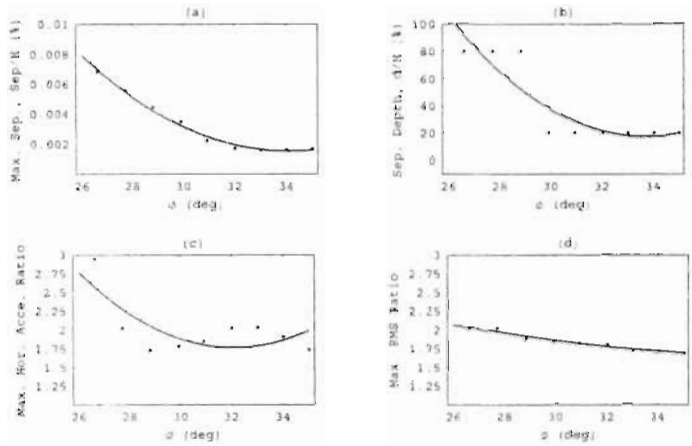

Figure A.90 Effect of ϕ on D/S response, H=300 ft.

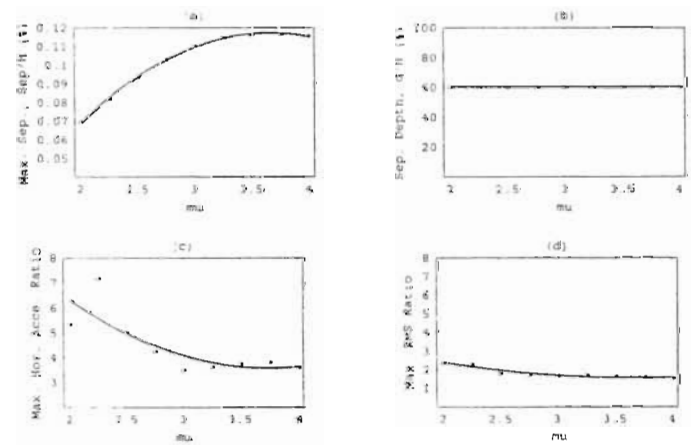

Figure A.91 Effect of mu on U/S response, H=300 ft.

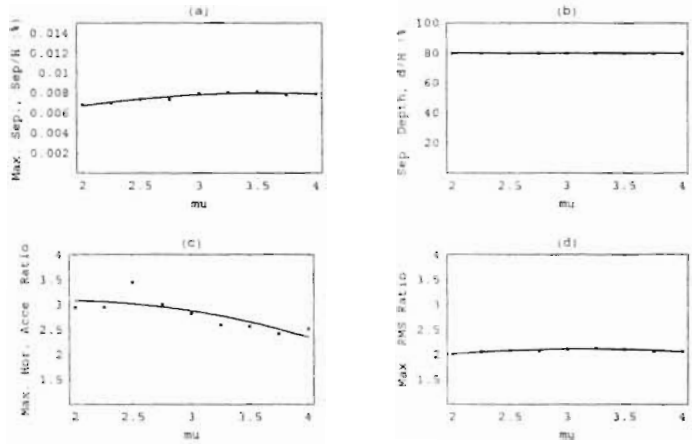

Figure A.92 Effect of *mu* on D/S response, H=300 ft.

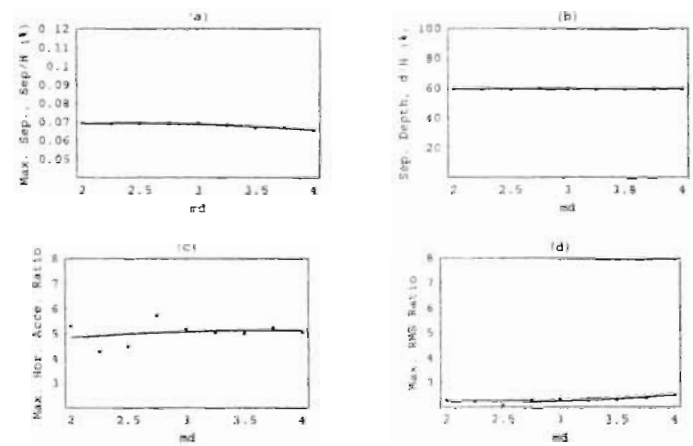

Figure A.93 Effect of *md* on U/S response, H=300 ft.

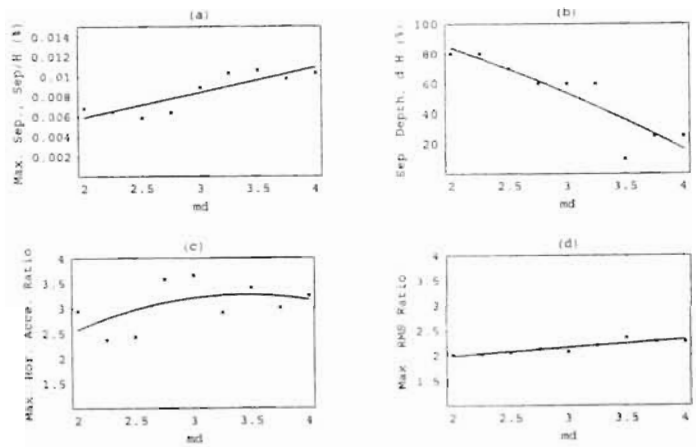

Figure A.94 Effect of *md* on D/S response, H=300 ft.

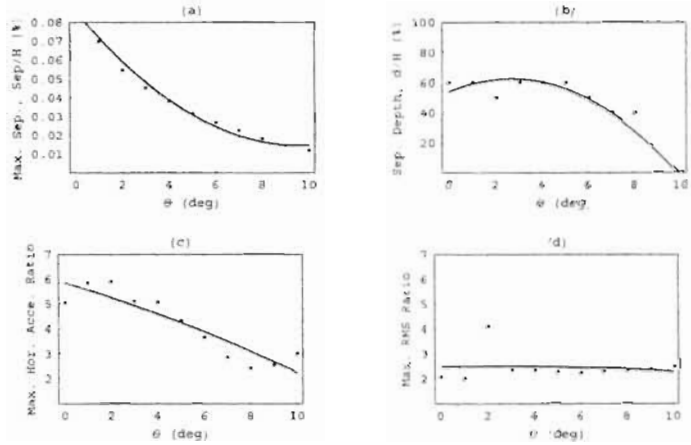

Figure A.95 Effect of θ on U/S response. H=400 ft.

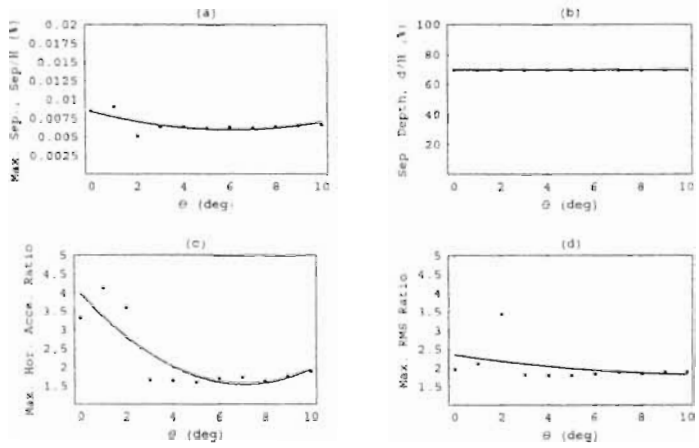

Figure A.96 Effect of θ on D/S response, H=400 ft.

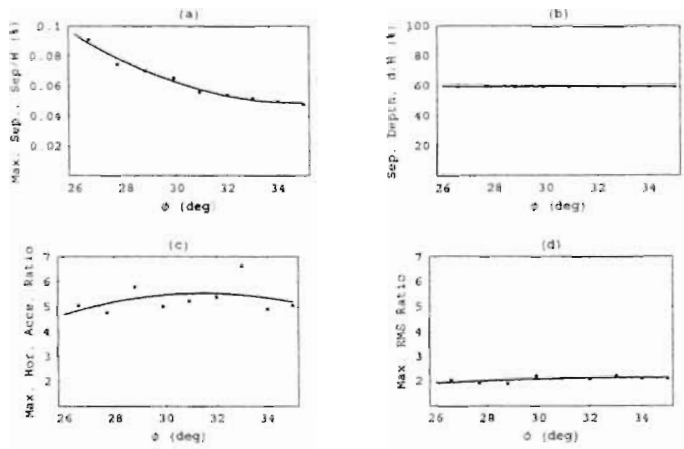

Figure A.97 Effect of ϕ on U/S response, H=400 ft.

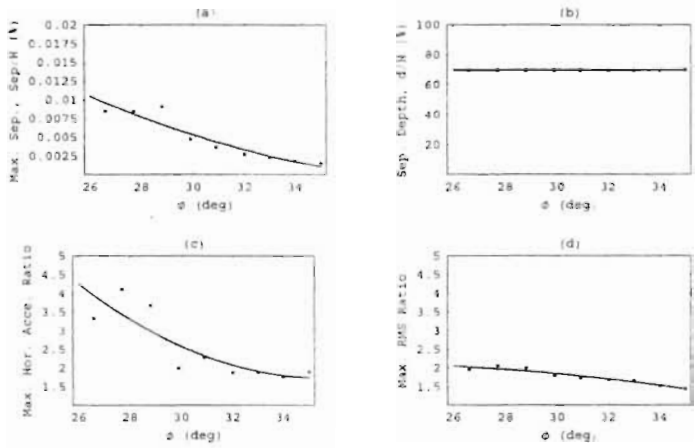

Figure A.98 Effect of ϕ on D/S response, H=400 ft.

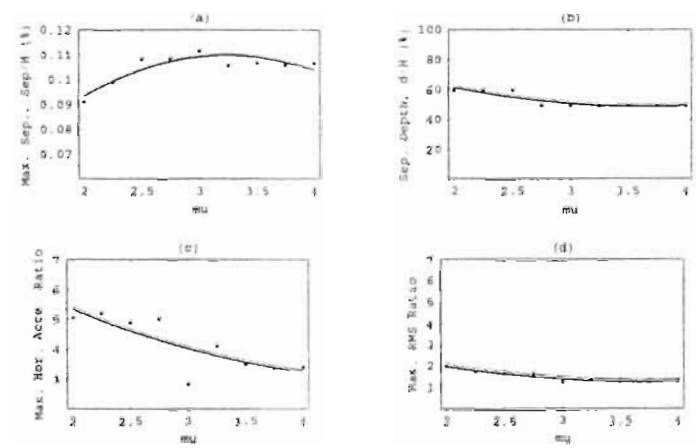

Figure A.99 Effect of *mu* on U/S response, H=400 ft.

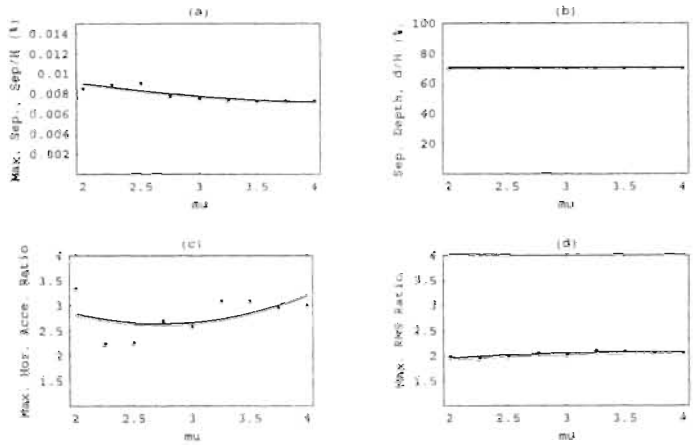

Figure A.100 Effect of *mu* on D/S response H=400 ft.

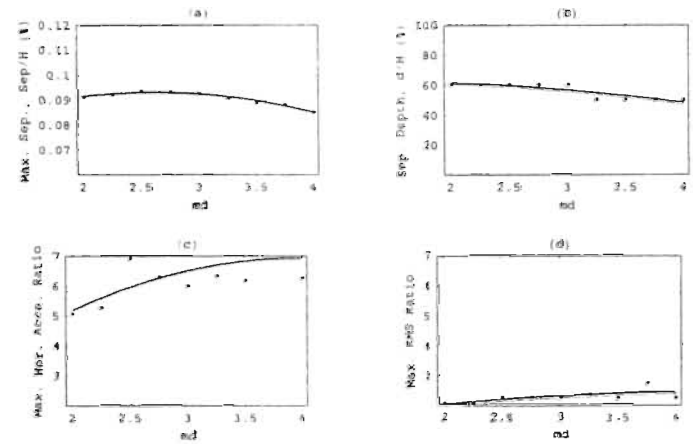

Figure A.101 Effect of *md* on U/S response, H=400 ft.

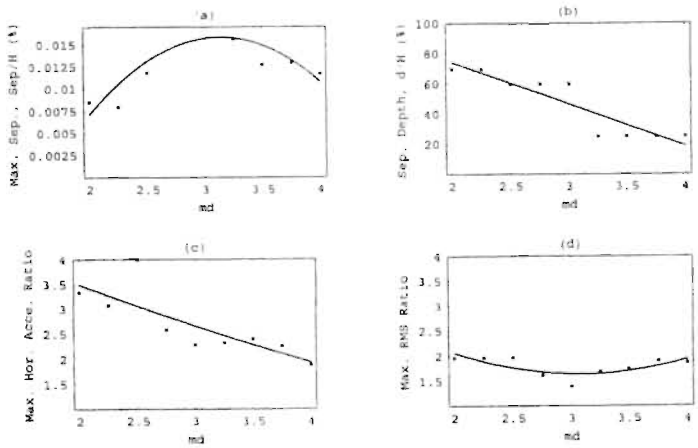

Figure A.102 Effect of *md* on D/S response, H=400 ft.

A.4 Bar Charts

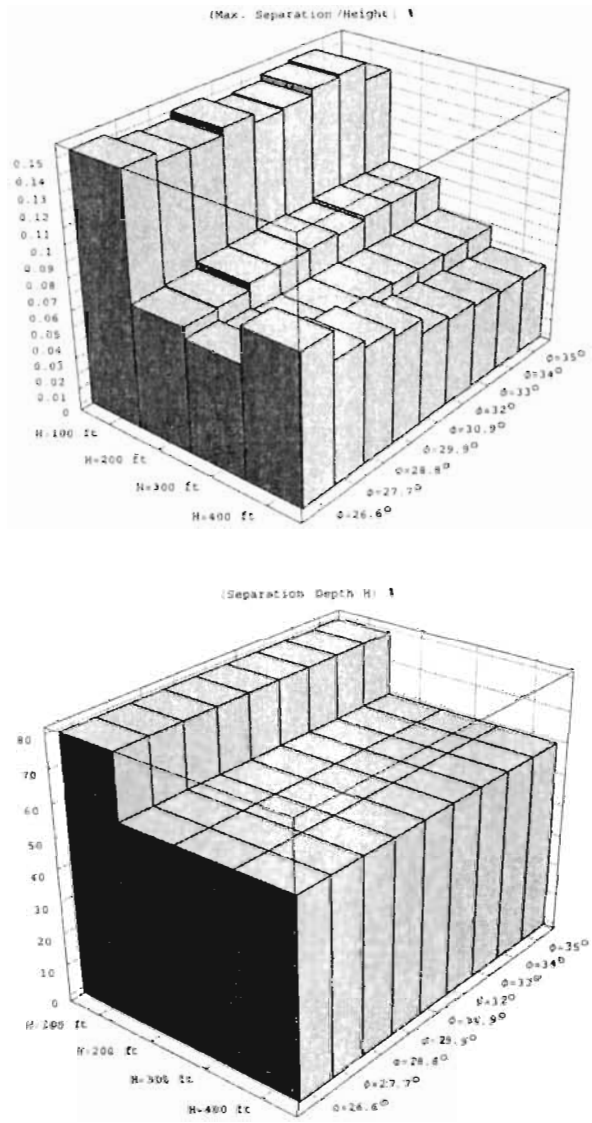

Figure A.103 Max. Separation and Separation Depth of U/S interface vs φ and Height.

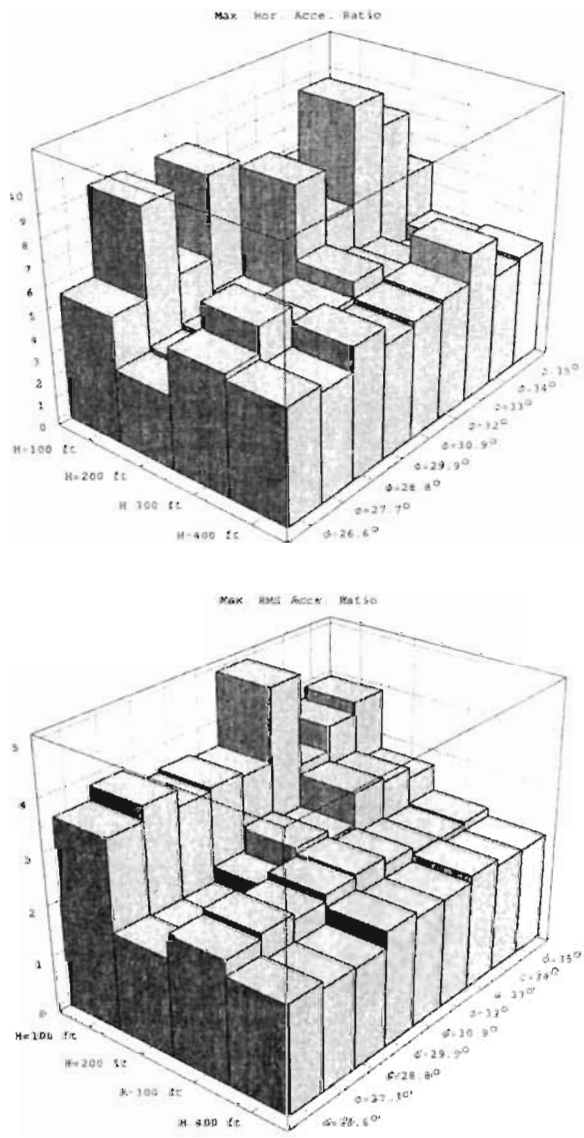

Figure A.104 Max. Acceleration Ratio and Max. RMS Acceleration Ratio of U/S interface vs ϕ and Height.

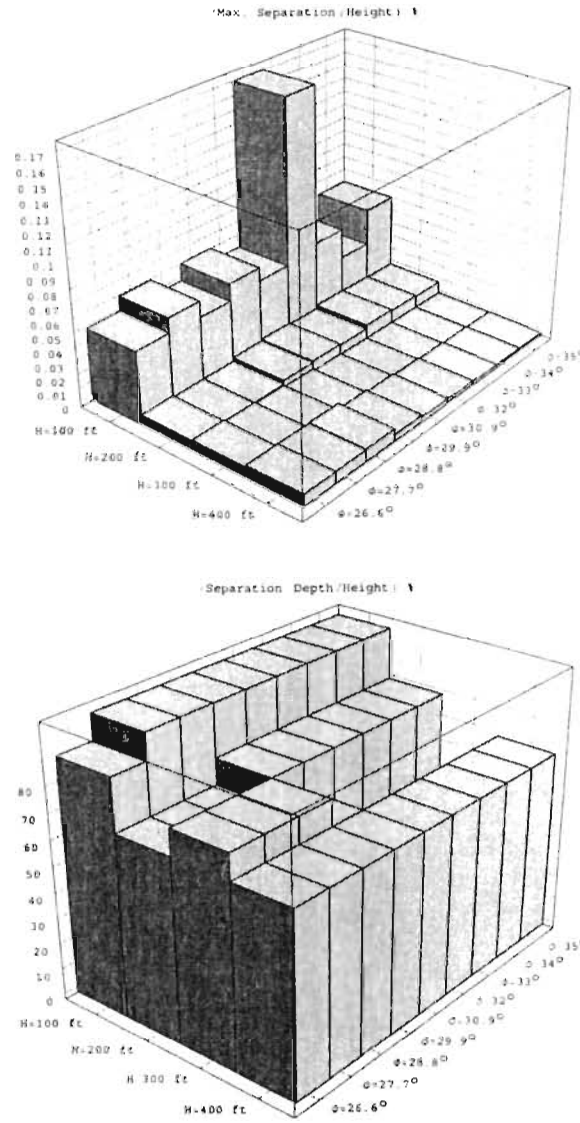

Figure A.105 Max. Separation and Separation Depth of D/S interface vs ϕ and Height.

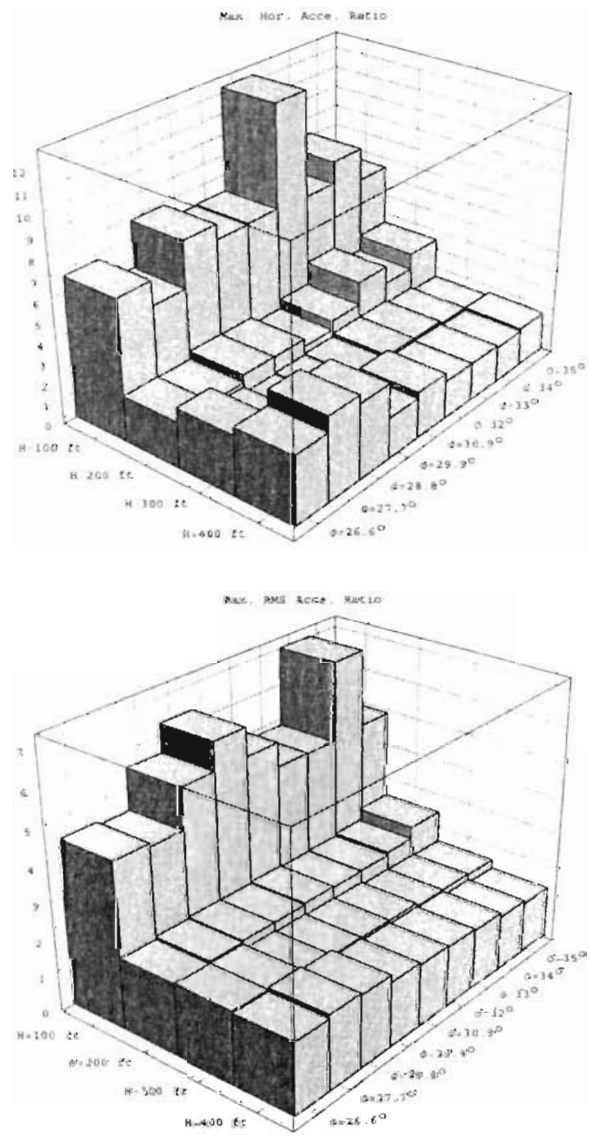

Figure A.106 Max. Acceleration Ratio and Max. RMS Acceleration Ratio of D/S interface vs ϕ and Height.

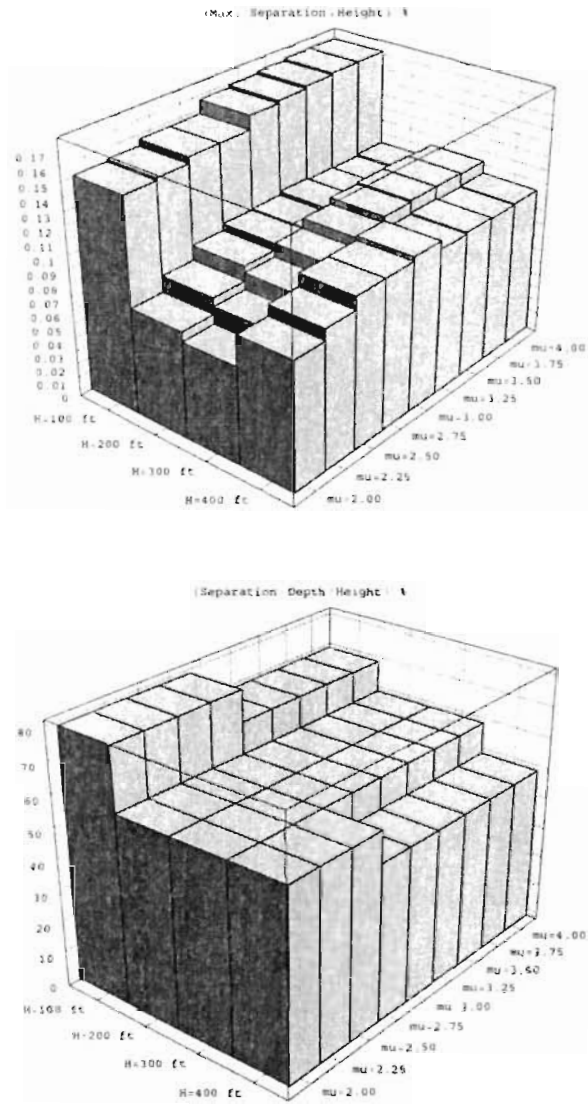

Figure A.107 Max. Separation and Separation Depth of U/S interface vs *mu* and Height.

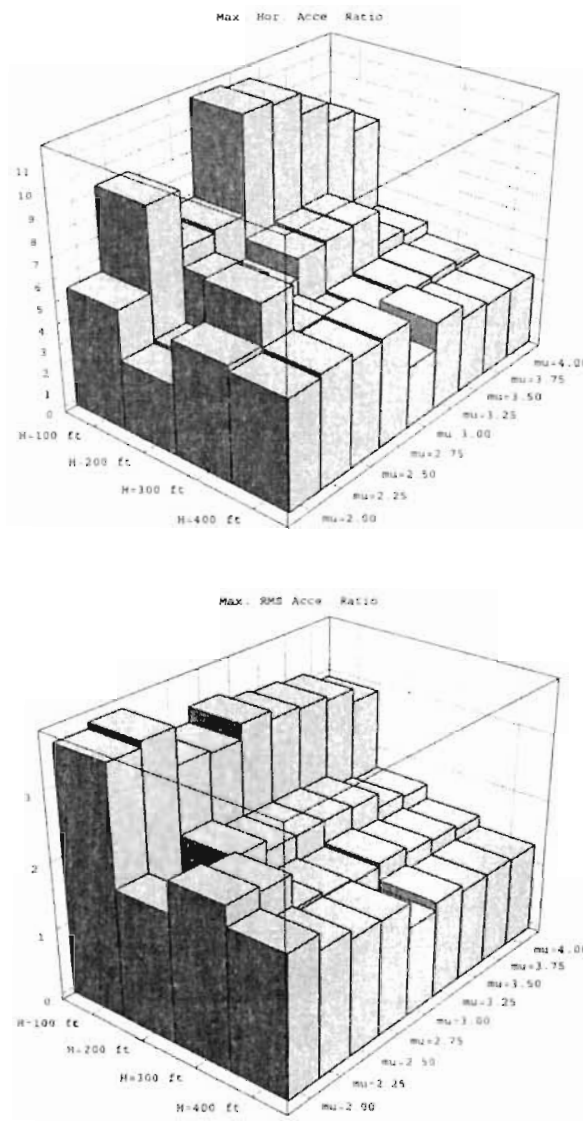

Figure A.108 Max. Acceleration Ratio and Max. RMS Acceleration Ratio of U/S interface vs *mu* and Height.

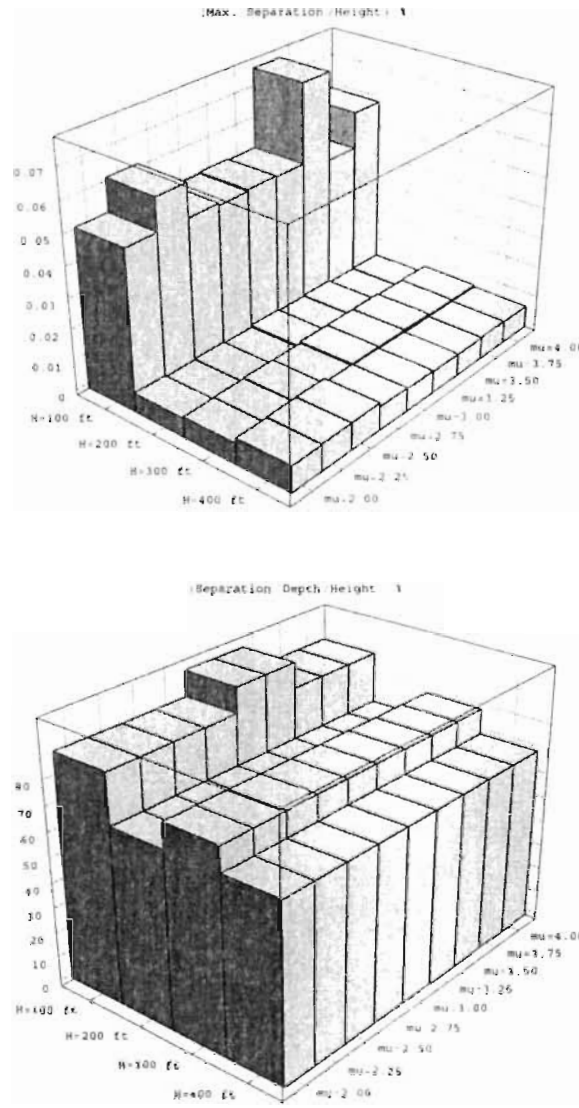

Figure A.109 Max. Separation and Separation Depth of D/S interface vs *mu* and Height.

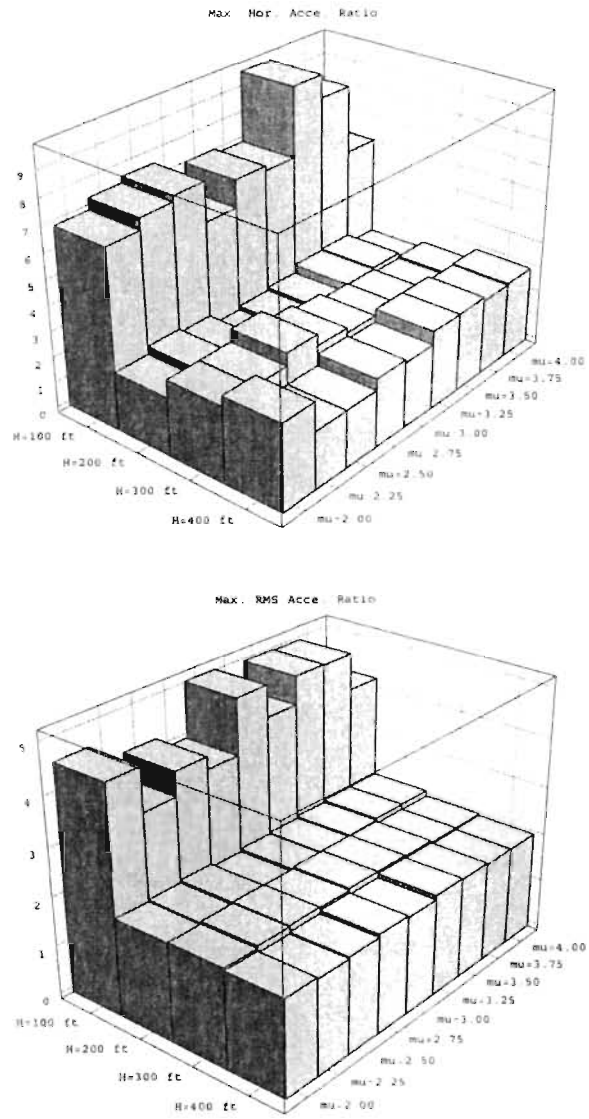

Figure A.110 Max. Acceleration Ratio and Max. RMS Acceleration Ratio of D/S interface vs *mu* and Height.

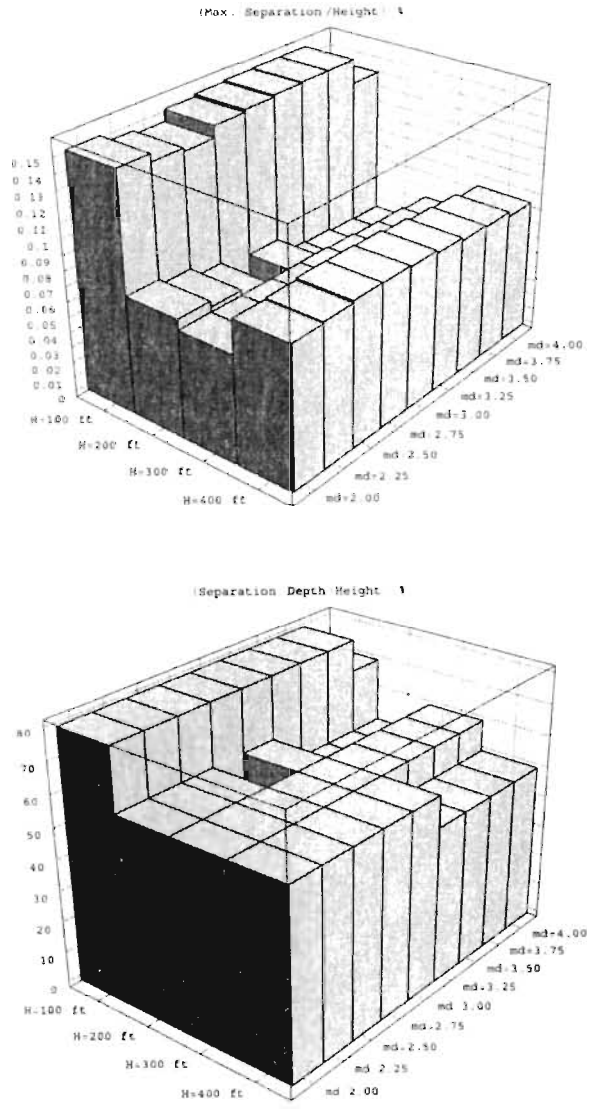

Figure A.111 Max. Separation and Separation Depth of U/S interface vs *md* and Height.

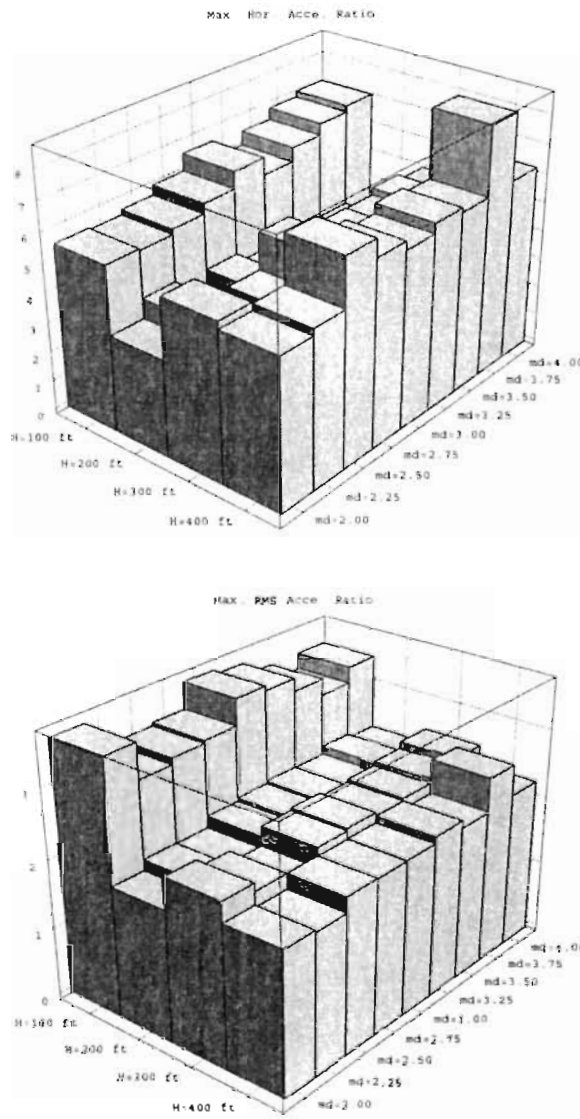

Figure A.112 Max. Acceleration Ratio and Max. RMS Acceleration Ratio of U/S interface vs *md* and Height.

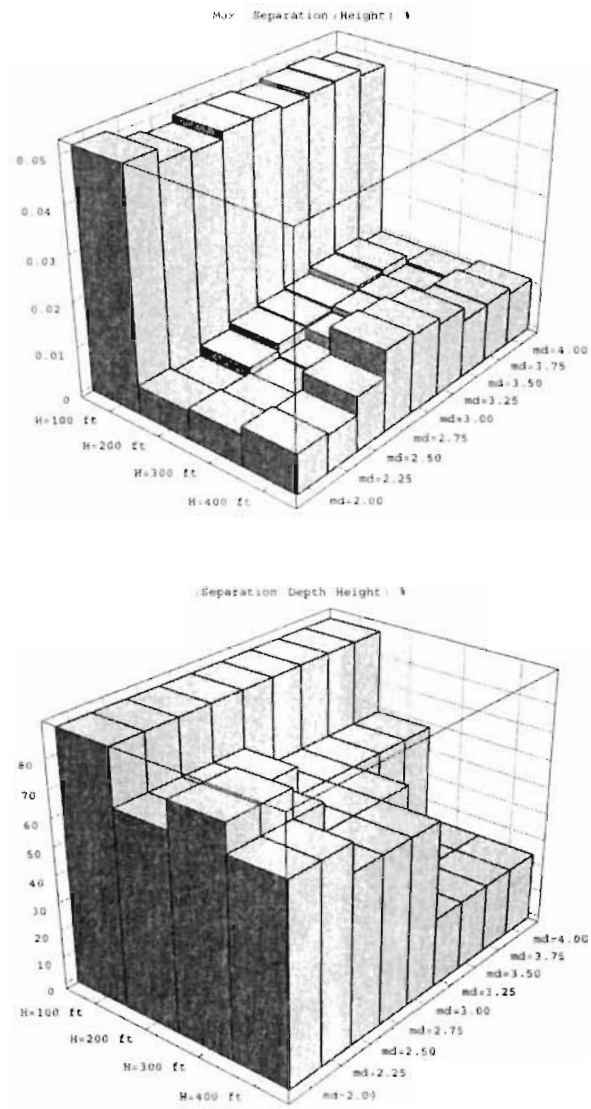

Figure A.113 Max. Separation and Separation Depth of D/S interface vs *md* and Height.

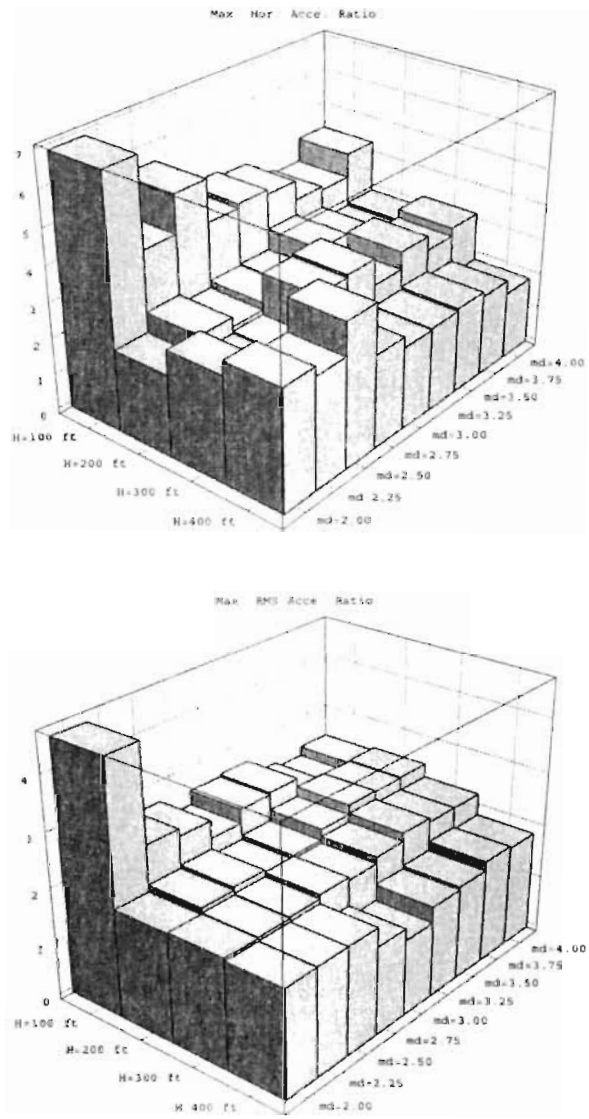

Figure A.114 Max. Acceleration Ratio and Max. RMS Acceleration Ratio of D/S interface vs *md* and Height.

A.5 Pressure Profiles

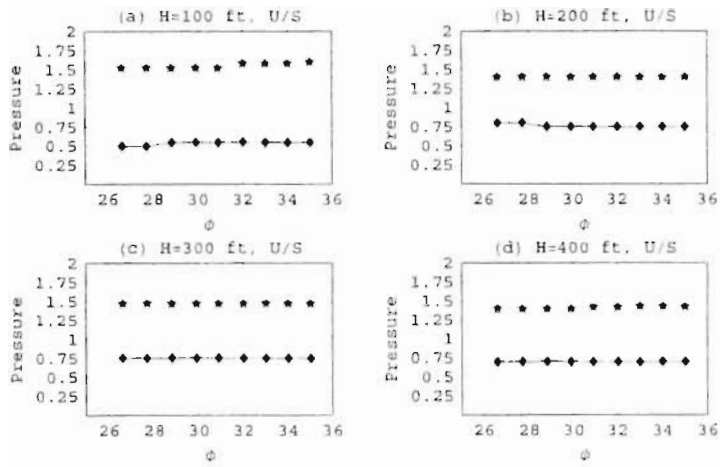

Figure A.115 The effect of ϕ on minimum and maximum interface pressures along the U/S interface.

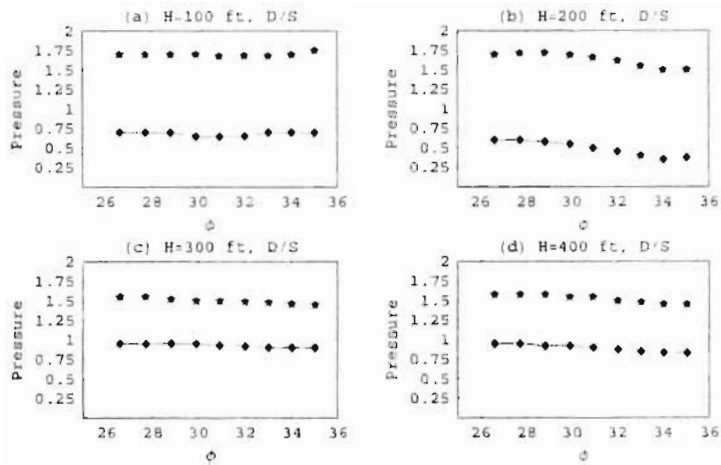

Figure A.116 The effect of ϕ on minimum and maximum interface pressures along the D/S interface.

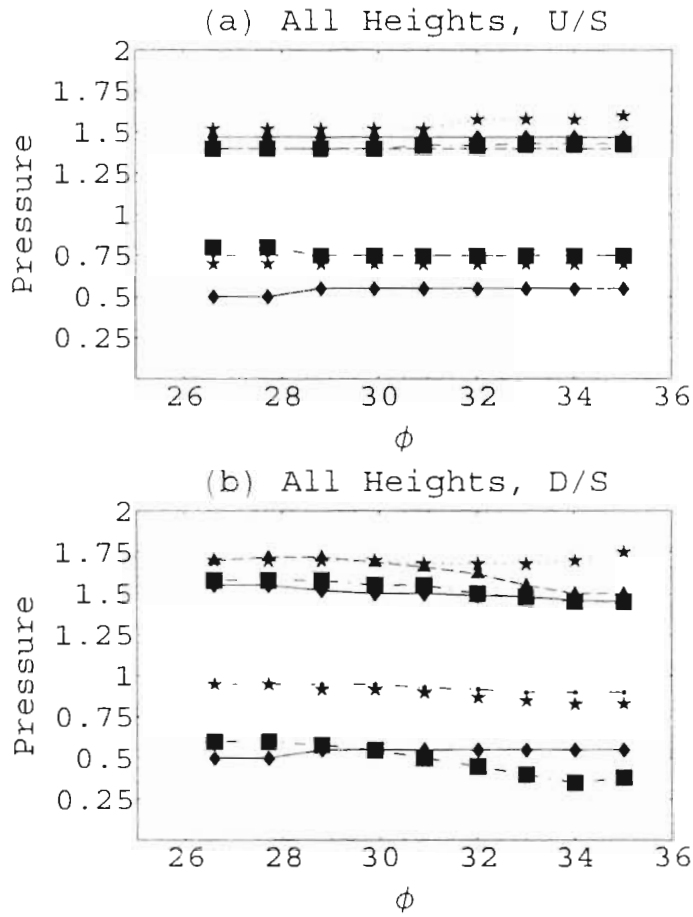

Figure A.117 Collective graphs of minimum an maximum pressures versus $\phi$for both U/S and D/S interfaces.

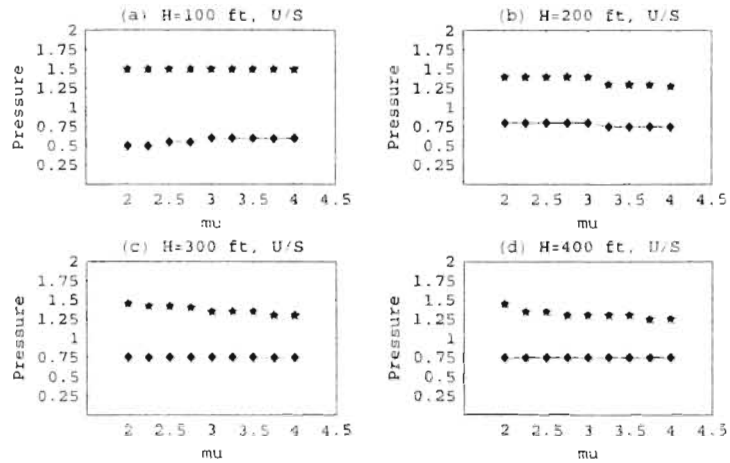

Figure A.118 The effect of *md* on minimum and maximum interface pressures along the U/S interface.

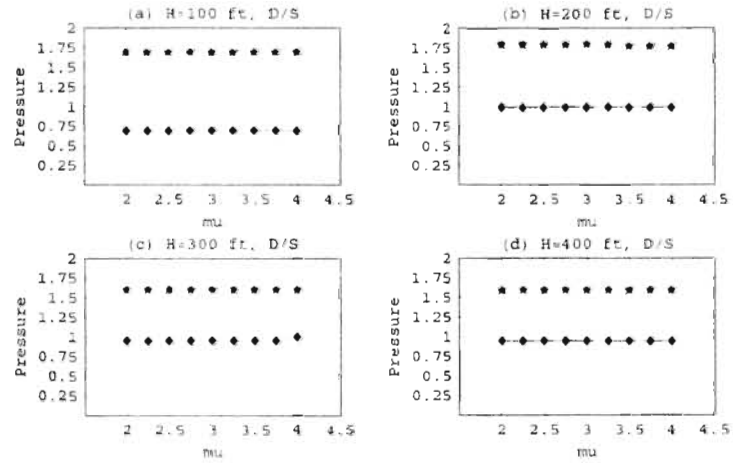

Figure A.119 The effect of *md* on minimum and maximum interface pressures along the D/S interface.

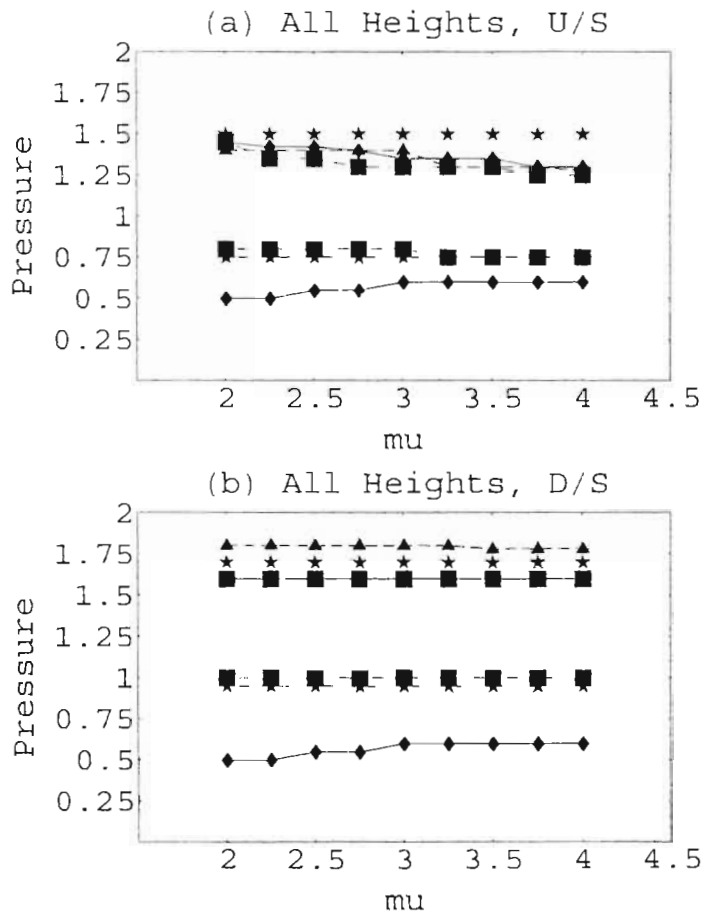

Figure A.120 Collective graphs of minimum an maximum pressures versus *mid* for both U/S and D/S interfaces.

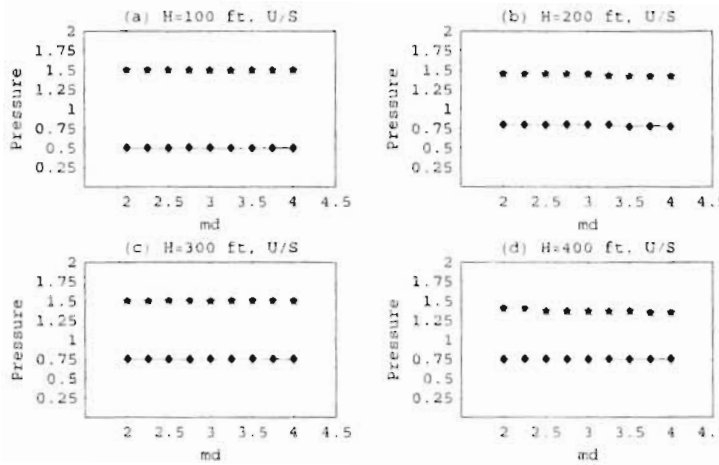

Figure A.121 The effect of mu on minimum and maximum interface pressures along the U/S interface.

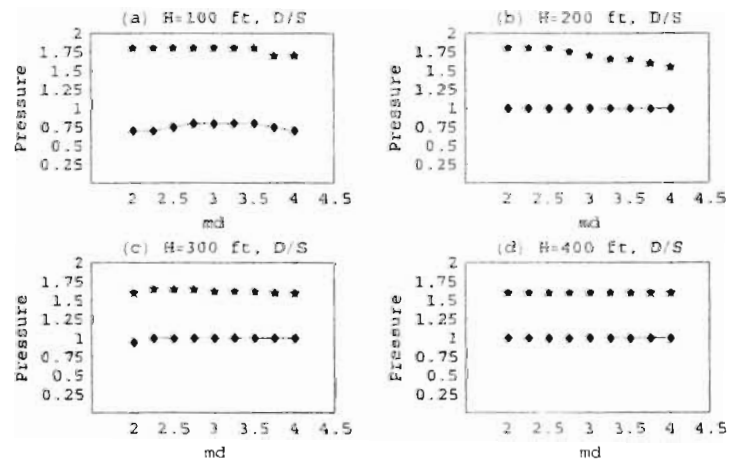

Figure A.122 The effect of mu on minimum and maximum interface pressures along the D/S interface.

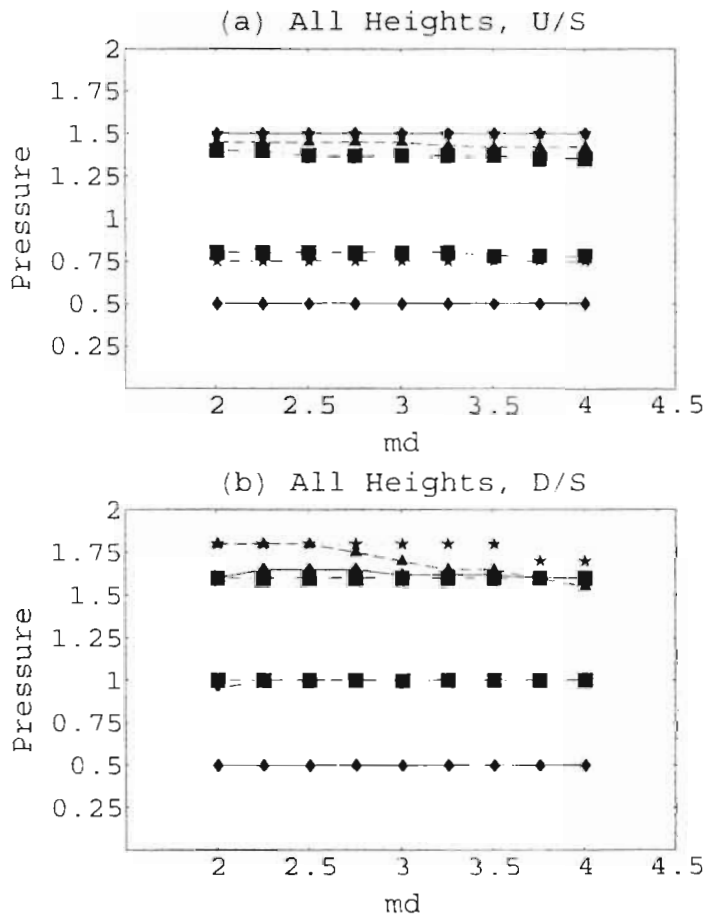

Figure A.123 Collective graphs of minimum an maximum pressures versus *mu* for both U/S and D/S interfaces.

B. APPENDIX Tables

Table B.1 Ramberg-Osgood material properties for Seed's [68] average sand with γ = 130 pcf.

Ramberg-Osgood Material Parameters for Average Sand (γ = 130 pcf)					
V_s (ft/s)	G_{max} $(10^3 psf)$	α	r	γ_y (10^{-3})	τ_y (psf)
100	45	1.1	2.35	0.105	4.74
150	101.25	1.1	2.35	0.105	10.66
200	180	1.1	2.35	0.105	18.94
250	281.25	1.1	2.35	0.105	29.6
300	405	1.1	2.35	0.105	42.63
350	551.25	1.1	2.35	0.105	58.02
400	720	1.1	2.35	0.105	75.78
450	911.25	1.1	2.35	0.105	95.91
500	1125	1.1	2.35	0.105	118.4
550	1361.25	1.1	2.35	0.105	143.27
600	1620	1.1	2.35	0.105	170.5
650	1901.25	1.1	2.35	0.105	200.1
700	2205	1.1	2.35	0.105	232.07
750	2531.25	1.1	2.35	0.105	266.41
800	2880	1.1	2.35	0.105	303.12
850	3251.25	1.1	2.35	0.105	342.19
900	3645	1.1	2.35	0.105	383.63
950	4061.25	1.1	2.35	0.105	427.44
1000	4500	1.1	2.35	0.105	473.62
1050	4961.25	1.1	2.35	0.105	522.16
1100	5445	1.1	2.35	0.105	573.08
1150	5951.25	1.1	2.35	0.105	626.36
1200	6480	1.1	2.35	0.105	682.01
1250	7031.25	1.1	2.35	0.105	740.03
1300	7605	1.1	2.35	0.105	800.41
1350	8201.25	1.1	2.35	0.105	863.17
1400	8820	1.1	2.35	0.105	928.29
1450	9461.25	1.1	2.35	0.105	995.78
1500	10125	1.1	2.35	0.105	1065.64
1550	10811.25	1.1	2.35	0.105	1137.87
1600	11520	1.1	2.35	0.105	1212.46
1650	12251.25	1.1	2.35	0.105	1289.42
1700	13005	1.1	2.35	0.105	1368.76
1750	13781.25	1.1	2.35	0.105	1450.45
1800	14580	1.1	2.35	0.105	1534.52
1850	15401.25	1.1	2.35	0.105	1620.96
1900	16245	1.1	2.35	0.105	1709.76
1950	17111.25	1.1	2.35	0.105	1800.93
2000	18000	1.1	2.35	0.105	1894.47
2050	18911.25	1.1	2.35	0.105	1990.38
2100	19845	1.1	2.35	0.105	2088.65
2150	20801.25	1.1	2.35	0.105	2189.3
2200	21780	1.1	2.35	0.105	2292.31
2250	22781.25	1.1	2.35	0.105	2397.69
2300	23805	1.1	2.35	0.105	2505.44
2350	24851.25	1.1	2.35	0.105	2615.55
2400	25920	1.1	2.35	0.105	2728.04
2450	27011.25	1.1	2.35	0.105	2842.89
2500	28125	1.1	2.35	0.105	2960.11

Table B.2 Ramberg-Osgood material properties for Seed's [68] average sand with γ = 135 pcf.

Ramberg-Osgood Material Parameters for Average Sand (γ = 135 pcf)					
V_s (ft/s)	G_{max} $(10^3 psf)$	α	r	γ_y (10^{-3})	τ_y (psf)
100	41.9	1.1	2.35	0.105	4.41
150	94.28	1.1	2.35	0.105	9.92
200	167.6	1.1	2.35	0.105	17.64
250	261.88	1.1	2.35	0.105	27.56
300	377.1	1.1	2.35	0.105	39.69
350	513.28	1.1	2.35	0.105	54.02
400	670.4	1.1	2.35	0.105	70.56
450	848.47	1.1	2.35	0.105	89.3
500	1047.5	1.1	2.35	0.105	110.25
550	1267.47	1.1	2.35	0.105	133.4
600	1508.4	1.1	2.35	0.105	158.76
650	1770.28	1.1	2.35	0.105	186.32
700	2053.1	1.1	2.35	0.105	216.09
750	2356.88	1.1	2.35	0.105	248.06
800	2681.6	1.1	2.35	0.105	282.23
850	3027.27	1.1	2.35	0.105	318.62
900	3393.9	1.1	2.35	0.105	357.2
950	3781.48	1.1	2.35	0.105	397.99
1000	4190	1.1	2.35	0.105	440.99
1050	4619.48	1.1	2.35	0.105	486.19
1100	5069.9	1.1	2.35	0.105	533.6
1150	5541.27	1.1	2.35	0.105	583.21
1200	6033.6	1.1	2.35	0.105	635.03
1250	6546.88	1.1	2.35	0.105	689.05
1300	7081.1	1.1	2.35	0.105	745.27
1350	7636.27	1.1	2.35	0.105	803.71
1400	8212.4	1.1	2.35	0.105	864.34
1450	8809.47	1.1	2.35	0.105	927.18
1500	9427.5	1.1	2.35	0.105	992.23
1550	10066.47	1.1	2.35	0.105	1059.48
1600	10726.4	1.1	2.35	0.105	1128.94
1650	11407.28	1.1	2.35	0.105	1200.6
1700	12109.1	1.1	2.35	0.105	1274.46
1750	12831.88	1.1	2.35	0.105	1350.53
1800	13575.6	1.1	2.35	0.105	1428.81
1850	14340.28	1.1	2.35	0.105	1509.29
1900	15125.9	1.1	2.35	0.105	1591.98
1950	15932.47	1.1	2.35	0.105	1676.87
2000	16760	1.1	2.35	0.105	1763.96
2050	17608.48	1.1	2.35	0.105	1853.26
2100	18477.9	1.1	2.35	0.105	1944.77
2150	19368.28	1.1	2.35	0.105	2038.48
2200	20279.6	1.1	2.35	0.105	2134.4
2250	21211.88	1.1	2.35	0.105	2232.52
2300	22165.1	1.1	2.35	0.105	2332.84
2350	23139.28	1.1	2.35	0.105	2435.37
2400	24134.4	1.1	2.35	0.105	2540.11
2450	25150.48	1.1	2.35	0.105	2647.05
2500	26187.5	1.1	2.35	0.105	2756.19

Table B.3 Ramberg-Osgood material properties for Seed's [68] average sand with γ = 140 pcf.

Ramberg-Osgood Material Parameters for Average Sand (γ = 140 pcf)					
V_s (ft/s)	G_{max} $(10^3 psf)$	α	r	γ_y (10^{-3})	τ_y (psf)
100	43.5	1.1	2.35	0.105	4.58
150	97.88	1.1	2.35	0.105	10.3
200	174	1.1	2.35	0.105	18.31
250	271.88	1.1	2.35	0.105	28.61
300	391.5	1.1	2.35	0.105	41.2
350	532.88	1.1	2.35	0.105	56.08
400	696	1.1	2.35	0.105	73.25
450	880.88	1.1	2.35	0.105	92.71
500	1087.5	1.1	2.35	0.105	114.46
550	1315.88	1.1	2.35	0.105	138.49
600	1566	1.1	2.35	0.105	164.82
650	1837.88	1.1	2.35	0.105	193.43
700	2131.5	1.1	2.35	0.105	224.34
750	2446.88	1.1	2.35	0.105	257.53
800	2784	1.1	2.35	0.105	293.01
850	3142.88	1.1	2.35	0.105	330.78
900	3523.5	1.1	2.35	0.105	370.84
950	3925.88	1.1	2.35	0.105	413.19
1000	4350	1.1	2.35	0.105	457.83
1050	4795.88	1.1	2.35	0.105	504.76
1100	5263.5	1.1	2.35	0.105	553.97
1150	5752.88	1.1	2.35	0.105	605.48
1200	6264	1.1	2.35	0.105	659.28
1250	6796.88	1.1	2.35	0.105	715.36
1300	7351.5	1.1	2.35	0.105	773.73
1350	7927.88	1.1	2.35	0.105	834.4
1400	8526	1.1	2.35	0.105	897.35
1450	9145.88	1.1	2.35	0.105	962.59
1500	9787.5	1.1	2.35	0.105	1030.12
1550	10450.88	1.1	2.35	0.105	1099.94
1600	11136	1.1	2.35	0.105	1172.05
1650	11842.88	1.1	2.35	0.105	1246.44
1700	12571.5	1.1	2.35	0.105	1323.13
1750	13321.88	1.1	2.35	0.105	1402.11
1800	14094	1.1	2.35	0.105	1483.37
1850	14887.88	1.1	2.35	0.105	1566.93
1900	15703.5	1.1	2.35	0.105	1652.77
1950	16540.88	1.1	2.35	0.105	1740.9
2000	17400	1.1	2.35	0.105	1831.32
2050	18280.87	1.1	2.35	0.105	1924.03
2100	19183.5	1.1	2.35	0.105	2019.03
2150	20107.87	1.1	2.35	0.105	2116.32
2200	21054	1.1	2.35	0.105	2215.9
2250	22021.87	1.1	2.35	0.105	2317.77
2300	23011.5	1.1	2.35	0.105	2421.92
2350	24022.87	1.1	2.35	0.105	2528.37
2400	25056	1.1	2.35	0.105	2637.1
2450	26110.87	1.1	2.35	0.105	2748.13
2500	27187.5	1.1	2.35	0.105	2861.44

Table B.4 Ramberg-Osgood material properties for Seed's [68] average sand with γ = 145 pcf.

Ramberg-Osgood Material Parameters for Average Sand (γ = 145 pcf)					
V_s (ft/s)	G_{max} $(10^3 psf)$	α	r	γ_y (10^{-3})	τ_y (psf)
100	40.4	1.1	2.35	0.105	4.25
150	90.9	1.1	2.35	0.105	9.57
200	161.6	1.1	2.35	0.105	17.01
250	252.5	1.1	2.35	0.105	26.58
300	363.6	1.1	2.35	0.105	38.27
350	494.9	1.1	2.35	0.105	52.09
400	646.4	1.1	2.35	0.105	68.03
450	818.1	1.1	2.35	0.105	86.1
500	1010	1.1	2.35	0.105	106.3
550	1222.1	1.1	2.35	0.105	128.62
600	1454.4	1.1	2.35	0.105	153.07
650	1706.9	1.1	2.35	0.105	179.65
700	1979.6	1.1	2.35	0.105	208.35
750	2272.5	1.1	2.35	0.105	239.18
800	2585.6	1.1	2.35	0.105	272.13
850	2918.9	1.1	2.35	0.105	307.21
900	3272.4	1.1	2.35	0.105	344.41
950	3646.1	1.1	2.35	0.105	383.75
1000	4040	1.1	2.35	0.105	425.2
1050	4454.1	1.1	2.35	0.105	468.79
1100	4888.4	1.1	2.35	0.105	514.5
1150	5342.9	1.1	2.35	0.105	562.33
1200	5817.6	1.1	2.35	0.105	612.29
1250	6312.5	1.1	2.35	0.105	664.38
1300	6827.6	1.1	2.35	0.105	718.59
1350	7362.9	1.1	2.35	0.105	774.93
1400	7918.4	1.1	2.35	0.105	833.4
1450	8494.1	1.1	2.35	0.105	893.99
1500	9090	1.1	2.35	0.105	956.71
1550	9706.1	1.1	2.35	0.105	1021.55
1600	10342.4	1.1	2.35	0.105	1088.52
1650	10998.9	1.1	2.35	0.105	1157.62
1700	11675.6	1.1	2.35	0.105	1228.84
1750	12372.5	1.1	2.35	0.105	1302.19
1800	13089.6	1.1	2.35	0.105	1377.66
1850	13826.9	1.1	2.35	0.105	1455.26
1900	14584.4	1.1	2.35	0.105	1534.98
1950	15362.1	1.1	2.35	0.105	1616.84
2000	16160	1.1	2.35	0.105	1700.81
2050	16978.1	1.1	2.35	0.105	1786.92
2100	17816.4	1.1	2.35	0.105	1875.15
2150	18674.9	1.1	2.35	0.105	1965.5
2200	19553.6	1.1	2.35	0.105	2057.99
2250	20452.5	1.1	2.35	0.105	2152.59
2300	21371.6	1.1	2.35	0.105	2249.33
2350	22310.9	1.1	2.35	0.105	2348.19
2400	23270.4	1.1	2.35	0.105	2449.17
2450	24250.1	1.1	2.35	0.105	2552.28
2500	25250	1.1	2.35	0.105	2657.52

REFERENCES

[1] Arulanandan, K., Seed, H. B., Yogachandran. C., Muraleetharan, K. K., Kabilamany, K., (1993), "Centrifuge study on volume changes and dynamic stability of earth dams." Journal of Geotechnical Engineering, vol. 119, no 11, pp. 1717-1731.

[2] Bahram, N-O., Wriggres, W., (1987), "A note on the Optimum Choice for Penalty Parameters", Communications in Applied Numerical Methods, Vol. 3, pp. 581-585.

[3] Bathe, K., (1996), "Finite Element Procedures", Prentice Hall Inc., New Jersey.

[4] Belytschko, T., Liu, W. K., and Moran, B., (2000), Nonlinear Finite Elements for Continua and Structures, John Wiley & Sons, New York, NY.

[5] Biot, M.A. (1941), General theory of three dimensional consolidation." J. Applied Physics, Vol. 12, pp. 155-164.

[6] Biot, M.A. (1955), "Theory of Elasticity and Consolidation for a Porous Anisotropic Solid." J. Applied Physics, Vol. 26, pp. 182-185.

[7] Bolton, M. D., Steedman, R. S., (1982), "Centrifugal testing of microconcrete retaining walls subjected to base shaking." Soil Dynamic and Earthquake Engineering Conference, Southampton, Cakmak, A. S. (ed), vol. 1, pp. 311-329

[8] Caughey, T., (1960), "Classical Normal Modes in Damped Linear Systems", J. of Appl. Mech. 27, pp 269-271.

[9] Chang, N. Y., Chiang, H. H., (1992). "Analysis of Possible Separation in A Composite Dam." Personal Communication.

[10] Chang, N. Y., Oncul, F., Chiang, H. H., (1997), "Earthquake Induced Seperation in a Composite Dam", Eight International Conference of Soil Dynamics and Earthquake Engineering, SDEE'97, Istanbul. Turke, Volume of Extended Abstracts, A. S. Cakmak, M. Erdik, E. Durukal (eds), pp:264-265.

[11] Chang, N. Y., Oncul, (2000), "A Parametric Study on Seismic Behavior of A Composite Dam.", ASCE, Proceedings of Sessions of Geo-Denver 2000, Geotechnical Special Publication No 107, R. S. Pak, J. Yamamura (eds), pp:178-190.

[12] Chameau, J-L. (1980). "Probabilistic and Hazard Analysis for Pore Pressure Increase in Soils Due to Seismic Loading." PhD. Dissertation, Stanford University, Stanford, California.

[13] Chopra, A. K., (1988), "Earthquake Response Analysis of Concrete Dams.", Advanced Dam Engineering, ed. Robert B. Jansen, Van Nostrand Reinhold, NY.

[14] Cook, R. D., Malkus, D. S., Plesha, M. E., (1989), "Concepts and Applications of Finite Element Analysis." John Wiley & Sons, Inc., Singapore.

[15] Culligan. P. J., Savvidau, C., Berry, D. A., (1996), "Centrifuge modelling of contaminant transport." Electronic Journal of Geotechnical Engineering,EJGE.

[16] Das. B. M., (1993). "Principals of Soil Dynamics." PWS-KENT Publishing Company, USA.

[17] Desai, C. S., Zaman, M. M., Lightner, J. G., Siriwardane, H. J. (1984), "Thin-Layer Element for Interfaces and Joints", Int. Journal for Numerical and Analytical Methods in Geomechanics, vol. 8, pp. 19-43.

[18] Desai, C. S., Drumm, E. C., Zaman, M. M., (1985), "Cyclic Testing and Modelling of Interfaces", Journal of Geotechnical Engineering, vol. 111, No. 6, pp. 793-815.

[19] Dewoolkar, Mandar M., (1996), "A study of seismic effects on centilever retaining walls with saturated backfill." Ph.D. Thesis, University of Colorado, Boulder.

[20] Duncan, J. M., Chang, C. Y., (1970), "Non-linear Analysis of Stress and Strain in Soils", Journal of the Soil Mechanics and Foundations Division, ASCE, vol 96, No. SM5, pp. 1629-1653.

[21] Engelmann, B. E., (1991). "NIKE2D: A Nonlinear, Implicit, Two-Dimensional Finite Element Code for Solid Mechanics - User Manual," University of California, Lawrance Livermore National Laboratory, UCRL-MA-105413.

[22] Fenves, G., and A. K. Chopra, (1984), "EAGD-84, A Computer Program for Earthquake Analysis of Concrete Gravity Dams," Report No. UCB/EERC-84/11, Earthquake Engineering Research Center, University of California, Berkeley.

[23] Finn, W. D. L., Yogendrakumar M., Yoshida N., Yoshida H.,(1986), "TARA-3 A program for Nonlinear static and Dynamic Effective Stress Analysis. Soil Dynamics Group, University of British Columbia, Vancouver, B.C., Canada.

[24] Finn, L. W. D., (1991), "Estimating How Embankments Behave During Earthquakes", Water Power and Dam Construction April 1991, pp. 17-22

[25] Finn, W. D. L., Lee, H. W., Martin, G. R. (1977), "An Effective Stress Model for Liquefaction." Journal of the Soil Mechanics and Foundation, vol. 103, no GT6, pp. 517-533.

[26] Fok, K.-L., J. F. Hall, and A. K. Chopra, (1986), "EACD-3D. A Computer Program For Three-Dimensional Earthquake Analysis of Concrete Dams." Earthquake Engineering Research Center, Report No. UCB/EERC-86/09, University of California, Berkeley.

[27] Ghaboussi, J., Wilson, E., Isenberg, J. (1973), "Finite Element for Rock Joints and Interfaces", Journal of the Soil Mech. and Foundations Division, Proc. of ASCE, vol 99, no SM10, pp. 833-847.

[28] Goodman, R. E., Taylor, R. L., Brekke, R. L., (1968), "A model for the Mechanics of Jointed Rock", Journal of the Soil Mech. and Foundations Division, Proc. of ASCE, vol 94, no SM3, pp. 637-659.

[29] Hall, R. L., Woodson, S. C., (1989). "Seismic Stability Evaluation of Folsom Dam and Reservoir Project", U.S Army Waterways Experiment Station. Technical report ; GL-87-14 rept. 3.

[30] Hall, J. F., and Chopra, A. K., (1982), "Hydrodynamic Effects in Earthquake Response of Embankment Dams.", Journal of the Soil Mech. and Foundations Division, Proc. of ASCE, vol 108, GT4, pp. 591-597.

[31] Hallquist, J. O., (1978). "A Numerical Treatment of Sliding Interfaces and Impact." Computational Techniques for Interface Problems,AMD Vol. 30, K. C. Park, D.K.Gartling (eds), ASME, New York, pp. 117-133.

[32] Hallquist, J. O., Goudreau, G. L., Benson, D. J., (1985). "Sliding Interfaces with Contact-Impact in Large-Scale Lagrangian Computations," Computer Methods in Applied Mechanics and Engineering, 51, pp. 107-137.

[33] Hardin, B. O., Richart, F. E., (1963). "Elastic Wave Velocities in Granular Soils." Journal of the Soil Mechanics and Foundation Division, ASCE. Vol. 89, No. SM1, pp. 33-65.

[34] Herrmann, L. R. (1978), "Finite Element Analysis of Contact Problems", Journal of the Engineering Mechanics Division, Proc. of ASCE, vol 104, No. EM5, pp. 1043-1057.

[35] Hughes, T. J. R., (1987), "The Finite Element Method.", Prentice-Hall, Englewood, N. J.

[36] Idriss, I. M., Duncan, J. M., (1988). " Earthquake Response Analysis of Embankment Dams,"Advanced Dam Engineering For Design, Construction and Rehabilitation, ed. Robert B. Jansen, Van Nostrand Reinhold Int. Comp. Ltd.

[37] Itasca Consulting Group, (1992), "FLAC: Fast Lagrangian Analysis of Continua," User's Manual.

[38] Jaworski, G. W., Ducan, J. M., Seed, H. B., (1981), "Laboratory Study of the Hydraulic Fracturing.", Journal of the Soil Mech. and Foundations Division, Proc. of ASCE, vol 107, GT6, pp. 713-732.

[39] Katona, M. G. (1983), "A simple Contact-Friction Interface Element with Applications to Buried Culverts". Int. Journal for Numerical and Analytical Methods in Geomechanics, vol. 7, pp. 371-384.

[40] Kleinbaum, D. K., Kupper, L. L., Muller, K. E., (1988), Applied Regression Analysis and Other Multivariate Methods. Duxbury Press, Belmont California, ISBN 0-87150-123-6.

[41] Ko, Hon-Yim., (1988a), "Summary of the state-of-the-art in centrifuge model testing." Centrifuges in Soil Mechanics. Craig James & Schofield (eds).. Balkema, pp. 11-18.

[42] Ko,Hon-Yim., (1988b), "The Colorado centrifuge facility." Proceedings of the International Conference on Geotechnical Centrifuge Modelling, Centrifuge 88, Corte, J.F. (ed), Balkema, Rotterdam, Paris France, pp.73-75.

[43] Krinitzsky, E. L. , Marcuson, W. F., (1983). "Principals for Selecting Earthquake Motions in Engineering Design." Bulletin, Association of Engineering Geologists, Vol VXX, No. 3, pp. 253-265.

[44] Law H., Ko, H. Y., Sture. S., Pak, R., (1991), "Development and performance of a laminar container for earthquake liquefaction studies.", Centrifuge 91, Ko (ed), Balkema, Rotterdam, pp. 369-376.

[45] Llopis, J. L., (1989). "In Situ Seismic Investigation of Folsom Dam and Reservoir Project", U.S Army Waterways Experiment Station, Technical report ; GL-89-10, Final Report.

[46] Lysmer, J., Udaka, T., Tsai, C. F., Seed, H. B., (1975). "FLUSH: A Computer Program For Approximate 3-D Analysis of Soil-Structure Interaction Problems." Report No. EERC 75-30. Earthquake Engineering Research Center, University of California, Berkeley, CA.

[47] Maker, B. N.,(1995). "NIKE3D: A Nonlinear, Implicit, Two-Dimensional Finite Element Code for Solid Mechanics - User Manual," University of California, Lawrance Livermore National Laboratory, UCRL-MA-105268 Rev. 1

[48] Makdisi, F. I., Seed, H. B., (1978). " Simplified Procedure for Estimating Dam and Embankment Earthquake-Induced Deformations," Journal of the Geotechnical Engineering Division,ASCE, Vol. 104, No. GT7, pp. 849-859.

[49] Makdisi, F. I., Seed, H. B., (1979). " Simplified Procedure for Evaluating Embankment Response," Journal of the Geotechnical Engineering Division, ASCE, Vol. 105, No. GT12, pp. 1427-1434.

[50] Man L., Gorman D. G., (1994), "Formulation of Rayleigh Damping And Its Extensions", Computers and Structures, Vol.57 No.2, pp 277-285.

[51] Martin, P. P., Seed, H. B. (1978). "APOLLO:A Computer Program For the analysis of Pore Pressure Generation and Dissipation in Horizontal Sand Layers During Cyclic or Earthquake Loading." University of California, Berkeley. Report No. UCB/EERC-78/21

[52] Mejia, L.H., Seed, H.B., Lysmer, J., (1982), "Dynamic Analysis of Earth Dams in Three Dimensions.", Journal of the Soil Mech. and Foundations Division, Proc. of ASCE, vol 108, GT12, pp. 1586-1604.

[53] Mermel, T. W., (1991), "The World's Majaor Dam and Hydroplants", International Water Power and Dam Construction, pp. 67

[54] Muraleetharan, K. K., Arulanandan, K., (1991), "Dynamic behavior of earth dams containing stratified soil." Centrifuge 91, Ko (ed).,Balkema, Rotterdam, pp. 401-408.

[55] Newmark, N. M., (1965). " Effect of Earthquakes on Dams and Embankments," Institute of Civil Engineers, London, Vol. 15, No. 2, pp. 139.

[56] Newmark, N. M., (1959), "A Method of Computation for Structural Dynamics," J. Engng. Mech. Div., Proc. ASCE, Vol. 85, No EM3, pp 67-94.

[57] Oncul, F., (1995), "Earthquake-Induced Seperation in a Composite Dam", Master Theisis submitted to University of Colorado at Denver.

[58] Ortiz, L. A., Scott, R. F., Lee, J., (1983), "Dynamic centrifuge testing of a centilever retaining wall." Earthquake Engineering and Structural Dynamics, vol. 11, pp. 251-268

[59] Pande, G. N., Sharma, K. G. 1979, "On Joint/Interface Elements and Associated Problems of Numerical Ill-Conditioning", Int. Journal for Numerical and Analytical Methods in Geomechanics, vol. 3, pp. 293-300.

[60] Prevost, (1997). "Constitutive Models for Soils." Electronic Journal of Geotechnical Engineering, EJGE

[61] Richart, F. E. (1975). "Some Effects of Dynamic Soil Properties on Soil-Structure Interaction." Journal of the Geotechnical Engineering Division, ASCE, vol. 101, No. GT12, pp. 1197-1240.

[62] Sandhu, R. S., Wilson, E. L. (1969), "Finite Element Analysis of Seepage in Elastic Media." Journal of Engineering Mechanics Division, ASCE. Vol. 95, No. EM3, pp. 641-652

[63] Seed, H. B., (1979). " Considerations in the Earthquake Resistant Design of Earth and Rock Fill Dams," Geotechnique 29, No. 3, pp. 215-263

[64] Seed, H. B., Martin, G. R., (1966). " The Seismic Coefficient of Earth Dam Design," Journal of the Soil Mechanics and Foundations Division, ASCE, Vol. 92, No. SM3, pp. 25-58.

[65] Seed, H. B., Wong, R. T., Idriss, I. M., Tokimatsu, K., (1984). "Moduli and Damping Factors for Dynamic Analyses of Cohesionless Soils." Report No. EERC 84-14. Earthquake Engineering Research Center, University of California, CA.

[66] Seed, H. B., Idriss, I. M., Keifer, F. W., (1969). "Characteristic of Rock Motions During Earthquakes." Journal of the Soil Mechanics and Foundation Division, ASCE, Vol. 95, No. SM5, pp. 1199-1218.

[67] Seed, H. B., Martin, P. P., Lysmer, J. (1975). "The Generation and Dissipation of Pore Water Pressure during Liquefaction." Erathquake Engineering Research Center Report, No. EERC 75-26, University of California, Berkeley.

[68] Seed, H. B., and Idriss, I. M., (1970), "Soil Modulii in Damping Factors for Dynamic Response Analysis." Report No. EERC 70-10, University of California, Berkeley.

[69] Sener, C. (1979). "An endochronic nonlinear inelastic constitutive law for cohesionless soils subjected to dynamic loading." Ph.D. Thesis Submitted to Northwestern University, Evanston, Illinois.

[70] Sherard, J. L., (1973). "Embankment Dam Cracking.", Embankment Dam Engineering, New York: Wiley, pp: 271-353.

[71] Simo, J. C., Laursen, T. A., (1992), "An Augmented Lagrangian Treatment of Contact Problems Involving Friction", Computers & Structures , Vol. 42, No. 1, pp. 91-116.

[72] Speck, D. E., and Donald, D. J., (1996), "GRIZ Finite Element Analysis Results Visualization for Unstructured Grids, User Manual", Report No: UCRL-MA-115696 Rev. 1.

[73] Stadler, A., (1996). "Static and Dynamic Behavior of Cantilever Retaining Walls", A Ph.D. Thesis Submitted to University of Colorado, Boulder.

[74] Sykora, David W., Hynes, Mary E., (1989). "Seismic Stability Evaluation of Folsom Dam and Reservoir Project", U.S Army Waterways Experiment Station, Technical report; GL-87-14 rept. 2, 1989.

[75] Tan, H-C. and A. K. Chopra, (1996), "EAC'D-3D-96: A Computer Program for Three-Dimensional Earthquake Analysis of Concrete Dams," Structural Engineering Mechanics and Materials, Department of Civil and Environmental Engineering, University of California, Berkeley, California, Report Number UCB/SEMM-96/06.

[76] Tierra Engineering Consultants, Inc. (1983). "Geologic and Seismologic Investigations of the Folsom, California Area." Contract Report DACW 05-82-C-0042, US Army Engineer District, Sacramento, CA.

[77] Ueng T., Chen, J., (1992). "Computational Procedures for Determining Parameters in Ramberg-Osgood Elostoplastic Model Based on Modulus and Damping Versus Strain." University of California, Lawrence Livermore National Laboratory, UCRL-ID-111487

[78] Waggoner, F. A., (1993), "Centrifuge tests of concrete gravity dams." Dam Engineering, vol. 4, issue 3, pp.145-171

[79] Waggoner, F. A., (1992), "Centrifuge modelling and analysis of concrete gravity dams." Master's Thesis, University of Colorado, Boulder.

[80] Wahl, Ronald E., Hyne, Mary E. S., Yule, Donald E., Elton, David J., (1989), "Seismic Stability Evaluation of Folsom Dam and Reservoir Project", U.S Army Waterways Experiment Station, Technical report : GL-87-14 rept. 6.

[81] Wilson, E. L. (1977), "Finite Elements for Foundations, Joint and Fluids", Finite Elements in Geomechanics, Ed. G. Gudehus, Chapt. 10, Wiley, Chichester.

[82] Wriggres, P., Simo, J. C., Taylor, R. L., (1985), "Penalty and Augmented Lagrangian Formulations for Contact Problems", Proc. of NUMETA'85 Conference, Sweansea, pp.106.

[83] XYZ Scientific Applications Inc., (2000), TrueGrid User's Manual.

[84] Zaman, M. M., Desai, C. S., Drumm, E. C., (1984), "Interface Model for Dynamic Soil-Structure Interaction", Journal of Geotechnical Engineering, vol. 110, No. 9, pp. 1257-1273.

[85] Zienkiewicz, O. C., Clough, R. W., Seed H. B., (1986). "Earthquake Analysis Procedures For Dams (State of the Art)." Report for ICOLD, Bulletin 52.